Normandie Université

THÈSE

Pour obtenir le diplôme de doctorat

Spécialité Energie

Préparée au sein de l'INSA de Rouen - Normandie

Experimental study of lean aeronautical ignition. Impact of critical parameters on the mechanisms acting along the different ignition phases.

Présentée par
Javier Marrero Santiago

Thèse soutenue publiquement le 21/03/2018 devant le jury composé de		
Mme. Simone HOCHGREB	Professor, University of Cambridge, UK	Rapporteur
M. Marc BELLENOUE	Professeur, Institut P' / ENSMA, Poitiers	Rapporteur
Mme. Eléonore RIBER	Chargée de recherche, CERFACS, Toulouse	Examinatrice
M. José Vicente PASTOR	Professor, Universidad Politécnica de Valencia, Spain	Examinateur
M. Alain CAYRE	Expert Combustion à SAFRAN Aircraft Engines	Examinateur
M. Gilles CABOT	Professeur, Université de Rouen / CORIA	Directeur de thèse
M. Bruno RENOU	Professeur, INSA de Rouen / CORIA	Co-Directeur de thèse

Thèse dirigée par Gilles CABOT et Bruno RENOU, laboratoire CORIA UMR 6614

INSA ROUEN NORMANDIE

ED PSIME

UMR 6614 CORIA COMPLEXE DE RECHERCHE INTERPROFESSIONNEL EN AEROTHERMOCHIMIE

Contents

List of Figures

Part I

BACKGROUND

Chapter 1

Introduction

Contents

1.1 Motivation

The design of modern aeronautical engines is guided by increasingly stringent environmental regulations. Indeed, the impact of human activity on planet Earth needs to be drastically reduced. Science and technology in renewable energy sources progresses more and more. Meanwhile, the aviation market keeps growing and aeronautical propulsion still requires powerful and autonomous systems to transport heavy weights and to cover long distances. Aeronautical engines, therefore, have to rely on the combustion of high energy density fuels. Hybrid systems of coupled electrical and combustion propulsion are however being considered and studied. The use of biofuels is another approach to more renewable strategies under investigation that must be managed carefully to avoid deforestation and impact on prices of potential raw materials.

The practical reality is that current aero-engines must meet the regulations imposed by organisms such as the Advisory Council for Aviation Research and Innovation in Europe (ACARE) and this forces manufacturers to continuously innovate the engine and aeroplane designs. In particular, fuel consumption and pollutant and noise emissions must be drastically reduced, being the goals proposed for 2050 by ACARE to reduce CO_2 emissions by 75% per passenger kilometre, NO_x emissions by 90% and noise by 65% with respect to the year 2000. Other targeted pollutants are CO, unburned hydrocarbons and soot. Fuel consumption and noise emissions are mostly controlled by general design parameters, such as the bypass ratio and the overall pressure ratio, and by the compressor, turbine and exhaust designs. The integration of engines in the main body of the aircraft in such way that the boundary layer is ingested by the intake, thus reducing the drag, is a new proposal under investigation to reduce fuel consumption and CO_2 emissions. Another promising technology that will increase propulsive efficiency is the open-rotor design [8]. To this end, mass reduction encourages industrial research for stronger and lighter materials and downsizing strategies (e.g.: reducing the number of injectors in the combustion chamber).

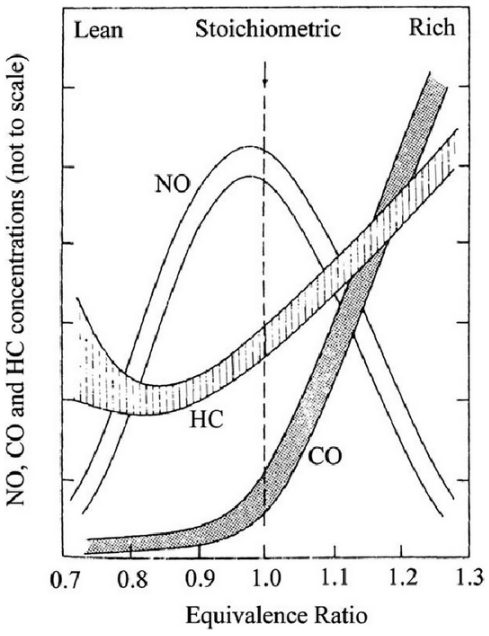

Figure 1.1: Pollutant emissions with equivalence ratio [1].

Concerning CO and NO_x emissions, they must be cut at their source: the

combustion sub-system. A major answer given by combustion experts to address this issue implies moving towards lean combustion systems where flame and burnt gas temperatures are lower, hence limiting the thermal NO_x (Zel'dovich mechanism). Figure 1.1 indicates how the pollutant formation varies with the global equivalence ratio of the combustion of hydrocarbons and demonstrates the benefits of using low equivalence ratios. Lean combustion systems carry intrinsic constraints manufacturers must deal with. Indeed, the decrease in equivalence ratio (ϕ) implies a decrease in the laminar burning velocity and, therefore, in the stability of the flame. Stable combustion regimes must be guaranteed and thermoacoustic oscillations avoided throughout all the operating conditions within a flight envelope, including water or ice ingestion, which can affect lean flames with disastrous consequences, such as complete extinction. On this basis, one of the tightest engine operability requirements is the in-flight relight capability at high altitudes in a flame-out event. The complexity of this multi-physical process will be detailed along this chapter. For obvious reasons, new lean burn engine configurations must assure re-ignition and transition to nominal operating regimes as fast as possible in safe conditions. There is an actual need for more academic and industrial research and collaborations to enable a better understanding of the ignition process in aeronautical combustion chambers, given the large amount of parameters involved simultaneously within very close and very distant times and lengthscales.

In the following, some general concepts of the jet engine will be addressed with a particular interest on the chamber, injection and ignition sub-systems. The re-ignition problem will then be discussed in detail, followed by a closer approach to the parameters governing ignition and a brief state-of-the-art review. This introduction ends with the organisation of the manuscript.

1.2 The jet engine

The jet engine or gas turbine, invented in the 30s by Frank Whittle in England and Hans Von Ohain in Germany, offers several advantages compared to piston engines, like its higher power-to-weight ratio and higher thrust potential. Based on Newton's third law, gas turbine propulsion can be simplified by the picture of a gas or air jet being expelled to the rear of the engine inducing a force of opposite direction on the engine itself. This thrust force can be expressed as

given in equation 1.1:

$$F = M(v_1 - v_0) \tag{1.1}$$

Where M is the mass of the gaseous flow crossing the engine and v_0 and v_1 the inlet and exhaust flow velocities.

1.2.1 Thermodynamic cycle and architecture

Aeronautical gas turbines are based on an open Brayton thermodynamic cycle, represented in Fig. 1.2. As described by the T-s diagram, the ingested air first follows a compression in an axial or radial compressor before burning the fuel at constant pressure in the combustion chamber. The hot flow then partially expands in the turbine supplying the work that moves the compressor provided that the turbine and the compressor are connected by a spool. The flow is finally accelerated through the nozzle to complete its expansion. Compression and expansion processes are ideally isentropical but the actual efficiency of each part yields a $\Delta s > 0$ at every stage. Numbers in Fig. 1.2 refer to typical notation, as shown in Fig. 1.3. This particular engine has two spools of different nominal rotating speeds: one connecting the low pressure (LP) compressor and turbine and another one connecting the high pressure (HP) compressor and turbine. Here, a part of the air that flows through the LP compressor enters the HP compressor while the remainder surrounds the main engine body to meet the hot jet at the exit. The ratio of surrounding air to the air entering the engine core is defined as the by-pass ratio and has great impact on propulsion efficiency. Jet engines can adopt several mechanical arrangements to conceive configurations including turbo-jets, turbo-fans and turbo-propellers, with simple, double or triple spools and different by-pass ratios. For more information the reader is referred to [2].

1.2.2 Chamber, injection and ignition systems

Combustion chamber

The main function of the combustion chamber is to mix the air coming from the compressor with the fuel coming from the injectors to establish a stable combustion process at constant pressure and send the hot combustion products to the

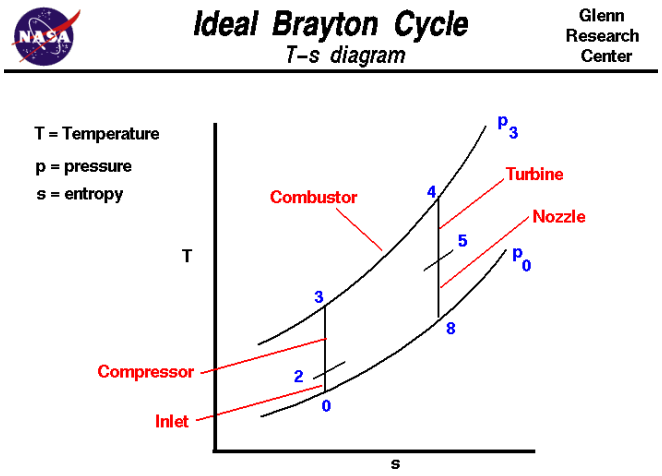

Figure 1.2: T-s diagram of ideal Brayton cycle.

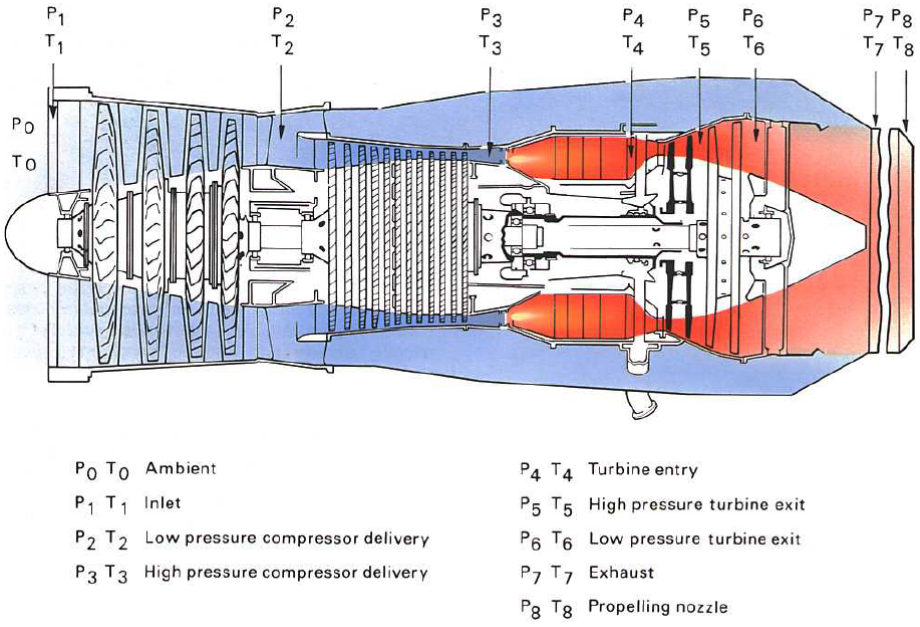

Figure 1.3: Typical pressure and temperature notation in a turbo-jet engine [2].

turbine. The design of the chamber and of the injectors must account for the mixing quality since the fuel must burn as efficiently as possible to minimise fuel consumption, as well as pollutant formation. The flow coming from the compressor presents an excessive velocity for flame stabilisation and it is, therefore, forced to pass through a diffuser raising its static pressure, thus reducing its velocity at the exit of the compressor. Furthermore, only a portion of this flow

enters the chamber through the injectors while the rest surrounds the chamber walls for cooling purposes. Cooling of the combustion chamber walls close to the flame is, indeed, a primordial issue in the design and it can be tackled through different solutions, such as cooling rings, cooling strips, internal cooling and effusion plates [2]. Typical flow repartition is represented in Fig. 1.4. Materials used for combustion chambers need to be light and temperature resistant. In the past, chambers were divided in sectors (e.g.: tubo-annular design) but the most accepted arrangement nowadays is the annular combustion chamber, which is lighter and facilitates flame propagation between injectors during ignition.

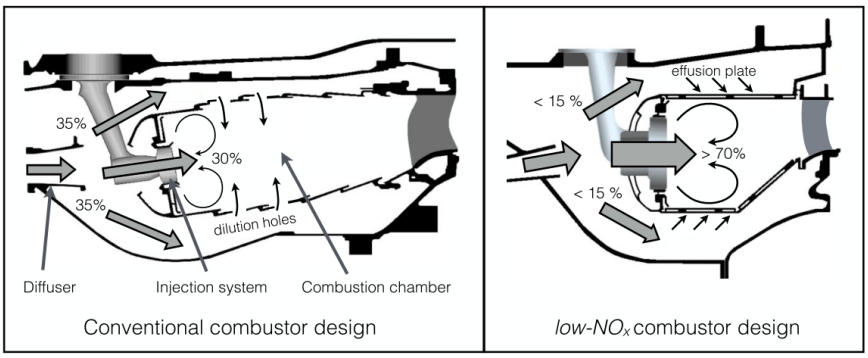

Figure 1.4: A section of conventional (left) and low-NO_x (right) combustion chambers [3].

A strategy used by early combustion chambers to stabilise the flame near the injector was to add an obstacle in the airflow producing a recirculation or a low velocity region where a flame could anchor. Currently, the use of swirled injection systems has been adopted by all major manufacturers. Axial or radial swirlers induce rotation in the airflow that enhances turbulence for mixing and creates a reverse flow if the swirl is high enough [9]. This inner recirculation zone (IRZ) forces the appearance of stagnation regions and acts as a strong mechanism to stabilise the flame [10]. In the transition from the injector to the chamber, the sudden change in flow section induces a toroidal outer recirculation zone (ORZ) at the base of the chamber. Typical wall-to-wall distances are $\approx 10\ cm$ at the injection plane. The length of the chamber is a parameter that needs to be optimised in the design stage. For instance, a shortening of this length yields a more compact engine and reduces the residence time of gases in the chamber, hence reducing NO_x formation [4]. This must be done carefully to guarantee a minimum residence time for CO oxidation to occur.

As introduced before, new burner configurations more towards lean combustion by introducing more air through the injector for the same fuel mass flow rate, as represented in Fig. 1.4 (right). Leaner flames are more prone to thermoacoustic instabilities and to extinction, and ignition becomes a more complicated task. Many laboratory-scale experiments and simulations have been performed in facilities representative of aeronautical combustion chambers where similar wall-to-wall lengths ($\approx 10\ cm$) confine a swirling flow. The typical flow patterns, such as the IRZ and the ORZ have been well studied and characterised in reacting and non-reacting conditions [11–15]. Lean flame stability has been investigated in these configurations [16,17] with different gaseous and liquid fuels and different operating conditions. Figure 1.5 illustrates the typical flame stability and ignition loops in a chamber, revealing that ignition is more restrictive than stabilising a flame, hence more complicated.

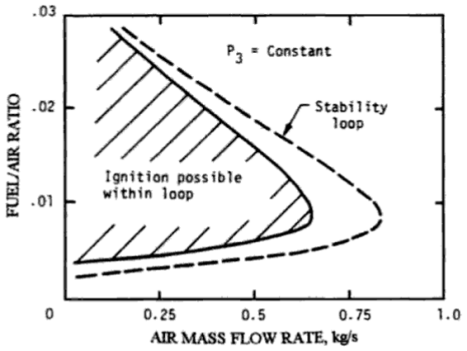

Figure 1.5: Typical stability and ignition loops [4] of real chambers.

Injection system

Jet engines burn liquid fuels because of their high energetic density. Kerosene is the most extended fuel for aviation due to its high heating value and its low pour point (-47^oC commercial standard). The desired functions of an injection system are to guarantee the constant fuel supply into the chamber, the vaporisation of the liquid and the mixing with the air to prepare it for an efficient combustion. Producing fine fuel droplet mists maximises the surface between the liquid and the gaseous phases and enhances heat and mass transfer, and thus evaporation. Turbulence contributes to a rapid mixture preparation. Atomisation is based on the destabilisation of a liquid sheet to generate ligaments (primary atomisation)

that are then broken into droplets (secondary atomisation). This can be achieved by means of different mechanical processes. Different injector technologies [18] include pressure swirl atomisers, vaporisers and air-blast atomisers. The former uses a pressure difference between the combustion chamber and a pressurised fuel line to force a swirling liquid sheet through a fine hole. The main disadvantages of this system is that the small injection orifices can clog and stop the fuel injection and that it requires adjacent fuel pressurisation systems that add complexity and weight to the engine. The main advantage is that atomisation does not depend on the air flow and droplet sizes are independent of the operating conditions. Vaporisers inject fuel vapour through a tube placed in the primary combustion zone. The fuel evaporates in the tube due to the high heat flux from the flame, which is disastrous for the tube lifetime. Air-blast atomisers are very extended and use the swirling airflow to breakup the liquid (Fig. 1.6). Generally, the liquid is splashed conically onto a metallic pre-filming cylindrical wall where a first swirling air jet drags it to the tip to generate ligaments. A second counter-rotating air jet participates in the secondary atomisation creating a strong shearing region. Air-blast atomisers are simpler systems that do not present the disadvantages of the other technologies but rely on the airflow. This becomes a real issue for re-ignition in high altitude and it will be explained below.

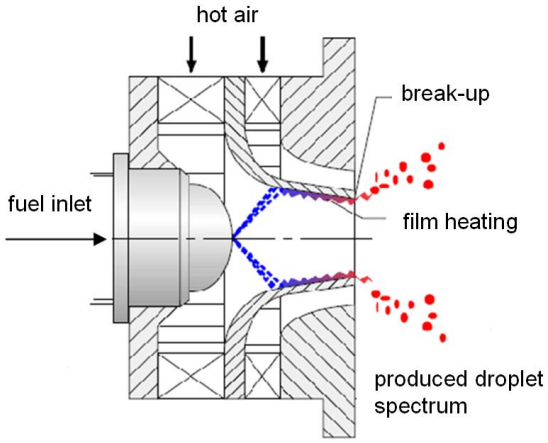

Figure 1.6: Air-blast atomiser [5].

Ignition system

The ideal ignition system should be lightweight, simple to integrate and reliable to assure the successful ignition of the fuel in the chamber in all possible operating conditions. Moreover, it should be resistant to erosion or degradation in order to reduce maintenance costs. Igniters work on the principle of depositing a very high localised energy quantity that will eventually activate chemical reactions to obtain a stable flame. The most common ignition system is the spark plug igniter, where the voltage between two electrodes raises above the breakdown threshold of the air gap between them establishing an ionised channel, thus closing the circuit. Spark plug discharges are characterised by three phases (i.e.: breakdown, arc and glow) with different durations, efficiencies and energies [19]. The voltage values expected in the pre-breakdown depend on the electrode gap and on the air properties [20] and the total spark duration can extend to some milliseconds [21, 22]. According to [23, 24] between 10% and 30% of the energy is transferred to the gas due to losses by conduction into the electrodes, by the shockwave and in the electrical circuit. In addition, the electrodes of the spark plugs are a heat sink term and cool down the flame kernel preventing its development [4, 25–27]. Another disadvantage of this system is its fixed location in the chamber wall, which is a suboptimal quench zone of the combustor. Indeed, the optimum spark position depends on the local flow conditions and should be distant from the quenching metal walls [28]. Moesl et al. [28] also stated that spark plugs show bad performances in ignition of lean mixtures below $\phi = 0.6$. Moreover, the isolation separating the electrodes in the spark plug can be eroded (Fig. 1.7), thus degrading the operability. On the other hand, spark plugs present the advantages of being cheap and light systems, robust and they can deposit high energies. An improvement of this technology can extend its operability range to meet complex objectives, such as re-ignition in high altitude.

Figure 1.7: Damaged spark plug.

There exist other known technologies such as the glow plug and the pyrotech-

nic igniter cartridge. The former consists in plugging a hot bar into the chamber to ignite the mixture. This is cheap and light but shows limited lifetime and introduces a risk of debris damaging the turbine. The pyrotechnic igniter cartridge is used in missiles and ignites the mixture due to the production of hot combustion gases directly in the chamber. It is a reliable system in complicated environments and reduces ignition delay times. However, it can only be used once.

Other ignition systems are the torch igniter [4], the plasma jet igniter [29] and laser-induced spark ignition. The latter presents a very interesting advantage, which is the lack of electrodes and the freedom to chose the desired chamber location for triggering a laser-induced spark [28,30]. It is a promising technology for future ignition of lean mixtures and, certainly, a useful tool for present studies on this topic. However, this technology is used in research approaches and still needs to evolve for industrial applications. Indeed, here it is used in order to select the ignition location in the chamber. Laser-induced sparks are based on the focalisation of a pulsed laser beam in one point using a convergent lens. If energy density is high enough in the focalisation point, multi-photonic ionisation occurs, hence a plasma is created. Laser-induced sparks last generally some nanoseconds [31, 32] and generate energetic plasmas [33] leading to a shockwave [34] that carries away a large portion of the deposited energy [35]. Lasers are very sensitive to temperature variations and to vibrations. A competitive laser ignition system would need to overcome these difficulties and must yield a compact and light device. Another critical constraint is imposed by the focalisation lens, which must withstand the chamber wall temperatures and must remain clean. This can suppose an issue if liquid fuel or soot deposition occurs. However, some studies have reported the capability of the laser beam itself to clean the lens [28].

Advanced ignition systems also include the radio-frequency initiated μ-wave ignition system (project by Safran HE, APOJEE and PPRIME), which is based on a radio-frequency discharge that spaces out the initial plasma followed by an injection of micro-waves enabling the expansion of the plasma with good energy transfer characteristics.

Concerning aeronautical engines and taking into account the fuel injection systems, the selected ignition technology must show efficient operation and large operability under spray flows, where fuel droplet sizes vary inside a wide range, namely in high altitude conditions where atomisation and evaporation are very

limited (next section). To this end, some designs still need to be improved or adapted because the presence of large droplets can modify the energy deposition (e.g.: laser focalisation problems, sparking in dense spray regions, repeatability, etc.).

1.3 The Ignition Process

Engine start involves turning the compressor and turbine with a starter device until enough air enters the chamber and igniting the mixture in the chamber. This occurs on land. Restart in-flight can be performed, where the starter device would turn the compressor and turbine and the chamber would be ignited. However, in a flame-out event during flight the high pressure body turns at a certain velocity induced by the air relative velocity (autorotation). This enables not to use the starter and relies on the reignition of the chamber, also called relight. The choice between restarting an engine or just relighting it depends on the autorotation speed and the flight Mach number. For relight, the autorotation speed must be high enough to assure the correct flows of air and fuel, and it can vary depending on the flight domain.

Considering the different issues addressed until now and the complexity of the chamber, injection and ignition systems, the aeronautical ignition process seems to involve a large list of elements of different nature simultaneously. The ignition process in real combustion chambers is, indeed, very complex [36–38]. For instance, the local non-reacting (not ignited) flow in the combustion chamber varies very strongly from one location to another and from one instant to the next one. Each region has different flow patterns with different velocities and fluctuation levels. The injection of liquid fuel can lead to strong mixture variations because droplets have finite evaporation times. Ignition is, therefore, governed by the design of the chamber and injectors but also by the ignition system: the location, duration and energy of the spark are critical aspects governing the process. The local temperatures, small-scale turbulent movements and droplet size distributions are also parameters of major importance. Concerning in-flight high altitude relight in a flame-out event, the compressor and turbine rotate at a low speeds minimising the air flow through the injectors with disastrous consequences in the fuel atomisation quality, hence in evaporation and mixing. In a short time lapse the fuel and the chamber surroundings cool down

due to the lack of compression and combustion, since air temperatures at high altitudes ($\approx 10\ km$) are of $T \approx -50\ ^oC$ while pressures are of $P \approx 0.3\ bar$. A such cold environment lowers the fuel volatility and increases its viscosity, thus preventing evaporation and causing accumulation of liquid in the chamber. Liquid accumulation in the chamber is not desirable because a successful ignition would potentially generate over-pressures and high heat fluxes under small air flows (minimal cooling) until nominal rotation velocities were again attained.

Despite all the difficulties, current engines working at near-stoichiometric mixture conditions ($\phi \approx 1$) manage to relight the engine in a flame-out event. Low-NO_x designs imply higher flow velocities in the chamber and lower equivalence ratios with direct negative consequences on the flame kernel initiation and development and on flame propagation. In order to ensure successful ignition and have the control of the process under such conditions, a deeper understanding of the multi-physical processes and mechanisms here involved is needed and ignition must be studied from the experimental and numerical points of view in industry and academia.

1.3.1 Aeronautical ignition phases and current research

Ignition in aeronautical engines occurs through particular paths involving different timings and different parameters. To tackle the problem it must be divided into different characteristic phases that present different mechanisms and critical interactions. Lefebvre initially identified 3 different phases [4] that are accepted and used by other authors, such as Boileau et al. [38]. Mastorakos [37] extended this to 4 phases considering Lefebvre's phase 2 as two separate steps. Hereafter, Mastorakos' aeronautical ignition phases will be considered:

- **Phase 1 - Flame kernel initiation:** energy deposit, evolution of the hot gas kernel and transition to a reacting flame kernel, with the initiation of chemical reactions. Typical timescales $t \approx 1 - 100\ \mu s$.
- **Phase 2 - Kernel growth and propagation:** flame kernel evolution, growth and interaction with the surroundings. Transition between different regions in the chamber and development. Typical timescales $t \approx 1 - 10\ ms$.
- **Phase 3 - Flame stabilisation on one injector:** transition from a flame kernel into a stable flame. Flame stabilisation over one single injector.

Typical timescales $t \approx 10 - 100\ ms$.

- **Phase 4 - Lightaround:** injector-to-injector propagation or light-around. The stable flame propagates crossing the inter-injector region (IIR) and lights neighbouring injectors successively until all injectors show a stable flame. Typical timescales $t \approx 100 - 1000\ ms$.

Once all the chamber has been ignited, a fifth phase must be considered. Phase 5 involves the transition from a situation of combustion with low air mass flows in the chamber due to a reduced compressor and turbine rotation to nominal operating conditions. This transition must occur as fast as possible to avoid overheating the chamber and turbine and to return to safe conditions in time.

Since ignition is controlled by so many fluctuating parameters, each individual process implies stochasticity [39] and investigations must account for stochastic approaches, such as ignition probability. The term of ignition probability was first introduced by Birch et al. [40] and Smith et al. [41]. In the literature, the term ignition probability may refer to different events [37] and this should be clarified. A first step is to define the flammability factor (F) as the probability of sampling an ignitable mixture at the spark location when triggering the spark. The flammability factor was proposed by [40] and is defined by equation 1.2, where ξ_{lean} and ξ_{rich} are the lean and rich flammability limits and $P(\eta)$ is the probability density function of the mixture fraction.

$$F = \int_{\xi_{lean}}^{\xi_{rich}} P(\eta) d\eta \tag{1.2}$$

Next, the probability of initiating a flame kernel after a sparking event, hence completing Phase 1 is defined as P_{ker}. A flame kernel can extinguish before arriving safely to Phase 3. P_{ign} is the probability of obtaining a stable flame over one single injector. Similarly to the different ignition probabilities, associated failure modes were proposed in [37]. The $first$ or *short mode* of ignition failure is attributed to the lack of success in initiating a flame kernel (Phase 1 failing), which can be caused by different reasons explained in the following. The *second* or *long mode* of ignition failure describes the failure of a flame kernel to ignite the burner; this is, extinction of the kernel during Phase 2. The *third mode* of ignition failure proposed by Mastorakos [37] occurs when a flame fills the combustor seeming to safely arrive to Phase 3 but then global extinction happens.

This seems to be specific to recirculating flames and may be connected to the phenomenon of blow-off [42,43], but will not be further commented in this work. Differences between F, P_{ker} and P_{ign} will be addressed below, in a more detailed description of the mechanisms controlling each ignition phase and of the current progress in research.

Phase 1: Flame kernel initiation

This is the most studied ignition phase in the past works. The initiation of a sustainable flame kernel depends on the flow characteristics at the spark location (i.e.: velocity, turbulence, droplet size, mixture quality, temperature) and on the spark properties. A spark can trigger a flame kernel due to its high temperature but also due to the radicals present in the plasma [44]. The size and temperature of the initial hot gas kernel (still not flame kernel) are critical for its later growth and the initiation of chemical reactions [45]. Indeed, as established by the Williams' criteria, the energy supplied must be enough to heat the critical gas volume from its initial state to flame temperatures [4, 46]. The duration of the spark is also important in fluctuating flows because a longer spark increases the probability of sampling favourable flows in terms of mixture and velocities.

A lot of research [47–52] has been conducted on the so-called minimum ignition energy (MIE), which involves Phase 1 and is defined as the energy needed to obtain $P_{ker} = 50\%$. The pioneer works of Ballal and Lefebvre accounted for the MIE in turbulent premixed flames, where the effects of turbulence, global equivalence ratio and pressures were also investigated [53–56]. Theoretical predictions of the minimum ignition energy [47] included the consideration of finite chemistry via the laminar burning speed and accounted for the influence of the vapour phase and of droplet size distributions in two-phase flows. With respect to two-phase flows, if the droplet vaporisation time is smaller than the heat diffusion time, the hot gas kernel yields a growing flame kernel [47].

The competition between the turbulence fluctuations and the chemical ignition delay time is critical for a flame kernel initiation from a sparking event. The failure of a spark to initiate a flame kernel can be attributed to local factors such as fluctuations of the mixture fraction [42] velocity fluctuations [22], strain rate [57, 58], turbulence [42] and droplet Sauter mean diameter [59]; but also to non-local effects including the diffusion of the spark energy [42, 57]. Concerning the latter, flow timescales may be able to transport or strain the spark

energy and radicals if its duration is too long [57], having a negative or positive impact. This makes possible that a spark deposited in a non-flammable region ($F = 0$) can initiate a flame kernel in a neighbouring region where $F > 0$, giving $\mathrm{P}_{ker} > F$, which would be otherwise counter-intuitive because it is expected that $\mathrm{P}_{ker} < F$. This long-range effect has been named *overdrive* and observed in simulations [58] and experiments [57].

Phases 2 and 3: Kernel growth, propagation and stabilisation

Investigations on Phase 2 and 3 are less numerous and the majority of them are focused on isolated parameters. They include premixed [36] and non-premixed [42, 60] studies, addressing laminar [61] and turbulent [36, 62, 63] problems in different configurations (i.e.: opposed-flows, co-flows, mixing layers or swirling flows), the majority of which deal with gaseous flows. Two-phase flows have also been discussed in detail in [43, 45, 64, 65].

In order to sustain the created flame kernel, the rate of heat release of the initial chemical reactions must equilibrate the rate of heat loss [46]. Scalar dissipation [66] and heat flux across its surface strongly impact the evolution of the kernel. If the kernel does not shrink, its early expansion is dominated by the hot to cold flow densities, the flame curvature and the laminar flame speed, which depends on the temperature and on the equivalence ratio of the mixture. The size of the flame kernel increases at a speed dictated by the local flame curvature and characteristic scales at play [47]. The next step involves large flow scales between the flame front and its surrounding, where turbulent lengthscales can interact with the kernel. Only if the flame front reaches sizes comparable to the smallest turbulent structures, transition to a turbulent flame occurs with the consequent wrinkling and stretching of the flame front, thus enhancing flame propagation (if the flame is not quenched by too high turbulence) [58, 67, 68]. The effect of turbulence on kernel growth was highlighted in simple and well-defined experimental configurations [69–72]: for mild turbulence, kernel growth is boosted by increasing turbulence intensity while for high turbulence, increasing turbulence intensity forces the growth rate to drop. Indeed, high turbulence is disastrous for the flame and can cause the extinction of the kernel. In [36], Ahmed mentioned that the main reasons causing ignition failure are strain rate, mixture fraction, mean flow velocity and mean turbulence ahead of the flame kernel. The effects of the mixture composition is less studied experimentally because it requires com-

plex set-ups [57,59,60,73]. DNS studies such as [67,74] have addressed this. Lean mixtures can contribute to kernel decay due to reduced laminar flame speed and heat release.

Spray combustion was studied by DNS in [75] where observed flame structures could be classified with respect to three dimensionless quantities characterising the equivalence ratio in the core of the spray, the ratio between inter-droplet distance and flame thickness and the ratio between evaporation times and flame times. Reveillon and Vervisch [75] observed partially premixed combustion regimes in most of the spray flames and proposed a three-dimensional combustion diagram to classify dilute-spray combustion regimes. Two-phase flows have been considered in [76–78]. The presence of droplets complicates the task to experiments and simulations as well as the physics here involved. Droplets inside the spark region evaporate instantaneously supplying vapour ready to mix and burn. When facing a flame front, droplets supply fuel vapour and increase the immediate local equivalence ratio in the preheat zone, but also act as heat sinks, requiring heat from the flame to evaporate. In addition, they can cross the flame front causing local flame extinction and drop-scale flame wrinkling. Moreover, in lean mixtures, inter-droplet regions can establish ignitable paths with nice mixture fraction values for the flame to develop. Several investigations have demonstrated the importance of droplet size, concentration and spacing in the ignition process [53, 79, 80]. Turbulent flame speed increases with decreasing Sauter mean diameters (SMD) and with increasing volatility but Moesl et al. [28] found that an increase in SMD carried an increase in the ignitable area of their chamber and drastic changes in D_{32} could even switch the ignitable regions inside the chamber.

Different sparking events in a same chamber location can give successful or missed ignitions due to the fluctuations of the fluid state. This is conditioned by turbulent mixing and velocity fields [74, 81, 82] and suggests the use of the ignition probability as a local parameter for combustor designs [28, 39, 42, 59]. Flame propagation in the chamber and the flow characteristics in the sparking location are both critical steps of the process [45]. The history of the kernel is, thus, an important issue, but not the only one. During Phase 2, the kernel will propagate and move into new chamber regions interacting with the flow. This aspect is also critical because it will be confronted to strong gradients and changes in the flow parameters. The flame kernel can be initially described as

a premixed flame. Surrounding droplets stratify enormously the mixture and the subsequent flame propagation spans a wide range of mixture fractions and abrupt gradients that can be favourable or detrimental.

For an expanding flame kernel to transit into Phase 3, the whole burner must be ignited, generally by propagation against the main flow. Bach et al. [83] found in a single-injector chamber through OH* chemiluminescence that successful ignitions were associated with the movement of the kernel upstream and that ignition probability decreased when sparking downstream. Upstream propagation requires a turbulent flame speed larger than the local flow speed [40, 41]. Recirculation zones are an alternative path for the flame where this is not necessary.

Despite the research devoted to flame kernel development under numerous varying conditions, there are scarce investigations on realistic aeronautical ignition in burners including swirl, confinement and liquid fuel [59]. Read et al. [7,84,85] tackled the relight problem under realistic high altitude conditions in a lean-direct-injection chamber from Rolls-Royce. These experiments evaluated the flame development by high-speed imaging and the qualitative fuel distribution by kerosene-PLIF at high airflow and at low airflow conditions. Some of the main conclusions were that the flame development is mainly controlled by the local flow field; that the spark kernel is rapidly disintegrated for unsuccessful ignition trials; that small droplets are trapped by recirculating flow zones and produced in greater numbers for high airflow rates; that large droplets impinge on the chamber walls; and that little fuel is apparent near the spark plug. They suggested that turbulent straining was more important than the local equivalence ratio, but experiments to characterise the flow velocity and turbulence were not performed and the local equivalence ratio was not quantified. In the same combustion chamber, propane concentrations were measured with a fast flame ionisation detector following pulsed fuel injections to identify transport and recirculation timescales in the chamber and to study the potential effect on a sparking event of previous sparks. Systematic fluctuations of the cold flow were observed and it was stated that sparking at a specific point of the cold flow cycle could improve relight performances.

Phase 4: Lightaround

Phase 4 has been less addressed by research until nowadays. Light-around was first investigated by Boileau et al. [38] for a helicopter engine using LES. The expansion of the burnt gases was found to be one of the mechanisms driving flame propagation from injector-to-injector. To experimentally investigate this phase in laboratory-scale facilities either linear or annular confined arrangements of swirling injectors are employed. Bourgouin et al. [86] used an annular configuration (MICCA) to study the propagation mechanisms in a premixed configuration and they identified one type of propagation guided by the volumetric expansion of the burnt gases behind the flame front, but also driven by the turbulent flame speed and convection of the flow. The effects of buoyancy were introduced to explain the propagation of a portion of flame downstream in the chamber. The ignition delay time of the complete chamber was found to depend inversely on the bulk injection velocity. Philip et al. [87,88] performed simulations of phase 4 in the MICCA annular chamber and identified different steps of the propagation from the ignition of the first injector until the merging of the fronts. A good prediction capability of the LES was shown and the flame geometry and the merging times were characterised. They found that the path followed by the flame in the chamber and the ignition delay changed for the flame front propagating in the clockwise direction to the flame front propagating in the anti-clockwise direction, highlighting the importance of swirl.

Cordier et al. [73, 89] and Barre et al. [90] studied a non-premixed linear multi-injector array (KIAI injector geometry) from the experimental and numerical viewpoints, respectively. For the first time, two distinct flame propagation mechanisms were observed and analysed and attributed to different inter-injector distances. Short distances reported a *radial* propagation mechanism that they called $span - wise$ and long distances yielded *axial* propagation mechanisms (named propagation in *arch mode* in this work) being the critical switching distance $d = 16\ cm$. This was analysed in terms of the local equivalence ratio and flow fields. LES captured well the ignition delay times and the mechanisms. Machover and Mastorakos [91–94] recently tackled premixed and non-premixed configurations in linear and annular injector arrays numerically and experimentally. They varied injector spacing from 29.5 mm to 44 mm and found the ignition speed to increase when adding swirl, when increasing the bulk velocity

and the global equivalence ratio and when decreasing the injector-to-injector distance. The importance of the inner recirculation zone (IRZ) in the propagation between injectors was underlined here, as well as the *bridges* of $F > 0$ established in the inter injector region (IIR). They identified, as well as [83] did, a sawtooth flame propagation pattern from injector-to-injector independently of the inter-injector distance. The aerodynamics of a linear array was investigated in [95]. Worth et al. [96] investigated the interaction of premixed neighbouring flames.

Works on two-phase flows are scarce. Prieur et al. [97] recently presented their results in the MICCA-Spray for propane (gaseous), n-heptane and dodecane, showing that the volatility of the fuel has an important impact on ignition delay times. Lancien et al. [98] performed the corresponding LES and described the thrust effect on the fresh mixture close to the propagating flame front, as seen in gaseous configuration by [99]. Another 5-linear spray arrangement was studied [100] and the observed flame spreading along the lateral direction was shown to be independent of the injector-to-injector distance, the fuel mass flow rate, the air pressure drop across the swirlers and the upstream air temperatures.

1.4 Objectives and organisation of the manuscript

The present experimental work is placed in the context of the critical mechanisms involved in aeronautical ignition at each phase, under the scope of moving onto more complex and realistic configurations. There is still a lack of research on complex two-phase flows concerning phases 2, 3 and 4 of ignition. The configurations studied here are highly turbulent, with swirling motion, globally very lean, confined and characterised by a high two-phase content. This is a previous necessary step to tackling low temperature and pressure conditions for high altitude relight.

Since Phases 2 and 3 only concern one single injector, the KIAI facility (studied in [73]) was adapted to the KIAI-Spray facility, giving a confined swirled jet-spray burner:

- The **first objective** is to characterise the local non-reacting flow to understand its behaviour in the different characteristic regions of the combustion chamber (IRZ, ORZ, spray-jet-zone) in terms of velocity of the dispersed

and carrier phases, turbulence, fuel droplet size and distribution and mixture formation. The latter specially poses a challenge for experiments in heterogeneous two-phase flows.

- Using this information, the **second objective** is to provide new insight on ignition Phase 2 from different points of view: first, the elaboration of an ignition probability map (of P_{ign}) whose analysis will be coupled to the non-reactive local flow properties; and second, the acquisition of high-speed image sequences of flame kernel evolution at different chamber locations that will enable to explain ignition more deeply and complementarily. Indeed, in this part a new classification of the mechanisms governing Phase 2 is proposed, introducing typical ignition modes, flame kernel extinction modes and their associated timings, causes and chamber locations. This will provide, for instance, an itemisation of what is considered actually as the *second* or *long mode* of ignition failure [37]. An ongoing and close collaboration between CORIA and CERFACS will contribute to a deeper understanding of Phase 2: LES results will be punctually presented, analysed and compared to the experimental results.

- The **third objective** is to analyse the stabilisation of the flame and the stabilised flame and reacting flow topologies to address Phase 3, which will also benefit from the comparison between LES (CERFACS) and experiments (CORIA).

Phase 4 is investigated in a multi-injector linear array where each injector is geometrically identical to the KIAI-Spray design and where inter-injector spacing can be varied. This facility is named the CORIA Linear Swirled Spray Burner (CLSSB). The simulations at CERFACS are currently addressing Phase 4 and cannot be included in the manuscript. Concerning Phase 4:

- The **fourth objective** is to investigate the effect of different inter-injector spacings on the local aerodynamics and on the local equivalence ratio of the non-reacting flow.

- The **fifth objective** is to study flame propagation between injectors (Phase 4) for different spacings and for fuels of different volatilities in order to show the effect of these parameters on total chamber ignition delay times and on

the characteristic propagation mechanisms. The results are analysed using the associated behaviour of the non-reacting flow.

This manuscript is divided in five parts:

- Part I: BACKGROUND

  Part I contains **Chapter 1**, the introduction.

- Part II: METHODS

  In Part II, **Chapter 2** and **Chapter 3** describe respectively the experimental facilities and the employed diagnostics and post-processing. A special effort is made here to detail the variables targeted by each technique, as well as their intrinsic difficulties and the acquisition strategies. The results are then presented and discussed following a chronological line in accordance to the ignition process.

- Part III: SINGLE-INJECTOR BURNER RESULTS. IGNITION PHASES 2 & 3

  Part III tackles ignition phases 2 and 3 in the single-injector KIAI-Spray facility through chapters 4, 5 and 6. In **Chapter 4** the non-reacting local flow properties are analysed to then address ignition probability and kernel evolution (Phase 2 of ignition) in **Chapter 5**. To finish Part III, **Chapter 6** offers a more brief description of the stabilisation and of the stable flame and reacting flow topologies associated to Phase 3.

- Part IV: MULTI-INJECTOR BURNER RESULTS. IGNITION PHASE 4

  Part IV concerns investigations in the CLSSB multi-injector facility on ignition Phase 4. Here, **Chapter 7** is devoted to the non-reacting local flow properties for different inter-injector spacings and **Chapter 8** contains the analysis of the flame propagation mechanisms, flame topology and ignition delay times for varying inter-injector distances and fuels.

- Part V: CONCLUSION

  This work finishes with Part V, where the conclusions and perspectives on the investigations are described in **Chapter 9**.

This thesis has been carried in the framework of the ANR TIMBER project, which joins Safran Tech, EM2C (Paris), CERFACS (Toulouse) and CORIA (Rouen).

Part II

METHODS

Chapter 2

Experimental Facilities

Contents

This chapter is devoted to the detailed description of the experimental facilities object of the study with special emphasis on the fuel and air injection systems and on the operating conditions. A single-injector burner and a multi-injector burner with identical injector geometries were employed.

2.1 Single-injector Burner

The KIAI-Spray single-injector burner is the two-phase flow version of the original KIAI burner (that worked in gaseous configuration) previously investigated by Cordier et al. [60]. The results of experiments carried on this facility are presented in Chapters 4, 5 and 6 and contribute to the analysis of Phase 2 and Phase 3 of aeronautical ignition (see Chapter 1). The investigation here performed enables the precise characterisation of the fuel droplet size distribution

and size-classified velocity, as well as the description of the instantaneous, mean and fluctuating air velocities by different experimental means. Experiments on this burner also contribute to the description of the mixing quality and the ignition properties and mechanisms. Measurements in this swirled, confined chamber contribute to a better understanding of the aero-thermodynamics and ignition of confined lean swirling spray flows.

Figure 2.1 shows a render of the CAD design of the single-injector burner (left) and a photo of the real burner (right). Four quartz windows enclose the chamber providing full optical access for the correct application of precise, non-intrusive measurements. Figure 2.2 illustrates the top view of the chamber base, where the liquid injection takes place at the centre and the air injection surrounds the liquid injector forming an annular co-flow.

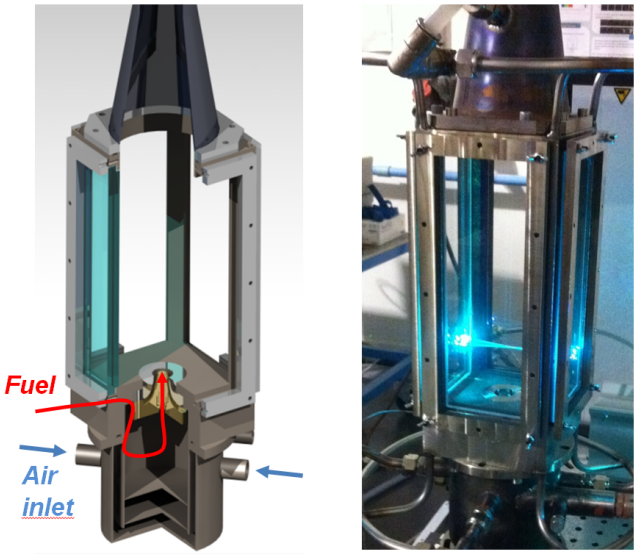

Figure 2.1: Left: render of the KIAI-Spray burner CAD design with detail of the air plenum and fuel injection system. Right: photograph of the burner during the PDA measurements.

The KIAI-Spray burner is composed of a fuel and an air injection systems, which are thoroughly described in the following sections. The chamber has a square section of 100 $\times$ 100 mm^2 and a height of 260 mm [73]. In addition, an exhaust convergent nozzle is incorporated at the top of the chamber to avoid possible external air entries, and a dynamic pressure sensor sampling at 10 kHz was installed in the exhaust nozzle. The burner is equipped with one thermocou-

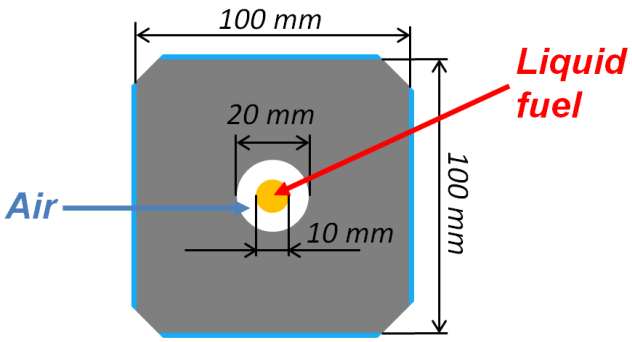

Figure 2.2: Top schematic view of the injection plane of the KIAI-Spray chamber where the air inlet (white) and the spray atomiser (yellow) are indicated.

ple in the airflow, close to the exit of the air duct, in order to control the co-flow inlet temperature. For the sake of repeatability and control during the ignition experimental campaigns, a 1.5 mm diameter thermocouple and a flat wall thermocouple were respectively installed at the internal and external surfaces of one quartz window at a height above the injection plane of $z = 100$ mm.

The fuel and air systems upstream the burner and the LabVIEW control system to ensure the reliability of experiments are the same as the ones used for the multi-injector facility and are, thus, detailed in section 2.2.

2.1.1 Plenum and air co-flow

The air is provided by an 8 *bar* compressed air supply from the INSA building, guided through a mass flow controller (see section 2.1.3) and, next, through 4 pipes into 4 identical openings (placed at 90^o relative to each other), in the upper part of the plenum (see Fig. 2.3). The top-left sketch in the figure illustrates the path followed by the air in the plenum since its entrance. First, the 4 jets impinge on an inner wall and spread sideways and down the duct where they merge into a central ascending airflow. This bulk flow ascends through the inner cylinder, traversing a metallic grid (Fig. 2.3 top-right and bottom-right) and a space filled with ≈ 3 mm diameter glass beads. Glass beads can be appreciated in the photo presented at the bottom-left part of the figure and are used to brake any possible large turbulent flow structures, hence, laminarising the flow. The air then continues towards the upper end of the plenum where it is forced to change direction in order to enter a radial swirler. The top part of the plenum

can be observed in Fig. 2.1 and the swirler is shown in Fig. 2.4 (top-right). The radial swirler in the air duct is composed of 18 rectangular (6 mm × 8 mm) channels inclined at 45^o with a corresponding swirl number of 0.76, precisely detailed in [60]. This part is placed around the fuel injection system, on top of the atomiser holder (represented in Fig. 2.4 (top-left)). One last metallic piece is installed on top of the swirler, as shown in Fig. 2.4 (bottom-left and bottom-right), to generate (together with the atomiser holder) a smoothly converging duct changing the air momentum from radial to axial and keeping the swirling motion of the jet, which immediately after, enters directly into the chamber, surrounding the liquid injection. The annular opening through which the air jet issues into the chamber has an inner diameter of 10 mm (that is the fuel atomiser itself), and an outer diameter of 20 mm. The air temperature is measured just before entering the swirler with a thermocouple, as stated above.

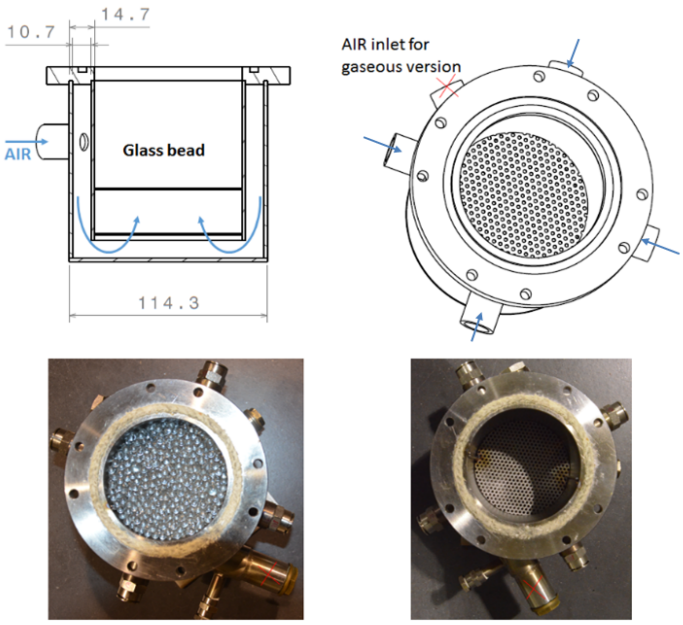

Figure 2.3: Plenum of the KIAI chamber. Top: drawing. Bottom: photographs with and without glass beads.

2.1.2 Fuel injection system

The fuel used in this facility was always n-heptane, which was stored in a 50 L reservoir placed at a height above the fuel pump and mass flow controller

(see 2.1.3) to guarantee the permanent priming of the pump. A 4 mm diameter metallic pipe guided the fuel from the control system, through the atomiser holder, into the atomiser. As shown in Fig. 2.4, the fuel pipe is welded to the atomiser holder, which is placed in the centre of the air plenum. Therefore, the fuel pipe is submerged in the airflow along the plenum (also sketched in Fig. 2.1 in red), implying a heat exchange between both flows and a consequent preheating of the fuel by the air. After the pipe and atomiser holder, the liquid fuel enters the atomiser, which is described in the following section. The approximate fuel temperature was measured directly in the liquid sheet immediately after the atomiser with a thermocouple that was, obviously, removed to perform any further experiments (see 2.1.3).

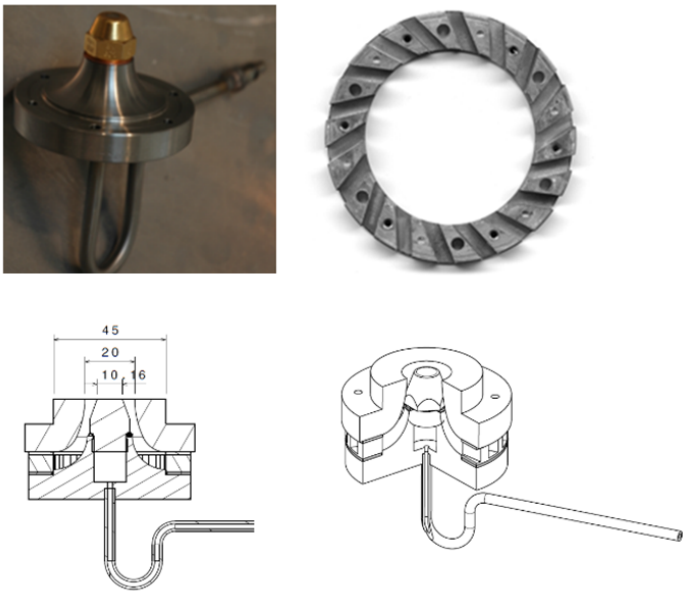

Figure 2.4: Injection system. Top-left: atomiser mounted on the fuel line. Top-right: air swirler. Bottom: drawing of the complete system.

Fuel atomiser

The n-heptane spray issued from a Danfoss simplex pressure swirl atomiser with the following fabrication specifications: 1.46 $kg.h^{-1}$, 80^o H (meaning hollow cone with an 80^o opening). Figure 2.5 (left) presents a cut of this type of atomiser, composed of a filter, three slots that guide the flow tangentially into a small swirling chamber and a tiny conical opening through which the swirling liquid is

forced to exit. The right part of the figure shows a microscopic reconstruction of the tangential distributor performed by a Keyence digital microscope. Microscopic measurements of the other parts enabled the elaboration of a dimensioned drawing, presented in Fig. 2.6, where it can be observed that the major diameter of the liquid swirling chamber is smaller than 1 mm and that the conical opening starts at a diameter of $\approx 50\ \mu m$ and ends at $\approx 200\ \mu m$.

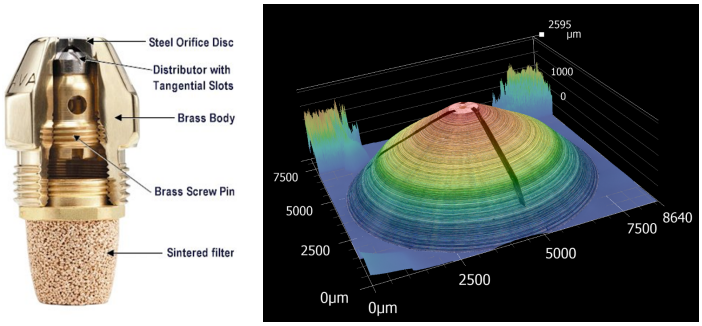

Figure 2.5: Pressure swirl atomiser. Left: detail of the different parts. Right: 3-D reconstruction of the piece containing the three tangential slots allowing fuel into the swirling chamber (the distributor).

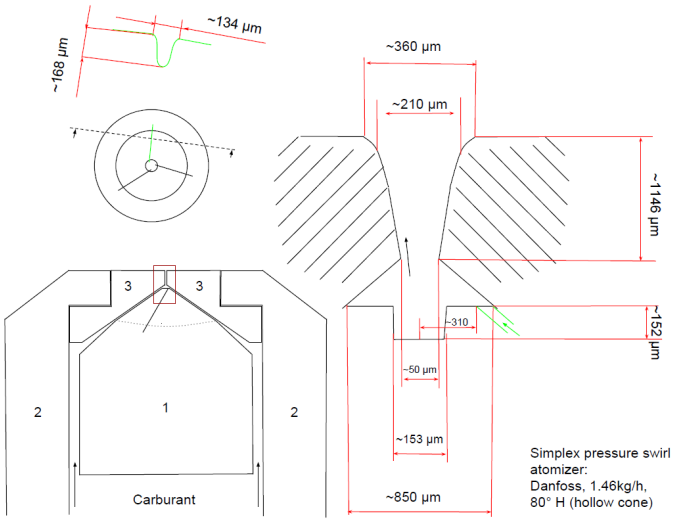

Figure 2.6: Sketch of the different parts of the simplex atomiser measured under the Keyence microscope.

These small dimensions are traduced in high liquid velocities at the exit. Since the liquid flow in the atomiser chamber has a strong rotational motion, pressures at the centre are forced to decrease and the fuel spills out of the conical

opening along the cone walls forming a very thin liquid conical sheet (80^o) on the immediate exit of the atomiser. Figure 2.7 illustrates through shadowgraphy acquisitions how the liquid sheet destabilises and generates filaments within the first 2 mm downstream (primary atomisation). Secondary atomisation takes place until ≈ 4 mm, where no further ligaments are observed and the majority of the droplets is already spherical. It has to be noted that the atomisation process occurs only due to the pressure difference upstream and downstream the simplex atomiser and to the design of the atomiser itself. There is no contribution of the air co-flow in the atomisation, oppositely to what happens in the main aeronautical injection systems.

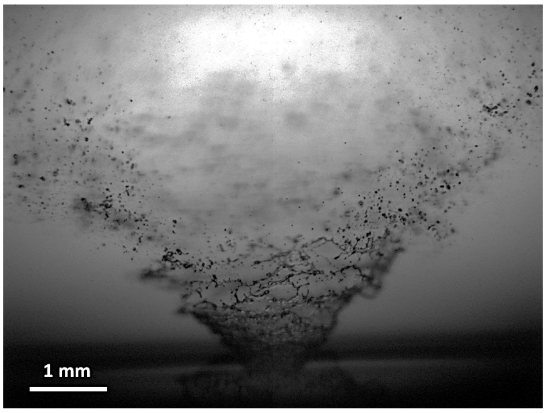

Figure 2.7: Shadowgraphy image showing primary and secondary atomisation in the first 3 mm.

2.1.3 Operating conditions

The nominal operating conditions of the burner were set in order to give a proper spray cone, a lifted stable flame and a very lean combustion process. Air and liquid fuel mass flow rates were controlled, respectively, by thermal and Coriolis mass flow controllers. Surface wetting and runoff by liquid fuel at the windows had to be prevented for stability of the system and the correct application of diagnostics. Table 2.1 indicates two different working conditions: configuration (A) and configuration (B). Both share the same conditions for the air phase. For both configurations, a co-flow inlet temperature of 416 K limited liquid impacts on the internal window surfaces and, thus, runoff. Configuration (A) yielded an ultra-lean global injected equivalence ratio of $\phi = 0.52$ and it was the

first configuration used. 0.28 $g.s^{-1}$ of fuel, close to the design conditions of the atomiser, imposed injection pressures of ≈ 8 *bar* and a good atomisation quality. Based on this fuel mass flow rate, the stability diagram of the flame was obtained by varying the air mass flow rate and temperature. Configuration (B) will be discussed and compared to configuration (A) later on in this section (2.1.3).

Configuration	**Phase**	**Substance**	$\dot{m}$ $(g.s^{-1})$	**T** (K)
A, B	carrier	air	8.2	416±3
A	dispersed	*n*-heptane	0.28	≈ 350
B	dispersed	*n*-heptane	0.33	≈ 350

Table 2.1: Nominal operating conditions of the KIAI-Spray burner for this study.

Effects of co-flow temperature and flow rate on flame and spray stability

In this part, a fuel flow rate of 0.28 $g.s^{-1}$ was fixed while air temperature and flow rate were varied. A first step was to investigate and understand the flame stability. For this, the air co-flow rate was varied between 6 and 10 $g.s^{-1}$ at injection temperatures of 373 K to 473 K. Figure 2.8 illustrates the results of this study. Here, flame images and green and blue laser beams (for PDA) can be observed. In the figure, as temperature increases and air mass flow rate decreases, the flame becomes less stable since it jumps between two different topologies. For $\dot{m} = 7\ g.s^{-1}$; $T = 413\ K$ and $T = 453\ K$, the flame photographs reveal attached-like flame structures that follow the spray cone shape. The other images show lifted V-shaped flames, which are well-known and have been the object of many studies (Chapter 1). To the left of the first red line, the flame either attaches to the injector permanently or it switches randomly between these two stable positions. On the other hand, for high air flow rates (e.g.: at $\dot{m} = 9\ g.s^{-1}$), the flame appears to be very de-localised and dimmer; blow-off occurs to the right-hand-side of this red line. Regarding the flame structures within the red box, for air temperatures of $T = 443\ K$ and above, a non-desirable flame topology appears. The type of flame searched for the current investigation was a typical swirling V-shape flame under lean combustion conditions. Under these air mass flow working restrictions, air inlet temperatures lower than $T = 403\ K$ did not avoid liquid impacts on the windows.

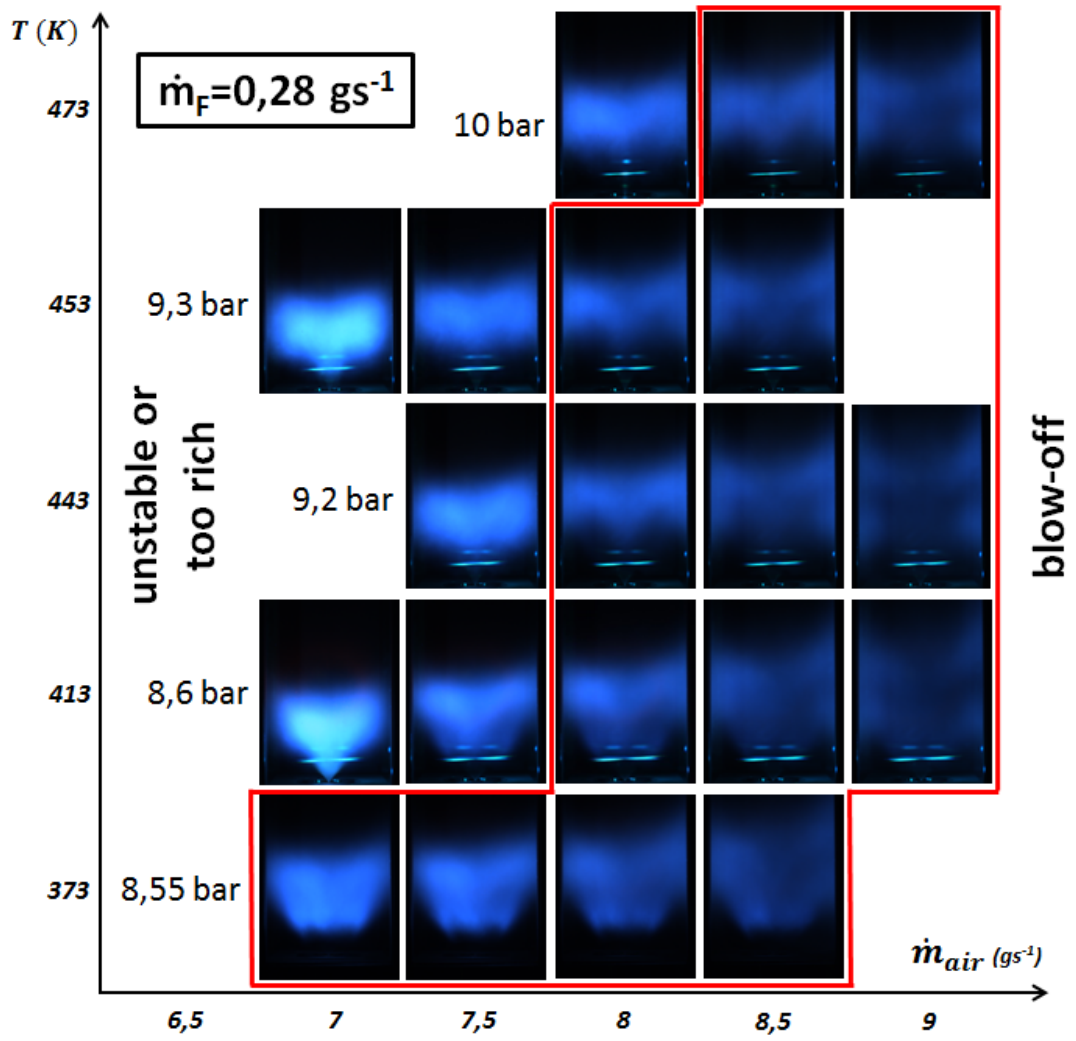

Figure 2.8: Stability diagram of the flame on the KIAI-Spray burner varying the air mass flow and temperature for a fuel mass flow of 0.28 $g.s^{-1}$.

Figure 2.9 gives a closer look at the spray cone for different air inlet temperatures at a fixed air mass flow rate of $\dot{m} = 8.2\ g.s^{-1}$. It is noticeable that the spray cone closes and separates from its nominal angle value of 80^o with increasing air temperature. The injection pressure also changes with air temperature and this is reported in Fig. 2.10 together with the spray cone angle. For airflow inlet temperatures of $T = 443\ K$ and above, the spray cone angle decreases drastically while the injection pressure grows vigorously. The mechanism responsible for this behaviour must be related to the increased heat exchange between air and fuel and, hence, the fact of the fuel reaching boiling temperatures during

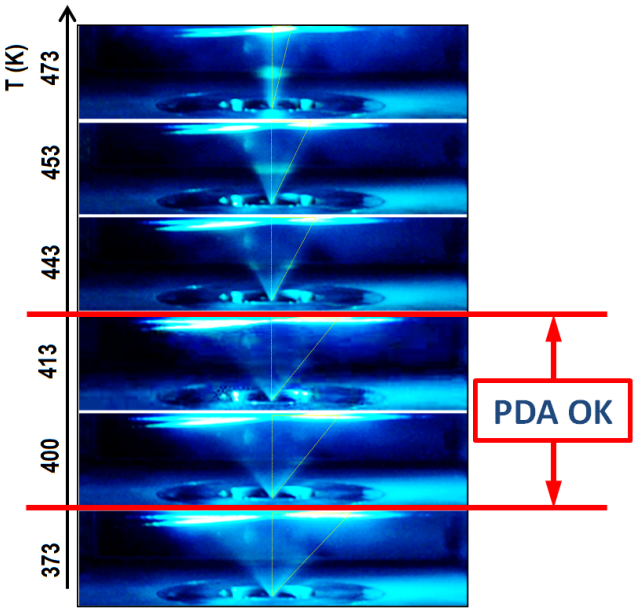

Figure 2.9: Photographs of the spray cone indicating its variation with air inlet temperature.

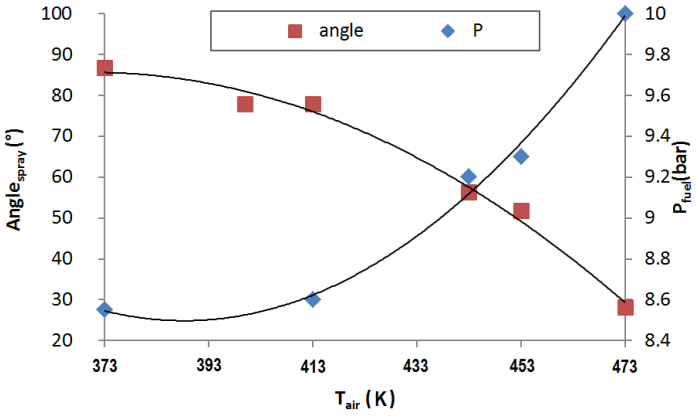

Figure 2.10: Spray cone angle and fuel injection pressure with air inlet temperature.

the expansion process through the atomiser orifice. These out-of-design conditions with bad atomising quality explain the undesired flames in Fig. 2.8 and must be avoided. This issue imposes a top-limit of $T \approx 423\ K$ to the air inlet temperature.

In addition, a study on the static and dynamic pressures in the chamber was also performed to justify the final choice for the air co-flow mass flow rate

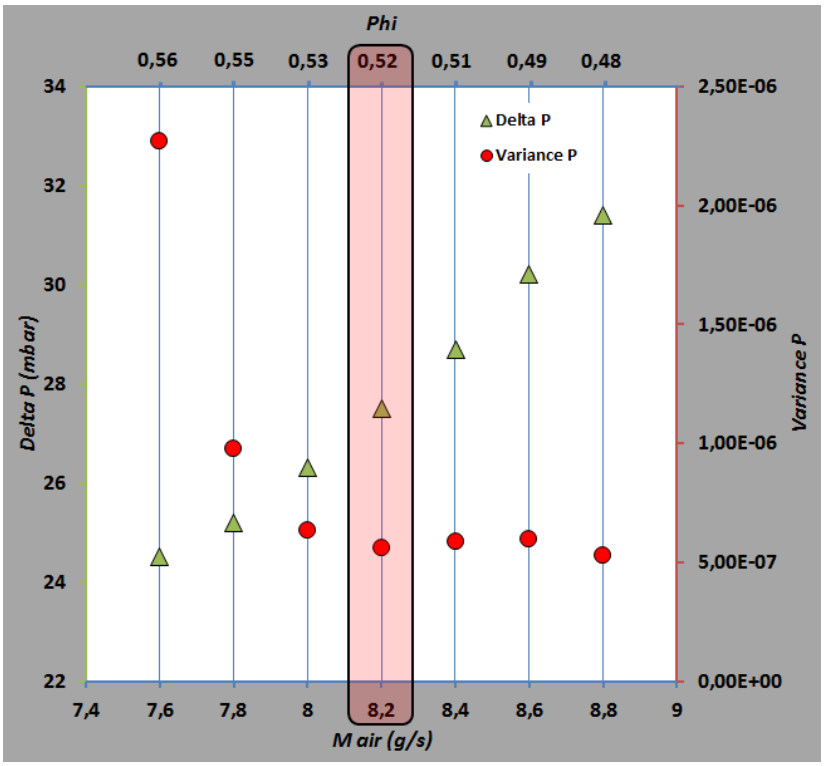

Figure 2.11: Static pressure and dynamic pressure variance in reacting conditions against air mass flow rate for reacting conditions. The global equivalence ratio (ϕ) is represented in the top horizontal axis.

of $\dot{m} = 8.2\ g.s^{-1}$. Figure 2.11 presents, in green (left axis), the static pressure difference between the plenum and the exhaust nozzle of the chamber and, in red (right axis), the variance of the dynamic pressure signal measured at the exhaust nozzle. The horizontal axes represent the air flow rate and the global equivalence ratio (for a fuel mass flow rate of $\dot{m} = 0.28\ g.s^{-1}$). The graph was elaborated in presence of the flame. From the figure, for air flow rates under $8\ g.s^{-1}$, the variance of the pressure reveals unstable configurations. Points at $\dot{m} > 8\ g.s^{-1}$, have a lower and constant pressure variance and show, indeed, much more stable working conditions.

In accordance to all the investigations above, the air co-flow mass flow rate was fixed to $\dot{m} = 8.2\ g.s^{-1}$ and its inlet temperature to $T = 416 \pm 3\ K$.

Configuration (B) vs Configuration (A)

This subsection is devoted to clarify the use of each configuration, to quantify the differences and to justify the validity of the comparisons between both of

them.

At the start of the investigation, the leanest possible configuration within the operability restrictions (described above) was selected. This corresponds, indeed, to configuration (A). Provided that the characterisation of the spray droplets (PDA) and the flame structures (Stability diagram and OH-PLIF) were, chronologically, the first experiments carried on the single-injector burner, configuration (A) was employed. Later on, during the ignition test campaigns, it was found that configuration (A) was far too lean to yield ignition probability experiments repeatable. In addition, it was not possible to find an adequate dynamic range of ignition probabilities within the chamber, even for the maximum possible sparking energies ($\approx 500\ mJ$). Therefore, the choice of increasing the fuel mass flow rate by 18% and keeping the same air co-flow conditions and flow patterns was taken. The new working conditions (configuration (B)) were used for all the other experiments. The new fuel mass flow rate was now $\dot{m} = 0.33\ .s^{-1}$ and the new $\phi = 0.61$, still representing ultra-lean conditions. Table 2.2 presents all the experiments with the respective nominal conditions used. The experiments and diagnostics will be detailed in Chapter 3.

Diagnostic or Study	**Configuration**	$\dot{m}_{fuel}$ $(g.s^{-1})$	**T** (K)
Flame stability	A	0.28	≈ 350
PDA	A	0.28	≈ 350
OH-PLIF	A	0.28	≈ 350
Chamber temperatures	B	0.33	≈ 350
HS-PIV	B	0.33	≈ 350
Toluene-PLIF	B	0.33	≈ 350
Ignition tests	B	0.33	≈ 350
HS-visualisation	B	0.33	≈ 350

Table 2.2: Classification of the experiments in function of the configuration used for the fuel mass flow rate.

Configuration (B) yields the same flame structure: lifted, stable, V-like shaped and slightly more compact. The flame regions and topologies do not change noticeably from configuration (A) to (B) and, hence, OH-PLIF images and the flame stability study are consistent.

In order to quantify the impact of changing from configuration (A) to (B), posterior PDA measurements were performed at two different axial stations (z=15 and z=35 mm) downstream the same atomiser. Figure 2.12 shows the

radial profiles for the mean droplet diameter and for the mean axial and radial velocities comparing $\dot{m} = 0.28$ and $\dot{m} = 0.33\ g.s^{-1}$. Mean velocities can be said to be conserved from one configuration to the other one, at least for $z > 15\ mm$. The mean diameter distribution yields slightly smaller values at high axial stations for $\dot{m} = 0.33\ g.s^{-1}$, reaching maximum differences of $\approx 10\%$ on the borders of the spray.

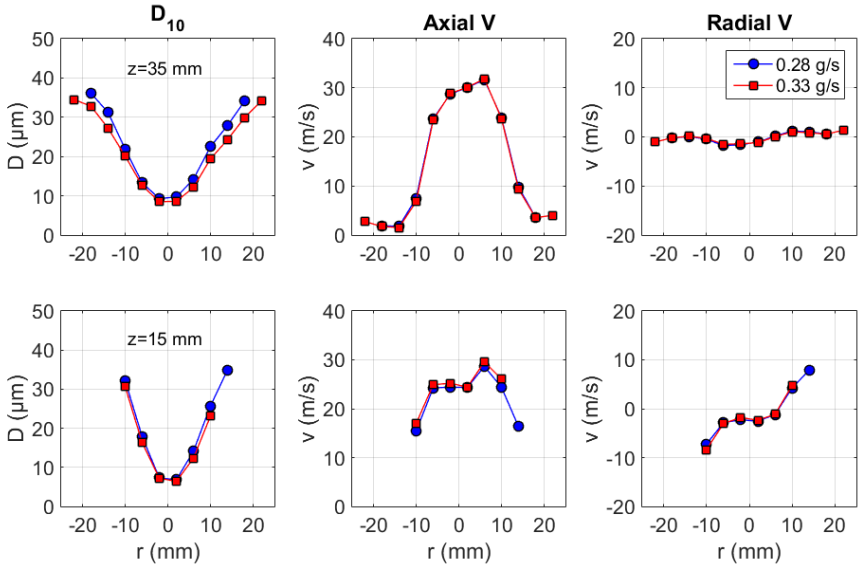

Figure 2.12: Radial profiles of D_{10}, Axial velocity and Radial velocity at two axial stations ($z = 15$ and $z = 35\ mm$) comparing configurations A and B.

Temperatures in the chamber

Temperatures in the chamber were estimated through point measurements using a thermocouple mounted on a micrometric translation system. To avoid any bias caused by liquid droplets impinging on the thermocouple, the fuel spray was turned off for the majority of the measurements. Only one point ($r = 0,\ z = 200\ mm$) was measured under spray presence since the flow is well mixed and no droplets are present at this axial station. Obviously, temperatures under spraying conditions are lower due to the evaporation of fuel droplets. Nonetheless, these measurements give an idea of the temperature variations inside the chamber and close to the windows.

Figure 2.13 illustrates the air temperature without spray for a radial profile at $z = 30\ mm$. Two temperature peaks can be appreciated at $r \approx 12\ mm$

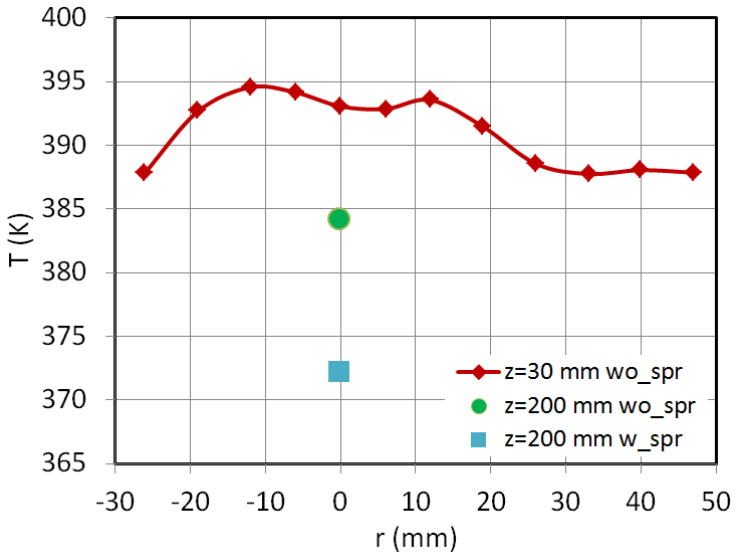

Figure 2.13: Air temperature profile (red) at $z = 30\ mm$ without spray and temperature at $r = 0,\ z = 200\ mm$ with (blue square) and without (green circle) spray.

reflecting the annular nature of the co-flow, which still at this axial station retains the effects of the injection geometry. Note that the injection temperature is $T = 416 \pm 3\ K$ and the maximum temperatures here are $T = 395\ K$. Outside the main air jet ($r > 25\ mm$) the temperature profile is quasi-constant until the chamber wall. The maximum ΔT at this axial station is $7\ K$. The green circle at $r = 0,\ z = 200\ mm$ presents an air temperature of $T = 384\ K$ far downstream in the chamber. When the spray is turned on, this temperature decreases down to $T = 372\ K$ (blue square in Fig. 2.13) due to the cooling effect of the fuel evaporation.

During the ignition test campaigns, the inner wall temperature was estimated by a thermocouple superposed to the inner window surface at $z = 100\ mm$ (and $x = 50,\ y = 0\ mm$). Using configuration (B), $T = 385\ K$ when the stability of the system is reached. This will be further detailed in Chapter 3.

2.2 Multi-injector Burner

The CORIA Linear Swirled Spray Burner is derived from the linear multi-injector burner used in previous premixed and non-premixed gaseous investigations [89, 90]. Experiments on this facility respond to the need of new insight

on multiple parameters and mechanisms associated to Phase 4 of aeronautical ignition (see introduction). The results of experiments carried here are presented and discussed in Chapters 7 and 8. The purpose of these studies is to identify and analyse the effects of the injector-to-injector distance and of the fuel nature on the flame propagation mechanisms and timings. This is done via high-speed visualisation of the spontaneous emission of the flame and of seeding tomographic images during the ignition process. In addition, the impact of modifying the inter-injector distance on the flow motion and on the mixture formation is analysed via HS-PIV and Toluene-PLIF, respectively. The latter is used to explain the propagation mechanisms during the light-around process.

2.2.1 Geometry

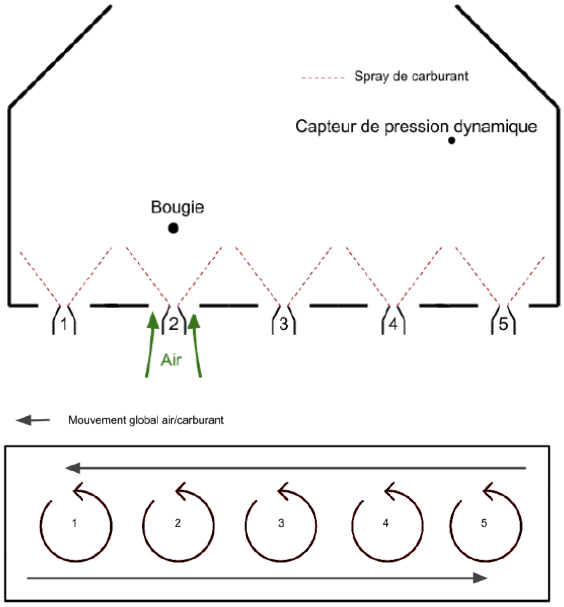

Figure 2.14: Sketch of the CLSSB. Top: front-view indicating the spray and air injections, as well as the spark plug and the pressure sensor. Bottom: top-view indicating the swirling motion.

The geometry of the multi-injector chamber is described by Fig. 2.14 and Fig. 2.15. This chamber is composed of several KIAI-Spray injectors, each having the same geometry as the one described for the single-injector burner in section 2.1. Instead of 4 air entries, there is only one per injector in this case. The convergent ducts that bring air into the chamber are the same, as well as the fuel atomisers.

In the multi-injector system, the chamber is enclosed by a large black metallic window, a large frontal quartz window and two lateral small quartz windows mounted on metallic supports. The four walls and the injectors are fixed on a metallic bench that guarantees the correct positioning of each piece. Sealing was used to protect fragile parts and to insure air-tightness in the chamber. A convergent exhaust nozzle is placed at the exit of the chamber to avoid external air entry, as in the single-injector case.

The number of injectors can vary depending on the configuration used, up to a maximum of 5. The distance between the back and the front walls is 11 cm, and the height from the injectors (chamber base) until the start of the convergent is 245 mm. The length of each injector block is of 90 mm, giving a minimum possible injector-to-injector distance of 9 cm. For longer injector-to-injector distances (d), metallic pieces of different lengths are placed between the injector blocks, generating in this way a tight chamber base.

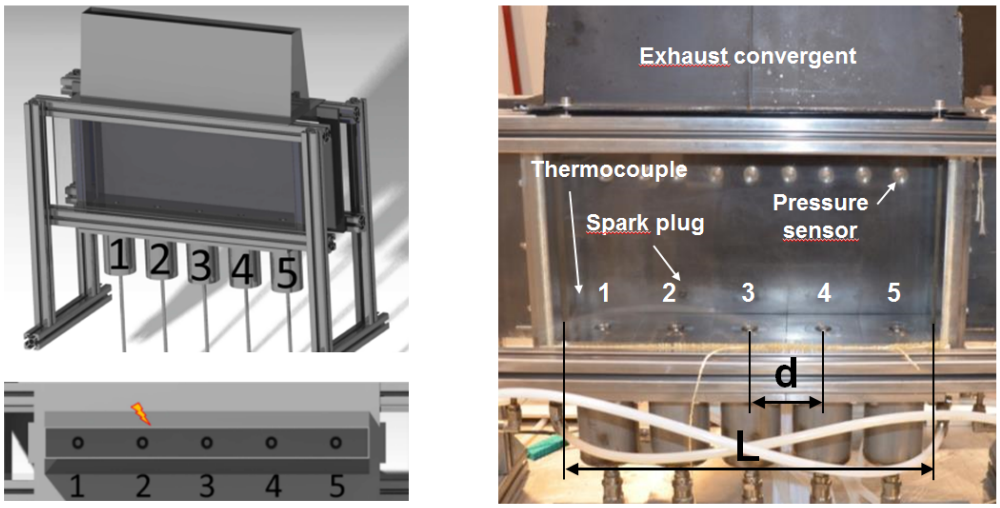

Figure 2.15: Left: CAD renders of the CLSSB. Right: frontal photograph of the CLSSB indicating the different elements and distances. Injectors are numbered 1 to 5 here.

Figure 2.14 presents a schematic of the frontal and top views of the chamber for a configuration containing 5 injectors. The air and spray are represented, and injectors numbered 1 to 5. The top view illustrates how the swirling motion of the air, in the same direction for all injectors, imposes a general circulation along the chamber walls. Figure 2.15 displays a CAD render of the burner on the left and a photograph on the right. Injectors are again numbered 1 to 5. On

the right, d represents the distance between injectors and defines the window-to-window length (L). A thermocouple is placed over the inner surface of the frontal window to control the approximate wall temperature. The back metallic wall holds an aeronautical spark plug centred on injector 2 at 25 mm above the chamber base, as well as a dynamic pressure sensor placed on the right top corner, near the exhaust.

2.2.2 Control

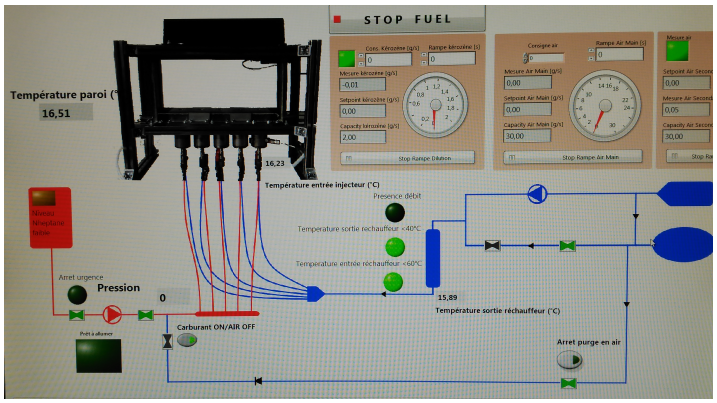

Figure 2.16: LabVIEW interface controlling the operation of the CLSSB.

The control of the system was tackled with a LabVIEW interface acting on different parts of the air and fuel circuits upstream the burner. The labVIEW interface is presented in 2.16. The stability of each flow is constantly checked, as well as the air inlet temperature and the window inner temperature. Figure 2.17 displays a schematic view of the air (green) and fuel (red) circuits. The air enters through two filters before arriving into two parallel thermal Bronkhorst mass flow controllers. The air is then guided into the air heater (8 kW) through a low-flow protection system that sends an alarm to LabVIEW under a certain threshold in order to protect the air heater. After the heating, the air enters a distribution chamber or plenum where the flow is equally divided into 5 isolated pipes of the same length that are connected to the plenum of each injector.

From the other side, fuel is stocked in a 50 L tank installed above the fuel pump, thus, guaranteeing its constant priming. The fuel exits the tank and crosses an open (emergency) valve before entering the fuel pump. Next, the flow crosses a Coriolis Bronkhorst mass flow meter and a second valve before entering

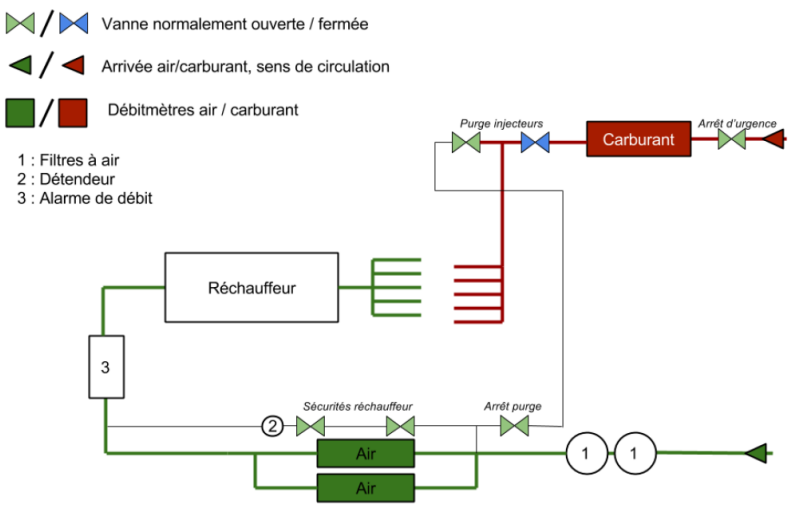

Figure 2.17: Sketch of the air and fuel circuits upstream the CLSSB.

a common rail that distributes equally the fuel into 5 pipes of equal length and into the injectors.

Additional elements are added to the system in order to protect the heater and to enable the purge of the injectors once the experiments are finished. Figure 2.18 shows a photograph of the control system.

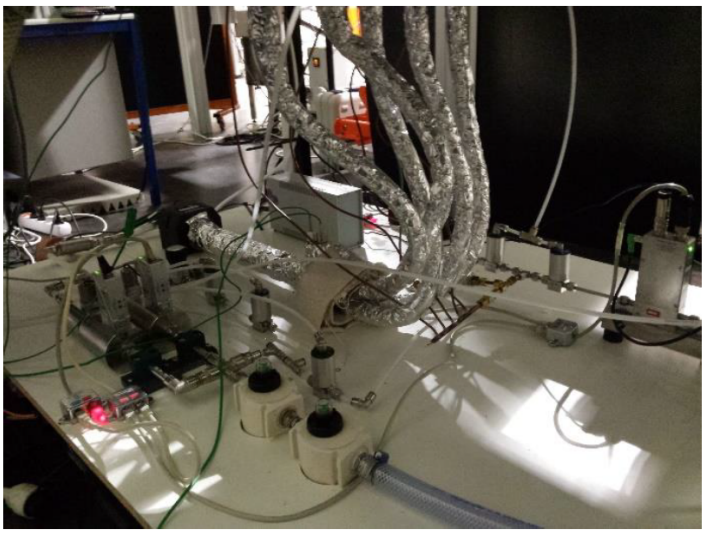

Figure 2.18: Photograph of the air and fuel circuits and control systems.

2.2.3 Operating conditions

This part is devoted to the description of the working conditions during the experiments. Compared to the single-injector study, the global equivalence ratio was increased to $\phi_g = 0.7$. This enriched mixture enables to systematically ignite with success the injector closest to the spark plug. Otherwise, the flame kernel is too weak and is easily subjected to the flow variations, hence giving rise to issues relative to ignition Phase 2. $\phi_g = 0.7$ avoids these problems and permits to place the focus on ignition Phase 4.

The objective of this study is to characterise the impact of the injector-to-injector distance and of the fuel nature on the lightaround. Therefore, four injector-to-injector distances were selected to be investigated. Table 2.3 presents the four values of d (9, 13, 15 and 18 cm) and the corresponding burner configurations. Five injectors were employed for $d = 9$ and 13 cm, four for $d = 15$ cm and three for $d = 18$ cm. The air and fuel mass flows per injector were respectively set to 6.86 and 0.316 $g.s^{-1}$, and were kept constant throughout all the configurations. Indeed, this varies the total flow rates and the total power of the system, as indicated in table 2.3. In the power column, the ranging values indicate the use of fuels with different low heating value.

d (cm)	**Injectors**	**Total** $\dot{m}_{air}$ ($g.s^{-1}$)	**Total** $\dot{m}_{fuel}$ ($g.s^{-1}$)	**Power** (kW)
9	5	34.3	1.58	68 - 70.4
13	5	34.3	1.58	68 - 70.4
15	4	27.4	1.26	54 - 56.2
18	3	20.58	0.948	41 - 42.2

Table 2.3: Operating conditions for each injector-to-injector spacing.

For each of the geometrical configurations exposed above, four different fuels were tested, i.e.: n-heptane, n-decane, n-dodecane and Jet-A1 kerosene (see table 2.4). The purpose of changing the fuel is to analyse the impact of the volatility in the ignition process and, notably in the flame propagation. Indeed, n-heptane and n-decane are very volatile fuels, oppositely to n-dodecane and Jet-A1 kerosene, which are heavier and less volatile. Table 2.4 provides, in addition, the boiling temperature, the low heating value and the laminar burning velocity of each fuel. The laminar burning velocity, given at a an equivalence ratio of 0.7 and at a mixture temperature of 400 K, shows very small variations between the

tested fuels, thus, enabling to study only the volatility.

Fuel	$\mathbf{T}_{boiling}$ (K)	**LHV** $(kJ.kg^{-1})$	**Volatility**	$\mathbf{S}_L^o$ $(cm.s^{-1})$
n-heptane	371.6	44566	high	38
n-decane	447.3	44240	high	41
n-dodecane	489.4	44147	low	38
kerosene	449	43105	low	-

Table 2.4: Characteristics of the different tested fuels. S_L^o at 400 K and $\phi = 0.7$ extracted from [101].

For every ignition trial, the same air inlet temperature (controlled at the plenum of one injector) was used, fixing the same value as that of the single-injector burner ($T = 416 \pm 3$ K). Moreover, the wall temperature was controlled at the spark triggering. The aeronautical spark plug and coil system are the same as the ones used in [73], delivering an energy of ≈ 450 $mJ/pulse$ in a single-spark mode.

Chapter 3

Diagnostics and Post-processing

Contents

This chapter is devoted to the description of the different techniques employed to measure physical quantities in the single-injector and in the multi-injector burners. A total number of 6 different laser and/or optical diagnostics, plus 1 probability study were applied either to one or both burners, in order to extract the maximum information to tackle as deep as possible the aeronautical ignition problem. The majority of the experiments were decoupled and their results are, thus, compared via statistical approaches, still uncovering new physical information on the processes here involved. Other experiments were performed simultaneously and provide very useful coupled data. The information gathered during this work conceives a multi-physical and multi-format database useful for the aeronautical industry and for numerical simulations.

Table 3.1 lists all the diagnostics used in this investigation and the respective measured variables, as well as the burner and the conditions in which they were applied.

Each technique is now addressed independently in the following sections. The physical principle is briefly introduced for each of them. Special emphasis is made on the specific experimental configuration and the post-processing methodology.

3.1 Phase Doppler Anemometry (PDA)

PDA was used in the KIAI-Spray single-injector burner to measure the velocity of the carrier phase in reacting and non-reacting conditions, as well as the droplet size and size-classified velocity of the dispersed phase in reacting and non-reacting conditions.

Technique	Target	S-I	M-I	Flow conditions
Shadowgraphy	Spray formation	-	-	NRC
PDA	Fuel droplet size-velocity	✓	-	NRC & RC
	Air velocity	✓	-	NRC & RC
HS-PIV	Air velocity	✓	✓	NRC
	Multi-phase velocity	✓	✓	NRC & RC
	Multi-phase velocity	-	✓	IGN
Toluene-PLIF	Mixture formation	✓	✓	NRC
OH-PLIF	Flame structure	✓	-	RC
HS-Visualisation	Kernel evolution	✓	-	IGN
	Flame propagation	-	✓	IGN
Ignition probability	Probability map	✓	-	IGN
Pressure sensor	Chamber pressure	✓	✓	IGN

Table 3.1: Classification of the experimental techniques applied either to one or both burners, indicating the measured variable and the measuring conditions. S-I stands for single-injector facility and M-I for multi-injector facility. Flow conditions are: NRC (non-reacting conditions), RC (reacting conditions) and IGN (ignition transition).

3.1.1 Principle

PDA is a well-known technique based on the scattering of a light interference pattern by the object to measure (namely a spherical droplet). It relies on the crossing of two identical laser beams generating a small measuring probe volume, as shown in Fig. 3.1. It is, thus, a 0-D technique. When a droplet crosses the interference volume, the signal is scattered in all directions, some of which are privileged depending on the refractive indexes of the droplet and the carrier phase, on the polarisation of the light and on the form of scattering (i.e.: reflection, refraction or 2^{nd} order refraction). This technique has been studied from different points of view [102–106] and described in detail [107].

The interference pattern generated by the crossing of the laser beams can be simplified by a fringe model that depends on the wavelength of the laser and on

the geometrical configuration of the optical system. The frequency of the signal emitted by the droplet enables to extract its velocity in the direction perpendicular to the fringes. The sense of the velocity is determined by a small shift imposed on one of the laser beams through a Bragg cell. This imposes a temporal pulsation of the interference pattern, this is, the fringes in the measurement volume appear to move in a defined direction. The sign of the velocity is then determined relative to this movement. The phase difference between the signals gathered by two photomultipliers (PMs) placed at slightly different angles in the receiving probe is proportional to the size of the particle. These technical and physical aspects are gathered in [107]. Most of the PDA systems measure two components of the velocity using two perpendicular pairs of laser beams, each at a different nominal wavelength. The third component is also measured by adding a third laser pair.

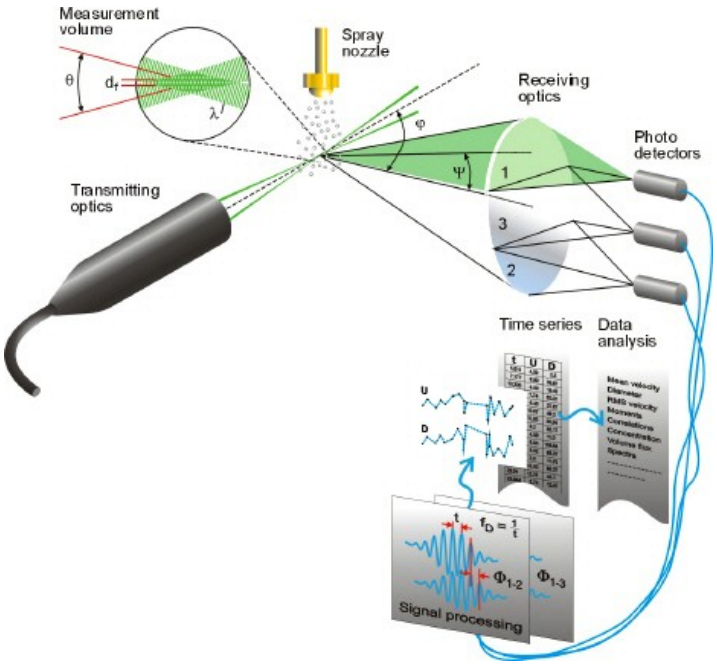

Figure 3.1: Schematic showing the PDA operating principle (DANTEC).

At this point it is necessary to dedicate some words to the accuracy of the technique and the potential sources of error. In terms of velocity, the software must be pre-set to determine the velocity range: the smaller the range, the higher the precision on the measurement and vice-versa. If the measured velocities fall outside the imposed range, signal validation decreases. Concerning the droplet diameter, the optical arrangement will determine the detectable size range. PDA

is more precise when measuring the velocity and diameter of one droplet than when exploring the statistical distribution in size of a very heterogeneous spray because the voltage in the receiving photomultipliers (PMs) cannot be optimised simultaneously for very large and very small droplets, provided that the scattered light intensity depends on d^2 according to the Mie scattering theory. This is, if the voltage and gain in the PMs are too low, the light scattered by small droplets will not pass the detection threshold imposed in the processor; if the voltage and gain are increased so as to detect these weak signals, the largest droplets will saturate the anode current in the PMs, hence, be rejected. This implies that the population of small and large droplets detected by PDA depends on the configuration of the PMs, affecting the determination of the mean diameter of the distribution in the measuring point. Moreover, flux measurements can carry errors of over $\approx 30\%$ because they depend on d^3 [104–106]. Nevertheless, the mean diameter is satisfactorily determined for not too wide distributions. Other potential error sources are listed below:

- The trajectory effect or Gaussian beam effect: attributed to non-uniform laser intensity in the measurement volume due to the Gaussian intensity distribution in the beams. If configured in refraction mode, intense reflections can bias the size detection [104, 107].
- The slit effect: the desired detection mode (refraction for instance) may be blocked at the limits of the measurement volume imposed by a slit in the receiver. This generates the same kind of errors in the estimation of particle sizes as the Gaussian beam effect [102, 106, 107].
- Sphericity: depending on the collection strategy, the sphericity of droplets can be evaluated using two perpendicular measurements of the diameter along the droplet. If a droplet exceeds a limit of unsphericity, it will be rejected. This threshold can be modified.
- Velocity sampling: fast droplets will be sampled more times than slow droplets, biasing the estimation of the velocity distribution in one point.

3.1.2 Experimental Configuration

PDA was applied in the single-injector chamber in non-reacting and in reacting conditions in order to measure the air velocity and the droplet size distribution

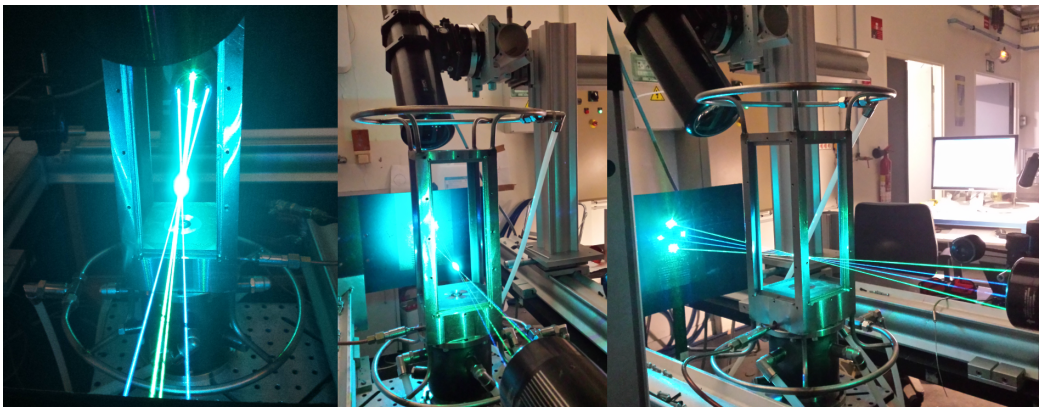

Figure 3.2: Photographs of the KIAI-Spray burner, the PDA lasers and acquisition system during some tests.

and size-classified velocity, as shown in Fig. 3.2 For this purpose, a commercial PDA system from Dantec was used operating in Fiber mode. An argon laser provided green (514.5 nm) and blue (488 nm) beams. Beam spacing was 50 mm; transmitting and receiving lenses focal lengths were 350 mm and 310 mm, respectively. Due to technical reasons, the off-axis angle of the receiving optics was 50^o (in front scattering position), not far from the Brewster angle which, in parallel polarization, enhances the refracted light detection over the reflected light, reducing the trajectory and slit effects. The laser energy before the beam separation was 2 W. The used aperture mask allows a detection diameter range of 139 μm. The measurement volume can be approximated by a cylinder of 120 μm in diameter and 200 μm in length. At each measurement location, data sampling was limited to 40,000 droplets or to 30 s of measuring time, allowing converged statistics of size-classified data. Due to the presence of ligaments or too high droplet concentration, the measurements were not possible below $z = 10$ mm.

PDA was used to characterise both the dispersed phase and the carrier phase. Droplets with diameters $d < 5$ μm were considered to have low Stokes numbers and used as tracers of the carrier phase. For the acquisitions focused on the carrier phase, the population of small droplets was strongly increased by seeding the air co-flow upstream with $d < 2$ μm olive oil droplets. According to this strategy, five different PDA acquisitions were performed and listed in Table 3.2 for clarity. Each configuration is now explained:

- **C1** was used to measure the velocity of the carrier phase (in non-reacting conditions) seeded with olive oil droplets without spray presence. For this,

the fuel spray was turned off. The voltage and gain of the PMs was increased as much as possible to enhance the detection of small droplets. All the sampled droplets were smaller than 2 μm.

- **C2** was used to measure the velocity of the carrier phase (in non-reacting conditions) exactly as in C1 but in presence of the spray, so the fuel spray was turned on. The voltage and gain were kept high to increase the sampling of small droplets. However, the majority of droplets detected belonged to the fuel spray and less small droplets than in C1 were available for statistics of the carrier phase. Measurement C2 was necessary to evaluate the influence of the fuel spray presence on the airflow velocity. C1 and C2 will be compared in Chapter 4. The fuel droplet data ($d > 5$ μm) was not used.

- **C3** was used to characterise the fuel spray size-velocity (in non-reacting conditions). The seeding was turned off but the nominal air co-flow was kept constant. The voltage and gain in the PMs were lowered so as not to saturate the anode current and to maximise the signal validation. This configuration yields a much more reliable set of data for the fuel spray than C2.

- **C4** was used, like C2, to prioritise the carrier phase measurements in presence of spray but in reacting conditions. Due to high temperatures and rapid evaporation, the sampling of small droplets was drastically reduced. The fuel droplet data ($d > 5$ μm) was not used.

- **C5** was used, like C3, to optimise the spray size-velocity detection (without olive oil seeding) and in reacting conditions.

Typical size histograms of each experimental configuration are sketched in Fig. 3.3. Seeder and spray distributions for C2 and C4 are sometimes overlapped and sometimes not.

3.1.3 Post-Processing

Raw data for each mesh point was exported and post-processed with Matlab. Concerning the air phase measurements (C1, C2 and C4), small droplets (seeding and/or n-heptane) were considered, as indicated in Fig. 3.3. This is, for PDA

	Target Phase	Conditions	Seeding Oil	Fuel Spray
C1	Air	NRC	✓	x
C2	Air	NRC	✓	✓
C3	Fuel	NRC	x	✓
C4	Air	RC	✓	✓
C5	Fuel	RC	x	✓

Table 3.2: Classification of the different PDA acquisitions, indicating the target phases in the different conditions.

configuration C1 the size of the droplets taken into account for the calculation ranged 0 to 2 μm; for PDA configurations C2 and C4, this was extended to 0 to 5 μm because less small droplets were proportionally available in presence of spray. This data was used to calculate the mean and the standard deviation values of the velocities, as well as other quantities such as the turbulent kinetic energy of the airflow. Concerning the spray droplets (C3 and C5), the mean diameter and the Sauter Mean Diameter together with their associated standard deviations were calculated from the detected populations. The droplet distributions were then divided into 7 size-classes: [0-10], [10-20], [20-30], [30-40], [40-50], [50-60] and [60-70] μm. The total number of droplets detected per second per group was then calculated for each mesh point, as well as the mean and standard deviation velocities of each size group. For the calculation of the mean velocity components of the air and of the spray, each droplet's velocity was weighted by its transition time in the probe volume, as done in [108].

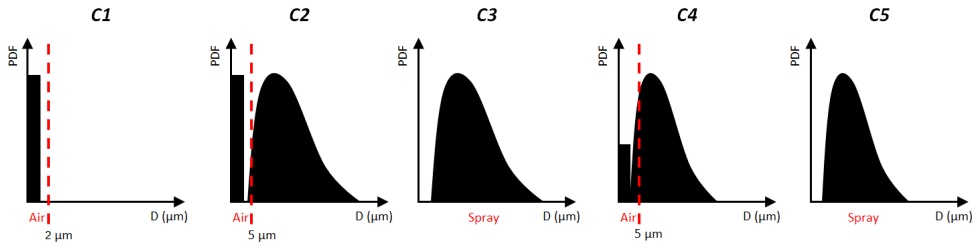

Figure 3.3: Sketch of typical seeder and/or spray size distribution histograms.

The hypothesis of rotational symmetry along the vertical axis ($z-axis$) of this flow configuration was made to give access to the three velocity components with only a 2-D PDA system. This enables stressing the velocity components in terms of radial profiles. Cylindrical coordinates were considered: u_1 represents the ax-

ial velocity (following the $z - direction$), u_2 stands for radial velocity (following the $x - direction$) and u_3 for azimuthal velocity (following the $y - direction$). Provided that this PDA configuration only measured simultaneously in 2 dimensions (relative to the laser position), and supposing rotational symmetry, axial and radial velocities were measured simultaneously along the $x - axis$ profile; and the y-axis profile enabled measuring axial and azimuthal velocities. The rotational symmetry is confirmed by the good agreement between the axial velocity profiles measured along the x and y axes. Figure 3.4 clarifies this paragraph.

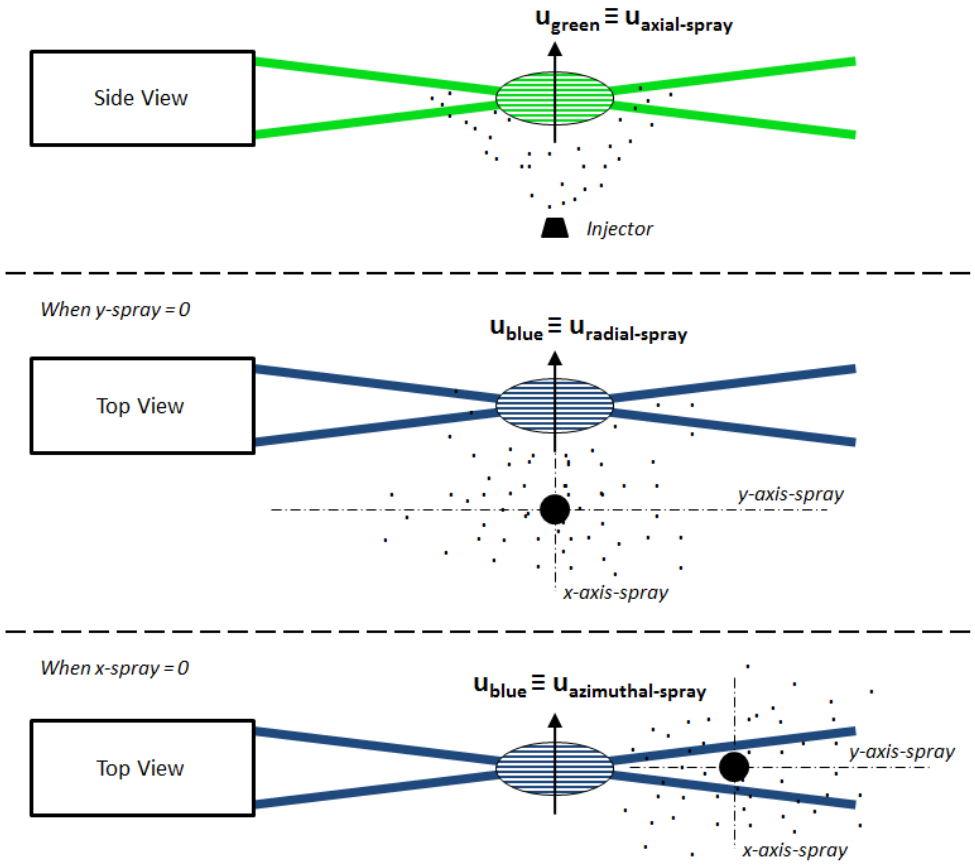

Figure 3.4: Sketch of the laser, spray and measured velocity components for the x-axis and y-axis profiles.

3.2 High-Speed Particle Image Velocimetry (HS-PIV)

Although PDA measurements give information of great value for this study, HS-PIV provides a different approach for measuring either the carrier phase velocity in non-reacting conditions or the weighted two-phase velocity during the ignition transition. Indeed, PIV provides instantaneous 2-D measurements, necessary to describe the flow behaviour. The need of high-speed diagnostics here is justified by the short time available before window dirtying caused by the seeding. HS-PIV was applied both to the KIAI-Spray single-injector facility and to the CLSSB multi-injector facility.

3.2.1 Principle

PIV is based on the paired imaging of a seeded flow illuminated by two laser pulses at two time instants of known Δt. Particles in a certain small region (interrogation window) of either image form a pattern that moves in one direction between the pair of images. Indeed, the cross-correlation of the corresponding interrogation windows yields a correlation peak that indicates the displacement of the pattern in pixels from one image to another [109]. In a second step, taking into account the optical system magnification and the time between images, a velocity vector resulting from this interrogation window can be calculated. This process is, thus, extended to all the image domain through small interrogation windows, giving a vector velocity field. PIV is a well-established technique and more information can be found in [110, 111].

The time between images, Δt, must be optimised relative to the flow velocity and to the magnification ratio. Special care must also be taken during the experimental campaigns so as to reduce uncertainties and produce reliable measurements, minimising the sources of errors in the following way:

- The size of the seeding particles and their Stokes number must be small enough to follow the flow velocity variations, since PIV assumes that particles are ideal flow tracers.

- The seeding density, the interrogation window size and the signal-to-noise ratio affect the resultant vector field and the minimum possible resolvable

lengthscale [111, 112].

- Out-of-plane particle motion induces errors in the cross-correlation calculation and must be minimised.
- In two-phase flows where the dispersed and carrier phases have different velocities, the application of a simple PIV technique is complicated. PIV in two-phase flows has been the object of many studies, such as [113], and can be addressed, for instance, by isolating the phases on two CCD cameras using two-colour fluorescence to separate the seeding and the dispersed droplets. A simple PIV image pair with both phases on it can be, however, processed and will provide an averaged information between the liquid and the air. This average velocity is weighted considering the size and luminosity of the particles in the interrogation window and can provide only qualitative information. Depending on many parameters, such as the luminosity difference between the air seeding and the liquid phase, a post-processing technique could eventually dissociate both phases, through complex procedures that are not the object of this work.

3.2.2 Experimental Configuration

In both burners several HS-PIV measurements were performed, three of which were exploited for the present work:

- With seeding and without spray in non-reacting conditions in the KIAI-Spray single-injector facility.
- With seeding and without spray in non-reacting conditions in the CLSSB multi-injector facility.
- With seeding and spray in igniting conditions in the CLSSB multi-injector facility.

Single-injector burner

In order to apply the technique on the KIAI-Spray single-injector burner, the carrier phase was seeded far upstream with $< 2\mu m$ Zirconium Oxide (ZrO_2) particles. Particle image velocimetry measurements were performed on the air-flow without spray presence at a 5 kHz repetition rate on the RZ plane (vertical

cut) with a magnification factor of 0.05 $mm.px^{-1}$. Provided that the spray is dilute, the influence of the droplets on the air motion is negligible; this will be confirmed by PDA results in Chapter 4. A double cavity 527 nm Nd:YLF laser (Darwin Dual Quantronix) and a Phantom V2512 high-speed camera were used. The time between laser pulses was set to $7\mu s$ enabling to correctly capture the wide range of velocities present in the flow and preventing the seeding particles from leaving the interrogation plane between pulses due to perpendicular velocity components (azimuthal). The confinement windows increased the complexity of the experiments enabling a short acquisition time before becoming covered by dust. 5000 raw single images were selected to calculate 2500 instantaneous vector fields. PIV images were also recorded in presence of the air seeding and the fuel spray simultaneously, in reacting and in non-reacting conditions. Although they are not exploited here, the data is available in the database.

Multi-injector burner

Concerning the linear burner, it is necessary to characterise in detail and analyse the instantaneous and mean air velocity fields in order to reveal the effects of injector-to-injector spacing on the aerodynamics of the flow and, thus, on ignition. The air was seeded with < 2 μm silicon oil particles and PIV was applied on the airflow without spray presence at 5 kHz for all distances. A magnification factor of 0.129 mm/px was used for $d = 9$, 13 and 15 cm while $d = 18$ cm required 0.147 mm/px. The same laser, camera and synchronisation than above were used. Time between laser pulses was set to 40 μs enabling to correctly capture the wide range of velocities present in the flow but prioritizing the inter-injector region. For each value of d, 2500 instantaneous vector fields were extracted. Figure 3.5 show the multi-injector burner with the air seeding in (top) and the fuel spray in (bottom) illuminated by the laser sheet.

3.2.3 Post-Processing

Raw images were normalised by their corresponding mean images to reduce any spatial energy variations and background scattering. For the single-injector facility, the 1280×800 px^2 images were processed with Dynamic Studio from DANTEC using the Adaptive PIV calculation, with initial and final interrogation windows of 64×64 and 16×16 px^2, 50% of overlap and a maximum

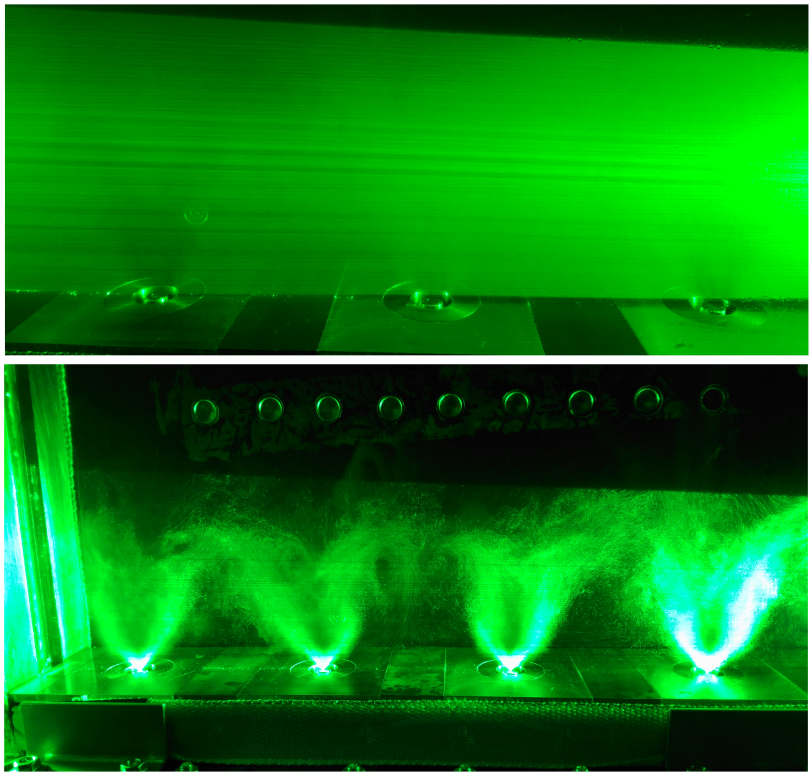

Figure 3.5: Photographs of some injectors of the multi-injector chamber during the HS-PIV experiments with the laser sheet arriving from the right-hand-side. The top part shows the Mie scattering from the silicon oil seeding droplets. The bottom part shows the Mie scattering from the issuing spray droplets without seeding.

iteration number of 10, yielding 159 $\times$ 99 vector fields. The signal-to-noise ratio acceptance was set over 1.5 and a 5 $\times$ 5 px^2 median validation was applied. Post-processing with Matlab enabled to further analyse the data. The mean velocity field and the total strain rate field (instantaneous and mean) were calculated.

PIV data on the multi-injector burner was also processed with an Adaptive PIV algorithm from Dantec, but this time initial and final interrogation windows were set to 128 $\times$ 128 and 32 $\times$ 32 px^2, giving 79 $\times$ 49 vector fields. The signal-to-noise ratio acceptance was set over 1.5 and range and median validation were applied.

3.3 Planar Laser Induced Fluorescence on Toluene (Toluene-PLIF)

Toluene-PLIF was used to measure the local vapour mixture formation in non-reacting conditions in both burners. This section needs a more detailed description since the use of Toluene-PLIF in two-phase flows is less extended and limited in the literature. The objective of this technique is the quantitative (where possible) or qualitative description of the fuel vapour locally in the chamber. This can be translated into a local equivalence ratio describing the mixture formation. Since *n*-heptane is not a fluorescent molecule, a tracing strategy was adopted: the fuel droplets were doped (mixed) with a tracer. The physical principle of the laser induced fluorescence is well-known [6, 114–116] and it will be briefly commented below. In the following, the scope is rather placed in the specificities of the Toluene-PLIF.

3.3.1 Principle

Fluorescence is the spontaneous emission of a photon by an atom or a molecule due to a energetic relaxation of an electron from a higher to a lower energy level. Fluorescence is explained by quantum mechanics, assuming that energy levels associated to a molecule are quantised and each quantum state has one quantum number, angular momentum and energy described by the following equation:

$$E_{int} = E_{vib} + E_{rot} + E_{elec} \tag{3.1}$$

where E_{int}, E_{vib}, E_{rot} and E_{elec} are respectively the internal energy of the molecule, the vibrational energy, the rotational energy and the electronic energy. Given that the energy levels are quantised, only specific excitation wavelengths are able to be absorbed and produce fluorescence. The energy absorbed and emitted by molecules, in the form of photons, is expressed with Planck's radiation law:

$$\Delta E = h\nu \tag{3.2}$$

where h is Planck's constant and ν is the frequency of the photon.

In laser induced fluorescence, the upper energy level is populated using a

laser excitation with a wavelength tuned to a resonance between the excited state and a discrete lower state. After excitation, the population in the upper state can follow different processes that can be defined by transitions between a high (E_2) and a low (E_1) energy in a two-level model, as presented in Fig. 3.6. The absorption rate populating E_2 is denoted b_{12} while b_{21} indicates the stimulated emission rate that goes directly to the lower state. A_{21} represents the spontaneous emission rate from E_2 to E_1 and corresponds to the fluorescence signal. The collisional quenching, denoted by Q_{21}, is a non-radiative de-excitation process caused by inelastic collisions between the excited molecule and other surrounding molecules. W means photoionisation and P predissociation, processes that are rare in PLIF. Another non-radiative de-excitation process is the internal relaxation of the molecule, K, via vibration for instance.

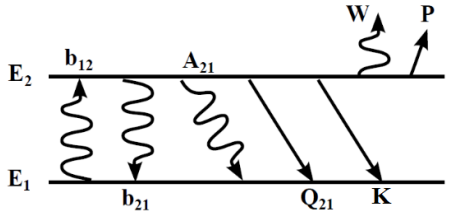

Figure 3.6: Two energy level model to explain the laser induced fluorescence process.

The fluorescence signal depends on the parameters shown in equation 3.3 [115] where $h\nu$ is a photon of energy $E_2 - E_1$, Ω is the solid angle of collection, V is the volume, N is the concentration of tracer molecules, σ_a is the absorption cross-section of the tracer molecules and A_{21}, K and Q_{21} control the fluorescence quantum yield, described below. The collected signal is, therefore, directly proportional to the number of molecules of the fluorescent species in the measurement volume, to the intensity of the exciting laser beam, to the absorption cross-section and to the fluorescence quantum yield (FQY). The latter is a ratio between A_{21} and the sum of A_{21}, Q_{21} and K. Both σ_a and the FQY are strongly dependent on the mixture temperature and the excitation wavelength (equations 3.4 and 3.5). The FQY also depends on pressure (P) and on the concentration of surrounding molecules that are responsible for the quenching process (χ_M).

$$S_f = h\nu \frac{\Omega}{4\pi} V N \sigma_a \frac{A_{21}}{A_{21} + K + Q_{21}} \tag{3.3}$$

$$\sigma_a = f_1(T, \lambda) \tag{3.4}$$

$$\frac{A_{21}}{A_{21} + K + Q_{21}} = f_2(T, P, \chi_M, \lambda) \tag{3.5}$$

For some fluorescent molecules, namely cetones, $K >> A_{21} + Q_{21}$, meaning that they are not sensitive to the quenching effect and, thus, can be used regardless of the surrounding atmosphere neglecting this effect. However, this implies that their FQY is very low and a great quantity of tracer would be needed so as to obtain acceptable signal-to-noise ratios. On the other hand, for aromatic molecules (and in general) $Q_{21} >> A_{21} + K$ and their FQY is higher. This demands less amount of tracer (less intrusive) but requires a control of the surrounding atmosphere and of the quenching effect. In air baths, O_2 is generally the main molecule responsible for collisional quenching.

3.3.2 The Tracer

The choice of the tracer is an important step that conditions the signal quality and dependency to parameters such as temperature and quenching, as well as the amount of tracer needed and the wavelengths involved. The ideal tracer would have all the properties listed below:

- To be injected with the fuel it must be liquid and evaporate with the same evaporation rate that the *n*-heptane in the droplets. To achieve this, the boiling points of the fuel and tracer must be very close, as well as other parameters such as the diffusion coefficients.

- A high absorption cross-section and a high fluorescence quantum yield (FQY).

- Low toxicity.

- Well-known photo-physical properties.

- Its fluorescence signal should be non-dependent or weakly dependent to temperature.

- Its fluorescence signal should be non-dependent or weakly dependent to quenching due to collisions with surrounding molecules or atoms because their molar fractions are not generally conserved locally.

These exigencies reduce considerably the number of fluorescent candidates to track the n-heptane vapour in the chamber. Table 3.3 lists some of the molecules commonly used in tracer-PLIF due to their thermophysical and photophysical properties [6, 115].

Molecule	**M**(g/mol)	$T_{boiling}$ ^oC
Acetone	58.08	56
Acetaldehyde	44.05	21
3-pentanone	86.1	102
Diacetyl	86.09	88
Anisole	108.14	153.8
1,2,4-trimethylbenzene	120.19	169
Toluene	92.14	110.6

Table 3.3: List of commonly used fluorescent tracers for tracer-PLIF.

From the potential fuel tracers listed in table 3.3, only the aromatic molecules were considered because they present much higher fluorescence efficiencies (stronger signals) than the rest. Among the latter, the tracer must be as close as possible to the fuel in terms of physical properties, namely in the evaporation rates. Anisole and 1,2,4-trimethylbenzene have too high boiling points, while the boiling temperature of toluene is much closer to that of n-heptane ($T_{boiling} = 98.4^oC$). Toluene was therefore the selected candidate, meeting satisfactorily all the above requirements except the dependency of S_f to temperature and quenching, which had to be minimised.

The fluorescence of toluene as a tracer of fuel has been studied in detail in [6, 114, 116, 117]. It is well-known that the fluorescence signal (S_f) of toluene is extremely sensitive to O_2 concentration and to temperature variations [6, 117]. Figure 3.7 is an extract from [6] showing (on the left) the normalised fluorescence signal of toluene varying with the mixture temperature and composition when excited with a 266 nm wavelength. The oxygen quenching effect is remarkable and divides the signal by nearly two orders of magnitude when comparing a nitrogen atmosphere to an air atmosphere at $T \approx 350\ K$. Temperature variations also imply significant modifications in the fluorescence of toluene, which simul-

taneously depend on the oxygen concentration. However, the objective of the Toluene-PLIF technique is to quantify the amount of toluene present in the local gaseous mixture in the chamber and the previous effects must be suppressed so that the fluorescence signal (S_f) depends only on toluene concentration, thus, on fuel concentration. With the purpose of minimising $\partial S_f/\partial T$, preliminary experiments were carried on two gaseous co-flowing jets and are presented below, immediately after the description of the potential error sources of the technique.

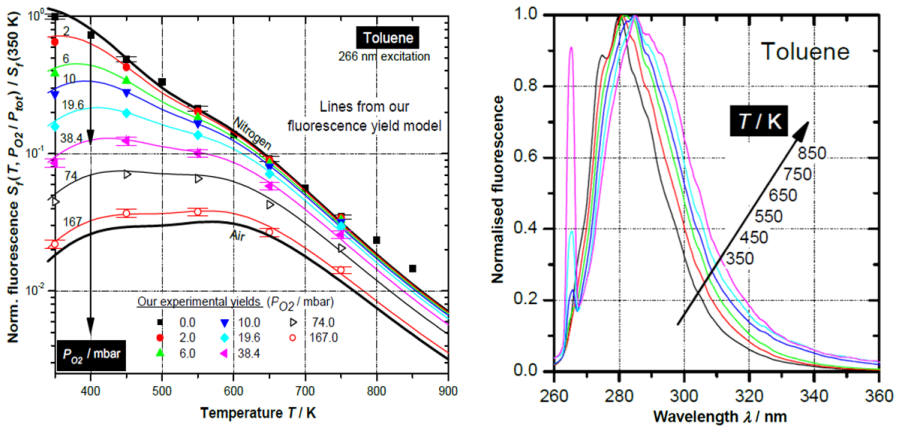

Figure 3.7: Extract from [6]: on the left, the normalised fluorescence signal of toluene is compared to the mixture temperature and the content in oxygen. On the right, the fluorescence spectrum of toluene is presented for different temperatures.

The right-hand-side of Fig. 3.7 illustrates the fluorescence spectrum emitted by toluene molecules when excited at 266 nm and reveals wavelengths ranging from 266 to 360 nm with a maximum between 280 and 285 nm depending on temperature.

3.3.3 Potential Sources of Error

One of the major difficulties of this technique when dealing with polydisperse sprays is the inevitable droplet presence in the region-of-interest. PLIF investigations in charged heterogeneous two-phase flows are really scarce. Some studies deal with large, single droplets or homogeneous droplet chains [118–120]. Other authors have performed PLIF measurements in polydisperse two-phase flows but the droplets and their potential biases are often not commented and, furthermore, not taken into account [121]. Some authors have proven the complexity of

the droplet position detection with post-processing tools or with the application of simultaneous techniques, in order to identify the liquid-vapour interface accounting for the blooming effect [120, 122]. The application of the Toluene-PLIF technique for heterogeneous two-phase flows in the present conditions is therefore a state-of-the art strategy and must be improved in the future to reduce the potential error sources so as to increase its accuracy. The following is a list of elements contributing to bias the measured signal:

- Since Toluene-PLIF is so sensitive to small variations of O_2, N_2 and toluene concentrations, the monitoring and control of the flows is primordial and the precision of the flow meters must be taken into account.
- The laser energy must be kept constant and the mixture preparation has to be done carefully.
- The O_2 concentration is supposed constant everywhere but this is not true near droplets, where fuel vapour concentration may reach 100%.
- Temperature variations must be known and kept within the acceptable limits.
- Differential evaporation of the fuel and the tracer can overestimate or underestimate the mixture fraction in regions where droplets are still evaporating.
- The strong fluorescence of the liquid phase imposes a limit to the signal-to-noise ratio in the vapour phase.
- Only droplets larger than the space resolved by a pixel can be detected. However, droplets smaller than a pixel also fluoresce and, depending on their size, they can bias or not the measurement of that pixel. The light collected by one pixel comprises the integration of the fluorescence in the volume formed by the laser sheet thickness and the 2-D space resolved by the pixel. This becomes a complex problem since the laser energy is not constant in the sheet thickness and the droplet size and concentration in this volume are not known and vary. Moreover, absorption can occur in the liquid phase [122], hence reducing the potential sub-pixel bias, depending on the size of the droplet. The fluorescence signal of small droplets can be

neglected compared to the signal of the fluorescent vapour in the volume, but the signal of larger, sub-pixel droplets can strongly bias the determination of the gaseous equivalence ratio. To our knowledge, there are no works in the literature accounting for this potential bias or just mentioning the fluorescent sub-pixel droplets.

3.3.4 Previous Tests

A series of preliminary experiments were performed in order to check that the system responded according to the fluorescence equation and to find a configuration minimising the dependence to temperature variations. A chamber with two concentric co-flowing jets was used for this purpose. The influence of temperature variations and of O_2 concentration variation was studied here, as well as the laser absorption and the linearity of S_f with laser energy and with toluene concentration.

Two-jet facility

The objective of this experiment was to find a N_2 to O_2 ratio in the mixture which nullifies the effects of temperature variations on the fluorescence signal of toluene. A gaseous approach was used in this experiment. A schematic of the system is presented in Fig. 3.8. Far upstream, three flow meters controlled the flow rates of two N_2 and one air flows. The air and one of the N_2 flows merged into one common pipe and into an electric heater. The second N_2 flow ($0.6\ g.s^{-1}$) was sent into a toluene reservoir and then joined the main heated flow charged in toluene vapour. Temperature of toluene in the reservoir was controlled and the piping connecting the reservoir and the main flow was heated up to avoid any condensation. The hot mixture was then divided into two pipes: an insulated one that guided the flow into the external co-flow jet and a second pipe with 3 possible insulation configurations that sent the mixture into the central jet. The temperature of the central jet (T_1) adopted, therefore, 3 possible values while the temperature of the surrounding co-flow (T_2) was higher and constant.

Figure 3.9 gathers thermocouple measurements following a horizontal profile some millimetres above the exit of the jets for the 3 insulation configurations of the central jet (T_1). The central jet is responsible for the local minimum found in the temperature signal and, indeed, the jet temperature changes with

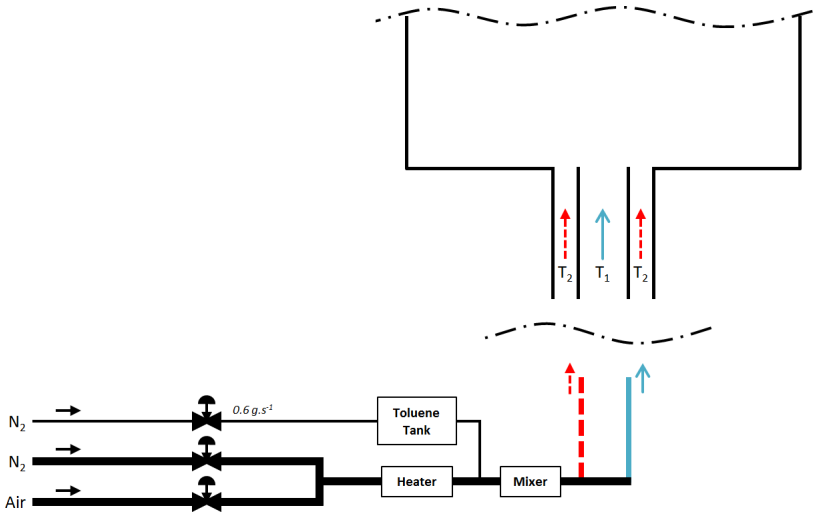

Figure 3.8: Sketch of the experimental configuration for the two-jet experiment.

the different insulations. Comparing for each insulation the local maximum at $r \approx 6\ mm$ to the local minimum at $r \approx 0\ mm$, 3 temperature differences can be obtained and are presented in table 3.4.

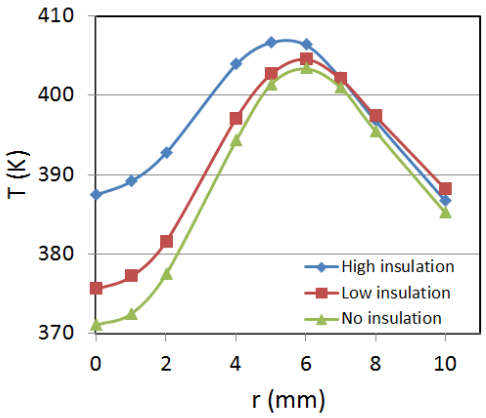

Figure 3.9: Temperature profiles of the two co-flowing jets in the inlet of the chamber for the three different insulation levels if the central jet.

Dependence of S_f to temperature and O_2/N_2 ratio

For each of the 3 insulation configurations of the central jet in the concentric-jet chamber, 6 N_2-Air mixtures with identical content in toluene were tested. A 266 nm laser sheet was sent into the chamber and a emICCD PiMAX filtered camera

Insulation	$T_{min} - T_{max}$
High	-18.9
Low	-29
No	-32.3

Table 3.4: Different ΔT obtained between the two co-flowing jets for different levels of insulation of the central jet.

collected the fluorescence signal. Specifications on the excitation and collection systems are given below, in section 3.3.5. Mixture configurations are labelled A to F and are indicated in table 3.5. The N_2 flow in the toluene tank was kept constant, as well as the total $Air + N_2$ mass flow rate, which was fixed to 8.2 $g.s^{-1}$.

Configuration	$\dot{m}_{N_2}$	$\dot{m}_{N_2\ in\ toluene}$	$\dot{m}_{air}$	χ_{N_2} (%)	χ_{O_2} (%)
A	7.59	0.6	0	100.00	0.00
B	7.38	0.6	0.21	99.45	0.52
C	7.28	0.6	0.31	99.19	0.77
D	7.18	0.6	0.41	98.93	1.02
E	7.00	0.6	0.59	98.46	1.47
F	6.77	0.6	0.82	97.86	2.04

Table 3.5: List of the six studied mixture configurations in order to minimise the signal dependency to temperature variations.

The recorded images reveal the fluorescence signals of two jets having the exact same composition and toluene concentration. Figure 3.10 gathers two instantaneous images of the fluorescing jets where jet 1 was not insulated ($\Delta_{max} = 32.3\ K$); 1 and 2 indicate the central and the surrounding jets entering the chamber. On the left image, configuration A shows outstanding differences in S_f values while on the right image, (configuration D) both jets have the same fluorescence intensity. It can be noted that the central jet is always brighter because it is the coldest, consistently with the left part of Fig. 3.7 (for mixtures with high N_2 content).

Results in Fig. 3.11 show that the relative deviation of the fluorescence signal ($\Delta S_f/S_f$) grows with temperature difference (ΔT). Configurations D, E and F minimise $\partial S_f/\partial T$ for a departure temperature of $T = 416\ K$. Configuration D (1% O_2 and 99% N_2 molar) was selected for the Toluene-PLIF experiment, showing a $\Delta S_f/S_f < 5\%$ for $\Delta T < 32.3\ K$. A collateral effect of this new con-

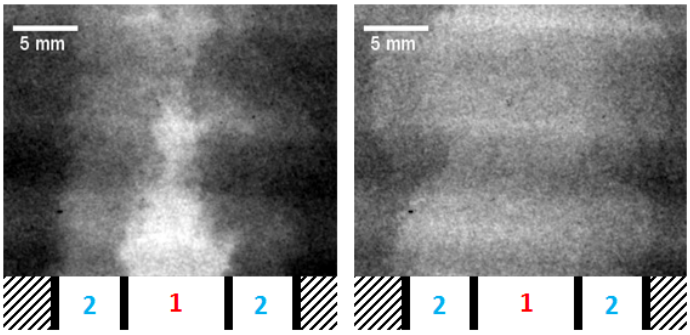

Figure 3.10: Two instantaneous images of the fluorescing jets with a maximum $\Delta T = 32.3\ K$. On the left (configuration A), jet 1 and jet 2 show different signal intensities while on the right (configuration D) they show the same.

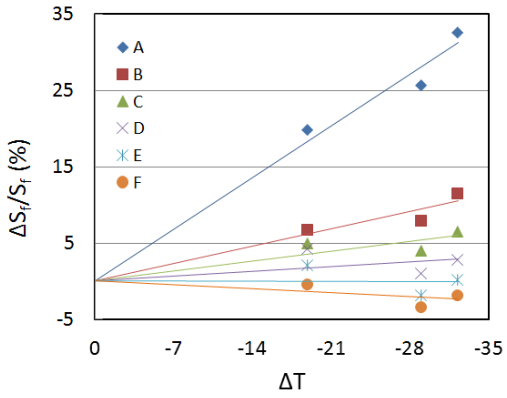

Figure 3.11: Relative variation of S_f for the three different ΔT for the six $Air-N_2$ studied mixtures.

figuration is that S_f is increased by a factor of ≈ 20 with respect to a pure air co-flow. These conclusions are consistent with Rossow's work [6] (Fig. 3.7). The co-flows of the KIAI-Spray burner and of the CLSSB were, hence, substituted accordingly for PLIF experiments and the hypothesis of similar fuel evaporation and mixing under the new conditions was adopted. This procedure made the fluorescence of toluene independent to typical temperature variations measured in the chamber and enabled measuring the fuel repartition in the non-reacting flow both in the single-injector and in the multi-injector facilities. Once the toluene, hence the fuel molar fraction, was available, the equivalence ratio was calculated in the post-processing stage as if the co-flow were 100% air and assuming that this does not change the fuel distribution.

Absorption study

The laser absorption is a critical issue for the LIF technique, and it has to be characterised. The absorption study was first performed with only the annular jet (central jet off) and only under a N_2 atmosphere. Molar concentration of toluene in nitrogen was set to 0.2% ($\phi = 4.1$), 0.5% ($\phi = 11.9$) and 1% ($\phi = 30.2$) and, for each, 500 fluorescence images and 100 noise images were recorded. The intensifier gain was increased for decreasing toluene concentrations in order to compare similar image intensity levels. The mean image corrected by the noise was calculated for each concentration and a horizontal signal profile was extracted from the top part of each image, where temperature variations are less important and representing a 60 mm horizontal profile along the chamber. The case at 0.2% concentration reveals no signal attenuation and was taken as a reference of no absorption. Figure 3.12 shows the relative variation of the signal profiles corrected by the mean noise and normalised by the mean 0.2% laser sheet image. A second test for 0.5% toluene under an atmosphere corresponding to configuration D was done and it is shown in red in the figure. Results indicate that for 0.5% of toluene, the maximum attenuation (in 60 mm) of the fluorescence due to absorption is under 4% in N_2 atmospheres and under 7% in configuration D.

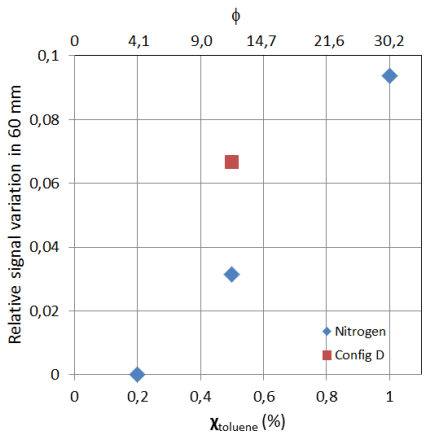

Figure 3.12: Diagram showing the relative signal variation due to absorption compared to toluene concentration.

Linearity of signal with laser energy and with toluene concentration

Equation 3.3 states that S_f is proportional to the incident laser energy and to the tracer molar concentration. This was also experimentally verified in the system. Laser energy was varied for two fixed toluene concentrations representing $\phi = 0.61$ and $\phi = 0.93$ and results in Fig. 3.13 (left) confirm the theory. The laser energy was then fixed to 38 mJ and the toluene concentration varied, obtaining a linear trend before reaching attenuation due to absorption. This is shown in Fig. 3.13 (right).

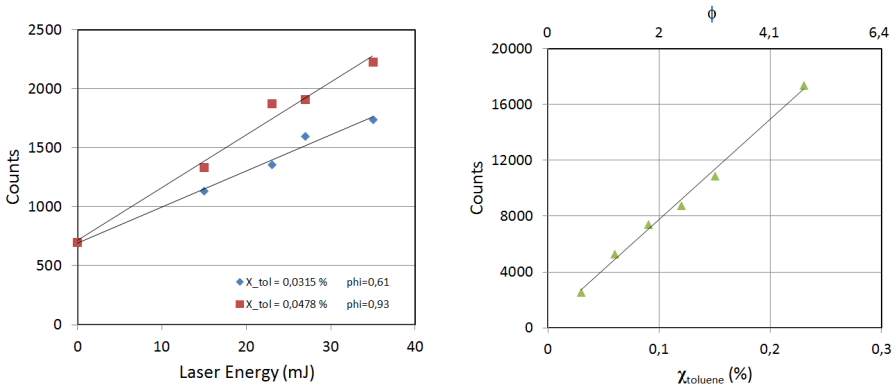

Figure 3.13: Diagrams showing the linear response of the fluorescence signal with the laser energy (left) and with the toluene concentration (right).

For the experiments toluene was mixed with n-heptane at 2% volume of tracer. For a global fuel to air equivalence ratio of 0.61, this quantity of toluene yielded a molar toluene concentration of 0.03% in the fully evaporated mixture avoiding absorption and providing enough vapour signal. Large droplets with this concentration already saturated the camera at low gain values. The experimental configuration is now detailed.

3.3.5 Experimental Configuration

It is reminded that the purpose of this technique was to characterise the gaseous equivalence ratio ϕ locally at the different regions of the KIAI-Spray and the CLSSB chambers in non-reacting conditions. ϕ is a necessary parameter to understand the mechanisms governing ignition. Indeed, for lean-mixtures, a slight variation of ϕ implies strong variations of the minimum ignition energy (MIE) [50].

Toluene was mixed at 2% volume with the fuel in the tank and the hypothesis of toluene-to-heptane molar fraction ratio conservation between liquid and vapour was made. A toluene quantity of 2% in the fuel droplets' volume was enough to reach the top limit of the emICCD range due to the fluorescence of liquid toluene in the largest droplets, at low gain values.

Single-injector burner

The experimental set-up (Fig. 3.14) included a 266 nm quadrupled Nd-YAG laser (10 Hz) forming a $\approx$ 200μm thick laser sheet sent into the chamber to excite the toluene molecules. The laser beam generated after the quadrupler 4ω contained an important amount of 532 nm energy that was eliminated by the use of a Pellin-Broca prism, which separated the different wavelengths. The green beam was then blocked and the ultra-violet light was sent into a spherical convergent lens of large focal distance ($f = 1500\ mm$) and through a cylindrical divergent lens to form the sheet. The distances were adjusted to adapt the sheet length to the field of interest and to optimise the laser sheet energy profile. All the optics had a high ultra-violet transmittance, as well as the confinement windows (Suprasil). For optimisation of the signal-to-noise ratio, the 266 nm laser energy was increased as much as possible without damaging the optics, to a value of 38 mJ. The collection of the fluorescent response (rejecting Mie scattering on droplets) was addressed with one 280 nm ($WG280 \times 3\ mm$) and two 275 nm ($ZUL275 \times 1\ mm$) high-pass filters placed on an emICCD PIMAX 4 intensified camera. This set-up enabled to visualise one half of the chamber ($43 \times 43\ mm$) with a magnification factor of 42 $\mu m/px$.

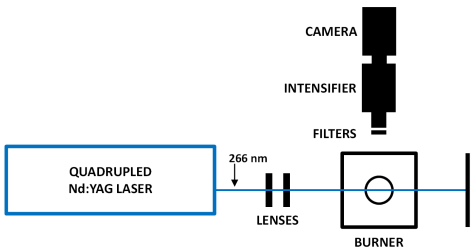

Figure 3.14: Experimental setup for the Toluene-PLIF measurements.

Multi-injector burner

The same strategies and optical configuration were used to apply the toluene-PLIF to the CLSSB. The laser energy was fixed to 38 mJ and the emICCD PIMAX 4 camera recorded a much wider field. The gain and the magnification changed but were kept constant for the four tested injector-to-injector distances. Indeed, the magnification factor was 175 $\mu m/px$, enabling the imaging of a $180 \times 63\ mm^2$ window giving access to two half-injectors and the inter-injector region at $d = 18\ cm$ and, hence, two lateral half-injectors plus a central complete injector and two inter-injector regions (IIRs) for $d = 9\ cm$.

Reference mixture

A reference value of S_f in a known mixture is needed to convert the raw data into equivalence ratio values. The injected fuel droplets evaporate steadily in the chamber and disappear at high axial stations. Indeed, there are no droplets observed at high axial stations and the turbulent mixing has already homogenised the flow. This hypothesis together with the mass conservation implies that at the top part of either burner chamber the homogeneous mixture will contain the χ_{Fuel} corresponding to the global ϕ injected in the system; i.e. $\phi = 0.61$ for the KIAI-Spray burner and $\phi = 0.7$ for the CLSSB. Figure 3.15 illustrates two instantaneous fluorescence images of the fully-evaporated homogeneous mixture at the top part of the single-injector (left) and multi-injector (right) burners. 1000 images of this kind, named LS for $LaserSheet$ in Fig. 3.16, were taken as a reference for each studied configuration and were also used to correct the laser energy profile spatial fluctuations. 500 noise images were correspondingly recorded at the top and at the bottom parts of the burners for each configuration. This is illustrated in Fig. 3.16.

3.3.6 Post-Processing

For each configuration, 3000 raw images and 500 noise images were acquired on the bottom part of the burners (in the regions of interest), and 1000 homogeneous mixture images plus 500 noise images were recorded at the top part of the burners. In Fig. 3.17, ND, NU, LS and S stand for Noise Down, Noise Up, Laser Sheet and Signal (raw) (see Fig. 3.16. The mean images were calculated for the collection of noise images, as well as for the laser sheet images. Any

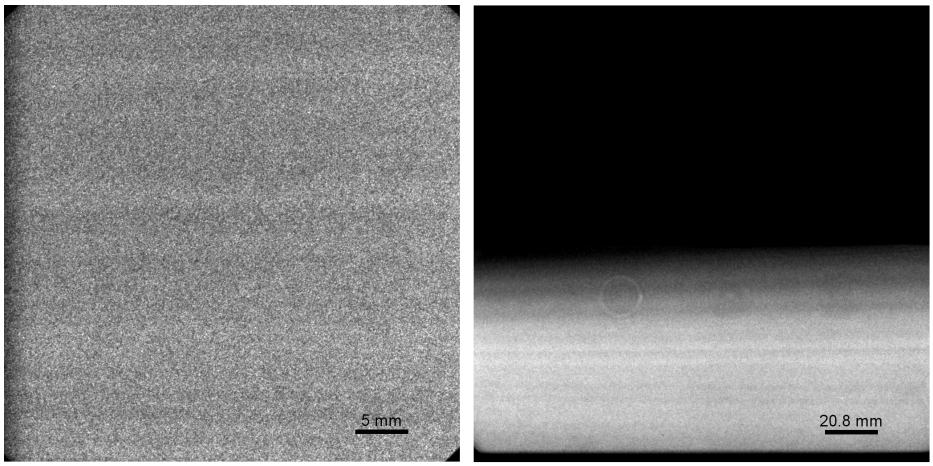

Figure 3.15: Two instantaneous laser sheet images at the top of the chamber for the single-injector burner (left) and for the multi-injector burner (right).

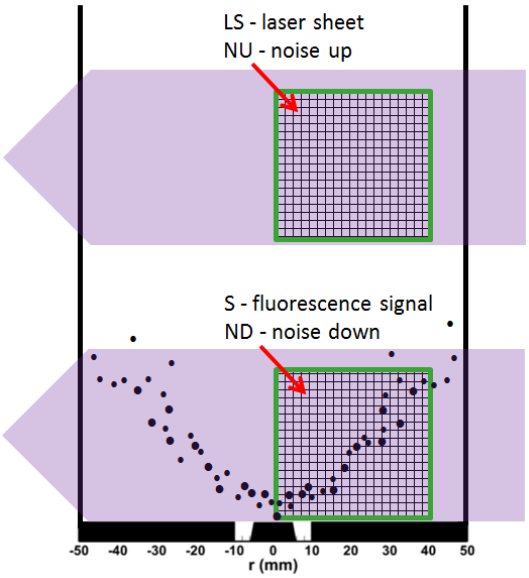

Figure 3.16: Schematic of the different acquisitions and locations for the Toluene-PLIF.

droplet present (representing an anomaly) in the LS images was filtered for the computation of the mean. Each S image was multiplied by an energy correction coefficient to homogenise the collection of 3000 images, thus, damping any shot-to-shot laser energy fluctuations. The energy corrected raw images (S_{ec}) were then corrected by the mean noise and mean laser sheet images, as indicated in Fig. 3.17. This accounted for the background noise and for the laser sheet energy

profile, simultaneously providing a reference χ_{Fuel} of the global equivalence ratio, as stated above. The corrected images, labelled S^*, were then used to calculate the local fuel molar fraction and the equivalence ratio via equations 3.6 and 3.7.

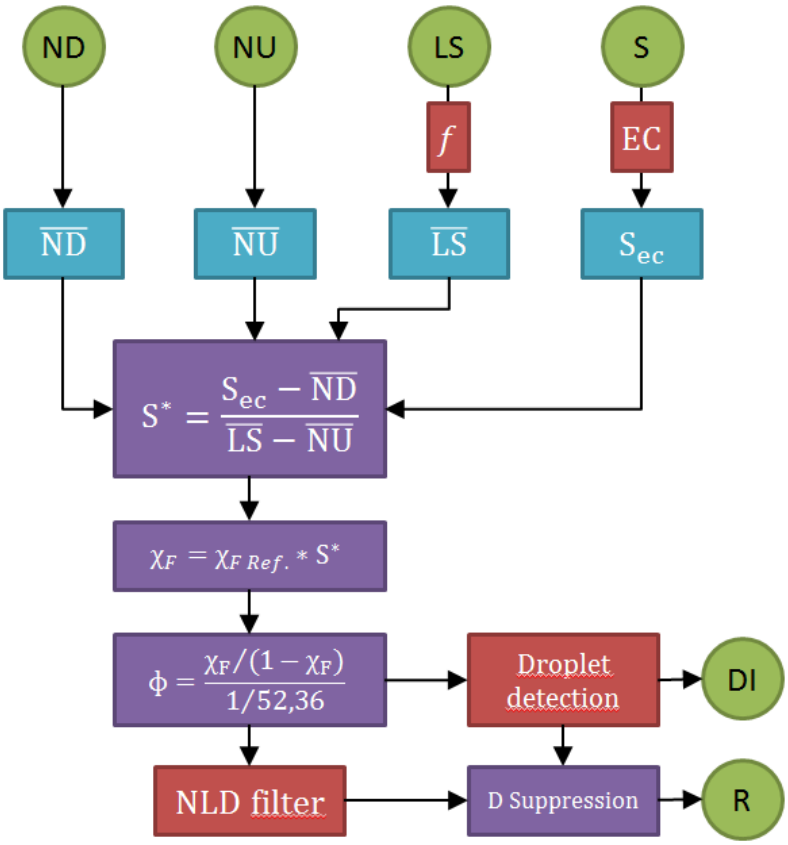

Figure 3.17: Post-processing strategy for the Toluene-PLIF images including image correction, calculation of ϕ, droplet suppression and image filtering.

$$\chi_F = \frac{n_F}{n_F + n_{gas}} \tag{3.6}$$

$$\phi = \frac{FAR}{FAR_{St}} = \frac{\dot{m}_F/\dot{m}_{air}}{(\dot{m}_F/\dot{m}_{air})_{St}} = \frac{n_F/n_{air}}{(n_F/n_{air})_{St}} \tag{3.7}$$

where χ_F is fuel molar concentration and n is number of moles.

In a final step, the instantaneous equivalence ratio images were filtered using a non-linear diffusive filtering method [123]. Large gradients of the fluorescence signal are found in the vicinity of the issuing co-flow jet and close to dense spray regions and large droplets. Large droplets posses a very energetic fluo-

rescence signal and can be easily detected with gradient and level thresholds. The post-processing strategy applied detected the position of the large droplets, which were not included in the mean and standard deviation calculations nor for the flammability factor [40]. R in Fig. 3.17 represents the 3000 instantaneous equivalence ratio results, with detected droplets set to $\phi = 0$.

In this work, PDA data helps to quantify the droplet content in each chamber region. For instance, PDA results (chapter 4) show that in the inner recirculation zone (IRZ) and in the outer recirculation zone (ORZ) of the single-injector burner there are no droplets, so Toluene-PLIF measurements are not biased and can be quantitative. In turn, the spray branch reveals a denser and denser droplet concentration towards the nozzle where Toluene-PLIF can only be qualitative, still providing very useful information. In the multi-injector burner, droplets are also more concentrated around the injector in the spray branches. Depending on the inter-injector distance, the droplet concentration varies. This will be addressed in Chapter 7.

3.4 Planar Laser Induced Fluorescence on OH (OH-PLIF)

OH-PLIF was applied in the KIAI-Spray single-injector burner to characterise the stabilised flame structure and stabilisation points. OH is a well-known tracer of the combustion process and the use and documentation of this technique is large [124–126]. Indeed, the OH gradient is a good marker of the flame front position. This radical is one of the most important intermediate species present during the combustion between fuel and air. OH is formed by fast two-body reactions and then consumed by slower three-body recombination reactions [127].

An Nd-YAG-laser operating at 532 nm was used to pump a tuneable dye laser (Quantel TDL90) supplied with Rhodamine 590 dye. The resultant output pulse energy was 30 mJ per shot in the probe volume. The excitation wavelength was tuned to the $Q_1(5)$ transition line of the $A^2\Sigma^+(v' = 1) \leftarrow X^2\Pi(v'' = 0)$ band of OH at $= 282.75$ nm because of its high intensity, its spectral isolation and its low dependence to temperature [119]. This transition if further discussed in [128]. The collection system consisted of an ICCD camera (PIMAX 4, Roper Scientific) equipped with UV lens ($f/2.8$). Background noise arising from elastic

scattering by the droplets was reduced with a high-pass optical filter (Schott WG295), but was not completely eliminated so as to detect the presence of fuel droplets. A broadband collection strategy of the fluorescence from 308 to 330 nm was adopted using a band-pass filter (Schott UG11).

A traditional mean noise and mean laser sheet energy profile correction was applied to the raw images. 100 instantaneous laser sheet images were previously recorded by filling the chamber with a homogeneous concentration of acetone vapour.

3.5 High-Speed Visualisation of Spontaneous Flame Emission

In order to explore the ignition process with instantaneous and temporally resolved information, the spontaneous emission of the flame was recorded by means of a CMOS Phantom V2512 high-speed camera. This was performed simultaneously with the ignition trials and with the acquisition of the dynamic pressure signal in the single-injector burner to record the development and evolution of the flame kernel into a stable flame. Concerning the multi-injector burner, the flame propagation was recorded simultaneously with the dynamic pressure, triggered by the electric spark.

3.5.1 Experimental Configuration: Single-injector Burner

The high-speed camera recorded through the same quartz window through which the laser-beam entered into the chamber, so as to reduce the collected light issuing from the spark. It was positioned at an axis perpendicular to the first burner window and slightly tilted downwards to appreciate the 3D nature of the motion, as indicated in Fig. 3.18. The size of the recording region was 1280 $\times$ 800 px^2, with a magnification of 0.139 mm/px. The camera worked at an acquisition rate of 4 kHz with a diaphragm opening of 2.8 and an exposure time of 240 μs. A 532 nm rejection filter blocked the laser light. The synchronisation settings were designed to trigger the acquisition with a delay of 150 μs after the sparking. However, there is a transient mark (intense small ovoid) on the images made by the spark on the CMOS due to excessive saturation during the spark existence. All high-speed images contain their "spark mark", which usefully indicates the

coordinates (r,z) of the sparking point. The "spark mark" disappears around $t \approx 30\ ms$. A dimmer "spark mark" is also observed in some images due to the light reflected on the second chamber window.

3.5.2 Experimental Configuration: Multi-injector Burner

The same Phantom V2512 camera was used at a frequency of 20 kHz in order to capture in detail the flame propagation during ignition Phase 4. It was placed in front of the quartz window recording the vertical plane of the entire CLSSB chamber. The high acquisition frequency limited the exposure time to 49 μs and the magnification ratio was optimised for each configuration in order to adapt the $1280 \times 800\ px^2$ CMOS to the region of interest. Thereby, the magnification ratios were 399 $\mu m/px$ for $d = 9$ and $d = 18\ cm$; and 526 $\mu m/px$ for $d = 13$ and $d = 15\ cm$. The energetic electric spark also saturated the CMOS at the start of each recording.

In addition, a 532 nm vertical continuous laser sheet (Diode-pumped solid estate laser, 1 W) entering from one side of the chamber illuminated the fuel droplets. No rejection filter was used this time and, thus, the Mie scattering signal was simultaneously collected by the camera.

3.6 Ignition Probability Mapping

It is very useful to tackle the ignition problem from different points of view given its complexity. For instance, statistical observations can supply valuable information that can be correlated to other variables of the problem and used in complementary numerical studies. Ignition probability was necessary to understand how the sparking position and the local flow influence the ignition process.

Ignition probability was explored only in the single-injector burner facility. For this study the mixture was ignited via a laser-induced spark, through a multi-photonic ionisation process [129]. There is a large amount of information in the literature on laser-induced sparks [44] but this is not the object of the present work. The advantages of laser-induced sparks compared to electric sparks include the lack of electrodes, which represent an important heat sink term, and the freedom to trigger the spark anywhere inside the chamber.

3.6.1 Experimental Configuration

An ignition probability map was obtained by performing 30 ignition trials in each point of a 2-D mesh. This gives a maximum standard deviation of 9% for an ignition probability of 50% [73]. The spark was generated by focusing a 532 nm laser beam in a selected location inside the combustion chamber. Figure 3.18 presents the apparatus used for this purpose, which was similar to the experimental set-up used in [52]. The laser beam was generated at 10 Hz by a Nd:YAG laser. The energy of the laser pulse was controlled and adjusted through the use of a coated variable dielectric attenuator (Laser Optik, Ref. 1Q2) without modifying the Q-switch delay in order to keep the physical beam properties constant. A chopper was used to operate in a single-shot mode and to control the spark triggering. After the chopper, the beam crossed a beam splitter and a beam expander to reduce the energy density on windows and for better focalisation. The laser beam was then focused by a convergent lens $f = 200$ mm through the first quartz window into the chamber. The burner was mounted on a 3-D micrometric position control system and, hence, the focal point position could be varied around the chamber. Behind the spark, the residual laser beam crossed the second quartz window. The energy deposited in the spark was obtained from the measurements of the reference (M1) and the residual (M2) laser pulse energies with two precision laser pyroelectric energy meters (Ophir: PE-25). Position M3 in the figure was used, together with M1, to perform a previous calibration of the incident energy. The residual energy reflected on the second (exit) window was also tabulated through a calibration and taken into account for the determination of the total residual energy. The deposited laser energy was around 405 mJ. This high value was necessary to ensure a full dynamic range of ignition probability within the domain, due to very lean operating conditions ($\phi = 0.61$). Droplet concentration can modify the incident and residual energies due to light-droplet interactions. However, during the experiments, beam focalisation problems were never observed. Another issue raised from the quartz windows, which had to be cleaned after some time due to droplet impact (after $\approx$ 150 shots).

The burner was positioned slightly tilted so as to reach farther radial locations for sparking and it was verified that this does not modify the ignition probability trends. The spark position was varied through a mesh of 120 interrogation points. For each spark position, 30 independent ignition tests were performed

and ignition probability in each point was calculated dividing the number of successful events by the total test number. The interrogation mesh was located in the XZ plane ($y = 0$) and its size was adapted to the ignition probability variations: in 5 mm steps for the z direction and either 1, 2 or 4 mm in x (or r).

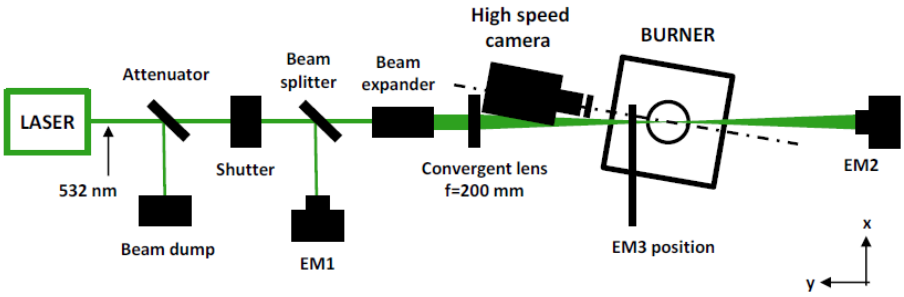

Figure 3.18: Experimental apparatus and setup for the laser-induced ignition experiment. The position of the high-speed camera for simultaneous kernel visualisation is also indicated.

3.6.2 Control and Repeatability

Internal wall temperature (T_{wi}) is a very important parameter in ignition, especially under two-phase flows and ultra-lean conditions. This has also been observed in other studies [97]. Indeed, T_{wi} can impact the flow temperature, thus, droplet evaporation rates; and small local equivalence ratio variations imply large minimum ignition energy (MIE) variations for ultra-lean configurations [50]. In addition, flammability limits are sensitive to mixture temperature variations [130].

To eliminate this variable and to make the experiment repeatable, it was crucial to keep the wall temperature constant. For this purpose, a thermocouple at the window centre and at $z = 100$ mm constantly measured the inner wall temperature. At nominal conditions, with the spray flowing, T_{wi} reaches a stable value of 385 K. Without the spray or when a flame has been previously ignited, T_{wi} is higher than this stable value, so between each ignition event a certain time has to pass in order to get back to nominal conditions. Provided that waiting for T_{wi} to descend back to 385 K would take too long, a T_{wi} threshold was fixed to 387 K.

Ignition was controlled and automated thanks to a LabVIEW code that took into account all the important parameters to guarantee the repeatability of the experiments. The program operated as follows:

- The stability of the air and fuel flows was constantly checked and was mandatory to enable the opening of the chopper.
- If the previous condition was satisfied, the chopper only opened when the T_{wi} descended below the threshold value (387 K).
- The opening of the chopper was short enough to allow only one laser pulse into the system.
- The acquisition of the dynamic pressure at the exit of the chamber (Kistler sensor at 10 kHz) was triggered simultaneously with the chopper. This signal enabled the detection of successful ignitions determined by a characteristic pressure peak occurring some milliseconds after the detection of the spark-induced shockwave.
- If ignition failed, another spark was triggered when the conditions were satisfied, but respecting some time so as to renovate the flow. Typical time between failed trials was ≈ 2 s.
- For successful ignitions, the fuel flow through the atomiser was stopped 300 ms after ignition so as to minimise the increase of T_{wi}. This time was enough to guarantee the formation of a stabilised flame. It was checked that a flame ignited under these conditions would never extinguish later on. The fuel pump rotation was never stopped during the experiments. In turn, a pneumatic valve deviated the fuel flow back to the reservoir during a very short time but enough to extinguish the flame, enabling a faster reinjection of the spray. The process then restarted by checking the stability of the flows and the wall temperature. Typical time between successful trials was ≈ 4 s.
- For every sparking event, the laser incident and residual energies were recorded, as well as the fuel injection pressure, the internal and external wall temperatures, the chamber dynamic pressure signal and the success or failure of ignition.

During the post-processing of the data, rare events with anomalous laser incident energy or T_{wi} were erased.

3.7 Large Eddy Simulation: Numerical Setup

A brief description of the numerical setup used by CEARFACS to simulate the KIAI-Spray burner is now provided. Some of the LES results they obtained will be presented and commented in Part III, with the objective of comparing experimental findings to numerical predictions. In some parts, a coupled Experimental-LES approach enables performing a deeper analysis of ignition Phases 2 and 3. The aerodynamics of the carrier and dispersed phase have been validated, thus a comparison of the experimental and numerical results concerning the local equivalence ratio reinforces the validity of the experimental results (Chapter 4). All the LES setups and results presented in this thesis belong to the ongoing PhD work of Felix Collin Bastiani.

The KIAI-Spray burner was investigated numerically using LES with the code AVBP co-developed by CERFACS and IFPEN (www.cerfacs.fr/avbp7x). The computational domain displayed in Fig. 3.19 contains the inlet pipe, the swirlers, the injection veins, the combustion chamber and the convergent at the outlet. A fully unstructured grid was generated for the stabilized non-reacting and reacting cases, containing more than 60 million tetrahedral cells and where the smallest cells are located in the swirler vanes ($\Delta x = 0.4\ mm$) and in the shear layer region ($\Delta x = 0.3\ mm$). AVBP solves the LES-filtered fully compressible reacting Navier-Stokes equations. For the gas phase, the third order in time and space Taylor-Galerkin scheme [131] was used for the non-reacting and reacting steady flow simulations whereas the second order in time and space Lax-Wendroff scheme [132] was used for ignition sequences to save CPU time. The Navier-Stokes Characteristic Boundary Conditions [133] were used for inlet and outlet boundary conditions while the combustor walls were considered as non-slipping and isothermal ($Tw = 387\ K$ for the non reacting case and $Tw = 1000\ K$ for the reacting case). Turbulent subgrid stresses were modelled using the SIGMA model [134].

A Lagrangian approach was chosen for the spray description using the same sub-models for drag, evaporation and injection (FIM-UR model to mimic a simplex pressure atomizer) as in the numerical study of the jet spray configuration

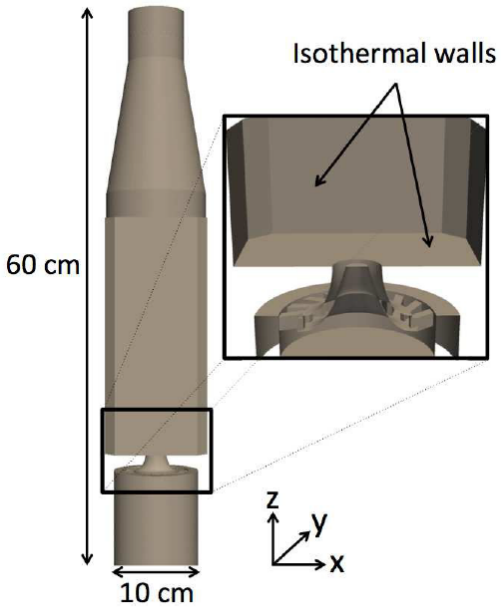

Figure 3.19: Computational domain for LES with detail of the injection system.

of the KIAI burner [135].

The n-heptane fuel oxidation was described using an Analytically Reduced Chemistry named ARC_25_C_7H_{16} derived from the skeletal mechanism of Jerzembeck et al. [136] using the reduction tool YARC [137]. It comprises 25 transported species, 27 species in Quasi-Steady State Approximation and 210 irreversible reactions. It was validated on one-dimensional gaseous laminar flames in atmospheric conditions and for equivalence ratios ranging from 0.6 to 1.6. The very refined mesh in the flame zone allows to fully resolve the flame front and neglect the subgrid-scale wrinkling of the flame.

Finally, the Energy Deposition (ED) model [138] was used to mimic the laser-induced ignition by recovering a kernel of accurate size compared to experiments hundreds of microseconds after the laser ignition. The corresponding deposition characteristic size is 8 mm and the total energy deposited is 25 mJ leading to an energy transfer efficiency in agreement with values from literature [34]. Following the ED procedure, the laser-induced spark region was refined during the early instants following energy deposition with a typical cell size $\Delta x = 0.17$ mm, leading to a larger grid containing about 70 millions tetrahedral cells. Once the kernel was big enough, the two-phase reacting flow was interpolated on the

reference grid to simulate the full ignition sequence.

Conclusion to Part II

This is the end to Part II, involving chapters 2 and 3. Here, the two experimental facilities have been described in detail, as well as the operating conditions for each of them and for each experiment. It has been made clear that each burner satisfies a different objective of the investigation, namely, the study of ignition Phases 2 and 3 (single-injector burner) and the study of ignition Phase 4 (multi-injector burner). All the diagnostics and experiments applied either to one or both burners have been thoroughly detailed, as well as their specificities. A special effort has been made to include the possible error sources and to cover all the major issues. In this sense, experiments were carefully performed so as to provide a thorough set of data.

To address aeronautical ignition Phase 2, PDA, HS-PIV and Toluene-PLIF were used to describe the non-reacting local flow in a first approach of the investigation. Droplet size, velocity and distribution, air velocity and turbulence, and fuel repartition (qualitative or quantitative) in liquid and vapour phases were extracted in order to analyse and understand the environment in which a flame kernel must develop. The ignition transition in the single-injector KIAI-Spray burner was tackled with an elaboration of an ignition probability map of the chamber and coupled data of dynamic pressure and high-speed visualisation of the kernel.

The high-speed images and pressure signals also enable the description of the stabilisation of the flame during Phase 3. OH-PLIF images were recorded to describe the stabilised flame structure. PDA and PIV data are also available for the analysis of the reacting flow.

The analysis of ignition phase 4 was performed in the multi-injector CLSSB facility. HS-PIV and Toluene-PLIF provided information on the airflow and on the mixture formation for non-reacting flow for the four injector-to-injector distances studied. HS-PIV data during ignition together with coupled pressure

and high-speed visualisation data give new insight on the flame propagation mechanisms observed for the different injector-to-injector distances.

In the following, the results are presented and discussed keeping the chronological order of the ignition process.

Part III

SINGLE-INJECTOR BURNER RESULTS. IGNITION PHASES 2 & 3

Chapter 4

Description of the Non-Reacting Local Flow

Contents

Part 3 of this manuscript involves chapters 4, 5 and 6 and is devoted to the analysis of the mechanisms occurring mainly in Phase 2. Phase 3 is tackled in Chapter 6.

More specifically, this chapter is dedicated to the description of the non-reacting flow in the single-injector burner, which is representative of the local conditions encountered by the flame kernel during its development in the chamber. As already mentioned in Chapter 1, different regions of the chamber show very different flow properties that can fluctuate with different timescales. Here,

the PDA results provide a rich description of the spray droplet velocities, sizes and distribution in the burner, as well as of the air velocity and turbulence. HS-PIV data gives access to the instantaneous 2-D air velocity field and Toluene-PLIF results are analysed to inform of the local mixture formation. Understanding this database is vital to explain the results presented in the following chapter dealing with ignition probability and kernel development.

Throughout Part 3, various comparisons to simulation results from LES are made and help the coupled understanding of certain processes. The numerical simulations were carried at CERFACS (and still continue) as stressed in the introduction of this document. Particularly, in this chapter, numerical simulations are used to compare the results describing the mixture formation and to assess the validity of the latter.

4.1 Typical Flow Structures and Regions

Aeronautical combustion chambers present characteristic flow patterns that depend on the design of each element of the chamber, such as the ratio of the injection inlet diameter to the chamber width, the swirl number or the chamber shape. As described in Chapter 1, the confinement of the chamber and the sudden change in cross section area experienced by the flow when passing from the injector duct to the chamber induce a toroidal external recirculation zone, sometimes called corner recirculation zone. Here it is labelled Outer Recirculation Zone (ORZ). In addition, when the swirl number exceeds a threshold value of 0.6, a central recirculation zone is created, where negative velocities yield a stagnation region enabling to hold the flame and flow recirculation shortens the flame length. In this work, this is labelled the Inner Recirculation Zone (IRZ). The greater the swirl number, the greater the IRZ volume and, consequently, the smaller the ORZ volume. In a 2-D cut (rz-plane) we will talk about IRZ and ORZ areas. In between both regions the main air jet flows in the Jet Zone (JZ) along the combustion chamber.

In order to describe these main regions, the use of PDA could only be extended to zones containing either fuel droplets or seeding droplets (Chapter 3), thus giving a limited view of the structures in the chamber. PDA was needed to characterise the fuel droplet presence, size and size-classified velocity. It was also used to describe the airflow, but it could not provide 2-D instantaneous

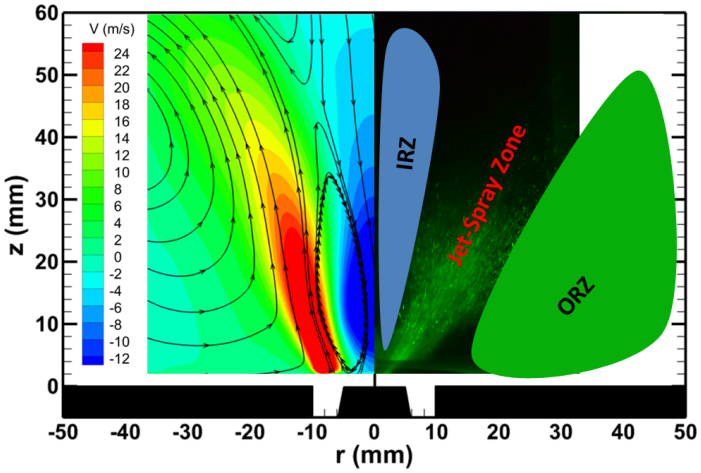

Figure 4.1: Characteristic chamber regions. Left: mean velocity field of the carrier phase coloured by the mean axial velocity (PIV). Right: Mie-scattering tomographic photograph of the fuel droplets and sketch of the IRZ and ORZ.

information of the flow patterns of the carrier phase. As an answer to this, PIV permitted the exploration of all the regions of the chamber and gave access to 2-D instantaneous information, which is necessary to understand mechanisms involved in flame kernel extinction or successful ignition during Phase 2. Figure 4.1 illustrates the IRZ, the ORZ and the Jet-Zone (JZ) in the KIAI-Spray single-injector burner. Due to the low swirl number (Chapter 2) the IRZ, in blue, presents a small area in the centre of the burner compared to the ORZ, in green. The right-hand-side of the figure shows a sketch of these regions overlapped to a Mie-scattering tomographic photograph of the spray droplets, where it can be observed that the spray is mainly overlapped to the main Jet-Zone (JZ) and slightly invades the borders of the IRZ and ORZ. The left-hand-side of Fig. 4.1 reveals the mean velocity field of the carrier phase extracted from the PIV results. Colours indicate the axial flow velocity while the streamlines clearly identify each region of the flow. The carrier and the dispersed phases are now described separately.

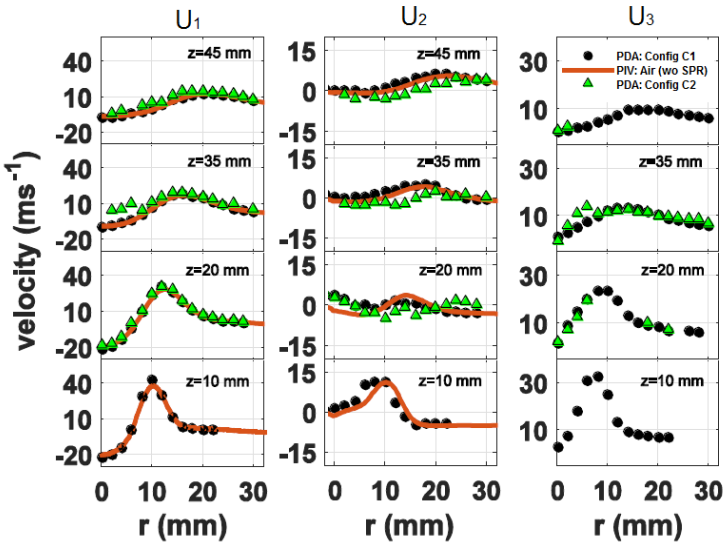

Figure 4.2: Mean air velocity radial profiles at four axial stations. Axial, radial and azimuthal components are respectively shown in the left, central and right columns. Black circles show PDA measurements of the carrier phase without spray presence (C1) while green triangles show PDA measurements of the carrier phase under nominal conditions (C2(with spray)). Orange lines represent the PIV results of the air without spray presence.

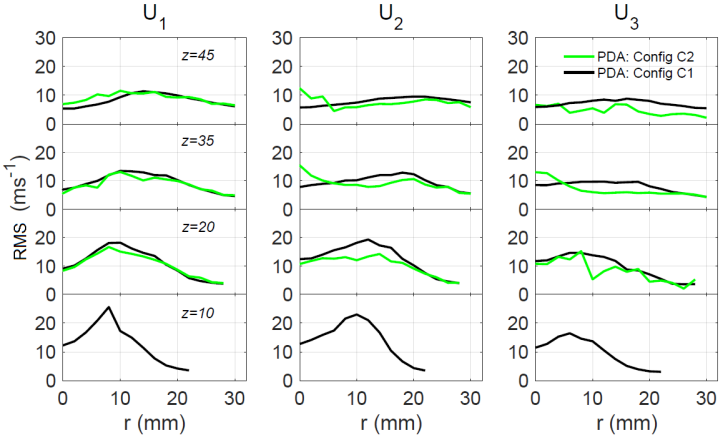

Figure 4.3: Standard deviation air velocity radial profiles at four axial stations. Axial, radial and azimuthal components are respectively represented by U_1, U_2, U_3. Black lines: PDA (C1); Green lines: PDA (C2).

4.2 Carrier Phase

4.2.1 Velocity

The air jet issues through the annular co-flow into the chamber at a bulk velocity of 41 $m.s^{-1}$ with a Reynolds number of $Re = 14797$ based on the hydraulic diameter. The swirling motion opens the jet and establishes an IRZ while the ORZ takes the space left between the co-flow entrance and the chamber walls. It is interesting to measure and quantify the velocity field and the influence of the fuel droplets on the air motion. The three components of the mean velocity of the air are plotted in Fig. 4.2, in the form of radial profiles for 4 axial stations. PDA 3-D data (black dots) and PIV 2-D data (orange lines) show a very good agreement, demonstrating the repeatability of the measurements and the robustness of the results. Both represent the mean velocity field of the airflow without spray presence. Whereas PIV calculations risk of being modified by fuel droplet presence, PDA can isolate the air data from measurements in presence of fuel droplets using PDA configuration C2, which was explained in Chapter 3. Therefore, green triangles can be compared to black circles to stress that the influence of the spray on the air mean velocity is almost negligible in the entire burner. Axial velocities in Fig. 4.2 show the co-flow peak at $r = 10$, $z = 10$ of 40 ms^{-1}, which then diffuses downstream. The negative peak velocity at $r = 0$ presents a magnitude of 20 ms^{-1} from $z = 10$ to $z = 20$ and then relaxes downstream. Radial velocities reach a maximum peak of 15 ms^{-1} at $r = 10$, $z = 10$, which then relaxes at higher axial stations, showing always much smaller values than the other 2 velocity components. The azimuthal velocity maximum reaches maximums of 35 ms^{-1}. Figure 4.3 compares the standard deviation of the measured air velocities without (C1) and in presence (C2) of the fuel spray for the same axial stations and profiles that Fig. 4.2. No significant differences are observed between C1 and C2 for the standard deviation meaning that there does not exist an important modification of the carrier phase velocity for $z > 10$. Measurements in configuration C2 were not possible at $z = 10$ due to the increasing fuel droplet concentration. Green lines in Fig. 4.3 appear more noisy than black lines because in C1 only seeding droplets were detected while in C2 the spray droplets were also detected, thus leaving less small tracer droplets available for the post-processing (Chapter 3).

4.2.2 Turbulence

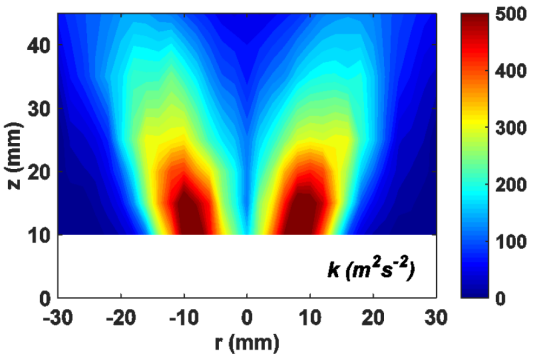

Figure 4.4: Turbulent kinetic energy of the carrier phase. Calculated from PDA data.

Velocity fluctuations from PDA C1 measurements are expressed in Fig. 4.4 in terms of the turbulent kinetic energy (k), which is calculated following equation 4.1:

$$k = \frac{1}{2}\left(\overline{(u_1')^2} + \overline{(u_2')^2} + \overline{(u_3')^2}\right) \tag{4.1}$$

The maximum turbulent energy ($\approx$ 550 m^2s^{-2}) is found at low axial stations, in the region where the air enters the chamber, and follows the same pattern as the axial and azimuthal velocities, with peaks diffusing radially with increasing axial stations. Given that energetic velocity fluctuations enhance mixing and that all droplets enter the region of maximum k directly after atomisation, their trajectories are strongly influenced by the airflow. This will be detailed in the following section (4.3). Zones outside the external shear layer of the air jet show blue colours indicating the lowest k measured values ($<$ 100 m^2s^{-2}). Air velocities and k appear to be very low in the ORZ, where burnt gases and/or fuel vapour may have longer residence times than in other regions. The IRZ shows high k for $z < 30$ mm and still, at $z = 45$ mm k values are higher than in the ORZ at $r = 30$, $z = 10$ mm for instance.

Another necessary information that completes the analysis of the carrier phase are the instantaneous velocity fields gathered with PIV. Figure 4.5 presents 4 instantaneous independent air velocity fields from HS-PIV measurements. The colour maps indicate the total strain rate imposed by the airflow. Equations 4.2 and 4.3 were used for the total strain rate, where E_{ij}, symmetric component of

the velocity gradient, is the 2-D strain rate tensor and σ represents the total rate of strain, including the 2-D expansion and shear terms.

$$E_{ij} = \frac{1}{2}\left(\partial_j v_i + \partial_i v_j\right) \tag{4.2}$$

$$\sigma = \left(\sum E_{ij}^2\right)^{\frac{1}{2}} \tag{4.3}$$

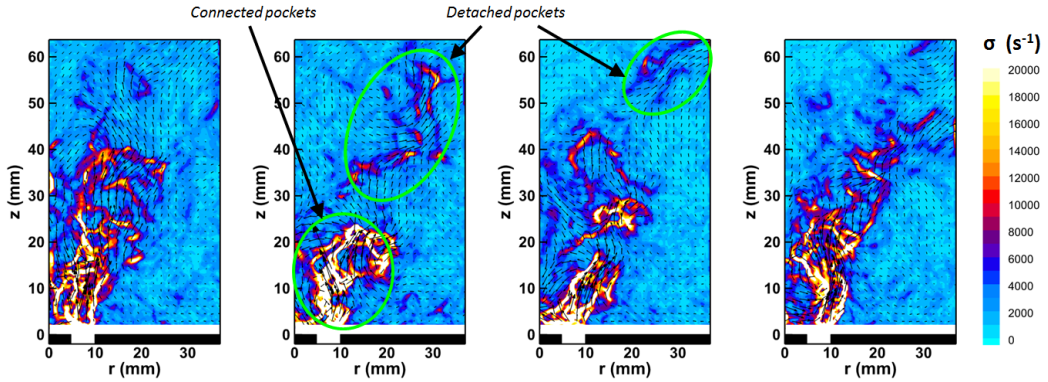

Figure 4.5: Four independent instantaneous air velocity fields from PIV data. The colour map illustrates the total strain rate calculated from the velocity gradients.

In Fig. 4.5, the air jet can be easily identified as a stream meandering diagonally upwards from $r = 7$, $z = 0$ to $r = 38$, $z = 60$. There is strong evidence of an energetic eddy generated by the contact between the vigorous airflow entrance and the important negative velocities in the IRZ. The most probable location of the centre of this eddy is $r = 5$, $z = 15$ mm. This can be directly observed on the streamlines of the mean flow in Fig. 4.1. It is the most energetic structure in the flow and it is responsible for the maximum values of strain rate observed in Fig. 4.5. Second and third order, less energetic rotational structures can be observed farther downstream and are responsible for the air jet deviation and for the generation of less intense strain pockets. This can be proven by projections of the instantaneous velocity fields on the second to fifth modes of the proper orthogonal decomposition (POD). The spatial evolution of the strain rate maps can be interpreted as an intense production of shear and dilation velocity gradients at low axial stations, under the form of filamentary pockets, which are then convected downstream by the mean flow, where they lose energy and relax.

Above $z \approx 35\ mm$, isolated, less intense strain rate filaments can be observed. This detachment implies a greater intermittency of the strain rate values, which turn the flow behaviour more random and less predictable. It is well known that too much strain rate is incompatible with self-sustained chemical reactions and, thus responsible for flame extinction [139]. The ORZ appears to be larger in terms of area than the IRZ and both present very low strain rate in comparison to the air jet zone ($\sigma \approx 1000\ s^{-1}$). Nonetheless, strain pockets reach more frequently the IRZ than the ORZ. The size and position of the IRZ and ORZ vary with time since they are determined by the air jet position, width and deviation. High strain rate regions will disturb the flame kernel shape and evolution due to the modification of the burning velocity increasing scalar dissipation [66].

4.3 Dispersed Phase

4.3.1 Fuel droplet size and distribution

At nominal conditions, the fuel injector yields a very heterogeneous spray in terms of droplet size and location. The ejection angle is 80^o, forming a hollow cone with the majority of the fuel mass located along the cone borders. Primary and secondary atomization processes take place in the first 4 mm downstream after the nozzle and are induced by the pressure swirl atomizer only: the air co-flow does not participate on droplet formation, oppositely to what happens in airblast atomizers. This was explained in Chapter 2. Figure 4.6 (top) shows Mie-scattering tomographic photographs of a vertical (left) and a horizontal (right) laser cuts of the spray, where the conical distribution of droplets is made evident. The two histograms at the bottom of the figure indicate the local droplet size distributions at points $r = 18$, $z = 35\ cm$ (orange triangle) and $r = 0$, $z = 10$ cm (blue circle), extracted with PDA (configuration C3). These results reveal a population locally heterogeneous in size with similar distributions in very distant points of the spray, with detected sizes ranging from 2 to 70 μm.

The global Sauter Mean Diameter (D_{32}) is equal to $\approx 30\mu m$. The hot airflow controls droplet evaporation rates and droplet distribution, mixing the droplets of different sizes in the jet zone. A more precise description of the size at different chamber locations is given by Fig. 4.7, where radial profiles of D_{32} are gathered at 4 axial stations (left). Here, the Sauter Mean Diameter reaches the smallest

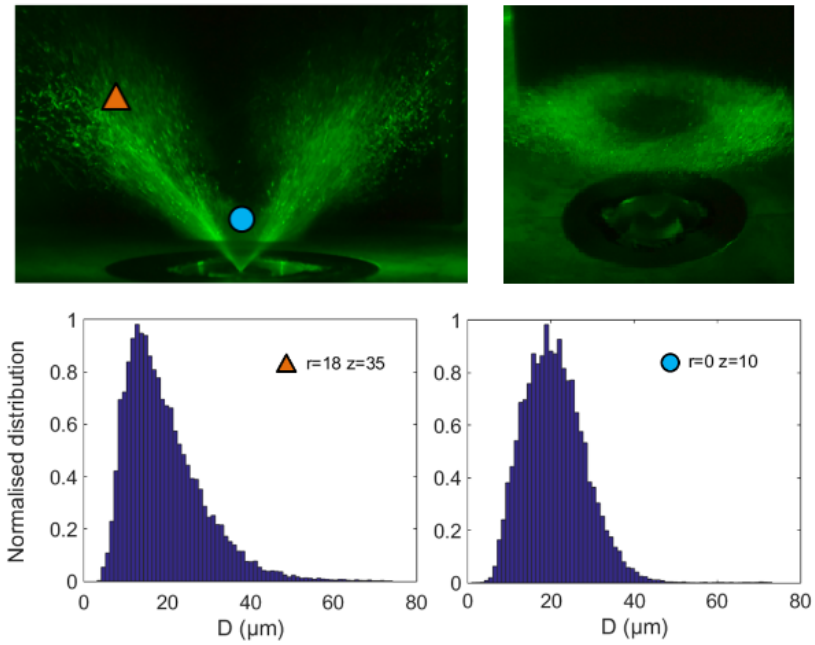

Figure 4.6: Top: Mie scattering photographs of the spray cone (vertical and horizontal cuts). Bottom: two droplet diameter histograms of data collected at $r = 18$, $z = 35$ mm (orange triangle) and $r = 0$, $z = 10$ mm (blue circle).

values at the centre of the chamber for high axial stations, where the size grows with the radial position. At low axial stations the influence of the ORZ modifies this trend and the population of small droplets increases close to $r = 20$ mm. Indeed, droplets with low Stokes number are captured by the IRZ and ORZ modifying the D_{32} in different regions of the chamber.

The right-hand-side of Fig. 4.7 and Fig. 4.8 represent the number of validated droplets detected per second by the PDA system, classified into five size groups of 10 μm span each and giving an indication of the position of the droplets. Droplet frequencies under 47 Hz are not shown in the colour maps in Fig. 4.8. The most populated group is [10-20] followed by [20-30] μm and all groups coexist in the outer parts of the jet resulting in a heterogeneous droplet size distribution. The IRZ and the ORZ are statistically free from droplets, although their borders (close to the JZ) still contain droplets. This is subjected to temporal fluctuations of the spray and the flow and sometimes individual droplets can be found in the IRZ and ORZ.

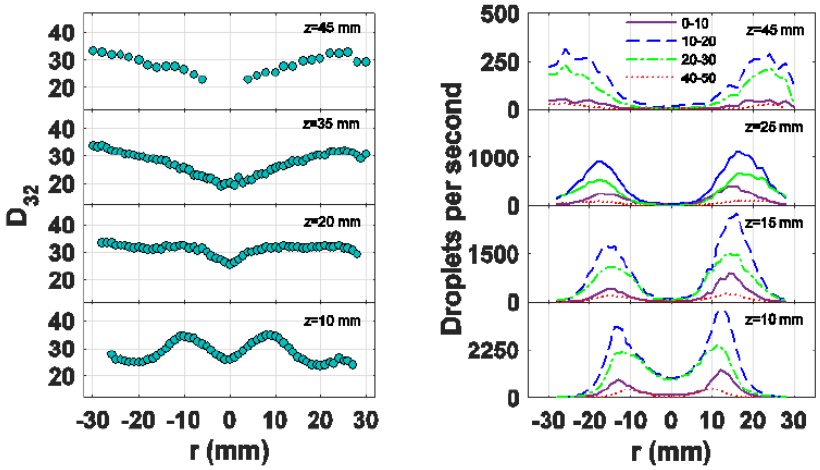

Figure 4.7: Left: Sauter Mean Diameter distribution in the chamber. Right: droplet detection frequency classified by size groups. PDA configuration C3.

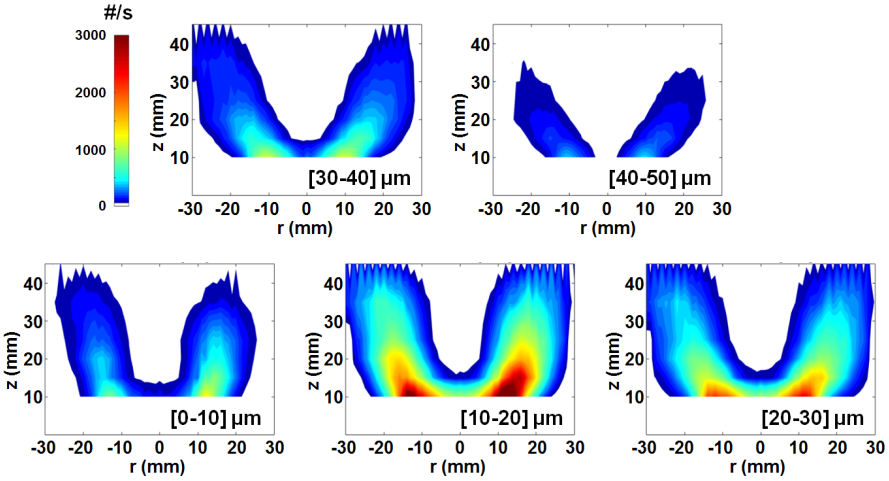

Figure 4.8: Number of valid droplets detected per second by the PDA system divided into 5 size classes. PDA configuration C3.

4.3.2 Fuel droplet velocity

The three mean velocity components are shown in Fig. 4.9 for three different size classes: [0-10], [20-30] and [40-50] μm. Values for the last group are not shown in the central region above $z = 15\ mm$ because less than 100 droplets were detected in 30 s per point in this region. The air velocity (PDA C1 from Fig. 4.2) is included in Fig. 4.9 as black lines. When comparing fuel droplet profiles to

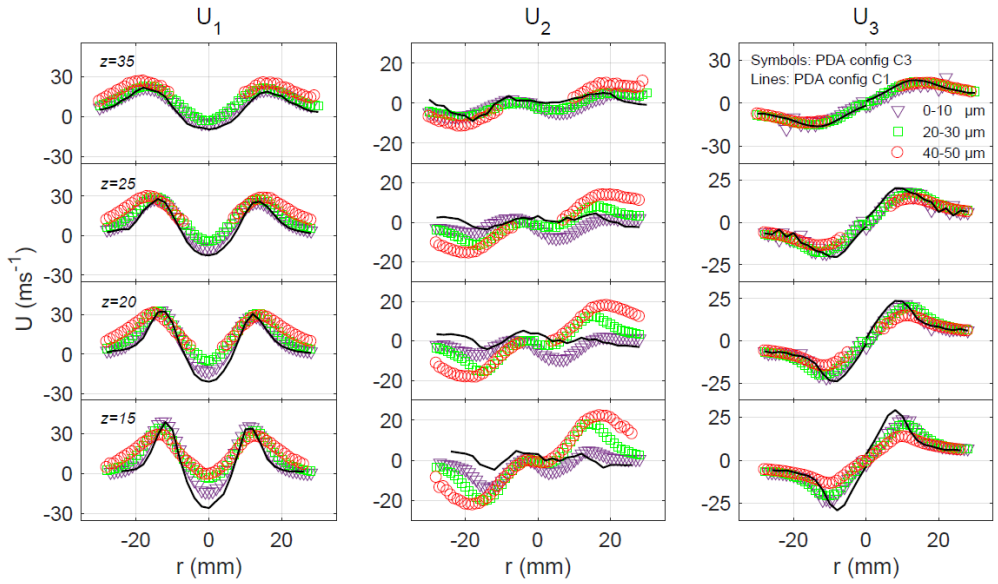

Figure 4.9: Droplet mean velocity components classified by size groups. Radial profiles at four axial stations. Axial, radial and azimuthal components are respectively represented by U_1, U_2, U_3. PDA configuration C3. Black lines represent the airflow (PDA C1) from Fig. 4.2.

the air, it can be seen that small droplets follow more closely the airflow velocity field than large droplets. This will also be indicated on the next page where the slip velocity is analysed. The main difference with the air velocity is observed at the mean radial velocity profiles. Spray droplets are ejected from the nozzle with strong radial velocities. At the first axial station, the three groups have important radial velocities ($\approx 30\ ms^{-1}$) but farther downstream small droplets adapt their velocity to the airflow. Large droplets follow more ballistic trajectories and continue to present important radial centrifugal velocities until $z = 35\ mm$, where they nearly join the other groups. When overlapped to the air stream, droplet axial and azimuthal mean velocities are smaller for the spray than for the air, so small droplets are strongly accelerated by the co-flow while large droplets continue their trajectories at smaller velocities until farther downstream. When fuel droplets exit the high air velocity region, the opposite occurs: they find a quiescent area where they still conserve a high axial velocity. This is more remarkable at low axial stations and for large droplets, and it is also observed for the azimuthal component to a lesser extent. Differences of more than $20\ ms^{-1}$ are observed between the [0-10] group and the [40-50] group. The other size-classes

present the same trends, but they are not presented here in order to facilitate the comprehension of the figure. The behaviour of [50-60] and [60-70] groups is very close to the [40-50] group, but, as they contain less droplets, they are not presented.

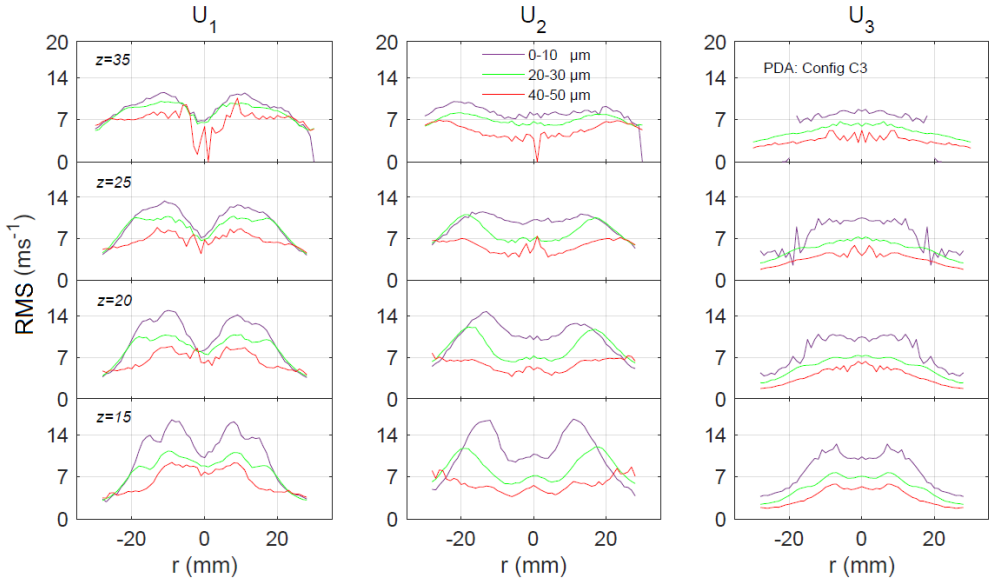

Figure 4.10: Standard deviation of the droplet velocity classified by size groups. Radial profiles at four axial stations. Axial, radial and azimuthal components are respectively represented by U_1, U_2, U_3. PDA configuration C3.

Figure 4.10 indicates the standard deviation of the fuel droplet velocities at the same mesh points revealing that fluctuations are always lower for larger droplets. The axial and radial components show more fluctuation than the azimuthal velocities and the maximum values follow the core of the air jet. The highest strain rates are $\approx 16\ m.s^{-1}$ and are found at the lowest axial stations.

Slip velocity

During their trip, droplets experience important slip velocities, which certainly control the evaporation process and, therefore, vapour production and local fuel-to-air ratio. Slip velocities correspond to the relative velocities between droplets and the airflow. They are a key parameter in two-phase combustion. In order to calculate the mean slip velocity (s) for each point, the spray mean velocity field was subtracted to the air mean velocity field component by component, group

by group, as equation 4.4 stresses:

$$\overrightarrow{s} = \overline{u_{i,air}} - \overline{u_{i,fuel}} \tag{4.4}$$

The magnitude of the resulting vectors is displayed in Fig. 4.11 for the same three size-classes as before. Mean slip velocities are more important close to the nozzle exit and for big droplets. The [0-10] group experiences lower values than the others but these are not negligible. Above $z = 15\ mm$, peaks remain under 20 ms^{-1}. For the [40-50] group, mean slip velocities grow up to 38 ms^{-1} and values above 20 ms^{-1} can be found below $z = 25\ mm$. The maximum slip velocities are found on the borders of the spray, at the same radial positions as droplet peak radial velocities. Here, droplets still have high axial velocities and they have exited the high air velocity region. In the centre, at low z, strong slip velocities are also observed. They are caused by the descending recirculating air flowing against the rising droplets. Vapour produced at the centre will be recirculated downwards along the centre. There is a minimum mean slip velocity for all size-classes above $z = 10\ mm$ placed over regions of medium turbulence intensity, where velocity fluctuations represent 40% of the mean velocities and where k is maximal. Provided that large droplets present far greater slip velocities than small droplets at many points along the profiles ($> 20\ ms^{-1}$), they will experience high evaporation rates. As they carry most of the fuel mass, they will contribute significantly to fuel vapour production and repartition along the burner. The vapour produced at the borders finds a region with low values of air velocity and may be entrained into the ORZ.

4.4 Mixture Formation

4.4.1 Equivalence ratio (ϕ)

The fuel droplet distribution, the evaporation rate of the droplets and the flow motion will determine the mixture fraction at every location and instant. The precision and the limits of the Toluene-PLIF technique were thoroughly described in Chapter 3. It is recalled that the main difficulty raises in regions with high droplet concentration and that small sub-pixel droplets can bias the quantitative information on the gaseous equivalence ratio. To the authors' knowledge, this is the first time that this technique is applied to such heterogeneous and realistic

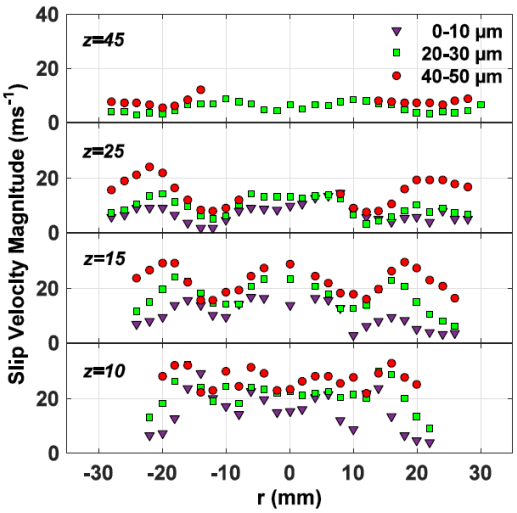

Figure 4.11: Droplet-air mean slip velocity magnitude classified by size groups.

two-phase flow conditions. A special effort has been made here to use the data extracted rigorously. Indeed, some regions of the chamber will be assessed quantitatively and others qualitatively. Namely, the IRZ and ORZ can be exploited in a quantitative manner since they statistically contain no droplets in the majority of their domains. The IRZ at low axial stations becomes too populated with droplets and the interfaces between the JZ and both the IRZ and the ORZ also contain fuel droplets. These regions and the Jet-Zone must be studied with precaution.

In a first step, the mean equivalence ratio field in presented in Fig. 4.12. On the left-hand-side a map shows a portion of half of the chamber while, on the right-hand-side, three vertical and three horizontal $\overline{\phi}$ profiles are plotted, corresponding to the lines traced on the map. Potential signals from any rare sub-pixel droplets present in the IRZ or ORZ are strongly suppressed from each of the acquired 3000 instantaneous maps by the NLD filtering step (Chapter 3) and, furthermore, suppressed here by the mean calculation. It is also reminded that droplets greater than the pixel resolution were detected and not included in the mean calculation. The crossed section in Fig. 4.12 represents the region containing the great majority of the droplets, extracted from Fig. 4.8 in section 4.3. On the mean image, the spray branch shows a high $\overline{\phi}$ diffusing evenly to find an ORZ with homogeneous $\overline{\phi}$ slightly richer than 0.6 and an IRZ with values descending for increasing axial stations. The air jet entrance is again

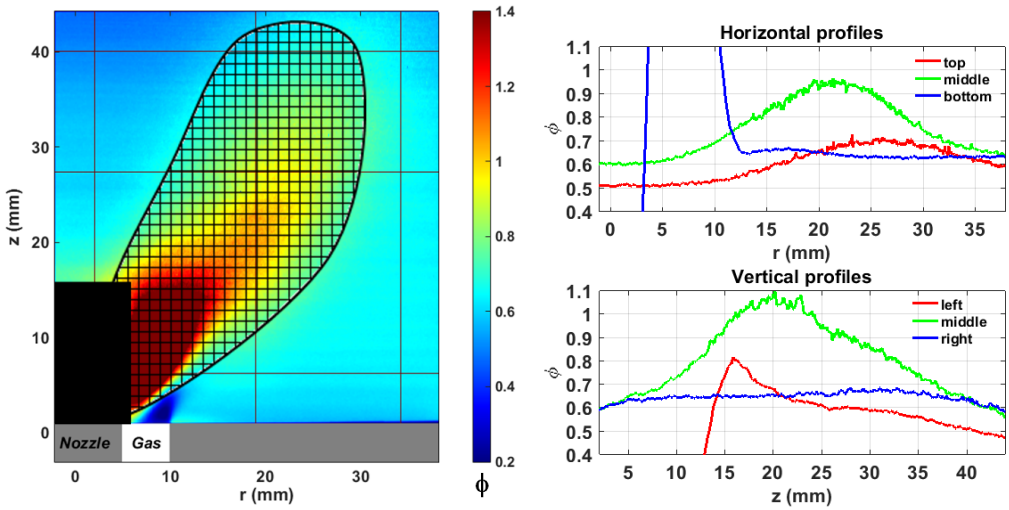

Figure 4.12: Mean gaseous equivalence ratio map of half of the chamber. Plots on the right illustrate the three vertical and horizontal profiles indicated with overlaid on the map. The crossed section represents droplet regions extracted from PDA Fig. 4.8.

clearly identified at r=8 mm. For the horizontal profiles, the red line shows how $\overline{\phi}$ is equal to 0.5 at the centre and increases towards the spray branch. Values between $r = 16$ and $r = 30$ mm must be ignored. The green line follows the same variation showing $\overline{\phi} = 0.5$ in the IRZ and $\overline{\phi} = 0.6$ in the ORZ (outside the crossed region). The blue line remains between 0.6 and 0.7 along the ORZ. The Vertical red profile shows that values decrease for $z > 16$ mm in the IRZ. In green, the bottom-left part of the ORZ presents an increase from $\overline{\phi} = 0.6$ to $\overline{\phi} = 0.8$ before arriving to the crossed region. Finally, values in the blue profile are all out of the crossed region and fall between 0.6 and 0.7 in the ORZ. The lower flammability limit for n-heptane being $\phi = 0.55$ [82], it can be concluded that the ORZ is a favourable region in terms of equivalence ratio for ignition, whereas the IRZ reveals lower values for which ignition becomes an impossible task.

The analysis of the local instantaneous equivalence ratio is important at this stage because it contains information that cannot be stressed by the mean equivalence ratio field. Figure 4.13 contains three independent instantaneous ϕ fields. Once a flame kernel is created, it will see a ϕ field similar to one of these. A close look at Fig. 4.13 reveals a homogeneous ORZ, despite being in a two-phase flow configuration. There are no longer droplets available here, as stressed by

the PDA data presented in section 4.3, and an efficient mixing process yields a constant ϕ value of ≈ 0.65. The IRZ contains few droplets but, due to the recirculation of air, ϕ decreases with increasing values of z. In the majority of its domain, the IRZ is below the lean flammability limit. In contrast, the jet-spray zone presents an intense temporal and spatial fluctuation of ϕ, with values ranging beyond the lean and rich limits. This effect is caused by the presence of evaporating droplets and enhanced by the turbulent air motion, which segregates the droplets and organises them around mid-scale eddies. Droplet segregation around vortices was studied with DNS in [140]. A probe placed at any point in this region will see alternating "pockets" of lean and rich mixture passing by. This intermittency explains why sparking in a certain point of the spray-jet zone at different times will never give the same kernel shape, burning velocity and, thus, flame evolution. An analogy can be made here in terms of turbulence and strain ratio with in section 4.2.

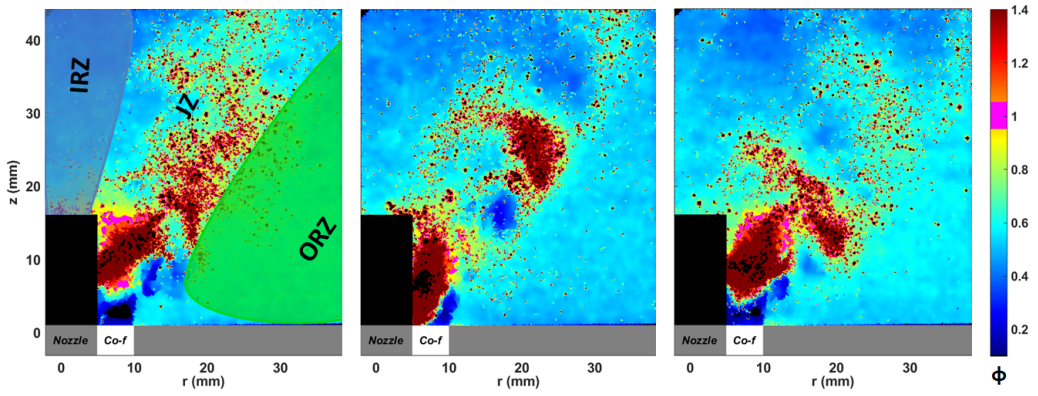

Figure 4.13: Three independent instantaneous gaseous equivalence ratio images of half of the chamber. Values of ϕ close to 1 are coloured in pink.

The numerical simulations offer the same observations and conclusions. However, Fig. 4.14 proposes a comparison between both approaches that enriches the analysis. It is, indeed, an example of the cross-benefit of coupling LES and experiments. Until now, the gaseous and liquid aerodynamics and transport match satisfactorily between both approaches and, assuming the evaporation model represents loyally the real physics, the prediction of the local gaseous equivalence ratio should be correctly achieved by the LES. In Fig. 4.14, (A) and (B) show an instantaneous and the mean ϕ fields. It is reminded that the mean was calculated from 3000 instantaneous fields and that the detected droplets were

not included in the calculation. From the LES, (C) represents an instantaneous field of liquid+gaseous ϕ, (D) the same instantaneous gaseous ϕ field and (E) the mean liquid+gaseous ϕ field. The IRZ and ORZ match between (A), (C) and (D), as well as when comparing (B) to (E). This corresponds to a real gaseous ϕ due to the absence of droplets in these regions. In contrast, the spray branch in (A) resembles much more that of (C) than to that of (D), meaning that the experimental gaseous ϕ is biased here by the presence of sub-pixel droplets, as explained in Chapter 3 as one of the current limitations of Toluene-PLIF in two-phase flows. When looking at the mean images, (B) and (E), the same conclusion is extracted. For this reason, in these experiments the IRZ and ORZ remain quantitative whereas the spray branch provides a very useful, but qualitative information. Having said that, vortex cores in the spray branch are free of droplets and, thus, low ϕ values are very close to reality.

Several studies defend that the presence of droplets in the unburnt gases of a propagating flame stratifying the mixture perturbs the flame propagation, increasing flame curvature and wrinkling and modifying the burning velocity [66, 74]. Others are concerned by the latent heat extracted from the flame by the evaporating droplets causing a significant reduction in burning speed [64] or an eventual flame quenching [79]. These state that small droplet sizes and high volatility are favourable for combustion because this sink term is then minimised. In this study, global ϕ is extremely lean and the only way of increasing local ϕ is finding regions near droplets or droplet clouds. For some areas of the burner, it is possible that the rise in ϕ caused by droplet presence is more important that the detrimental effect of temperature diminution. This will be shown in the following chapter. For instance, at high axial stations of the IRZ, eventual droplet presence can sustain a flame kernel that otherwise would suffer from fuel starvation.

Figure 4.15 shows the PDFs of the experimental equivalence ratio values sampled at 3 points representative of the IRZ, ORZ and JZ in the chamber for all the 3000 available datasets. This information gives evidence of the dispersion differences between regions and confirms that the IRZ and ORZ have narrow distributions outside and inside the flammability limits, respectively. The spray branch values span from 0.4 to infinity, proving the high variability of possible situations that a flame front will face. Note that the distribution of values in the PDF of the spray branch is not real due to sub-pixel droplet bias.

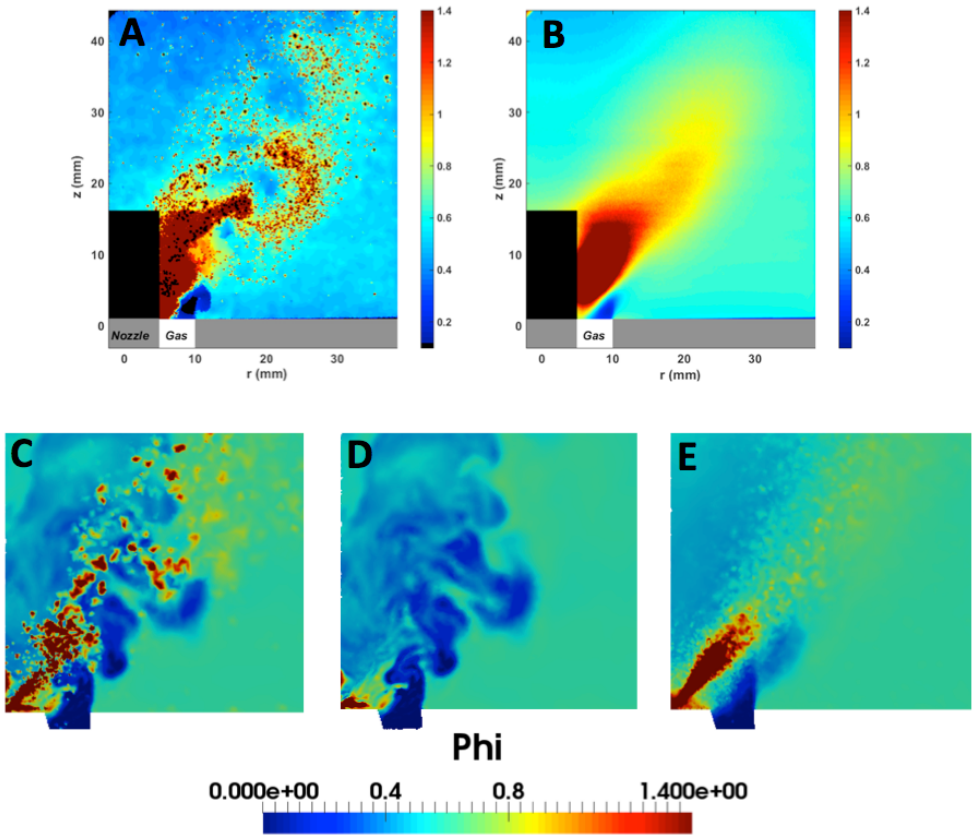

Figure 4.14: Experimental (top) and LES (bottom) equivalence ratio data. A and B are an instantaneous and the mean field. C, D and E are respectively an instantaneous liquid+gaseous ϕ field, an instantaneous gaseous ϕ field and the mean liquid+gaseous ϕ field.

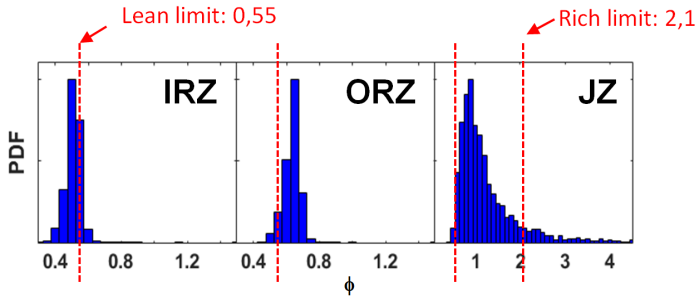

Figure 4.15: PDFs of the equivalence ratio measured in the three main regions of the chamber (IRZ, ORZ and Spray branch) for all the images. Dashed lines indicate the lean and rich flammability limits.

4.4.2 Flammability factor (F)

When integrating ϕ values between the lean and rich flammability limits for all pixels along the 3000 images, a map of the flammability factor (F) is obtained (Fig. 4.16). F represents the probability of encountering a flammable mixture in a certain chamber location [40] and it is obtained from equation 4.5, where ξ_{lean} and ξ_{rich} are the lean and rich flammability limits and $P(\eta)$ is the probability density function of the mixture fraction. The calculation is performed in terms of the equivalence ratio yielding the exact same result. Each region presents a different nature. The IRZ at $z < 20\ mm$ has $F \approx 1$. Here, the strain rate was reported to reach very high values. For $20 < z < 40\ mm$, F decreases from 1 to 0, presenting harsh conditions in terms of fuel availability. At the spray-jet region near the nozzle, the spray and the co-flow cores are identified with values of $F \approx 0$. Farther downstream, evaporation and mixing start taking place and progressively increase F. However, the ORZ presents constant $F \approx 1$ in its entire domain, suitably supporting flame generation and propagation. The boundary between the ORZ and the spray-jet zone is defined with very steep F gradients. The use of F is only justified outside the region of high droplet concentration, determined by Fig. 4.8 and marked by a dashed pattern in Fig. 4.16.

$$F = \int_{\xi_{lean}}^{\xi_{rich}} P(\eta) d\eta \tag{4.5}$$

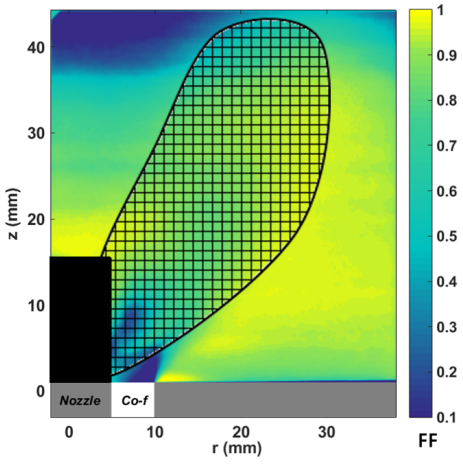

Figure 4.16: Flammability factor of the mixture inside the chamber. The shaded region is biased by high droplet concentration. The crossed section represents droplet regions extracted from PDA Fig. 4.8.

Chapter 5

Ignition Phase 2

Contents

This chapter contains a detailed analysis of the ignition transition in the context of ignition Phase 2. In a first step, the ignition probability map resulting from the stochastic study (Chapter 3) is presented and discussed using the results shown on the previous chapter as a support for the analysis. Secondly, the high-speed visualisation images are analysed under different scenarios and shed light on the kernel extinction and survival mechanisms, which are then classified into different characteristic modes, times and locations.

A coupled numerical-experimental (CERFACS-CORIA) analysis is then addressed, extracted from a 2017 INCA joint conference paper and a joint study

recently submitted to the 37^{th} International Symposium on Combustion.

5.1 Ignition Probability Map and Correlation to Local Flow Variables

The ignition probability map was calculated from the ignition study presented in Chapter 3, where 30 laser-induced ignition trials per point were performed in a 120-point 2-D mesh. Ignition probability here is defined as the probability of obtaining a long-term stabilised flame on the injector (P_{ign}), implying safe arrival to Phase 3, as it was specified in Chapter 1. In this work, Phase 1 was successful in the entire investigated domain and, therefore, P_{ign} denotes success of Phase 2. Some studies have reported failure of Phase 3 (blowout of the stabilised flame after a certain time) possibly due to initial fuel accumulation and posterior starvation [37]. In the present investigation this was not observed and the success of Phase 2 implied the success of Phase 3; this is, every time a flame kernel managed to develop and grow into a stable flame, this stabilised flame never extinguished.

The ignition probability results are presented on the left side of Fig. 5.1 (colour map), with the mean velocity streamlines of the airflow overlapped. The right-hand-side of Fig. 5.1 indicates a schematic of the different flow regions described in Chapter 4 for comparison. P_{ign} is 0 in the centre of the burner, in the entire domain of the IRZ and in part of the jet zone. Between $r \approx 20$ and $r \approx 30$ mm there is a steep growth of P_{ign} to reach a more constant region on the outer part, with values over 0.7 and maximums ($P_{ign} \approx 0.9$) at $r \approx 44$ mm and $20 < z < 40$ mm, close to the windows. The shape revealed by the P_{ign} isolines matches very well with the airflow streamlines and mean velocity gradients at the interface between the ORZ and the jet zone. All high values of P_{ign} are contained in the ORZ. These observations diverge from the ones made by Marchione et al. in spray conditions [59] and from the studies of Cordier et al. in premixed conditions [60]. A comparison to the other works is developed in section 5.5. In this format, the ignition probability information presented here cannot be extrapolated to be used out of the KIAI-Spray facility. This is why the available data must be expressed in a different, more universal form. For this purpose, Fig. 5.2 compares P_{ign} to the 3-D turbulent kinetic energy (k)

of the airflow and to the flammability factor (F) of the mixture obtained in all the chamber, but only validated in the IRZ and ORZ. Points are coloured by the flow regions. Green represents the ORZ, red the spray branch and Jet-Zone (JZ) and dark blue, the IRZ, respecting the colour code from Fig. 5.1 (right). In addition, points corresponding to the frontiers between the previous zones are also identified: cyan for the ORZ-JZ interface and yellow for the IRZ-JZ border. These two plots enable attributing statistical local flow properties to each sparking point and, hence, local ignition probability:

- ORZ: green circles show the lowest values of k ($< 20 m^2 s^{-2}$) and the highest values of F (> 0.9) in the burner. F and k distributions are very homogeneous here and contained in part A of the plots. These conditions are beneficial for ignition and make the ORZ the most ignitable zone, with the majority of P_{ign} over 0.4. Points with $P_{ign} < 0.4$ resemble, a priori, strange because the sparking location exhibits favourable conditions. They must be explained with other variables, such as the trajectory of the flame kernel, which is addressed in detail in the following sections.

- IRZ: denoted by dark blue circles, this region presents a much wider range of k (10 - 220 $m^2 s^{-2}$) and F (0.1 – 0.95). Here, $P_{ign} < 0.15$ because one of the two parameters (F or k) adopts unfavourable values for kernel development (i.e.: either both are high or both are low for a given point). Still, the IRZ and ORZ do not describe a trend between P_{ign} and F or k.

- Jet-Spray-Zone (in red): as it was already presented, the spray-jet zone contains the highest fluctuations of turbulence and equivalence ratio. Here, k ranges from 5 to 500 $m^2 s^{-2}$. It must be reminded that a quantitative description of F is not allowed, so red, yellow and cyan dots in Fig. 5.2 (bottom) must be ignored despite yielding an apparently logical trend. In zone B of the plots P_{ign} decreases with increasing turbulent kinetic energy and P_{ign} increases with increasing flammability factor. In fact, zone A of the graphs denotes favourable k and/or F (where allowed), whereas in zone B, either k is too high or F (where allowed) is too low to enable the development and evolution of a kernel.

I has been made obvious that this analysis must take into account both, k and F in a simultaneous 3D analysis with P_{ign}. However there are other parameters

governing the kernel development, such as droplet sizes and concentration or the local flow properties at locations other than the sparking point into which the kernel may be transported.

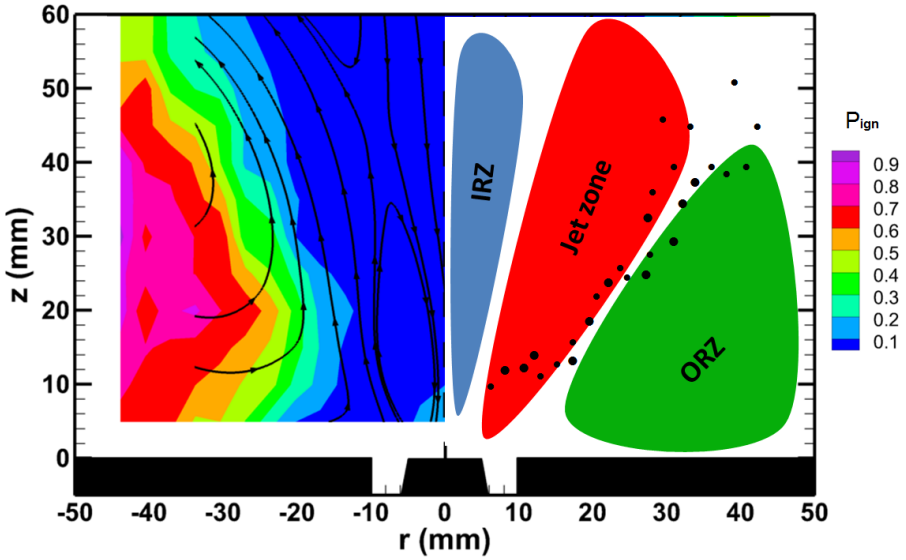

Figure 5.1: Left: Ignition probability map of the chamber with black streamlines illustrating the mean airflow motion. Right: sketch of the three main zones of the swirled-confined flow. Black dots represent the droplet presence.

The present stochastic description of the ignition phenomenon reveals the importance of local flow properties and spark location in the chamber. Still, it is not enough to completely explain and identify the reasons and underlying mechanisms taking place. The analysis has to be completed with a description of the possible flame kernel shapes, trajectories and evolutions in order to highlight the importance of local interactions under an instantaneous scope. This complementary approach is addressed in the following section, where delay times and kernel extinction causes are shown to be very varied.

5.2 Transitory Flame Kernel Observations

High-speed visualisation of the ignition process is available $t = 150\ \mu s$ after the laser-induced spark triggering and onwards. As already described in [37], Phase 1 is accomplished when a flame kernel is formed and Phase 2 involves

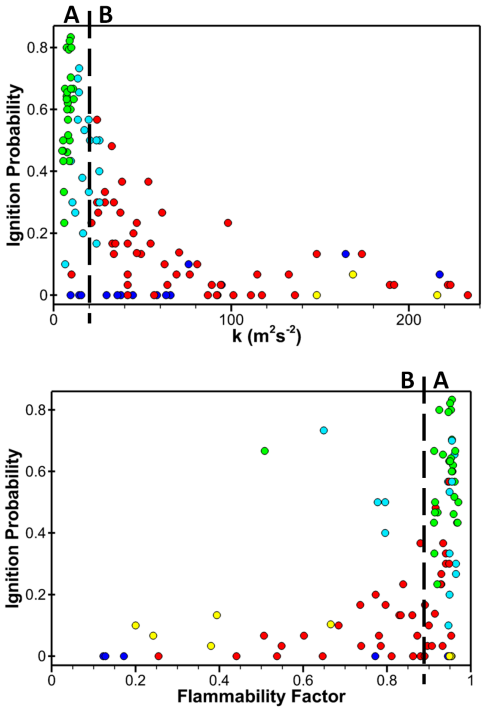

Figure 5.2: Correlations between ignition probability and: (top) turbulent kinetic energy of the airflow; (bottom) flammability factor of the mixture. Colours indicate the chamber zones: green (ORZ), cyan (ORZ-JZ interface), red (JSP), yellow (JZ-IRZ interface), blue (IRZ).

the propagation and evolution of this kernel inside the chamber until completely igniting the first injector. The current section is focused in Phase 2, which is found to evolve through many different possible pathways. Being the purpose to examine Phase 2, Phase 1 has to be guaranteed. In the present experiment, P_{ker} was ≈ 1 in the entire interrogation domain, even in locations where F was ≈ 0. This phenomenon was already observed and identified as the overdrive effect in [37], and it is caused by the non-negligible size of the spark, high spark energy and by the movement of hot gas and radicals into nearby flammable regions. Figure 5.3 illustrates this concept and demonstrates how a flame kernel is generated when sparking in one of the harshest regions of our domain ($r = 0$, $z = 40\ mm$), where $F < 0.2$. The top sequence describes the first millisecond after the spark under nominal operating conditions whereas, for the bottom sequence, the fuel flow was stopped (labelled *wo spray*). For every test in $r = 0$, $z = 40\ mm$, the amount of light and the number of illuminated pixels is higher with fuel presence than without, due to the existing chemical reactions in the first case. At $t =$

150 μs, both cases present similar rounded and smooth shapes, but the case with fuel shows a greater diameter. The area of the illuminated region immediately increases ($t = 400\ \mu s$) with spray but decreases without spray. At $t = 900\ \mu s$, the *wo spray* image shows no light other than the transient mark made by the spark on the CMOS due to excessive saturation during the spark existence ($\approx 10\ ns$), as detailed in the description of the technique in Chapter 3. The sequence under nominal conditions presents, therefore, a reacting flame kernel that expands and stretches under the action of the IRZ, reaching regions closer to the nozzle while the case without fuel represents the non-reacting hot gases generated by the spark. Figure 5.4 supports this reasoning with the comparison of both cases in terms of the temporal evolution of the mean illuminated area extracted from several tests. "Extinction" occurs clearly for $t < 1\ ms$ without spray and for $t > 1\ ms$ with spray. Indeed, at $r = 0$, $z = 40\ mm$ P_{ign} is zero. The high-speed images and the equivalence ratio data suggest that the possible cause is a combination of fuel starvation from one end and excessive stretch from the other.

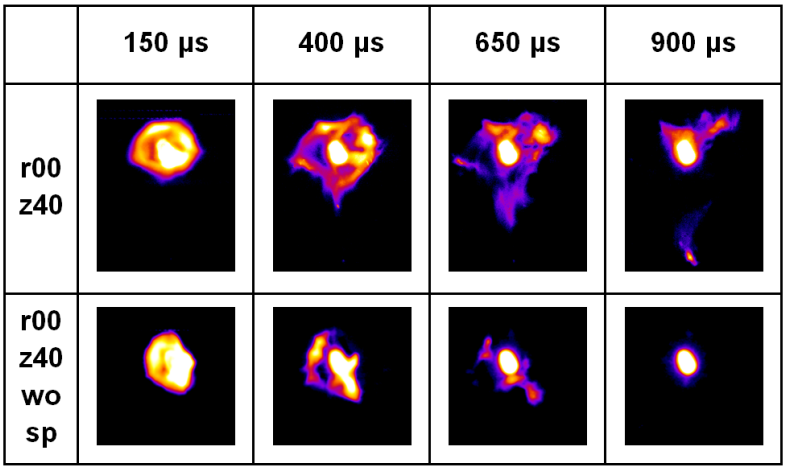

Figure 5.3: Two sequences of high-speed images after sparking at r=0, z=40 mm. The top sequence was sparked at nominal air and spray conditions ($F < 0.2$ in this point). The bottom sequence represents a sparking under nominal air conditions but without spray (fuel mass flow=0 $g.s^{-1}$).

Depending on the spark location, flame kernels have different initial properties and will undergo different trajectories. Mastorakos [37] defined the kernel extinction during Phase 2 as the *second* or *long mode* of ignition failure. The present work moves a step further and identifies several typical extinction mechanisms

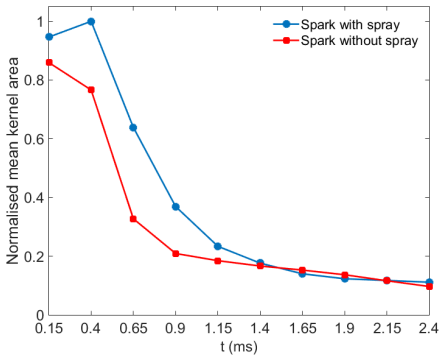

Figure 5.4: Mean evolution of the illuminated area after sparking in r=0, z=40 mm. Blue circles represent sparking at nominal air and spray conditions ($F < 0.2$ in this point) and red squares represent sparking at nominal air conditions but without spray (fuel mass flow=0 $g.s^{-1}$).

and associated times and locations amongst the long-term category. Different ignition delay times and mechanisms are identified and explained in the following sections.

5.2.1 Kernel topology

It is interesting to see how the initial properties of a flame kernel change in function of where it is started. For this purpose, 13 individual kernels at their earliest recorded stage ($t = 150\ \mu s$) are placed in the sketched chamber at their corresponding locations in Fig. 5.5. The figure is complemented by the mean flow streamlines (from PIV) on the left and by a sketch of the characteristic flow regions on the right. The kernels images here are approximately to half-scale in comparison to the chamber sketch; otherwise they would overlap to each other. At $r \approx 40\ mm$, all kernels reveal smooth curves in the reacting fronts without much wrinkling and remain quite compact inside the core of the ORZ ($z < 40\ mm$). For $z > 40\ mm$, their structures appear slightly more open. No droplets are observed to interact with any of them. All kernels at $z = 60\ mm$ present a hollow-kind shape and smooth reacting fronts. At $r = 0$, $z = 40\ mm$, the kernels exhibit similar properties. All the positions described up to now remain outside the jet-zone (JZ), in regions characterised by low velocities and low turbulent kinetic energies. Oppositely, flame fronts of kernels triggered at locations in the JZ and next to it, possess a high degree of curvature, wrinkling

and strain, revealing shapes more distant of ideal circles than the latter. A direct connection with turbulence can be, thus, extracted from these observations. At $r = 0$, $z = 5$ mm the kernel adopts the shape of the base of the spray cone covering a large area. Kernels in locations with peaks of strain rate and k such as $r = 10$, $z = 10$ mm and $r = 20$, $z = 20$ mm are the most sheared and even torn into smaller pieces. Farther away from the air jet, at $r = 20$, $z = 30$ mm and $r = 30$, $z = 40$ mm, flame fronts are still very wrinkled but remain in one piece (less strained). These observations are coherent with the previous airflow analysis. Turbulent lengthscales are much smaller in the JZ and manage to interact with the flame front whereas, in the other regions, the characteristic lenghtscales of the flow just convect the kernels as a whole piece into other positions in the chamber. Another interesting feature about JZ kernels is the immediate interaction with droplets, which appear as luminous dots arriving to the flame brush from the spray side. The high light intensity emitted by the droplets indicates that they burn in an isolated droplet mode or in pockets of few droplets. From the analysis of the ϕ histograms it can be deduced that flames in the ORZ progress in a mainly premixed homogeneous environment and that flames in the JZ see a large spatial and temporal stratification of the mixture within a range exceeding the lower and upper flammability limits. This can cause extra wrinkling and strong scalar gradients within the kernel. The contribution of droplets has been studied in several investigations and their antagonist effects have been exposed [66, 74]. In this particular configuration (ultra-lean conditions), the presence of droplets can be beneficial because combustion can be accelerated or reactivated in some cases through near-stoichiometric mixture paths. This will be tackled numerically in section 5.6. An increase in laminar burning speed and in the temperature of the flame and burnt gases can be, hence, achieved. To enter into a more detailed analysis, the roles of small and large droplets must be now differentiated. Clouds of small droplets will evaporate nearly instantly when approaching the flame front, supplying fuel vapour to the incoming fresh gas mixture and increasing the equivalence ratio without causing too much thermal losses. The droplets that can be pointed in Fig. 5.5 are large droplets that evaporate faster when approaching the flame front but not quick enough to disappear. Hence, they locally impinge on the reaction zone and penetrate into the burnt gases towards the central part of the kernel. This has been already assessed in DNS studies [74] and by OH-PLIF experiments [141], where local extinctions and reaction zone thickness

perturbations were observed. After crossing the flame front, large droplets in Fig. 5.5 enter an oxygen-rich, high temperature zone and evaporate and burn using the heat from burnt gases and from their self-combustion, re-injecting heat into the system.

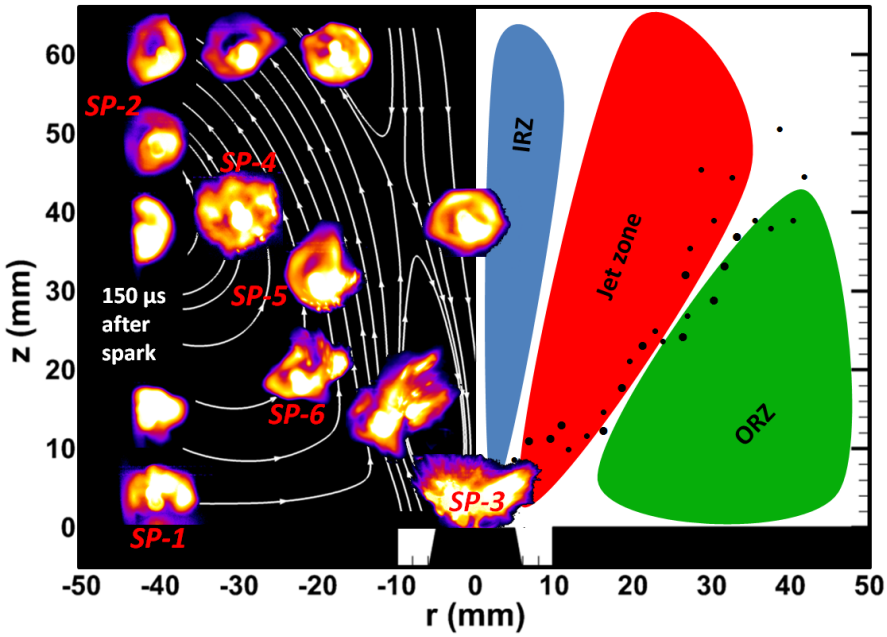

Figure 5.5: Left: typical kernel shapes at $t = 150\ \mu s$ characteristic of the different sparking regions where they appear on the graph. White streamlines describe the mean flow motion (from PIV) and red labels (SP-1 to SP-6) indicate sparking positions that will be further analysed in the following figure. Right: sketch of the three main zones of the swirled-confined flow. Black dots represent the droplet presence.

5.2.2 Kernel evolution observations

It has been demonstrated that the initial kernel location (spark location) is decisive in conditioning the shape and curvature of the flame fronts due to mixture fraction distribution (either premixed or either stratified), to droplet presence and to possible small-scale fast action of the flow aerodynamics over chemistry. The description of the earliest characteristics of the kernel and its surroundings is very useful and necessary to tackle the ignition problem. Nevertheless, at such early stages, the success or failure of an individual sparking event is still not determined in most of the cases. In fact, the kernel-flow interactions at later times

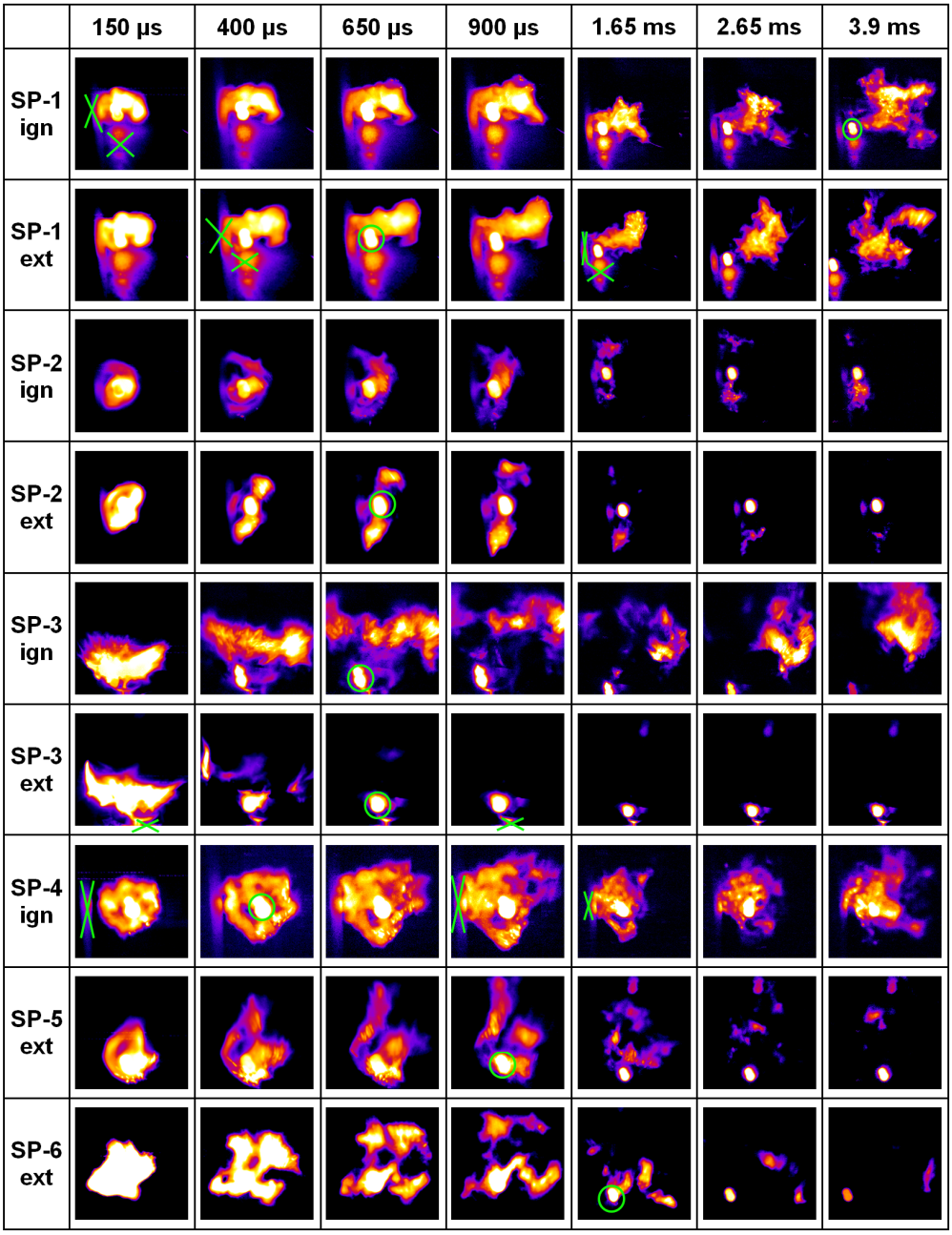

Figure 5.6: High-speed sequences of kernel evolution for successful and missed ignition trials at different sparking points (SP from Fig. 5.5).

are also responsible for the survival or the extinction of the chemical reactions. After its generation, the flame kernel starts moving and transits different locations in the chamber, encountering a detrimental situation at some stage (e.g.: shearing pocket). The key for Phase 2 to succeed lies on keeping the kernel safe

from disruptive conditions or on the survival of the kernel to such disturbances. If this is not met, the chemical reactions will eventually stop, causing a *second mode* of ignition failure [37].

This section is dedicated to the possible extinctions or successful evolutions that a kernel can face. Two kernels departing from the same point at two different times will probably experience similar flow properties, but never exactly the same. The repeatability of the local surrounding flow properties depends on the initial location of the kernel in the chamber: some regions present more fluctuation than others. Figure 5.6 shows the evolution of kernels in 9 independent sequences (4 successful and 5 failed trials) taking place in 6 different points (marked SP-1 to SP-6 in Fig. 5.5). The first 4 images of each sequence describe the first millisecond and the remaining 3 (in a smaller magnification) describe longer times. Green crosses indicate reflections on metallic parts of the chamber and green circles show some spark marks left on the CMOS due to saturation. At this point it is important to make clear that the kernel evolution sequences presented here are a selection out of all the recorded high-speed videos. The analysis of this figure and the analyses performed in sections 5.3 and 5.4 are based on and supported by a detailed examination of each recorded ignition and extinction sequence. Now, concerning Fig. 5.6, SP-1, SP-2 and SP-3 show one successful and one missed sequence each. SP-4, SP-5 and SP-6 only show one successful and two missed sequences, respectively. The big differences in kernel shapes and propagation paths are evident from one point to another. Nevertheless, within the same sparking point, differences between successful and failed kernels are sometimes immediately appreciable and sometimes not. From this perspective, the *second mode* of ignition failure can be itemised into different extinction mechanisms and characteristic times.

- A close look at the first two sequences ($SP-1-ign$ and $SP-1-ext$) reveals substantially no differences between kernels during the first millisecond: both propagate along the chamber base in a quiescent area (ORZ) where they can grow robust, and approaching the JZ frontier where velocity gradients are very intense. It is, indeed, the strong strain rate that tears apart the propagating kernel and causes its extinction at $t > 3,9\ ms$.

- For the next point ($SP-2-ign$ and $SP-2-ext$) differences are remarkable at $t = 400\mu s$, where the failing kernel is divided into two smaller pieces

that move apart while the successful kernel remains more compact. Total extinction is reported at $t \approx 4\ ms$.

- Another kind of behaviour is observed at SP-3 where ignition probability is $\approx 10\%$. Here, the second-extinction mode occurs promptly and there is merely nothing left at $t = 650\ \mu s$. Although at $t = 150\ \mu s$ the illuminated area is greater for the extinguishing case, the kernel vanishes at $t = 400 \mu s$ due to the harsh local conditions (maximum strain rate and air velocities). The ignition event $SP-3-ign$ is, therefore, a rare event in this location; it may be possible due to a beneficial fluctuation of the turbulent kinetic energy or of the surrounding mixture fraction distribution. Nevertheless, the kernel shows clear signs of unfavourable interactions with the airflow.

The three extinction mechanisms here presented are representative of the extinction processes taking place in these three locations and similar ones. In the following, SP-4, SP-5 and SP-6 illustrate the 3 main characteristic behaviours of kernels belonging in the JZ. Due to the high level of turbulence and intermittency in the JZ, these mechanisms can be de-localised for the analysis and attributed to points in the JZ in general, depending on the flow conditions.

- For instance, point SP-5 can experience any of the three mechanisms (or a combination of them) when sparked at different times. This explains why kernel shapes and evolutions present more variability in the jet-zone. The JZ presents a low flammability factor in comparison to the ORZ. However, this parameter remains a tool describing the mean behaviour of the flow. To deal with the real process, especially in the JZ, one must look to the instantaneous ϕ images and the corresponding histograms. As described in 4.4, pockets of droplets alternate with air vortices inducing a large fluctuation of ϕ. The turbulent convection of eddies also adds intermittent strain pockets to the system (see Chapter 4). SP-4, SP-5 and SP-6 in Fig. 5.6 compare a successful ignition event to two extinction mechanisms of the *second mode* of ignition failure.

- At SP-4 it is very probable to find a wrinkled kernel in one piece with droplets arriving from the spray nozzle. The kernel practically stays in the same position revealing that its propagation velocity equals the airflow velocity. Regions of the reaction brush containing droplets seem to propagate

towards the nozzle at a higher burning speed. If the flow velocity increases due to fluctuations and the reaction rate is not capable of overcoming this, the kernel is convected upwards and out of the flammable region, as seen in SP-5. The kernel is also broken into smaller pieces in this example and extinction is reported at $t > 4\ ms$.

- At SP-6, turbulent velocity fluctuations and gradients are always too high to sustain a flame. Indeed, images show a prompt division of the kernel into 4 pieces (made clear at $t = 400\mu s$) that leads to early extinction due to reduced flame speed and increased scalar dissipation [66]. This example still shows some remaining reactions taking place at $t = 3.9\ ms$, near complete extinction.

5.3 Kernel Extinction Mechanisms: Locations and Times

The analysis of the previous high-speed flame kernel visualisations reveals several different extinction mechanisms which are, indeed, driven by different causes and yield very different kernel behaviours. In an effort to identify and classify the observed differences in the extinction processes, Fig. 5.7 presents five extinction modes, named E1 to E5. Figure 5.8 shows the typical kernel extinction times on its left and, on its right, the regions in the chamber where each extinction mechanism takes place. Crosses and markers in the figure indicate the points where times and mechanisms where investigated through the high-speed images. The different extinction modes are now described through the analysis of both figures simultaneously:

- The **Delayed-Shearing Extinction Mode**, labelled E1, acts on flame kernels initiated at locations in the ORZ. The main flow movement brings the smooth and small kernel into the jet-zone and the flame is torn by a combination of high velocity, high turbulence and high gradients before it has had enough time to grow robust. Figure 5.8 (right) indicates that this mechanism takes place mainly when sparking at the bottom part of the ORZ. In this case, when a kernel is created it faces an initial beneficial phase inside the bottom part of the ORZ during which its volume increases under

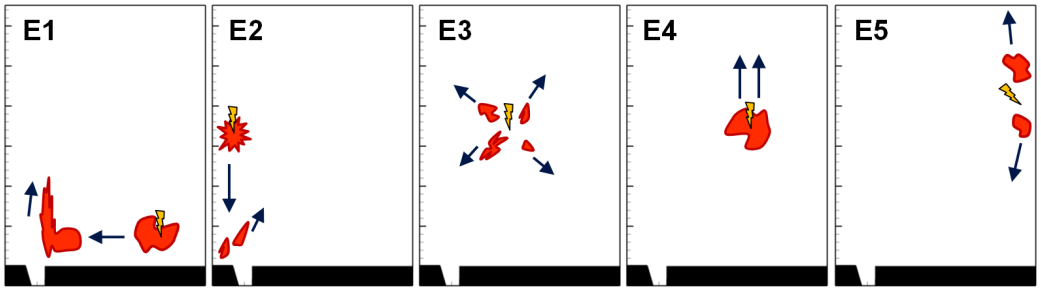

Figure 5.7: Classification of the different observed flame kernel extinction mechanisms. Arrows indicate the typical trajectories followed by the kernels or by the kernel pieces.

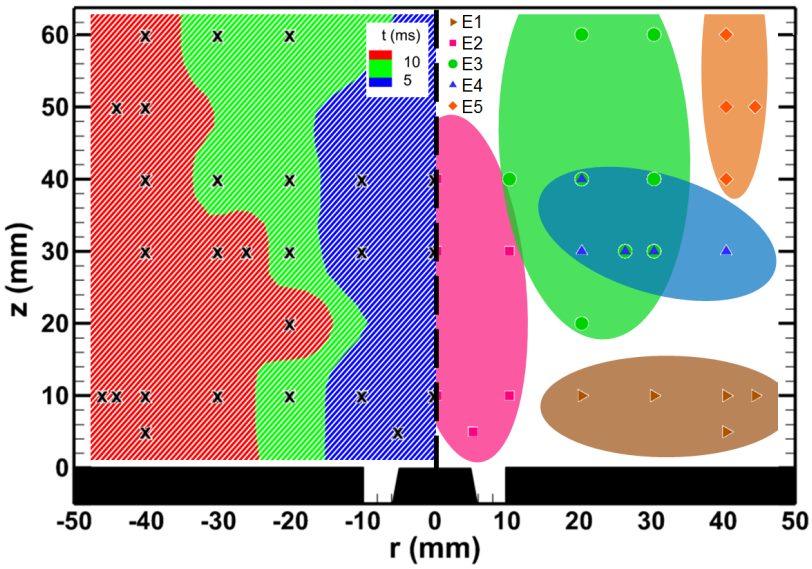

Figure 5.8: Left: Mean kernel extinction delay times extracted from high-speed visualisation images. Blue colour illustrates times under 5 ms, green between 5 and 10 ms and red over 10 ms. Right: Regions of the chamber attributed to the different extinction mechanisms.

a quiescent environment. It is, therefore, during a second stage that the kernel is disturbed by the issuing air jet and, eventually extinguished. If the initial step enables the kernel to develop large enough and the second step does not impose too much strain, then the ignition event will be successful. Kernel extinction delay times are high here (> 10 ms) due to the first beneficial instants of its propagation. The initial kernel position in the chamber and its evolution during E1 correspond to SP-1 in Figs. 5.5 and

5.6.

- The **Prompt-Continuous-Shearing Extinction Mode**, labelled E2, takes place at the central part of the burner (Fig. 5.8 (right)). Kernels triggered at high axial stations here find a very lean mixture, mainly below flammability limits and they are then stretched by the IRZ recirculation. Moreover, after this sudden action, kernels or kernel parts arrive into the core of high turbulence and shearing flow and undergo complete extinction very rapidly ($t < 5\ ms$), as shown on the left part of Fig. 5.8. When sparking occurs at low axial stations in the IRZ, the flammability factor is high and the equivalence ratio presents appropriate values for ignition, but the kernel immediately faces the highest strain rates detected in the entire burner. Sequences in Figs. 5.3 ($SP-0-w-spr$) and 5.6 ($SP-3-ext$) represent behaviours typical of this mode.

- The **Multi-Shearing Extinction Mode**, labelled E3, occurs in the jet-spray zone at mid radial positions $r \in (10, 30)\ mm$ and for $z > 20\ mm$, as shown in Fig. 5.8 (right). Here, turbulence and strain rate are still intense, either by a constant supply of energy from the large flow scales at low z, either by a fluctuating small-scale shearing generated by detached eddies at high z (strain rate pockets in 4.2). Despite immediately interacting with fuel droplets, the kernel is quickly broken into several wrinkled and small pieces, the majority of which extinguish some milliseconds after the division. Sometimes one kernel piece survives a longer time, yielding more variability to the extinction times. Characteristic times for this extinction mode are between $t = 5\ ms$ and $t = 10\ ms$. This depends again on the highly aleatory nature of the flow in this region. The higher the strain, the shorter the extinction time. The influence of alternating rich and lean mixture pockets has to be also highlighted here. Sequence SP-6 in Fig. 5.6 backs the current description.

- The **Starving-Blowout Mode**, labelled E4, occurs when the characteristic turbulent lengthscales and timescales are larger than in the **Pulsed-Shearing Mode** and the kernel stays in one piece but the main flow velocity convects it downstream, out of the flammable region. Blue triangles in Fig. 5.8 (right) show the positions where this phenomenon was observed.

A possible explanation to why this does not occur at higher axial stations is the relaxation of the airflow velocity with height. Indeed, this extinction mode needs a high air velocity capable of rejecting the kernel downstream against its burning velocity. The blue triangle in $r = 40$, $z = 30\ mm$ implies that there is a positive flow velocity in what would be the mean ORZ. The reader is reminded that the fluctuation of the air jet can enclose the ORZ within a very small area sometimes (previous chapter). Characteristic extinction times for the **Starving-Blowout Mode** are $t > 5\ ms$. A typical sequence controlled by this mechanism can be observed at SP-5 in Fig. 5.6.

- To finish with, the **Clean-Division Mode**, labelled E5, occurs always near the wall of the burner (orange diamonds in Fig. 5.8) on the top part of the mean ORZ. In fact, since the ORZ can be larger or smaller depending on the air-jet fluctuations, these points are sometimes placed out of the ORZ or in the frontier with the jet-zone. When this occurs, the flame kernel undergoes separation due to the action of the flow. The top sub-kernel normally extinguishes early and the bottom sub-kernel extinguishes some milliseconds after. Mean extinction times of $t > 10\ ms$ were reported for this mechanism. The reason why this mechanism needs more time to stop chemical reactions is that, generally, the descending sub-kernel encounters in the ORZ a beneficial atmosphere but its size and volume are already under a critical value. This extinction mode is very repeatable and can be found in SP-2-ext in Fig. 5.6.

Looking at Fig. 5.1 and Fig. 5.8 it seems that there is a relationship between ignition probability in the chamber and mean kernel extinction time. In a certain way we can state that the higher the ignition probability is, the more difficult it is to extinguish a flame kernel and, hence, the more time this process will take. From another point of view, it can be said that a combustion chamber that provides large areas of beneficial flow characteristics will increase the life of potentially extinguishing kernels, hence giving them more chances to survive and increasing the probability of obtaining a successful ignition.

5.4 Ignition Mechanisms: Locations and Times

After describing the possible pathways causing the so-called *second* or *long mode* of ignition failure (i.e.: failure of ignition Phase 2), the mechanisms responsible for successful ignition and safe flame stabilisation must be now assessed. Figure 5.9 illustrates five ignition modes identified from thorough analysis of all the high-speed images (like the ones in Fig. 5.6). Blue arrows indicate the initial kernel movement until a considerable volume is ignited. Green dashed arrows describe how developed kernel attaches to the injector to finish the complete ignition of the single-injector. Figure 5.10 (left) describes the mean ignition delay times captured by the pressure peaks measured in the chamber. The right part of the figure shows the regions of the burner prone to exhibit each of the different ignition mechanisms. As before, a joint analysis of both figures will be now addressed:

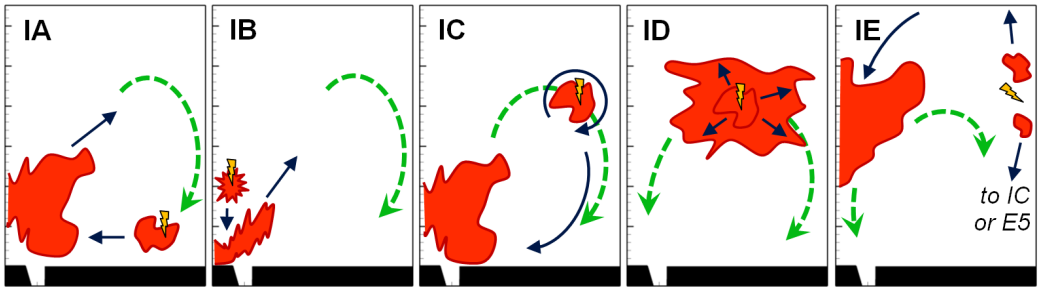

Figure 5.9: Classification of the different observed ignition mechanisms. Blue plain arrows indicate the typical trajectories followed by the kernels or by the kernel pieces. Green dashed arrows show the trajectories of the developed kernel in a second stage before complete flame stabilisation.

- The **Delayed-Shearing Ignition Mode**, labelled IA, occurs at the same location as the **Delayed-Shearing Extinction Mode** and follows the same processes. This is backed by visualisations $SP-1-ign$ and $SP-1-ext$ in Fig. 5.6. Differences between both mechanisms are not appreciated until late times ($t \approx 4\ ms$) after the sparking. Regarding the ignition probability map (Fig. 5.1), IA is preferential for $r > 30\ mm$ and E1 is preferential for $r < 30\ mm$. This means that the more time the kernel resides in the ORZ, the more chances it will have to succeed due to its major increase in size. This process is fed by the characteristic randomness

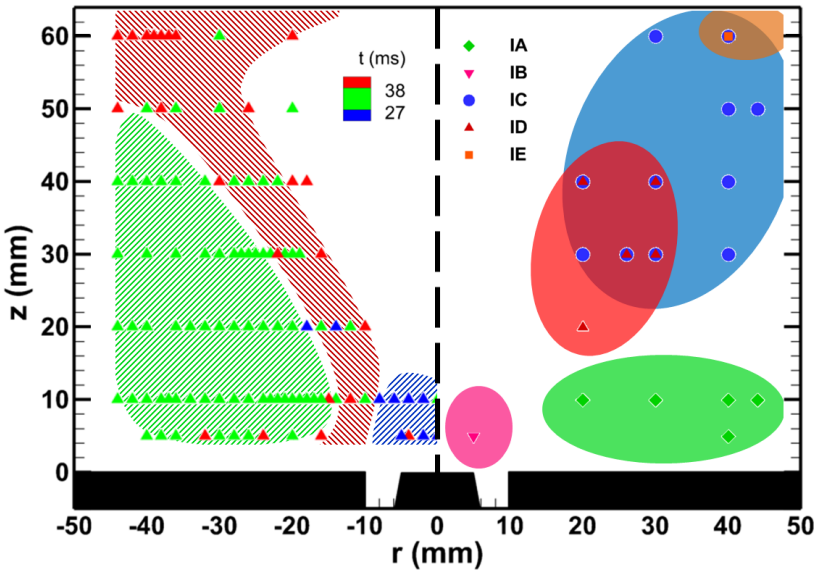

Figure 5.10: Left: Mean ignition delay times extracted from pressure peak values. Blue colour illustrates times under 27 ms, green between 27 and 38 ms and red over 38 ms. Right: Regions of the chamber attributed to the different ignition mechanisms.

of the flow in the jet zone (ϕ and strain rate fluctuations), that can enhance the kernel propagation with fuel-rich mixtures or vice-versa. During the **Delayed-Shearing Ignition Mode**, the developed kernel will always face a strong shearing force to which it must survive. It is then aided by the movement of the ORZ (green dashed arrows), which will trap the large but torn kernel again assuring the flame growth and enabling its complete attachment to the injector. Mean ignition delay times are $t \in (27, 38)$ ms for this mechanism.

- The **Prompt Cone-Ignition Mode**, labelled IB, is very difficult to achieve due to the low ignition probability ($< 10\%$) in the centre of the chamber and to the high turbulent kinetic energy. It can only occur when sparking next to the spray cone (Fig. 5.10) and presents the shortest ignition delay times ($t < 27$ ms). An adequate mixture and strain rate fluctuation must happen in order to enable a flame kernel to develop in this region. It is, nevertheless, immediately torn and blown downstream but posteriorly captured by the ORZ, as in IA. Sequence $SP-3-ign$ in Fig. 5.6 illustrates this description.

- The **Long-ORZ-Growth Ignition Mode**, labelled IC, is very common since it takes place in the majority of the burner (blue circles in Fig. 5.10 (right)). It presents characteristic ignition delay times above $t = 27\ ms$. As already explained, when sparking in these regions, the flame kernel can suffer some deformation and it can be even torn into some pieces. Therefore, the **Long-ORZ-Growth Ignition Mode** overlaps with the **Multi-Shearing Extinction Mode**. However, this does not always occur and it is frequent to see a smooth or a slightly deformed kernel rotating and being captured by the flow motion in the ORZ. This mechanism is preferential close to the wall. The kernel evolves quiescently traversing the entire ORZ and encountering the spray from the bottom. The flame is then lifted by the air jet and captured a second time by the ORZ to complete the injector ignition (green dashed arrows). $SP-2-ign$ in Fig. 5.6 shows how a kernel rotates and brakes in two pieces. The bottom part then follows the **Long-ORZ-Growth Ignition Mode**.

- The **Spray-Branch Ignition Mode**, labelled ID, takes place when sparking closer to the spray branch but shares many points with the **Long-ORZ-Growth Ignition Mode**. In this case, the kernel is not trapped by the ORZ and experiences a favourable environment for instantaneous growth due to droplet presence. The flame front propagates towards the injector through the spray branch. The IRZ and ORZ also bring the flame fronts that enter these regions towards the spray nozzle in order to start the flame stabilisation. Ignition delay times here are more fluctuating since the high flow fluctuation imposes randomly favourable and unfavourable conditions for flame propagation. Still, the majority of the points in Fig. 5.10 (right) indicate $t \in (27, 38)\ ms$. The **Spray-Branch Ignition Mode** can be observed in $SP-4$ in Fig. 5.6.

- The **Downstream-to-IRZ Ignition Mode**, labelled IE, is difficult to obtain in this specific burner configuration due to the small size of the IRZ and the large size of the ORZ. This mechanism departs as an ascending kernel or as a division of the kernel (as in E5). The bottom sub-kernel can either extinguish or give an ignition (as IC). If the top sub-kernel (or ascending kernel) survives long enough, it can be trapped by the IRZ from the top and re-descend under the form of a swirling conical flame into the

spray cone. When the flame reaches the spray branches from the interior, it experiences a sideways propagation and it can also be captured by the ORZ. This mechanism was only observed at $r = 40, z = 60\ mm$ and yielded the longest ignition delay times ($t \approx 50\ ms$).

A global view of the left part of Fig. 5.10 shows again a good match with the ignition probability map. The green-shaded region reflects the ORZ, where ignition delay times are always between $t = 37$ and $t = 38\ ms$ and ignition probability is highest. The red-shaded region represents the steep ignition probability gradient. Here occur all the "slow" ignitions ($t > 38\ ms$). To finish with, the blue-shaded zone represents "fast" ignitions due to the proximity to the spray nozzle. This last observation does not correlate with the ignition probability results.

5.5 Comparison to other investigations

The correlations between ignition probability and the flow properties, and the extinction and ignition mechanisms described in this chapter have been observed in the KIAI-Spray facility under the nominal operating conditions (Chapter 2). However, to prove that these observations and mechanisms can be extrapolated and used universally, results from other investigations are now briefly commented. Provided that each experiment is different (e.g.: configuration, operating conditions, etc.) flame kernel extinction mechanisms and ignition mechanisms may occur at different locations, depending, as it has been explained, of several parameters such as the aerodynamics of the flow in each chamber:

- Letty et al. [43] conducted experiments on spark ignition of swirling and non-swirling confined flows using ethanol and n-heptane as different fuels. They employed the same facility as Marchione et al. [59] and sparked at two different locations with a 140 mJ spark. Referring to ignition probability, they concluded that: (i) the higher the flow velocity, the lower P_{ign}; (ii) $P_{ign} = P_{ker}$ for low flow velocity and (iii) $P_{ign} < P_{ker}$ for high velocities. In the present work, Chapter 4 reflects that flow velocity and turbulent kinetic energy (k) are intimately related, hence Fig. 5.2 (top) shows that our P_{ign} follows the same trend as described by Letty et al. They also mentioned that "some records of n-heptane show the initial kernels splitting

into separate smaller kernels" giving evidence of mechanism E3, the **Multi-Shearing Extinction Mode**. The latter was also observed for kerosene in high altitude relight conditions in a real combustion chamber from Rolls-Royce by Read et al. [7, 84], where extinction times were smaller than 10 ms and ignition times larger than 20 ms. Extinction and ignition times in their study (Fig. 5.11) match very closely the ones observed in the present study (Figs. 5.8 and 5.10). Continuing with Letty et al. [43], when sparking in the IRZ (but very close to the bluff-body ($z = 10\ mm$)), they found the kernel to move rapidly towards the bluff-body with a fast growth rate. Indeed, the ignition mechanism IB, proposed here as the **Prompt Cone-Ignition Mode** causes the shortest ignition delay times (sparking at $r = 0,\ z = 10\ mm$ in the KIAI-Spray) and can be approximated to their observation. On the other hand, when Letty et al. sparked in another location, $r = 10,\ z = 10\ mm$, they stated that the kernel size did not grow until reaching the bluff-body: ignition mechanisms IA and IC proposed in this work yield kernels that do not grow initially during their transit in the ORZ but then grow rapidly when approaching the spray cone. In addition, they mentioned that "some rotating motions can happen too" referring to the flame kernels: in mechanism IC, the majority of the observed kernels revealed auto-rotation. More generally, they commented that "the kernel sometimes extinguishes before reaching the bluff-body", which is also the case in the present study, and that "initiation can only be achieved once the flame is attached to the bluff-body", which is reflected in Fig. 5.9 and more detailed in Chapter 6.

- Another investigation performed by Marchione et al. [59] focused on the spark ignition of turbulent swirling n-heptane spray flames using a hollow-cone pressure atomiser. The mean overall (liquid plus vapour) fuel concentration was measured here using a fast flame ionisation detector, revealing a maximum local equivalence ratio in the IRZ and minimum in the ORZ with the mean stoichiometric line laying inside the IRZ. This is a vague approximation to reality since the liquid and vapour phases could not be identified. With respect to the velocities, they appear high at the jet entrance and in the ORZ (which was much smaller than in the KIAI-Spray compared to the rest of the flow). The IRZ yielded lower velocity values

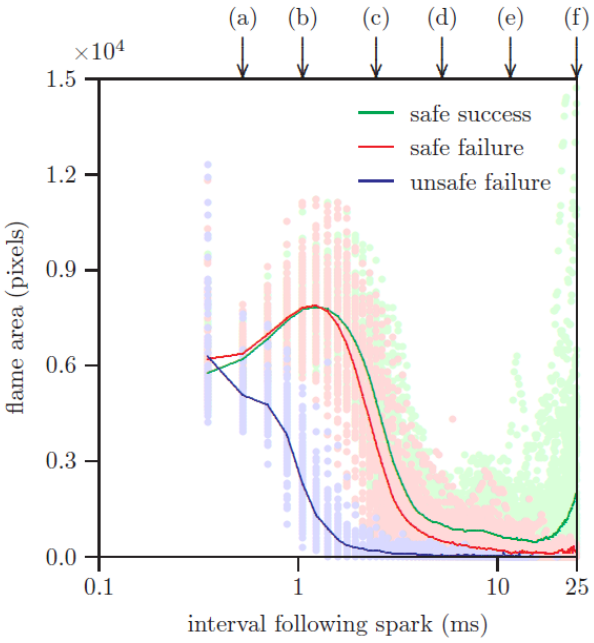

Figure 5.11: Variation of the flame area with time after the spark. Figure from [7].

and turbulence than the jets and the ORZ. Therefore, the ignition probability map obtained by Marchione et al. diverges from ours: the ORZ is not ignitable while the IRZ shows high P_{ign} in nearly all its domain. Paradoxically, this agrees with our observations when comparing to the flow characteristics: P_{ign} is highest in regions of low velocity and low turbulence when the mixture is flammable. They mentioned that downstream of $z = 35\ mm$ "there is no ignition; kernels do appear, but they cannot propagate back and establish the whole flame". This corresponds to extinction mode E4, the **Starving-Blowout Mode**. Figure 10b of Marchione et al. illustrates an ignition sequence where a flame kernel is initiated by an electrical spark at $r = 30\ mm$ (5 mm away from the chamber wall) and $z = 15\ mm$. Initially the flame kernel moves downstream and then it moves and propagates back upstream along the left-side wall, in the region corresponding to the ORZ. This gives evidence of mechanism IC of the present study: the **Long-ORZ-Growth Ignition Mode**.

- Another variety of extinction mode E4, the **Starving-Blowout Mode** is found in Fig. 3 of Ahmed et al. [62]. They performed ignition experiments

in a different flow field configuration in non-premixed conditions. In this case, the flame kernel grew but was not able to propagate against the flow to reach stabilisation, so the observed mechanism would only be described as **Blowout Mode**. However, similarities with E4 are evident.

- In another paper, the same author, Ahmed [36] performed electrical spark ignition experiments in lean gaseous flows of premixed and non-premixed nature using counter-flow and bluff-body configurations. With a spark energy (200 mJ) much higher than the minimum ignition energy, he varied the equivalence ratios and the flow velocities to find that increasing the shear rate decreases the size of the ignitable region and reduces ignition probability. He also found that a spark in a non-flammable region can generate a flame kernel in a neighbouring flammable zone. The analysis concluded that in locations with low strain rate or turbulence, high ignition probability is associated with stoichiometric mixture fractions, whereas high turbulence or strain rates are detrimental regardless of the mixture strength. Figure 14 of [36] provides two ignition scenarios that recall ignition mechanisms IB and ID, respectively the **Prompt Cone-Ignition Mode** and the **Spray-Branch Ignition Mode**. It is reminded that, in the KIAI-Spray, IB only happens when sparking very close to the spray cone, which is not the case in Ahmed's burner.

- Eyssartier et al. [45] proposed a LES modelling strategy for ignition sequences in two-phase flows that enabled the prediction of failed and successful ignitions with different timings. They highlighted the difficulties of the numerical approach to ignition under two-phase flows and, despite their innovative results, still the experimental observations were not completely matched. This work accounted for many critical aspects of ignition, such as spray droplet size, turbulence level, flow velocity and the different steps followed by the process guided by characteristic mechanisms. Indeed, the proposed model used 5 criteria including the flammability of the mixture, the evolution of gas and liquid temperatures during the deposit of energy (e.g.: by a spark), the comparison of vaporisation, combustion and diffusion timescales, the kernel quenching and the upstream turbulent flame propagation. Ignition probability in the MERCATO facility from the experimental and numerical points of view was higher in the recirculation

zones (lower velocities) and very low close to the fuel injection and in the high speed regions. Their flammability factor yielded ≈ 1 in the ORZ and was minimum in the IRZ. These conclusions are similar to our P_{ign} and F maps (Chapter 4). A diverging point is the ignitability of their IRZ, but it was ignitable only in some regions.

- Cordier et al. [60] conducted laser-induced spark ignition experiments in the KIAI chamber in pre-mixed conditions using methane as the fuel for two swirl configurations. The lower swirl ($S_n = 0.76$, like in the present work) yielded a large ORZ and a narrow IRZ whereas the higher swirl ($S_n = 1.09$) gave a larger IRZ and much smaller ORZs. As in the present work, their ORZ showed low mean velocities and turbulent kinetic energies (k) and the IRZ revealed higher values. For both swirling configurations, their P_{ign} map presented high probability in all the burner except in the IRZ and the inner parts of the Swirled-Jet Zone, where P_{ign} decreased towards the centreline and towards the injection plane. A beneficial effect of increasing the swirl number was reported for the IRZ, while the opposite occurred for the ORZ. Figure 10 of [60] shows that there is no correlation between ignition probability and k in their experiments, where maximum values reached $k \approx 115\ m^2 s^{-2}$. In the present work, Fig. 5.2 (top) shows a clear correlation for $k > 20\ m^2 s^{-2}$, where the detrimental effect of turbulence is gathered. These differences can be explained by the different nature of the configurations: premixed ($\phi = 0.74$) vs spray ($\phi = 0.61$), being the second one much more fragile or weak in ignition terms. Regarding high-speed visualisations and comments from [60], they also observed kernels broken into several pieces in the IRZ and the Swirled-Jet Zone. In Fig. 15 and Fig. 16 they showed ignition sequences initiated by sparks in the ORZ that reveal very similar sequences to SP-1 ign in Fig. 5.6 described above. Moreover, they did not find broken kernels in the ORZ. Differences in pressure peak delay times are outstanding: in their study, ignition was achieved earlier in almost every chamber zone than in the present KIAI-Spray investigation, which can be explained by their more favourable conditions for ignition.

5.6 Comparison to LES ignition results

A complementary study to the analysis and discussion presented just above is now addressed. This section provides a coupled analysis of some observed *second mode* extinctions and of ignition events, made possible thanks to a close and ongoing collaboration between CERFACS and CORIA. The objective of this section is to provide a complementary analysis and discussion to the mechanisms dictating success or failure of Phase 2. The validated numerical approach has access to many parameters that are still impossible to detect with experiments. A deeper analysis is, therefore, made possible here. The capability of LES to forecast some of the different mechanisms presented above is also demonstrated here.

5.6.1 Kernel Extinction Events

Two points were selected for the investigation of ignition failure. They were named P2 and P3. Point P1 has been studied from the point of view of ignition success and it will be discussed in the next section. Concerning P2 and P3:

- Position P2: x=0 mm & z=5 mm, located in the IRZ close to the injector tip where the ignition probability is very low (10%) ;
- Position P3: x=10 mm & z=30 mm, located in the turbulent jet where the ignition probability is very low (10%)

From Chapter 4, P2 and P3 are both located in regions of high turbulent intensity but P3 is located in a lean mixture region whereas P2 is located in a rich mixture region. For each point, 3 sequences were simulated numerically, denoted P#_SEQ1 to P#_SEQ3, and 9 high-speed visualization sequences are available. The evolution of maximal temperature in the domain versus time for the 6 numerical ignition attempts is plotted in Fig. 5.12 (left) whereas the temporal evolution of experimental kernel intensity is displayed in Fig.5.12 (right) for the longest and shortest extinction times at points P2 and P3. The overall agreement between experiments and LES is good, showing a quick kernel extinction. Point P3 shows repeatable extinction delays close to $t = 2\ ms$ both numerically and experimentally. Experimentally, point P2 reveals more variability and extinction

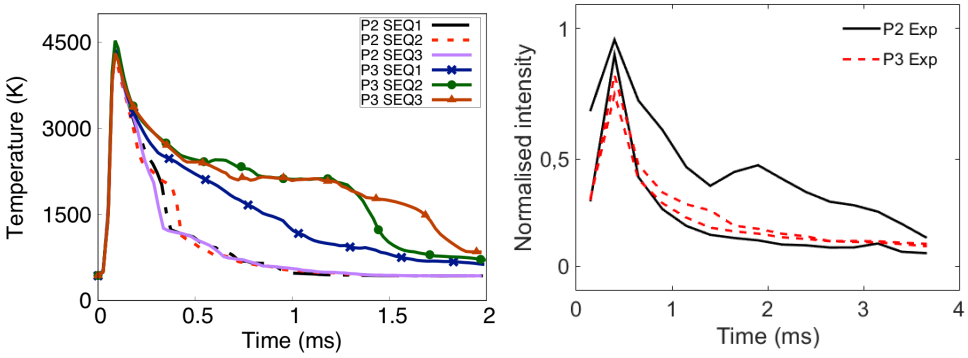

Figure 5.12: (Left): Temporal evolution of the maximal temperature in the domain for the 6 unsuccessful ignition sequences simulated. Lines without symbols : Ignition at position P2 ; Lines with symbols : Ignition at position P3. (Right): Temporal evolution of the experimental kernel intensity versus time. Continuous lines represent P2 and dashed lines represent P3. Longest and shortest extinction times are shown for each point.

times are a bit longer than the ones observed numerically, ranging from 1 to 3 ms.

To understand the mechanisms leading to very fast extinction times at point P2, Fig. 5.13 presents one experimental (top) and one numerical (bottom) event of extinction, called P2_SEQ1. Looking first at the numerical results, the kernel that is initially spherical appears to be already very shredded after 0.3 ms due to the very high values of velocity fluctuations encountered in this zone due to the shear stresses induced by the air co-flow surrounding the IRZ. After 0.6 ms, the kernel is totally scattered in multiple small pieces and is therefore too weak to survive. The same behaviour is observed experimentally but the different events occur at a slower timing (shredding at 0.6 ms, tearing into pieces at around 1 ms and final extinction before 2 ms). Reflections and spark marks are circled in the experimental images. These observations correspond clearly to the **Prompt-Continuous-Shearing Extinction Mode** (labelled E2) described in section 5.3.

At position P3, the reason of ignition failure is different from point P2. Figure 5.14 presents one experimental and one numerical event yielding unsuccessful ignition at P3, named P3_SEQ1. The kernel is not as distorted as for attempts at point P2, it remains all-in-one and is convected slowly downstream. These observations correspond to the **Starving-Blowout Mode** presented before, in

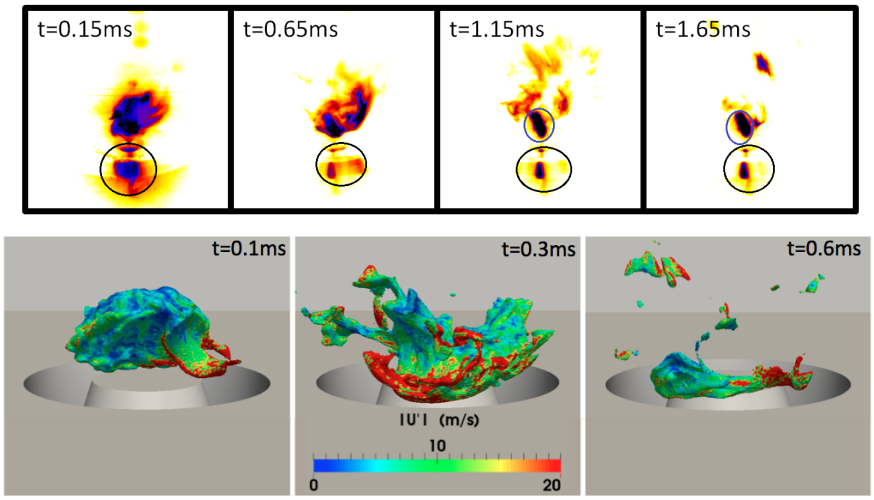

Figure 5.13: (Top): Experimental spontaneous flame emission sequence at P2. (Bottom): Numerical front view of failed ignition sequence P2_SEQ1, at 3 different times after ignition triggering: iso-contour of progress variable $c = 0.1$ coloured by velocity fluctuation norm.

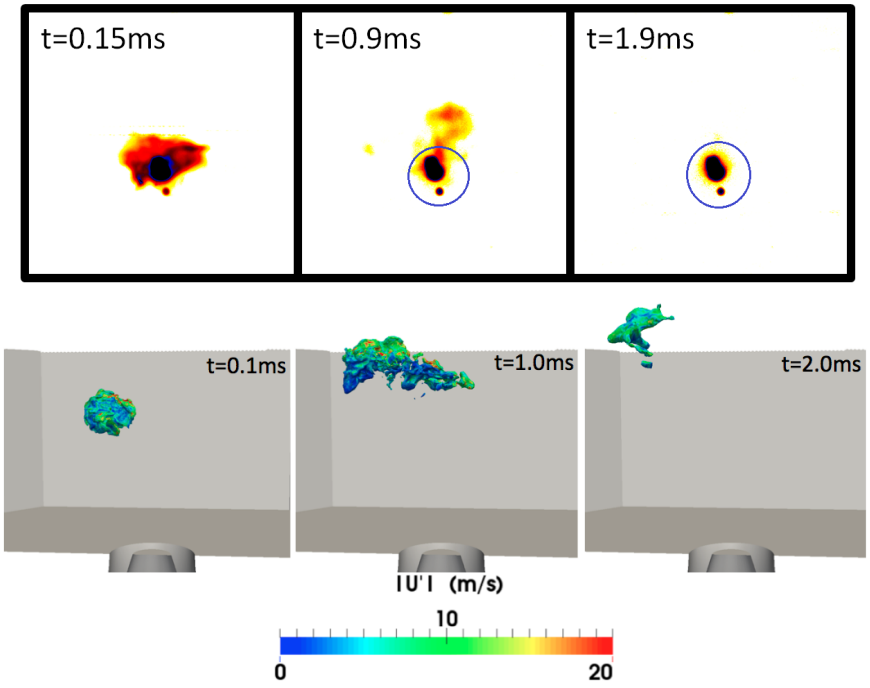

Figure 5.14: (Top): Experimental spontaneous flame emission sequence at P3. (Bottom): Numerical front view of failed ignition sequence P3_SEQ1, at 3 different times after ignition : Iso-contour of progress variable $c = 0.1$ colored by velocity fluctuation norm.

section 5.3. Figure 5.15 displays the instantaneous cut of gaseous axial velocity (LES) at the spark deposit of P3_SEQ1, showing that the high mean axial velocity at P3 is in this case the main cause of failure. This upstream convection is observed both in the three independent events simulated at this position and experimentally. The top part of Fig. 5.14 shows from experiments the same upward convection of the kernel, which suffers strain but stays in one piece. Extinction times fall in the same range here experimentally and numerically, around 2 ms after sparking.

Note that for P3, depending on the instantaneous axial velocity field at the spark position, the evolution of the kernel can slightly differ, as shown in Fig. 5.16 for ignition sequence P3_SEQ2. Quickly after spark deposit, the hot kernel separates into two parts, one being convected downstream and one propagating upstream in the IRZ. Whereas the first one extinguishes as classically observed at position P3, the second one reaches a region too lean and subject to too high shear stresses. Experiments also identify this kernel extinction mechanism with a similar timing at about 1.5 ms. This mode corresponds to the **Prompt-Continuous-Shearing Extinction Mode**, labelled E2 in section 5.3.

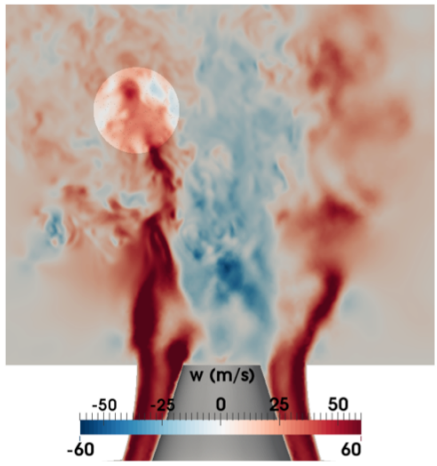

Figure 5.15: Instantaneous cut of gaseous axial velocity at the time of ignition of P3_SEQ1.

This section reveals the good capacity of the LES strategy implemented by CERFACS to capture the different extinction mechanisms and modes observed experimentally. It is, indeed, a very important step in two-phase flow simulation and backs the experimental analysis done in section 5.3, adding useful information that would otherwise be inaccessible to experiments. This section has

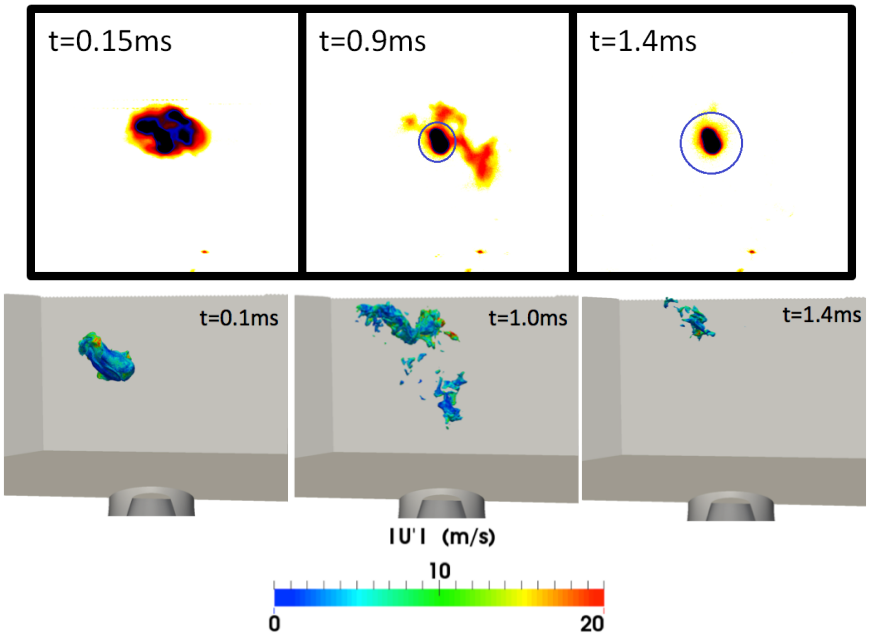

Figure 5.16: (Top): Experimental spontaneous flame emission sequence at P3. (Bottom): Numerical front view of failed ignition sequence P3_SEQ2, at 3 different times after ignition : iso-contour of progress variable $c = 0.1$ colored by velocity fluctuation norm.

been focused only on two chamber locations. The other locations will be soon simulated in order to deepen the analysis and understanding on these processes.

5.6.2 Successful ignitions at r=40 mm, z=30 mm

For the following, the investigated location, r=40 mm, z=30 mm, is referred to as point P1. From Chapter 4, at point P1 the mixture exhibits a rather homogeneous ϕ_{tot} distribution close to the global equivalence ratio ($\phi_{glob} = 0.61$). From time to time however, pockets of high ϕ_{tot} reach the vicinity of P1, indicating the presence of evaporating droplets. Interaction of droplets with the developing flame may therefore occur and will be discussed later. Although point P1 is located in a region of low turbulent kinetic energy compared to the air jet (Chapter 4), it exhibits non-negligible velocity fluctuations which significantly vary with time. This is illustrated in Fig. 5.17 numerically and experimentally. The figure displays the experimental normalized distribution of two-component absolute velocity fluctuations in the neighbourhood of P1 (within a square of 5 mm length) for low and high turbulence levels with respect to the levels found near P1. To

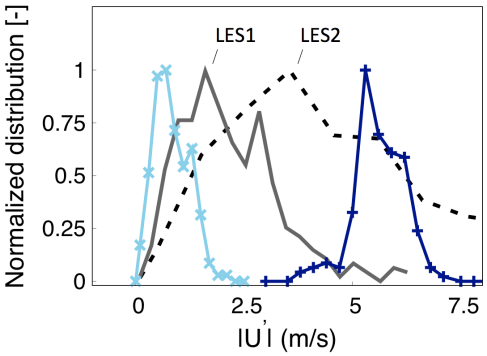

Figure 5.17: Normalized distributions of absolute velocity fluctuations on the cold flow at point P1. Curves with symbols are experimental distributions representative of low and high turbulence levels found near P1. LES distributions correspond to ignition trials shown in Fig. 5.20.

evaluate the role of the non-reacting flow state before sparking, two LES of ignition sequences (referred to as LES1 and LES2 in the following) were performed at point P1, starting at two different instants (t_1 and t_2 respectively) of the established non-reacting two-phase flow. Both instants were chosen to describe the flow variability around P1 observed experimentally. At both instants, P1 is surrounded with a lean gaseous mixture $\phi_{tot} \approx \phi_{glob}$. The two instants mainly differ by the turbulence intensity in the vicinity of P1, as shown in Fig. 5.17, where the normalized distributions of the three-component absolute gaseous velocity fluctuations recorded around P1 in both LES are also shown. The two numerical initial conditions are in between the experimental range, centred around 1.5 m/s and 3.5 m/s respectively. Note that the range of velocity fluctuation magnitude obtained numerically is not as wide as in the experiments, and the distributions are less peaked, which may be due to the shorter investigated time.

Among the 30 experimental ignition tests at position P1, 9 high-speed videos were recorded, 8 of which reported successful events. Only two experimental sequences, named EXP1 and EXP2, are used here together with the two numerical ignition sequences (LES1 and LES2). These sequences EXP1 and EXP2 correspond respectively to the shortest and longest trials among the 9 recorded ones. EXP1 lies in the low range of turbulence intensity while EXP2 was triggered in the high range of turbulence intensity at P1.

Figure 5.18 (Top) shows the high-speed images of the flame kernel for EXP1. The visualization box size is 98 mm $\times$ 98 mm for all images in the figure and shows both halves of the chamber. At $t = 2.4$ ms the kernel develops

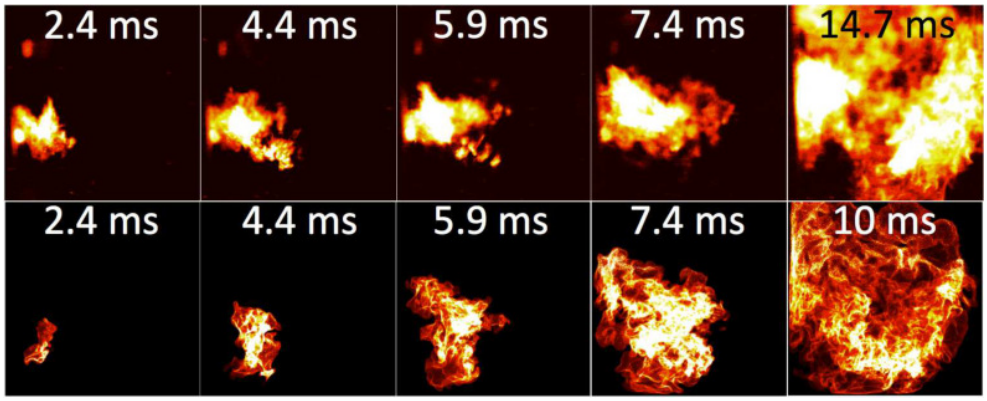

Figure 5.18: (Top): Experimental spontaneous flame emission sequence at P1 (EXP1). (Bottom): Numerical integrated heat release during ignition sequence at P1 (LES1).

around P1 and has little distortion due to the initial low turbulence. At kernel regions closer to the spray, interaction with fuel droplets can be identified as intense luminous patterns. By $t = 4.4\ ms$, the kernel has sufficiently expanded to come very close to the spray branch. At $t = 5.9\ ms$, a part of the flame kernel evolves towards the spray nozzle keeping a strong azimuthal motion. Once the kernel has been convected, intense, luminous parts in the images reveal the presence of a strong fuel stratification. At further times, the flame propagates and expands in all directions, in particular towards the injector. By $t = 14.7\ ms$ the flame has reached the opposite wall. This behaviour is characteristic of an coupling between the **Long-ORZ-Growth Ignition Mode** and the **Spray-Branch Ignition Mode**. Once attached to the spray cone, the flame describes a spiral motion due to the swirling flow and finally reaches the injector. The bottom part of Fig. 5.18 illustrates the numerical sequence LES1, where the integration of the heat release through the entire volume of the chamber allows to track the evolution of the flame kernel. All the successive steps of kernel growth experimentally observed are reproduced numerically, assessing the capacity of LES to reproduce the mechanisms involved in ignition by the modes mentioned.

The interaction between the flame kernel and the fuel droplets noted in Fig. 5.18 is now detailed, looking in Fig. 5.19 at an instantaneous iso-contour of progress variable $c = 0.5$ (based on gaseous temperature) after 3.5 ms for LES1, coloured by gaseous equivalence ratio (Left) and heat release (Right).

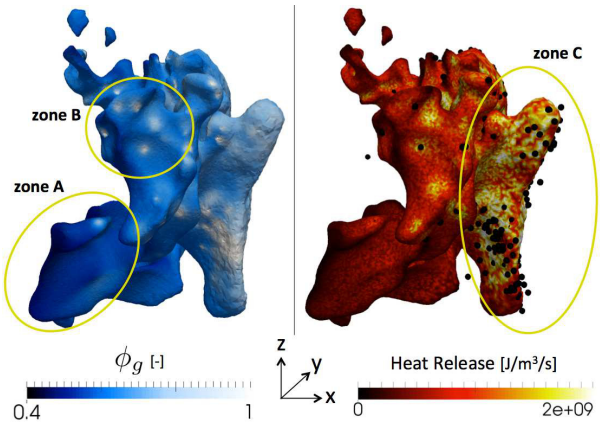

Figure 5.19: Zoom on the iso-contour of progress variable $c = 0.5$ after 3.5 ms during sequence LES1 colored by (Left) gaseous equivalence ratio and (Right) heat release. Evaporating fuel droplets in this zone are represented on the right side by black spheres.

Equivalence ratio is here based on the mixture fraction defined by Bilger [142]. Evaporating fuel droplets are represented by black spheres in Fig. 5.19 (Right). Three regions can be distinguished. In zone A where there are very few particles, the liquid fuel evaporation rate is not sufficient to compensate the gaseous fuel consumption, and the flame can not survive. The heat release is very low and the flame locally extinguishes. In zone B, fast single droplet evaporation occurs near the flame, generating a locally rich gaseous mixture and possibly high heat release in cases of individual burning droplets. However, the contribution of these isolated droplets to the main flame is marginal. The major impact of evaporating fuel droplets on the flame kernel is found in zone C. The spray is dense in this region, leading to high and flammable gaseous equivalence ratios. This region is the most reactive one, evidencing the preferential direction of the kernel towards zones of high fuel droplet number density.

Finally, the capacity of LES to accurately predict ignition delay times is evaluated by plotting in Fig. 5.20 the temporal evolution of the pressure in the combustion chamber for the four experimental and numerical ignition sequences. First comparing with Fig. 5.17, a general trend can be observed: higher turbulence intensity before ignition leads to longer ignition delay, both experimentally and numerically. Both EXP2 and LES2 show very shredded kernels due to high strain limiting the kernel growth during the first 10 ms for LES2 and for 20 ms for EXP2. This confirms the detrimental impact of the initial turbulent field

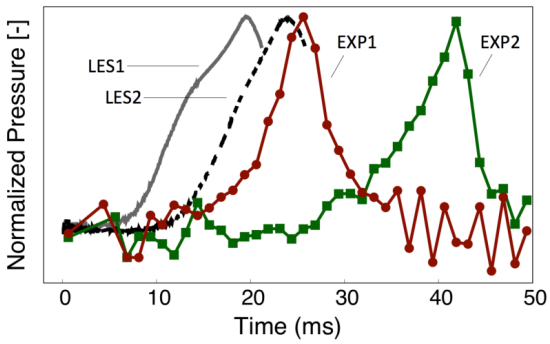

Figure 5.20: Temporal evolution of pressure at P1 for the experimental sequences EXP1 and EXP2, and the numerical sequences LES1 and LES2.

at spark location on the flame kernel growth highlighted in [37, 143] for gaseous flames. However, the difference between the two numerical delay times is smaller than for the two experimental ignitions. This may be due to the closer and wider velocity fluctuation distributions of LES1 and LES2 compared to the two experimental ones. Yet, as soon as the flame holds on the injector ($t = 14.7\ ms$ for EXP1 and $t = 10\ ms$ for LES1 in Fig. 5.18), the agreement between LES and experiments is very good, the slope of the increase in pressure being very similar for the 4 experimental and numerical ignition sequences. Note that the total ignition delays predicted by the two LES are shorter than for experiments, the difference being mostly due to the kernel phase. Since this phase is the most stochastic phenomenon, many other LES sequences with various turbulence intensities and spray densities should be performed to quantitatively compare with the experiments.

It is worth making a comment on the mode of depositing the spark energy in the LES. From discussions with CERFACS, it has been underlined that a change in the deposited amount of energy can strongly influence the ignition delay time, so this is an important point that needs attention. To this end, the literature has uncovered that estimating the correct deposited energy either with a laser-induced spark or with an electrical spark is not an easy task [31, 34, 144, 145]. Moreover, simulations usually model the spark with a sphere or an ovoid of hot gases without radicals. With the purpose of depositing the same energy as done in experiments, this volume is often larger than the initial spark because combustion models cannot withstand such high temperatures and energy densities. This demonstrates that reproducing Phase 1 is still not mastered by numerical models,

and doing so would improve the forecast of the following ignition phases too. Following this direction, the information contained in the present experimental work can contribute in the validation of numerical simulations.

Chapter 6

Ignition Phase 3

Contents

The present chapter describes the stabilisation process of the flame on the single-injector burner. The analysis is divided into three sections: the transition from a flame kernel into a stable flame coupled to the evolution of the pressure, the description of the stable flame structure and the analysis of the reacting flow.

6.1 From kernel to stable flame

If the flame kernel survives long enough, it will follow one or a combination of the ignition mechanisms described in the previous chapter, leading to a stabilised flame. The complete burner ignition takes some time and undergoes different stages, which are captured by the high-speed images and by the chamber pressure signal, illustrated in Fig. 6.1. The different observed stages can be classified into the following (times describe the event shown in the figure):

- Kernel growth and movement: 1 - 20 ms
- Developed kernel settling in the ORZ: $\approx$ 20 ms

- Spray light-around: 20 - 40 ms
- Maximum heat release: $\approx$ 42 ms
- Flame attachment to nozzle: $\approx$ 50 ms
- Flame lifting: $\approx$ 70 ms

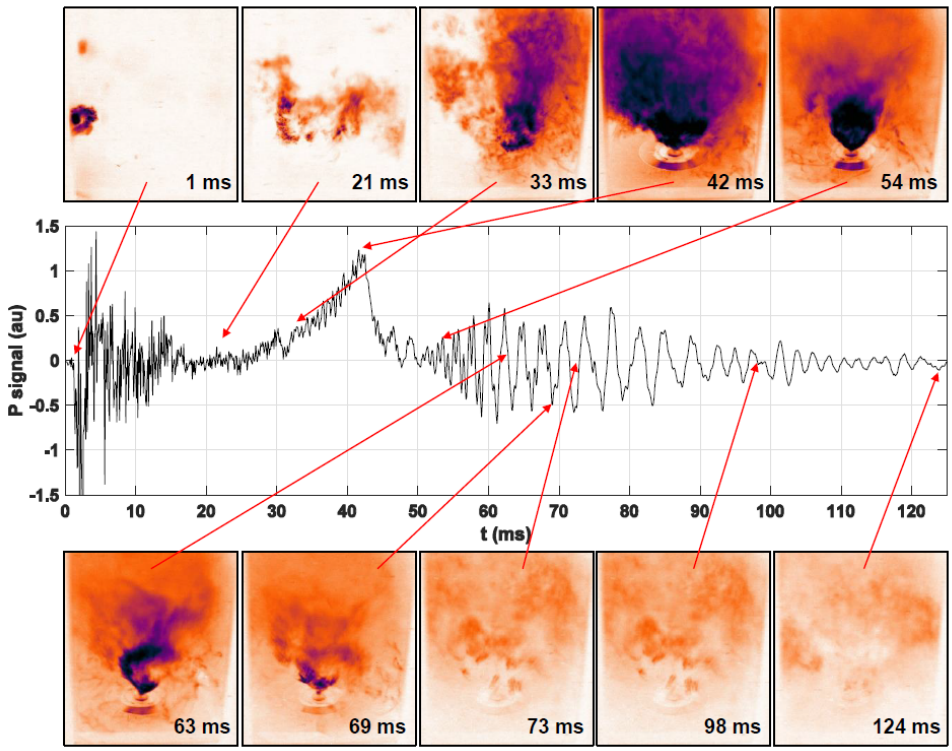

Figure 6.1: Evolution of the pressure signal inside the chamber during an ignition event. Images of the different ignition phases at instants from 1 to 125 ms after the energy deposition.

The pressure signal shows strong pressure variations generated by the spark from 0 ms to 15 ms after breakdown, which can be parasite signals. During this time, the flame kernel moves through the chamber and grows into a little weak flame that often touches the opposite wall to descend into the ORZ at about 20 ms after breakdown. The different possible kernel trajectories and timings were addressed in the previous chapter. At this moment, pressure starts to increase in the chamber and the spray light-around starts, following an anti-clockwise movement imposed by the swirling motion. A pressure peak is reached when

the entire spray has been lighted, 42 ms after breakdown (for the case shown in Fig. 6.1). This moment is coupled to the maximum heat release observed in the images and may be caused by fuel vapour accumulation. This stage is followed by a noisy conical flame attached to the spray cone that generates strong and high-frequency pressure oscillations and becomes unstable to disappear at about 70 ms after breakdown. After this, the pressure signal presents oscillations with lower frequencies and decreasing amplitudes. When the conical intense flame disappears, it leaves a lifted, lean and stable blue flame, as the one shown in Fig. 6.2 (here, the last image at 124 ms). Characteristic times vary from one event to another but Fig. 6.1 is representative of the process.

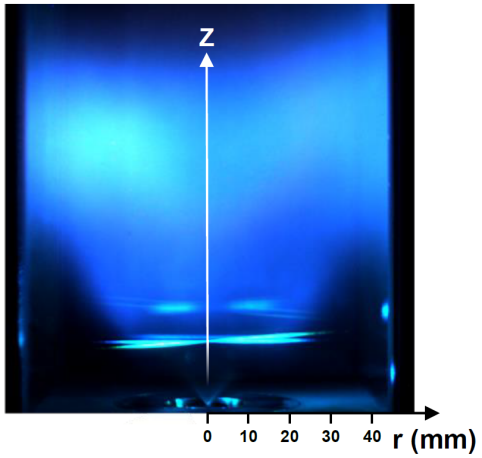

Figure 6.2: Photograph of the spontaneous emission of the stable lifted blue flame.

6.2 Stabilised flame structure

The flame structure analysis is now performed through the OH-PLIF images. The instantaneous corrected images in Fig. 6.3 show the OH fluorescence field at 8 independent moments, labelled from (a) to (h). All reveal a very turbulent flow with sharp angles and wrinkled flame fronts. The following main zones are identified:

- The spray cone and droplets in (a) and (h).
- The air co-flow entering the chamber in (b) and (c).

- The unburnt gases in (c).
- The burnt gases in grey.
- The outer reaction zone in (d).
- The inner reaction zone in (e).
- The outer recirculation zone (ORZ) in (f).
- The inner recirculation zone (IRZ) in (g).
- The flame leading edge is defined in the outer reaction zone and indicated with two green diamonds.

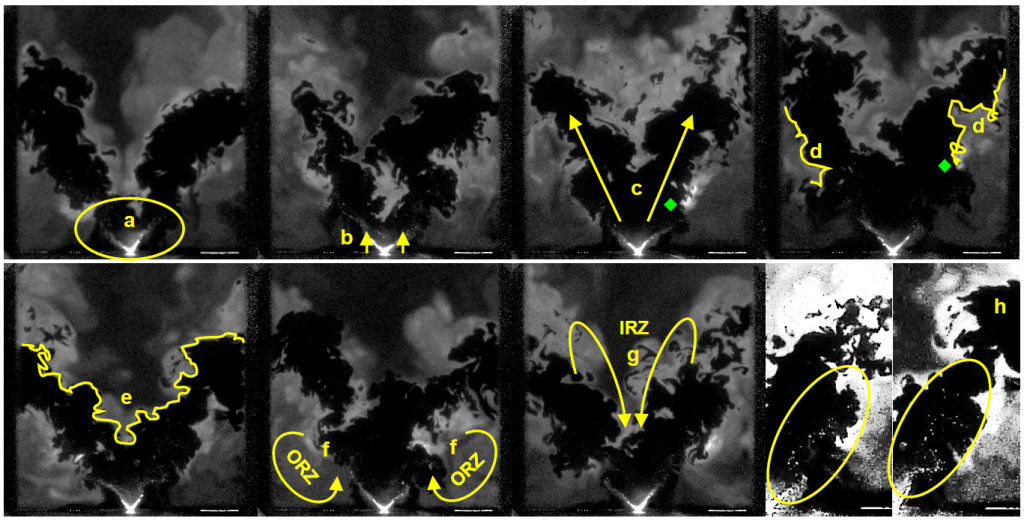

Figure 6.3: OH-PLIF corrected images describing the flame structure and identifying different regions.

The spray droplets are detected on the bottom part of the images scattering very intensely the laser light. The fresh air co-flow surrounds the spray cone as black regions on the images entering the chamber from the bottom in a turbulent motion. The two black diagonal zones correspond to the fresh gases (air, fuel droplets and fuel vapour). The strong gradient between the dark zones and the high OH concentration reveals the position of the two branches of the flame front (upper and lower reaction zones). Given that this is a highly turbulent configuration, the flame location varies from one image to another and

the flame front presents strong wrinkling everywhere. Two reaction zones are observed: the lower-external brush (d), starting at the leading edges, and the upper-central brush (e), defining a central stabilisation point. They often reach the wall and appear disconnected one from the other but, obviously, this is a three-dimensional problem and they may be connected at another point. The regions under the outer flame front, which are delimited by the lower corners of the chamber, contain the burnt gases and probably fuel vapour trapped in a recirculating motion defined by the ORZ. The top part of the images contains the burnt gases produced by both flame brushes. The inner recirculation zone (IRZ) is well defined too. This type of M-flame is typical of swirled confined burners [146–148]. It presents a lifted nature with varying stabilisation points and the leading edge positions depending on velocity fluctuations and local equivalence ratio variations, as indicated by the two green diamonds in Fig. 6.3 (c) and (d). Here, leading edge stabilisation heights are of about 15 and 30 mm. Depending on the leading edge stabilisation height and on the velocity field, fresh air can reach the ORZ if it is not blocked by the flame front, as it occurs in Fig. 6.3 (d) in contrast to Fig. 6.3 (c). This configuration leads to partially premixed combustion modes provided that the fresh air and the vast majority of the droplets are present on the same side of the flame (dark side). However, there might be a non-negligible fuel vapour concentration stored in the ORZ. This has to be investigated by other means. When looking at the different images in Fig. 6.3, the spray cone slightly varies in shape and it appears to oscillate with a certain frequency. Isolated droplets are also found following the spray direction, farther away. Yellow selections in Fig. 6.3 (h) highlight droplet strings that reveal a sinusoidal form. This is probably related to spray oscillation and interaction with the flame reaction zones.

An interesting observation is displayed in Fig. 6.4. Droplets that reach the flame front do not disappear instantaneously, hence they cross the flame front entering in an enhanced evaporation regime. The vapour production behind the droplets leaves n-heptane vapour wakes as black lines in the reaction regions. These wakes are too rich to burn and droplets are colder than the reaction zone. This causes local extinctions of the flame and may send fuel vapour towards the ORZ or it may be burnt by the lower flame brush in the following time instants. This has to be studied in more detail. Local extinction in spray flames has been recently analysed in detail by Verdier et Al. [141].

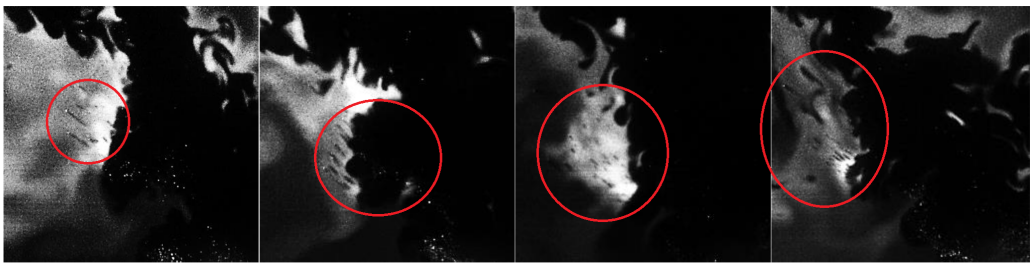

Figure 6.4: Zoom of OH-PLIF corrected images showing fuel droplets crossing the flame front generating local extinctions.

In Fig. 6.5, the mean (a) and the standard deviation (b) of 1000 OH-PLIF corrected images confirm the M form of the flame and help determining a mean flame stabilisation height. The flame contour generates a steep gradient in both images. Although there is a high OH intensity in the ORZ (left image), this is due to burnt gases and the high gradient is still observed at axial stations close to $z = 20\ mm$ and $r = 24\ mm$.

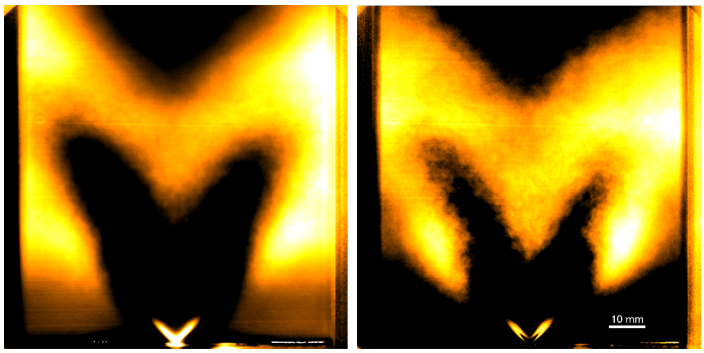

Figure 6.5: OH-PLIF mean image (left) and standard deviation image (right).

This section finishes with Fig. 6.6 showing the comparison between 3 instantaneous experimental OH-PLIF images (top) to 3 instantaneous OH mass fraction fields from LES (bottom), demonstrating the capacity of the numerical simulation to accurately describe two-phase flow combustion. The typical flame characteristics described in Fig. 6.3 are predicted by the LES. Figures 6.6 (A and D) show very low central stabilization points just above the fuel injector with well defined M-shaped flames. Both right branches reach the wall far downstream. Figures 6.6 (B and E) highlight situations where the stabilization point is far downstream ($z \approx 40\ mm$). In these cases, the flame is much more compact exhibiting large fresh gas pockets accumulated between the injector and the

inner flame front. Finally, Figs. 6.6 (C and F) allow to highlight flame shapes with leading edges being high ($z \approx 35\ mm$, left side of both images). In such situation, fresh gases are not blocked by the outer flame front and thus feed the ORZ. The leading edge then comes down to consume the available fuel thereby continuing the flame position intermittency. These images show that there is large variability of the flame shapes and on the positions of the leading edges, as well as on the height of the central stabilisation zone.

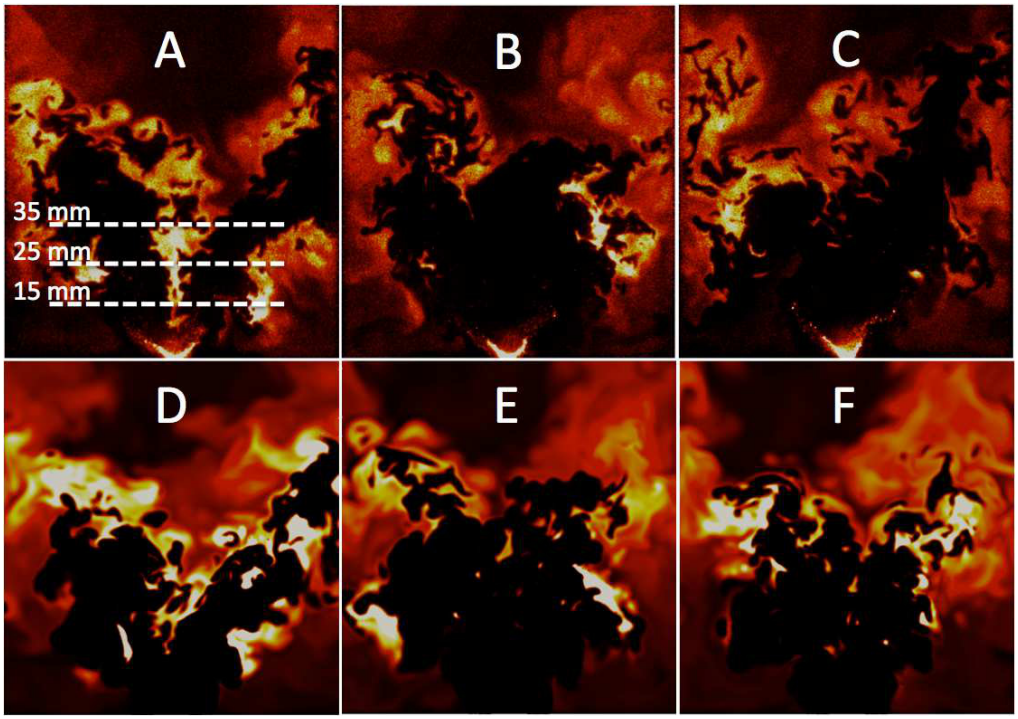

Figure 6.6: Reacting flow. A-B-C: Experimental OH-PLIF images. D-E-F: Instantaneous fields of OH mass fraction from LES, with maximum value $Y_{OH} = 0.001$. Dimensions of visualization boxes are 90 $mm \times 94\ mm$.

Figure 6.7 compared the mean stabilised flame from the experimental and the numerical points of view. The overall agreement between experiments and LES is fairly good showing the capability of LES to reproduce the main behaviour of the two-phase flame in the KIAI-Spray burner. Looking at the images, the main difference is the flame lift off height, which is not perfectly predicted. A comment on this will be given at the end of the next section. However, it is difficult to identify a clear lift off height using OH-PLIF since there is OH recirculating in the ORZ.

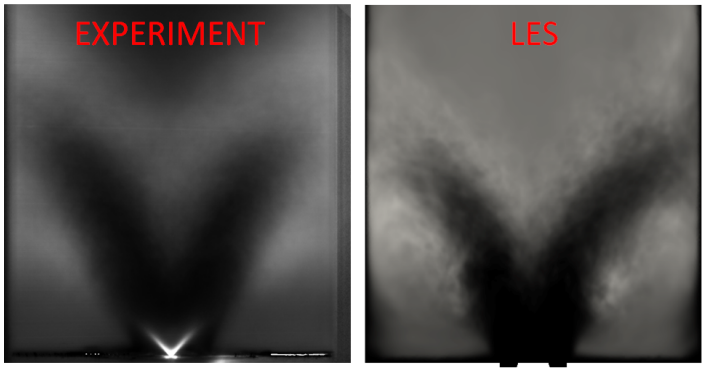

Figure 6.7: Comparison of the mean experimental and numerical stabilised flames.

6.3 Description of the reacting flow

The last part of this chapter addresses the flow aerodynamics and the fuel droplet properties in reacting conditions thanks to the exploitation of the PDA results.

6.3.1 Carrier phase properties

The mean air velocity field components are plotted in Figure 6.8. Reacting conditions (C4) are compared to non-reacting (C1) values recalled from Fig. 4.1 in Chapter 4. In reacting conditions it is even more difficult to find small seeding droplets due to higher flow temperatures imposed by the flame. The reacting air velocity is still well described for many axial stations. At $z = 45\ mm$ no small droplets were detected. Therefore, the 4 presented axial stations for the carrier phase in Fig. 6.8 are: $z = 15$, 20, 25 and 35 mm. The impact of the flame on the carrier phase velocity is very strong for the radial component, important for the axial component and negligible for the azimuthal component. Thermal expansion increases axial velocities, reducing the descending velocity along the IRZ and making positive peaks grow by more than 20 ms^{-1} at some points. This effect is observed at all axial stations and axial profiles keep the same pattern as in non-reacting conditions. For radial velocities the profile patterns are modified in reacting conditions. The air is submitted to expansion forces that increase its velocity by more than 20 ms^{-1} finding new peaks from $r = 15\ mm$ to $r = 25\ mm$ for axial stations from $z = 15\ mm$ to $z = 35\ mm$. Near $r = 0\ mm$ the centripetal velocities are higher. Towards the borders, the centripetal velocities described in Fig. 4.1 are not observed anymore. This phenomenon would modify the ORZ,

pushing it towards the chamber walls. The standard deviation of the velocity is very similar to the one in non-reacting conditions except for the radial component at low axial stations, where the peak fluctuations are lower in reacting conditions.

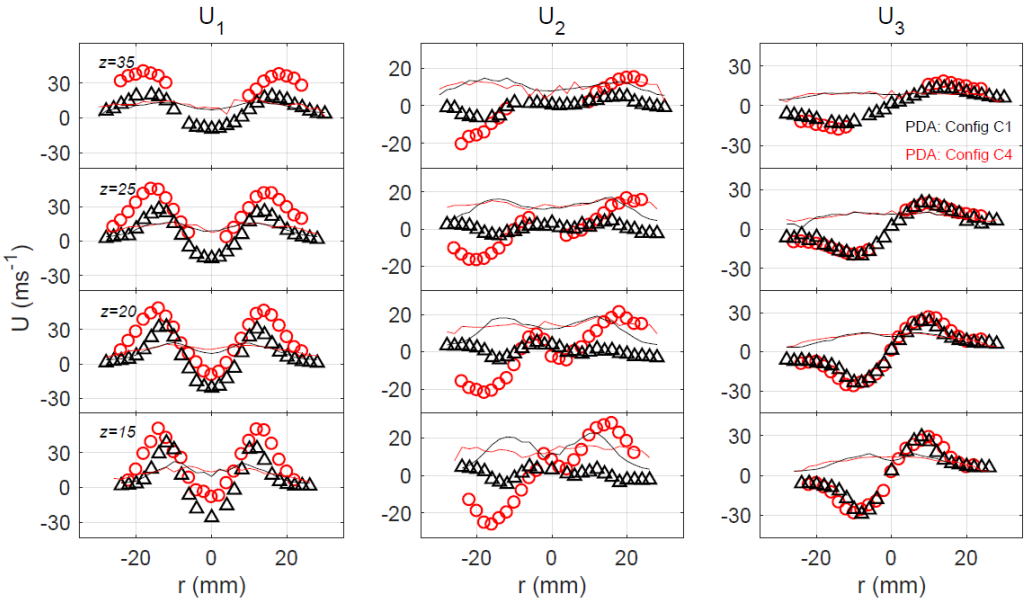

Figure 6.8: Mean components of air velocity flow. Red circles: C4 (air in reactive conditions). Black triangles: C1 (air in non-reactive conditions: seeding oil without fuel spray). Red (C4) and black (C1) lines show the standard deviation of the air velocity.

6.3.2 Dispersed phase properties

The analysis continues with the liquid phase. The fuel droplet distribution in reacting conditions exhibits similar ratios between size-classes to those shown in non-reacting conditions (in Fig. 4.6). Figure 6.9 (left) shows the droplet detection rate. Profiles follow the same radial patterns as in non-reacting conditions but with a smaller amount of droplets per second. The main difference is found at the lowest axial station ($z = 10\ mm$), where droplets between 10 and 30 μm appear to concentrate close to the IRZ. This is seen on the blue and green lines for $r = 4\ mm$ and disappears downstream. It may be related to the increase in the centripetal air velocities observed in the previous figure. Mean diameter (D_{10}) profiles in reacting conditions (C5) in Fig. 6.9 (right) show a similar behaviour as in non-reacting conditions (C3), with less variation along the central

axis ($r = 0\ mm$). Values are a little higher than in non-reacting conditions due to an enhanced reduction of small groups produced by evaporation.

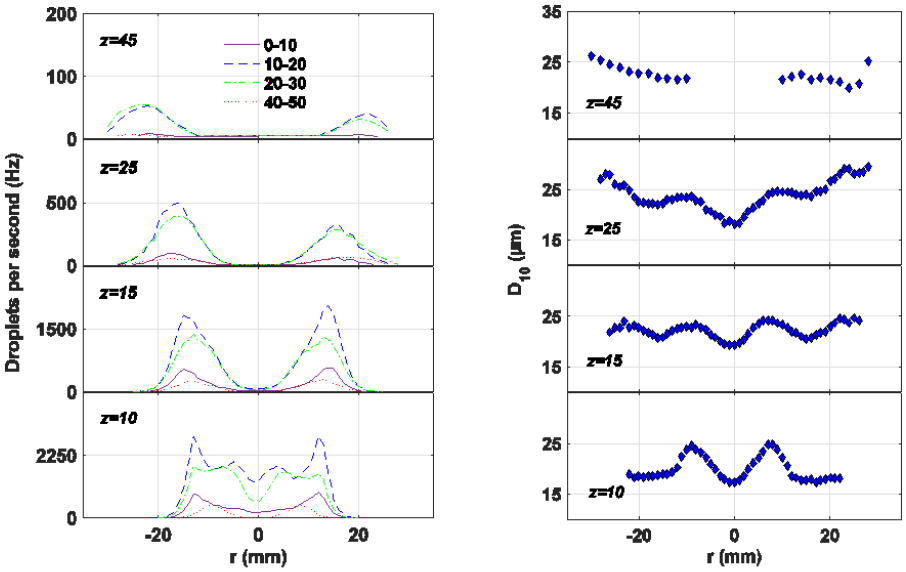

Figure 6.9: Left: droplet detection frequency in reactive conditions for the fuel droplets divided by size-classes (C5). Right: droplet mean diameter in reactive conditions for the fuel droplets (C5).

Figure 6.10 presents the mean and standard deviation of the velocity field of two droplet size-classes in reactive conditions: the small droplets [0-10] μm and the large droplets [40-50] μm. The other groups follow the same patterns. All groups have greater velocity values in reacting conditions than in non-reacting conditions, being this less important for the azimuthal velocity component. The smaller droplets show a higher increase in axial ($> 10\ ms^{-1}$) and azimuthal ($< 5\ ms^{-1}$) velocities than large droplets. For radial velocities, all groups adopt the same velocity values for all points, with peaks of about $30\ ms^{-1}$. The standard deviation is slightly higher for small droplets than for large droplets, as it was noted in non-reacting conditions (Chapter 4).

To finish this section, numerical and experimental radial profiles of mean gaseous axial and radial velocities are compared Fig. 6.11 at three stations downstream the injector ($z = 15,\ 25,\ 35\ mm$, see Fig. 6.6). Mean axial and radial liquid velocities per diameter class are also compared in Fig. 6.12. The underestimation of the mean gaseous axial velocity and, consequently of the mean liquid axial velocity can be related to the difference in the flame stabilisation height.

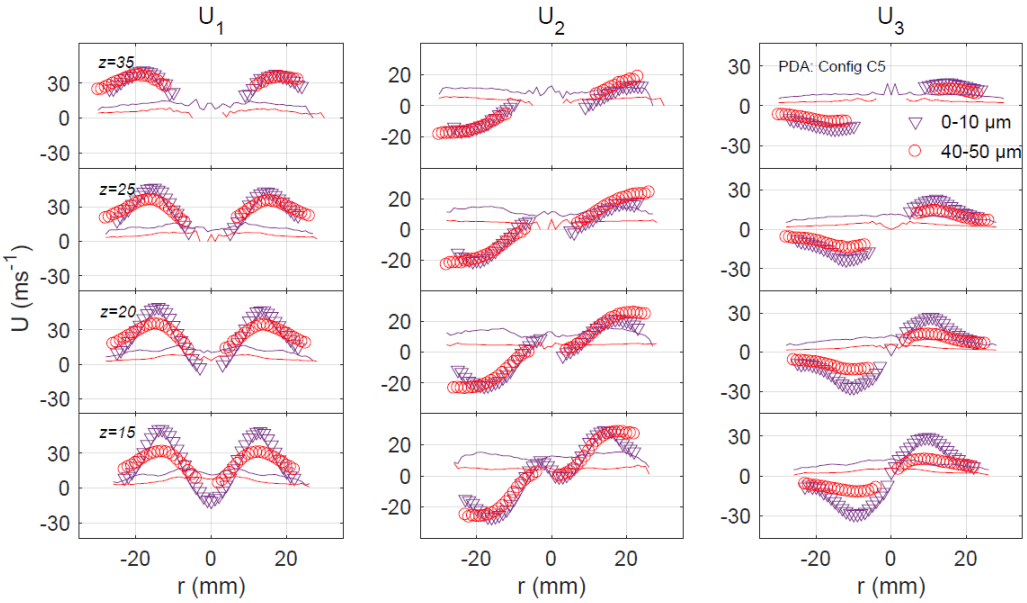

Figure 6.10: Mean components of fuel droplet velocity in reactive conditions (C5) separated in two size-classes. Purple triangles represent the [0-10] μm group and red circles the [40-50] μm group. Correspondingly, purple and red lines show the standard deviation of the air velocity.

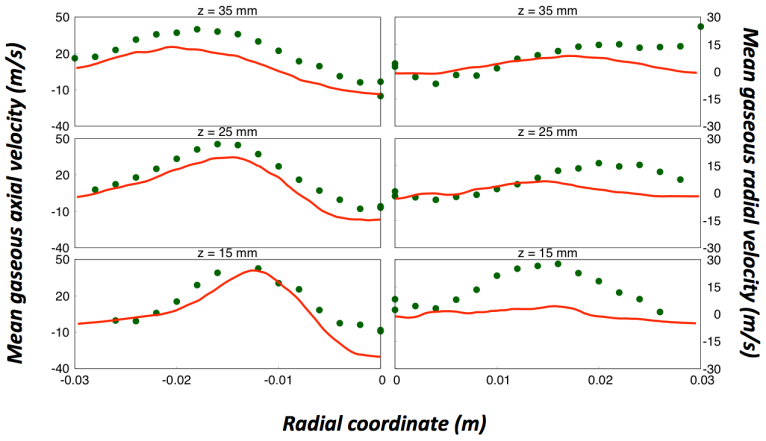

Figure 6.11: Comparison between experiments (symbols) and LES (lines) for the reacting flow. Radial profiles at 3 stations (see Fig. 6.6) of mean gaseous axial and radial velocities.

Note that the same difference was observed on the KIAI-Spray jet flame [135] and that this point is still under investigation on both configurations. The radial acceleration due to thermal expansion is not correctly captured by LES. Different wall conditions were tested to change the flame stabilisation or topology

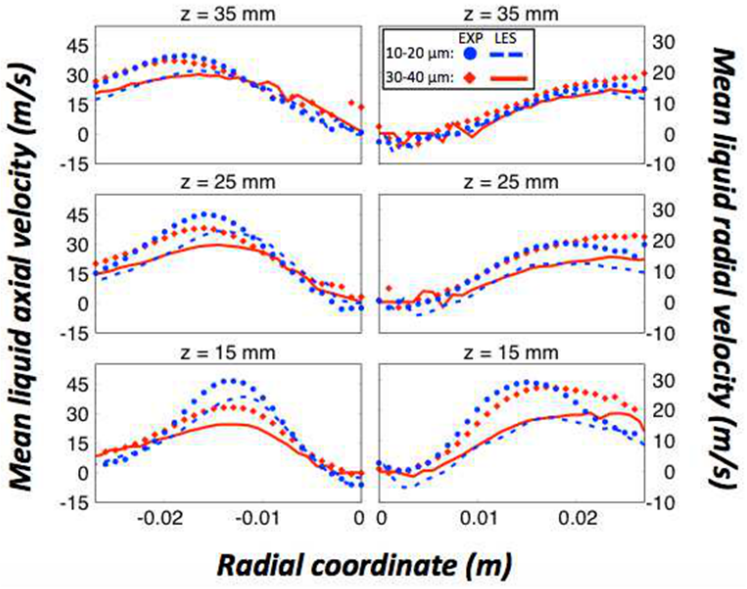

Figure 6.12: Comparison between experiments (symbols) and LES (lines) for the reacting flow. Radial profiles at 3 stations (see Fig. 6.6) of mean axial and radial droplet velocities for 2 diameter classes.

(e.g.: adiabatic, isothermal) with no success on this parameter. The literature demonstrates that the evaporation models are still not capable of reproducing all possible situations [149, 150]; this would have a great impact in spray flows like the present one and could explain differences in the flame stabilisation height and consequently in radial gaseous velocities. A more detailed analysis in the flame dynamics, namely at the central stabilisation point would maybe unveil more possible reasons under the observed differences.

Conclusion to Part III

This is the end of Part III, containing chapters 4, 5 and 6. All the exploitable results obtained in the KIAI-Spray single-injector burner have been presented and thoroughly discussed. The main scope of this part was placed on the investigation of ignition Phase 2. For this, the non-reacting flow properties were discussed in Chapter 4 and then used to study the flame kernel nature and propagation in Chapter 5. Here, the ignition probability map was correlated to the local flow variables and further explained by the analysis of the high-speed kernel visualisation. Different characteristic ignition mechanisms and their typical times and locations were proposed. Concerning the failed ignitions and more specifically the second-mode extinction proposed by Mastorakos [37], five different kernel extinction mechanisms were observed and classified, as well as their typical timings and occurring locations, providing new insight on the critical situations a kernel might face.

A coupled LES-experimental study was presented in the last part of Chapter 5, introducing a new analysis of the ignition and the kernel extinction mechanisms that complements the discussion on Phase 2. LES results match and make solid the experimental observations and the ignition and extinction modes proposed in this manuscript. Numerical simulations also give access to a wide range of parameters controlling ignition and enable a deeper analysis of the processes.

Ignition Phase 3 is described in Chapter 6, where experimental and numerical results are also compared to describe the flame stabilisation, structure and the reacting flow properties.

Ignition Phase 4 is now addressed in Part IV, in the multi-injector CLSSB facility.

Part IV

MULTI-INJECTOR BURNER RESULTS. IGNITION PHASE 4

Chapter 7

Impact of the Injector-to-Injector Distance on the Local Flow

Contents

Part IV deals with Phase 4 of aeronautical ignition, studied in the multi-injector CLSSB facility. In Chapter 7 the impact of the injector-to-injector distance on the non-reacting flow is evaluated in terms of aerodynamics (HS-PIV) and mixture formation (Toluene-PLIF). This step is necessary to understand the flame propagation mechanisms described in Chapter 8. As it was detailed in section 1.3.1 of the introduction, Phase 4 has been less studied than the others. Indeed, there only exist 2 recent investigations on this process in two-phase flows: experiments [97] and simulations [98] in the MICCA-Spray annular chamber, located at Ecole Centrale Paris, and experiments in a 5-linear spray arrangement at University of Cincinnati [100]. In the MICCA-Spray configuration (as well as in the previous gaseous MICCA facility) inter-injector distances have never been varied. In the linear facility from Cincinnati two inter-injector spacings were tested with no impact on the flame propagation mechanisms. Nevertheless, in previous gaseous premixed and/or non-premixed studies it was found that different inter-injector distances could yield different flame propagation mechanisms. This was found by Cordier et al. [73, 89] and Barré et al. [90] in the non-premixed linear chamber preceding the current CLSSB used in the present work. Machover and Mastorakos [91–94] also evaluated Phase 4 in gaseous lin-

ear and annular chambers. Different flame propagation mechanisms associated to different injector-to-injector distances have still never been found in aeronautical spray flows, placing the CLSSB in the leading edge of this investigation.

The aerodynamics and mixture formation are now assessed below.

7.1 Airflow Velocity Fields

The dynamics of the carrier phase are modified when varying the distance between neighbouring injectors and this must be investigated in order to explain the different ignition mechanisms observed in the following chapter. For this purpose, HS-PIV was applied on the air co-flow without spray presence. It was proven in the KIAI-Spray single-injector chamber under similar flow conditions, that the impact of fuel droplets on the airflow velocity is negligible, especially for axial stations higher than 20 mm (Fig. 4.2 in Chapter 4). Therefore, the separate study of the airflow velocity is justified. Figure 7.1 presents the mean air velocity fields for d = 9, 13, 15 and 18 cm. The colour map describes the axial (vertical) component of the velocity where blue colours indicate negative velocities. The field of view starts at ≈ 25 mm above the injection for $d = 9$, 13 and 15, and at $z = 20$ mm for $d = 18$ cm, due to a different image magnification factor for the latter. Figure 7.1 reveals outstanding differences between the different configurations:

- At $d = 9$ cm, the swirling air jets open very quickly to touch the neighbouring jets at $z \approx 65$ mm and leaving a large space for the inner recirculation zone (IRZ). Negative velocities in the IRZ reach regions of $z < 20$ mm. The inter-injector region (IIR) is characterised by positive velocities of low magnitude (≈ 2 $m.s^{-1}$).

- The following configuration ($d = 13$ cm) reveals longer main jet zones that penetrate farther than the latter, keeping high peak velocities. Neighbouring jets seem to merge just above the field of view, at $z \approx 120$ mm. The IRZ appears displaced upwards with the stagnation point shifted to $z \approx 85$ mm. The space between injectors shows negative velocities which bring mixture from the top of the jet branches. Provided that the spray branches nearly touch each other, a stagnation point must exist at $r \approx 60$,

$z \approx 110\ mm$, implying that the descending flow must be charged in fuel due to interaction with droplets.

- The long d configurations will be now analysed together. In mean terms, there are no indications of a strong IRZ. Extrapolation from short injector-to-injector distances suggests that the IRZs have moved upwards downstream and are less intense. The main air jets show a straight profile that does not open at high axial stations, oppositely to the previous configurations. This is supported by the presence of two counter-rotating vortices, one separating each air jet branch from the descending flow. These vortices are present for $d = 13\ cm$ fairly close to the tip of the jets where the merging takes place, whereas for $d = 15$ and $18\ cm$, these two vortices are too far from one another to induce such jet opening and, thus, prevent neighbouring air jets from establishing a solid connection. Inevitably, this effect will carry mixture from the top part of the burner into the inter-injector zone avoiding any contact with fuel droplets.

The velocity fluctuations were used to calculate the 2-D turbulent kinetic energy (k) in the CLSSB multi-injector burner with the purpose of comparing the turbulence of the different injector-to-injector distances. This is presented in Fig. 7.2. As expected, shorter d values yield higher turbulent kinetic energy in the IIR, since the maximum k is contained in the jet zones (JZ) and these are closer. This information will be used in Chapter 8 in the analysis of the flame topology.

The analysis of the instantaneous velocity fields offers further information that can reveal interesting aspects of the interaction between injectors. Figure 7.3 illustrates four instantaneous velocity fields coloured by the axial component, one for each d. Injectors show again a strong and large IRZ for $d = 9\ cm$, the shape of which is submitted to the flow fluctuations. Here, the inter injector regions show some negative velocities at certain points depending on the jet dynamics. Air jet branches appear connected to their neighbours and disconnected from their opposite branches within the same injector. For $d = 13\ cm$ one of the jet branches shows a wide opening with a large IRZ ($r = 0\ mm$) while its neighbour branch ($r = 120\ mm$) penetrates the flow vertically. Indeed, for this injector (placed at $r = 130\ mm$) both branches are closed and do not posses an IRZ at this precise moment. Again, jets for $d = 15$ and $18\ cm$ show very vertical and penetrating

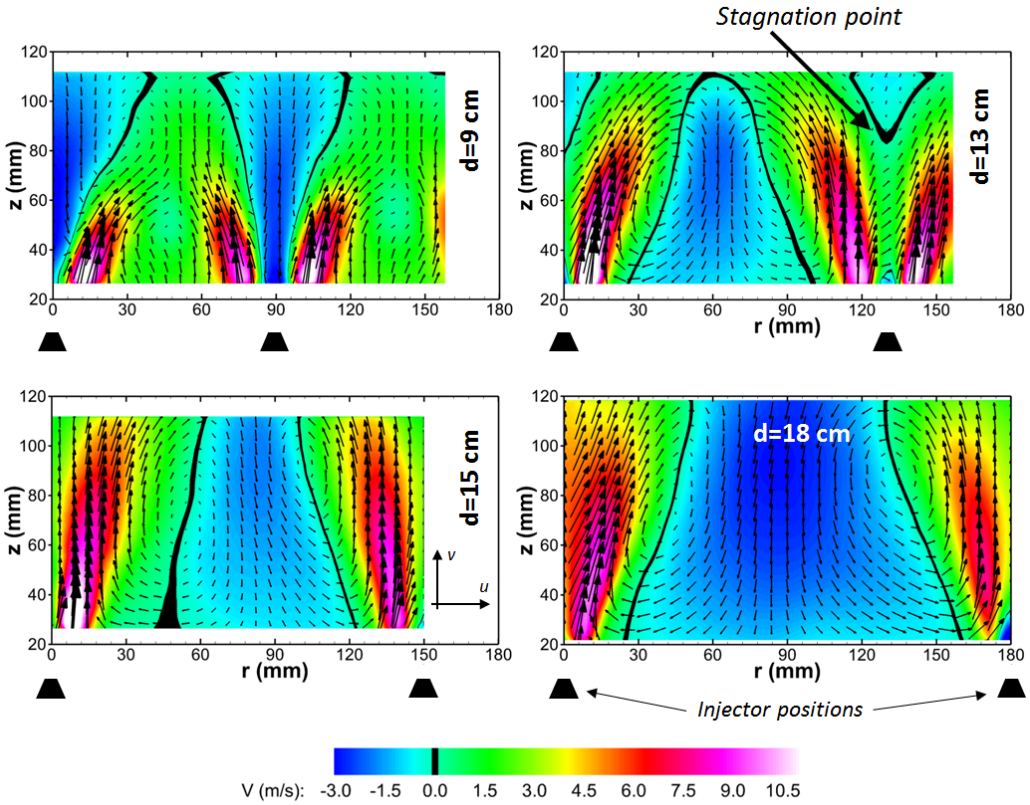

Figure 7.1: Mean velocity fields for the four injector-to-injector distances. Colours represent the axial velocity component.

trajectories although eventually some IRZs can reappear due to fluctuations of the flow. Jets are totally independent from their neighbours and the negative velocities (dark blue zones) occupy a large part of the region between injectors. The jet dynamics are governed by many parameters and have been studied deeper in [95]. Here, five linearly arranged counter-rotating radial-radial swirler injectors were employed to evaluate the impact of the injector-to-injector distance on the confined flow field, which was measured by Laser Doppler Velocimetry (LDV). In addition, the wall distance was also varied. They observed that for short inter-injector spacings, the IRZs revealed a wide-compact-wide distribution from the centre to the corner injectors and that this was reversed for long distances. These differences between neighbouring injectors are not observed in the mean flow field (Fig. 7.1) of the present work; maybe a greater field of view would be necessary to appreciate such effects or perhaps a temporal analysis of the instantaneous fields would reveal periodic differences between adjacent injectors.

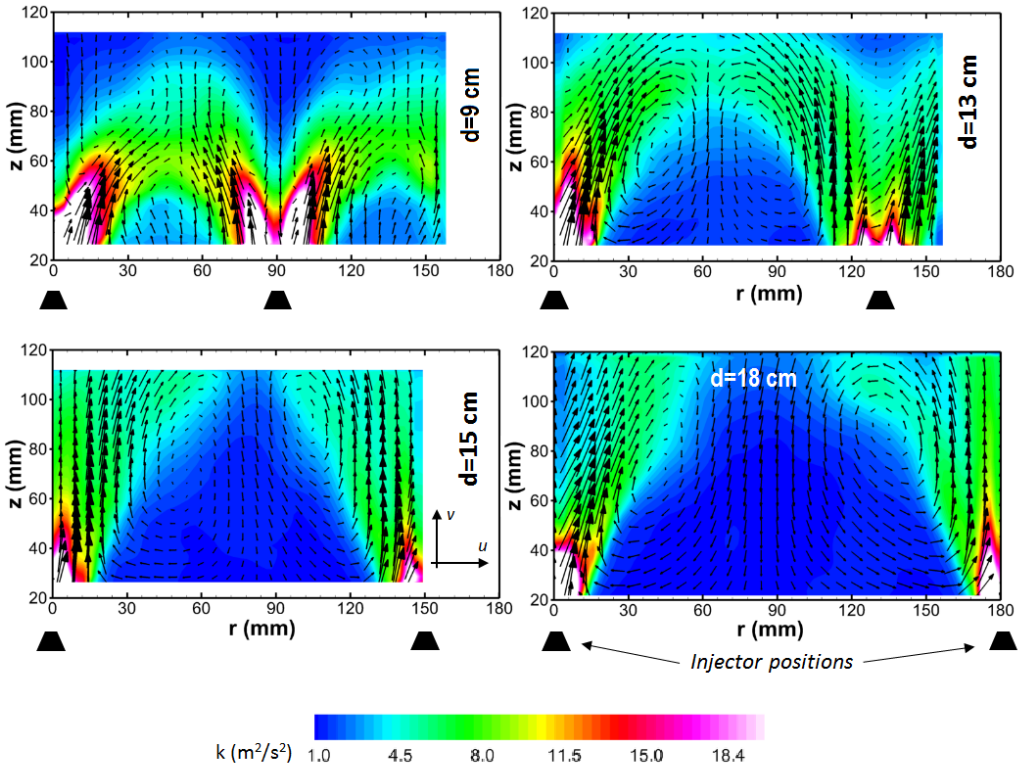

Figure 7.2: Turbulent kinetic energy fields for the four injector-to-injector distances.

Indeed, Fig. 7.3 suggests some differences in the instantaneous IRZ behaviour of adjacent injectors.

7.2 Local Equivalence Ratio

The Toluene-PLIF images show the repartition of the equivalence ratio locally in the chamber and helps to further understand the nature of the regions between injectors. Large droplets were filtered with a level and a gradient threshold, as explained in Chapter 3. Figure 7.4 presents the mean equivalence ratio and the standard deviation for the four different injector-to-injector configurations. On the images, a cover can be observed at the spray cores, immediately after the injectors. This was added to the system so as not so saturate the intensifier in the dense-spray region. The mean ϕ maps reveal an interesting evolution of local ϕ in the IIRs and in the IRZs when changing values of d. For $d = 9\ cm$, the IIR

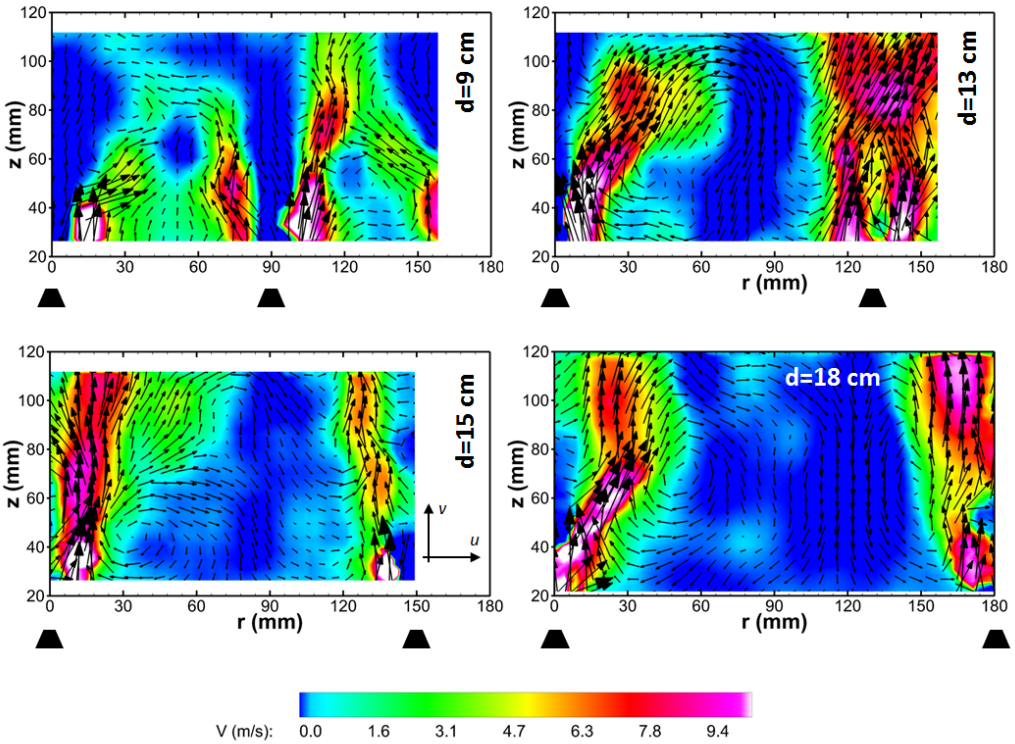

Figure 7.3: Instantaneous velocity fields for the four injector-to-injector distances. Colours represent the axial velocity component.

shows higher ϕ values (around 0.73) than the IRZ (around 0.69). For $d = 13\ cm$, ϕ values in the IIR and the IRZ are very close, while for d=15 and 18 cm the tendency is inverted: the local equivalence ratio decreases more and more in the region between injectors and the IRZ presents increasing values of ϕ, higher than those observed in the IIR.

Figure 7.5 illustrates the evolution of local gaseous ϕ in the IIRs and IRZs against d, which has been just described. Boxes in Fig. 7.4 indicate the regions from which local spatially-averaged values of ϕ were extracted to elaborate Fig. 7.5. This behaviour is intimately related to the velocity field of the flow and the previous analysis on the existence or absence of the IRZs. In configurations where the IRZ has a strong presence, such as $d = 9\ cm$, ϕ is lower in the IRZ because mixture from the top of the chamber is introduced into this zone without direct contact to new issuing spray droplets. The air in contact with the issuing fuel droplets transports the fuel vapour into the IIRs. On the other hand, long d configurations reveal in Fig. 7.1 how the air motion transports the fuel vapour

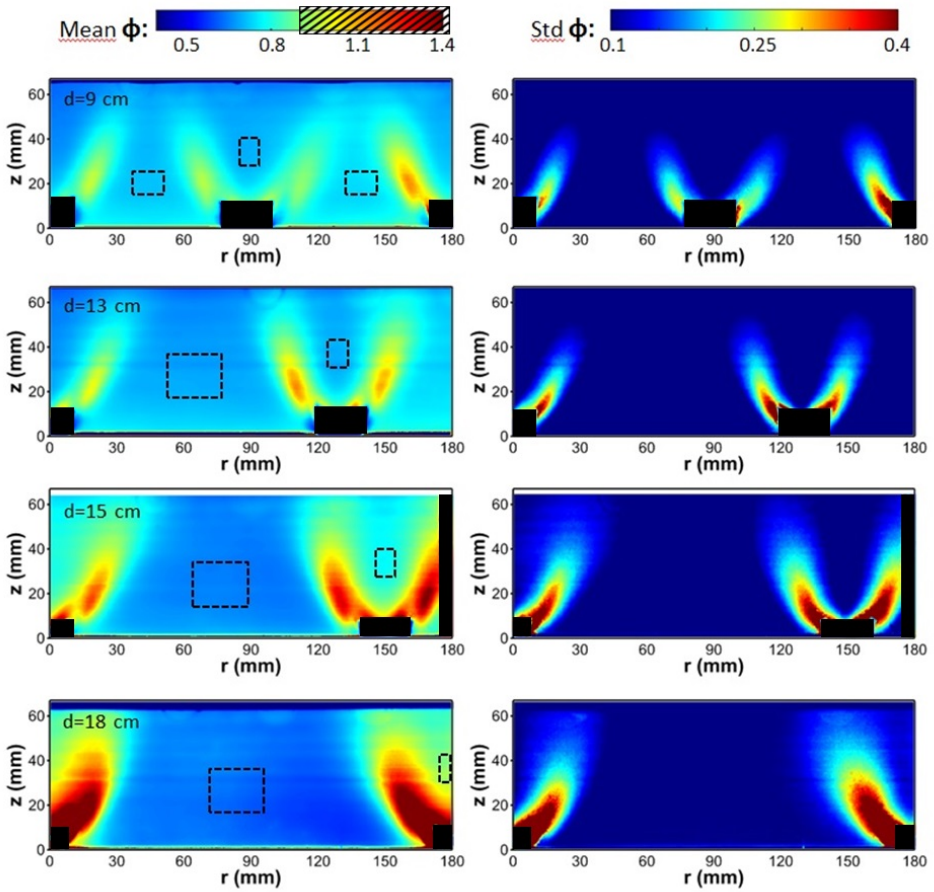

Figure 7.4: Mean and standard deviation fields of the equivalence ratio for each of the four injector-to-injector distances. Dashed-line boxes indicate regions used for mean calculations of ϕ at the IIRs and IRZs.

into the IRZs an impedes the fuel to pass directly into the IIRs. The standard deviation on the right part of Fig. 7.4 shows low ϕ variations in the IIRs and IRZs, and high variations in the spray branches.

More information is provided by the instantaneous equivalence ratio fields, which are shown in Fig. 7.6. Here, two independent ϕ images are shown for each d. Black-coloured pixels represent the fuel droplets, that were detected in the post-processing. The detected droplets were not taken into account for the calculation of the mean fields. In Fig. 7.6, at $d = 9\ cm$, a well-premixed homogeneous inter-injector region is observed while the IRZ shows more ϕ variations. For $d = 13\ cm$, more mixture inhomogeneities can be observed in the IIR, apparently due to the eventual descending pockets from the top part of the chamber. For long spacings ($d = 15$ and $18\ cm$) high values of ϕ appear more concentrated

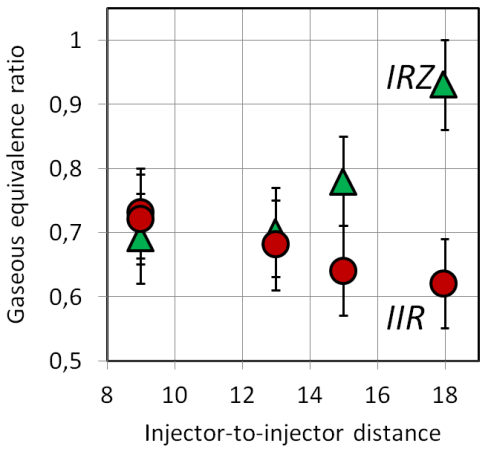

Figure 7.5: Local mean gaseous equivalence ratio at the IIR and in the IRZ for the four injector-to-injector distances. Error bars indicate the measurement inaccuracy caused by possible slight variations in laser energy and in mass flows.

in the spray branches and the IRZs. Here, the IIR becomes very irregular: ϕ values fluctuate spatially more and more with increasing values of d. Values of $\phi < 0.55$ (Chapter 4) are more and more frequent for increasing d and indicate a mixture below the flammability limits.

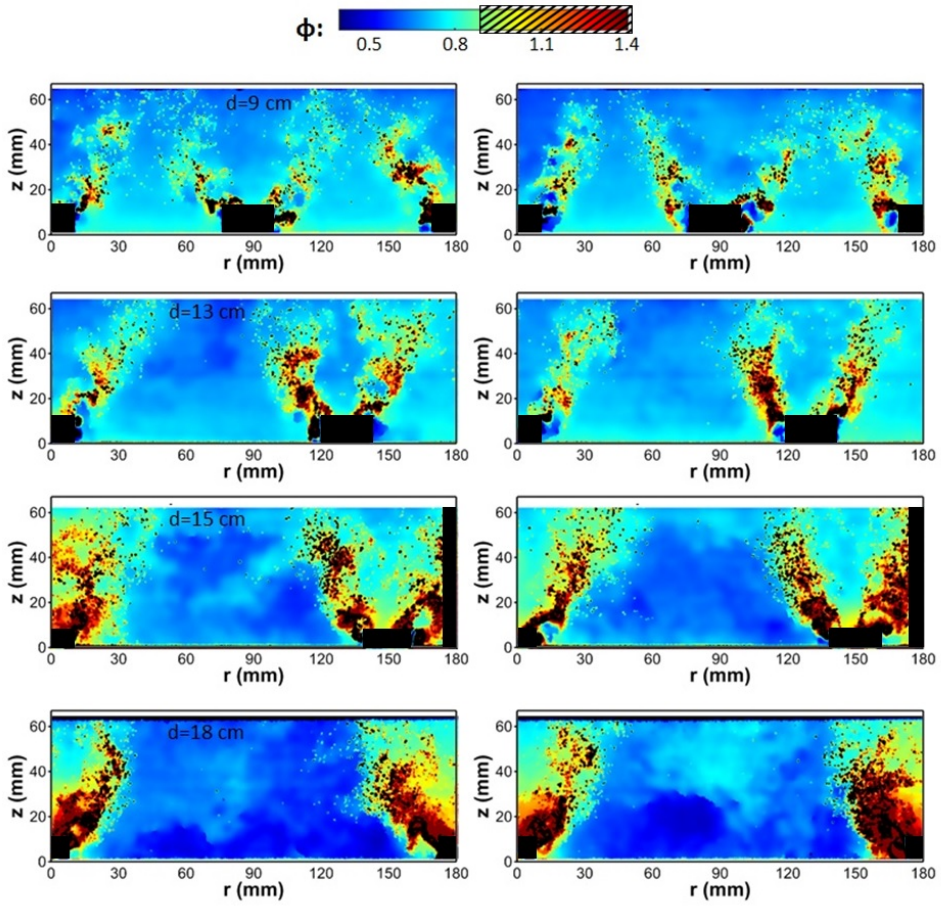

Figure 7.6: Two instantaneous equivalence ratio fields for each of the four injector-to-injector distances.

Chapter 8

Ignition Phase 4

Contents

This chapter addresses ignition Phase 4 for the four studied values of d and the four tested fuels of different volatilities. The analysis is divided into 3 sections: the flame propagation mechanisms, described by the high-speed visualisation images and the high-speed tomographic images for HS-PIV; the evolution of pressure and luminosity signals; and the droplet and mixture migration effect, studied thanks to the HS-PIV results during ignition.

8.1 Flame Propagation Mechanisms, Flame Wrinkling and Flame Propagation Velocity

8.1.1 Analysis of high-speed spontaneous emission images

The flame propagation is revealed through the high-speed images, enabling the analysis of the total ignition delay time and the identification and analysis of

different propagation mechanisms. To illustrate this, Figs. 8.1, 8.2, 8.3 and 8.4 show one ignition sequence for each injector-to-injector distance: 9, 13, 15 and 18 cm respectively. All show the flame propagation for n-heptane only. For the sake of conciseness, only 9 negative images are shown on each figure. The $d = 9$ cm and $d = 13$ cm configurations used 5 injectors while the $d = 15$ cm and $d = 18$ cm cases used, respectively, 4 and 3 (see Chapter 3). The fuel sprays issuing from each injector can be observed in the four sequences thanks to the Mie scattering of a laser sheet (entering the burner from the right) on the fuel droplets. Injectors in Fig. 8.1 are denoted from A to E on the first image. The image sequence starts at 6 ms after the spark triggering and time between images is $dt = 4.5$ ms. The spark is triggered at the wall at injector B. On the first image a growing flame kernel can be appreciated on the right branch of B. This kernel evolves and propagates under time and lengthscales characteristic of ignition Phase 2. By 24 ms, injector B is completely ignited. In this particular example, B and C are lighted practically simultaneously. This can be explained by the high equivalence ratio revealed in the IIR for $d = 9$ cm (see in Fig. 7.3 and 7.5 in the previous chapter). The flame then propagates (Phase 4) under a turbulent flow and showing highly wrinkled reaction fronts. Arrows in Fig. 8.1 indicate that flame propagation takes place in all the volume in a radial way, with leading fronts sweeping the inter-injector regions vigorously. Total chamber ignition here is reported at $t = 50$ ms. The mean total ignition delay time calculated from the high-speed spontaneous flame emission images for 20 independent ignition trials at $d = 9$ cm yields 46.75 ms.

Figure 8.2 reveals the same flame behaviour during the propagation between injectors. Here, the first image shows $t = 6$ ms and the inter-frame time is $dt = 7.5$ ms. The flame leading fronts are able to cross actively the IIR, as for the previous case, but total ignition delay times are longer for this configuration. This ignition configuration reports a mean total ignition delay time of $t = 67.49$ ms. Note that the ignition time of the first ignited injector remains very close to that of $d = 9$ cm. This also happens for the longer inter-injector distances and is characteristic of Phase 2.

Injectors in Fig. 8.3 are named A, B, C and D and time difference between images is $dt = 9$ ms. For this configuration the flame finds more difficulties to propagate at low axial stations between injectors. Indeed, the flame propagation is much slower and it follows an arch-type trajectory, as indicted by the arrows on

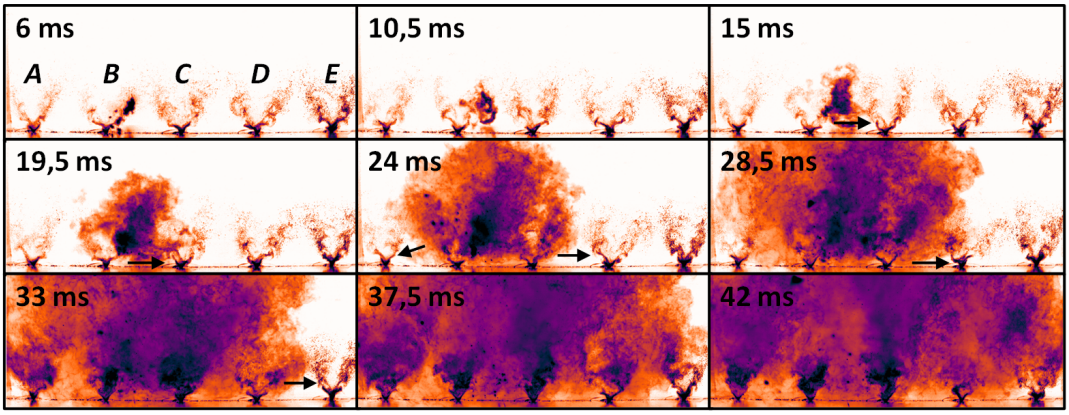

Figure 8.1: Ignition sequence for n-heptane and $d = 9\ cm$. High-speed spontaneous flame emission images. Injectors are labelled A to E.

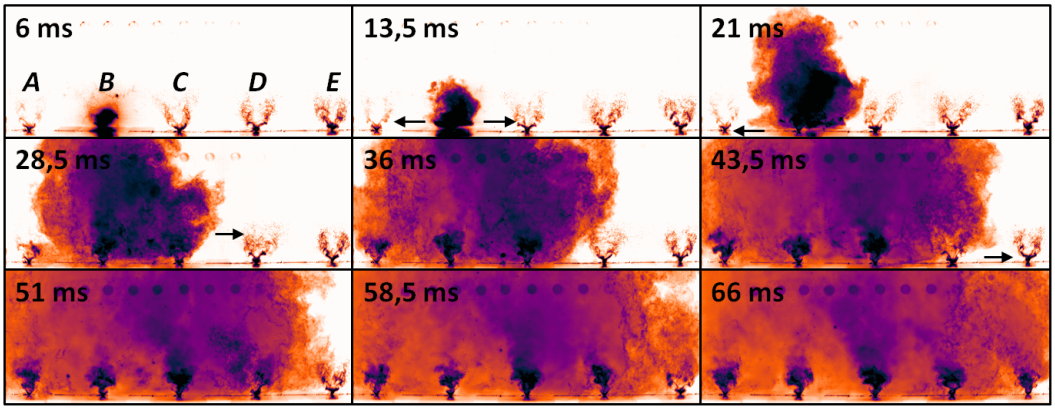

Figure 8.2: Ignition sequence for n-heptane and $d = 13\ cm$. High-speed spontaneous flame emission images. Injectors are labelled A to E.

the images. Total mean chamber ignition delay time (from 20 independent trials) is reported at $t = 85.97\ ms$. This slower mechanism, named arch propagation, is also found for $d = 18\ cm$, where it is even more outstanding.

Time between images in Fig. 8.4 is $dt = 10.5\ ms$. Ignition is triggered at injector B and a compact flame kernel can be observed on top of it, in the centre of the chamber. The flame kernel then evolves and grows systematically in the region attributed to injector B, which appears to be completely ignited at 27 ms. In the following stage, the flame does not evolve along the lower part of the chamber since any lateral fronts emerging at low axial stations are either quickly extinguished or cannot propagate. The flame then propagates with a low velocity at the top part of the burner aided by the thermal expansion of the

burnt gases. At 58.5 ms injectors B and C appear connected by a flame branch in an arched shape; the same happens at 69 ms for injector A. Complete ignition of the whole chamber is reported at ≈ 100 ms for this sequence. The mean total ignition delay time extracted from the 20 ignition tests at $d = 18$ cm is 77.14 ms. This second flame propagation mechanism yields much lower propagation velocities that the radial mechanism observed for small inter-injector distances.

Figures 8.1 to 8.4 show ignition sequences only for n-heptane but are representative of what happens for the other fuels, although the timings change between fuels. This is summarised in table 8.1, where the mean total ignition delay times obtained from the 20 tests carried for each fuel and distance are presented.

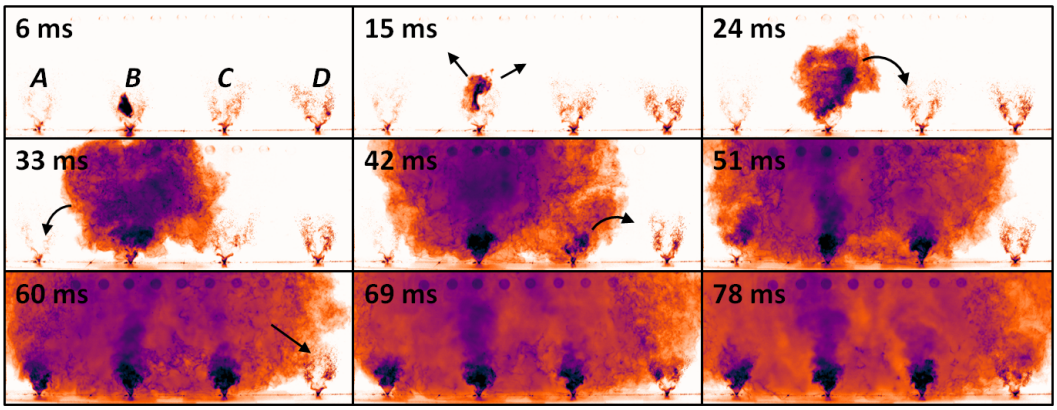

Figure 8.3: Ignition sequence for n-heptane and $d = 15$ cm. High-speed spontaneous flame emission images. Injectors are labelled A to D.

d (cm)	**n-heptane**	**n-decane**	**n-dodecane**	**kerosene**
9	46.75	42.76	53.33	56.11
13	67.49	65.76	70.33	80.51
15	85.97	74.03	81.71	91.61
18	77.14	84.87	99.20	110.55

Table 8.1: Mean total ignition delay times for each configuration. All values are in ms.

Two different propagation mechanisms have been identified from these observations: the radial mechanism for short inter-injector distances ($d = 9$ and 13 cm) and the arch mechanism for large distances ($d = 15$ and 18 cm). A glance at other investigations reveals the following:

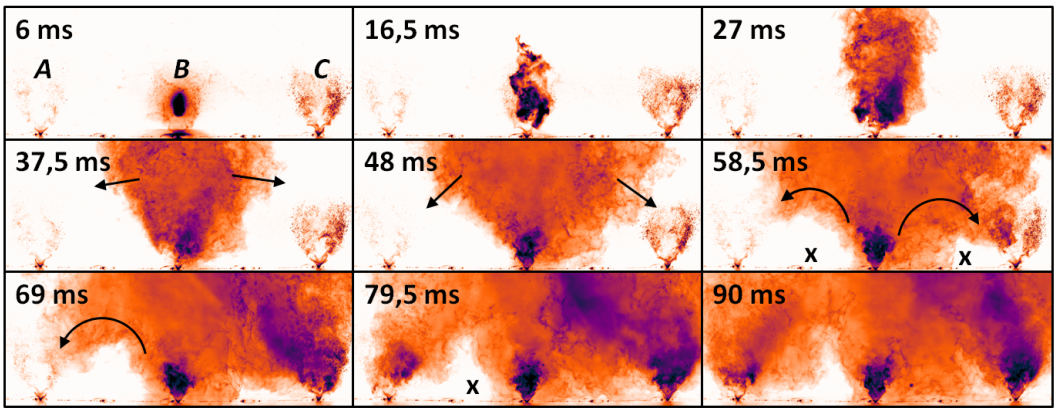

Figure 8.4: Ignition sequence for n-heptane and $d = 18\ cm$. High-speed spontaneous flame emission images. Injectors are labelled A to C.

- These two flame propagation mechanisms were already identified and analysed for gaseous non-premixed flows in [73, 89, 90] where the influence of the inter-injector distance on the velocity field and on the equivalence ratio was evaluated and injectors were said to be connected for $d_{crit} < 16\ cm$ and independent for $d_{crit} > 16\ cm$. This critical d_{crit} value is close to the one in the present study ($13 < d_{crit} < 15\ cm$) but remains slightly higher. Interactions between flow velocity fields were studied by [73] in gaseous flow. The variation of parameter d modifies the velocity field and the mean equivalence ratio fields (see Chapter 7). A narrowing of the IRZ and an increase of the penetration height of the swirling jet were observed for growing values of d. In [90], the authors showed that the IRZ was larger for short d and smaller for large d, as we observe here; but a complete disappearance of the IRZ for long distances was not reported, diverging from the present study. Comparing the equivalence ratio, in [90] it was observed to be very homogeneous even close to the injectors and to vary in the injector region, however, local ϕ varies much more intensely in the present study. This is explained by the presence of fuel droplets, which follow different trajectories inside the chamber and deposit fuel vapour at regions that are inaccessible to a gaseous fuel injection. They also noted the acceleration of the flame caused by the thermal expansion of the burnt gases. This was analysed in detail by Philip [99], who said that the volumetric expansion of the gases behind the flame is of major importance and enables the flame fronts to propagate at higher velocities than its characteristic turbulent

flame speed.

- In a linear multi-injector facility (gaseous, non-premixed), [92], Machover and Mastorakos found that injector-to-injector flame propagation takes place through bridges of positive flammability factor values (F). They highlighted the importance of the role of the IRZ in flame propagation, fact that is not observed in the present investigation. This is logical provided that the mixture fraction grew towards the centre of the injector where the gaseous fuel was injected. Their F maps revealed maximum values in the IRZ for axial stations higher than $z = 10\ mm$. The same reasoning that for [90] can be now made: the introduction of sprays expelling fuel droplets at a certain angle yields a completely different local equivalence ratio, hence F distribution. In [92], the flame propagation was said to travel from one IRZ to the next; here it would be rather from spray branch to spray branch since there regions boost flame speed through beneficial ϕ pathways. As a curiosity, they performed sparking experiments and found that sparks located in the bridges connecting injectors implied misfiring.

- In an annular non-premixed [91] and premixed [93] multi-injector facility, Machover and Mastorakos found that the ignition speed increased with the number of burners and with the global equivalence ratio. They said that the flame propagation was driven by favourable local conditions and they reported the flame to first propagate downstream first and to be captured by the IRZ of the following burner generating a "sawtooth" pattern. The use of swirlers favoured the "sawtooth" behaviour, which was nearly suppressed in configurations without swirl. Minimum and maximum inter-injector distances were $d = 29.5\ mm$ and $d = 44\ mm$, much smaller than ours. For small distances we do not find a "sawtooth" propagation pattern. This would rather resemble more to our **arch propagation mechanism** but this only occurs at long injector-to-injector distances. A possible explanation is the difference in the flow nature: again the use of sprays is demonstrated to modify significantly the mixture fraction repartition and, thus flame propagation mechanisms.

- In the present configuration, spray droplets add a new variable to the connection between neighbouring sprays and stratify even more the mixture.

Connection bridges of higher equivalence ratios can be found in two-phase flows (see Chapter 7). Other flame propagation studies [88, 97] performed in MICCA and MICCA-Spray were done in gas-phase and two-phase flow respectively. The injector-to-injector distance here was not varied for neither and ignition was evaluated at high wall temperature ($T = 900\ K$). In [97], dodecane and n-heptane were used as the liquid fuels and propane for gas-phase conditions. Here, authors identify an ignition phase as "the arc phase" referring to a convecting reaction zone left behind the ignition of the first injectors until it exits the height of the chamber (200 mm). This must not be mixed up with the **arch propagation mechanism** described in the present work. In fact, the images presented in [97] clearly reveal the direct radial propagation mechanism proposed here, consolidating the present text, provided that the injector-to-injector distance in these studies was fixed to 6.9 cm.

These observations prove the existence of a switching phenomenon between two different flame trajectories but until now there are no investigations in spray flows of the reasons behind this behaviour. This is further detailed in Fig. 8.5, where the mean propagation speed of the flame is plotted for each d and for each fuel. This mean propagation speed was calculated dividing the longest distance to ignite by the mean total ignition delay time. For clarity, the mean total ignition delay time is the time at which the last ignited injector is totally ignited (mean from the 20 trials using the high-speed images); the longest distance to ignite is the horizontal distance from the spark plug to the last ignited injector. This is a practical manner of comparing the ignition performances of the different investigated conditions; otherwise, ignition delay times for different distances to ignite are not comparable. Error bars in the chart indicate the standard deviations (estimated from the 20 trials per studied case). Looking at Fig. 8.5, two different behaviours can be identified with a change of slope in the tendencies shown by all fuels. In general, all fuels reveal a very low or nil variation of the mean propagation speed with d for short inter-injector distances, where the radial propagation mechanism takes place. This behaviour then switches for $d = 15$ and $d = 18\ cm$ to a strong dependency of the mean propagation speed on the injector-to-injector distance, representing the arch propagation mechanism. This break in the slope seems logical because when the flame propagates between injectors forming an arch it travels a longer distance that may be proportional to

d. Concerning the different fuels, in general kerosene shows the lowest ignition speeds, followed by n-dodecane and n-heptane; n-decane presents the highest propagation speeds. The laminar burning velocities of the different fuels are very similar to each other (provided at nominal conditions in Table 2.4 of Chapter 2). The differences in volatility between the fuels are much higher and, therefore, this should be the predominant effect. In [97], different equivalence ratios, powers and flow velocities were used while investigating two-phase ignition for small d values ($d = 6.9\ cm$) in an annular chamber of $L \approx 1.1\ m$. This was performed at a constant wall temperature of $T = 900\ K$, obtaining ignition delay times between 20 and 50 ms. These times cannot be compared to the ones obtained in the present study, which would give extrapolated times of ≈ 176 to 220 ms for a distance of $L \approx 1.1\ m$. Indeed, parameters between both investigations differ too much, notably the internal wall temperature, which is $T \approx 360\ K$ here). Still, in [97], an increase of $\approx 21\%$ was observed on delay times for dodecane compared to n-heptane. In the present work, n-dodecane delay times show an increase of $\approx 14\ to\ 29\%$ with respect to n-heptane, indicating a similar behaviour.

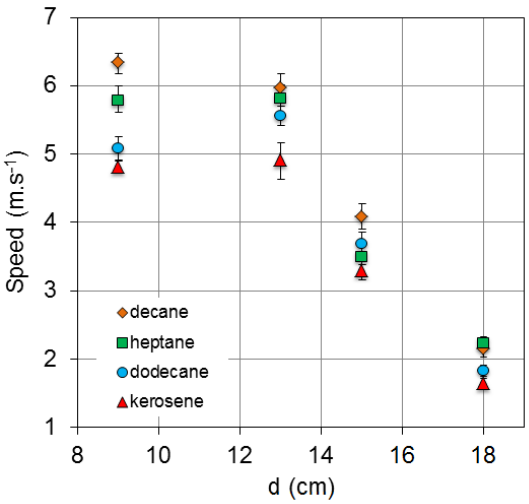

Figure 8.5: Mean propagation speed for each injector-to-injector distance for each fuel. Error bars indicate the standard deviation.

8.1.2 Relationship with the non-reacting local flow properties

Flame propagation is governed by the local properties of the flow, namely by the aerodynamics and by the mixture properties. The results discussed in the previous chapter provide an explanation of the switching between the two propagation mechanisms described above. Aerodynamically, we could distinguish $d = 9\ cm$ from the other configurations provided that axial velocities in the inter-injector region (IIR) are generally positive here and negative for the other values of d. Under this scope, $d = 13\ cm$ should eventually exhibit an arch-type propagation mode, but actually it does not. A possible explanation for this is the spray opening, which is 80^o (40^o from the axial line for each spray branch) independently of the injector-to-injector distance. This brings large inertial droplets into the top part of the inter-injector region enriching it in fuel vapour and enabling a radial flame propagation mechanism to take place at $d = 13\ cm$. The aerodynamics change for long injector-to-injector distances and, hence, modify the mixture formation. It is very probable that, for long injector-to-injector distances, there does not exist a complete flammable pathway directly between the branches of two adjacent injectors. This happens the majority of the time and, hence, impedes the direct flame propagation. This explains why the flame cannot propagate at low axial stations between injectors. When this happens, the flame finds an alternative path from the top forming an arch between neighbouring branches. This mechanism takes place thanks to the thermal expansion of the hot gases, which push the flame fronts onto the adjacent sprays from the top. After this, the flame finds the neighbour spray branch and descends completing the arch. For short d distances, the flame propagates actively through the inter-injector region because the equivalence ratio is high enough and the reactants are usually premixed. In addition, the effect of an increased presence of fuel droplets in the IIR enhances the existence of punctual rich mixtures, which strongly increase laminar flame speeds and, thus, propagation velocity. Discussion about the antagonist effects of droplets remains open but the analysis performed in Chapter 5 section 5.5 suggests that in the multi-injector burner conditions, the presence of droplets is still beneficial.

8.1.3 Analysis of high-speed tomographic images

High-speed tomographic images of the igniting flow seeded with silicon oil droplets were recorded for PIV analysis. Only n-heptane was used as the fuel here; Fig 8.5 proves that the behaviours of the different fuels are similar, being the dominating variable the injector-to-injector distance. The flame propagation evaporates the seeding droplets quasi-instantly leaving a marker of an isothermal line that is very close to the flame front position. These images were used for PIV calculations and results are presented in section 8.3 but more information can be extracted. This section is devoted to the analysis of the isothermal line (binarised gradient images) representing the flame front properties.

Using a minimum filtering, a level threshold and a posterior 2-D gradient calculation, the flame contour was extracted from the raw images and the leading edges of the flame were identified at the top and bottom of the investigation window, so as to track the flame front position and dynamics. Figure 8.6 illustrates the isothermal line evolution in a 3-image sequence for $d = 9\ cm$ on the left and $d = 13\ cm$ on the right. Time between frames is 5 ms. Near injectors, the flame detection is slightly biased by the presence of fuel droplets intensely scattering light. These images give information on the flame wrinkling and on the propagation. Any point could be selected as a leading edge for the investigation of the flame dynamics: here, the highest and the lowest parts of the flame front were selected for this and are marked on the images with white squares. There are obviously 3-D propagation effects that cannot be accounted for in this analysis. Figure 8.7 presents the corresponding binarised gradient images for $d = 15$ and $d = 18\ cm$ with the same timings. Compared to Fig. 8.6, the flame propagation is slower and the flame front appears to be less wrinkled.

The wrinkling factor of the flame is a parameter that explains the boost of the burning velocity from a laminar to a turbulent flame. In this work, the wrinkling factor is defined as the ratio between the length of the detected flame front and the straight length between the top and bottom flame leading edges. Given the potential error of the calculation due to non-suppressed droplets near injectors in the images, this wrinkling factor must be used carefully and only a qualitative description will be made. Figure 8.8 illustrates how flames at $d = 15$ and $d = 18\ cm$ are generally less wrinkled than flames in shorter injector-to-injector configurations. Moreover, $d = 9$ and $d = 13\ cm$ show each an outstanding peak

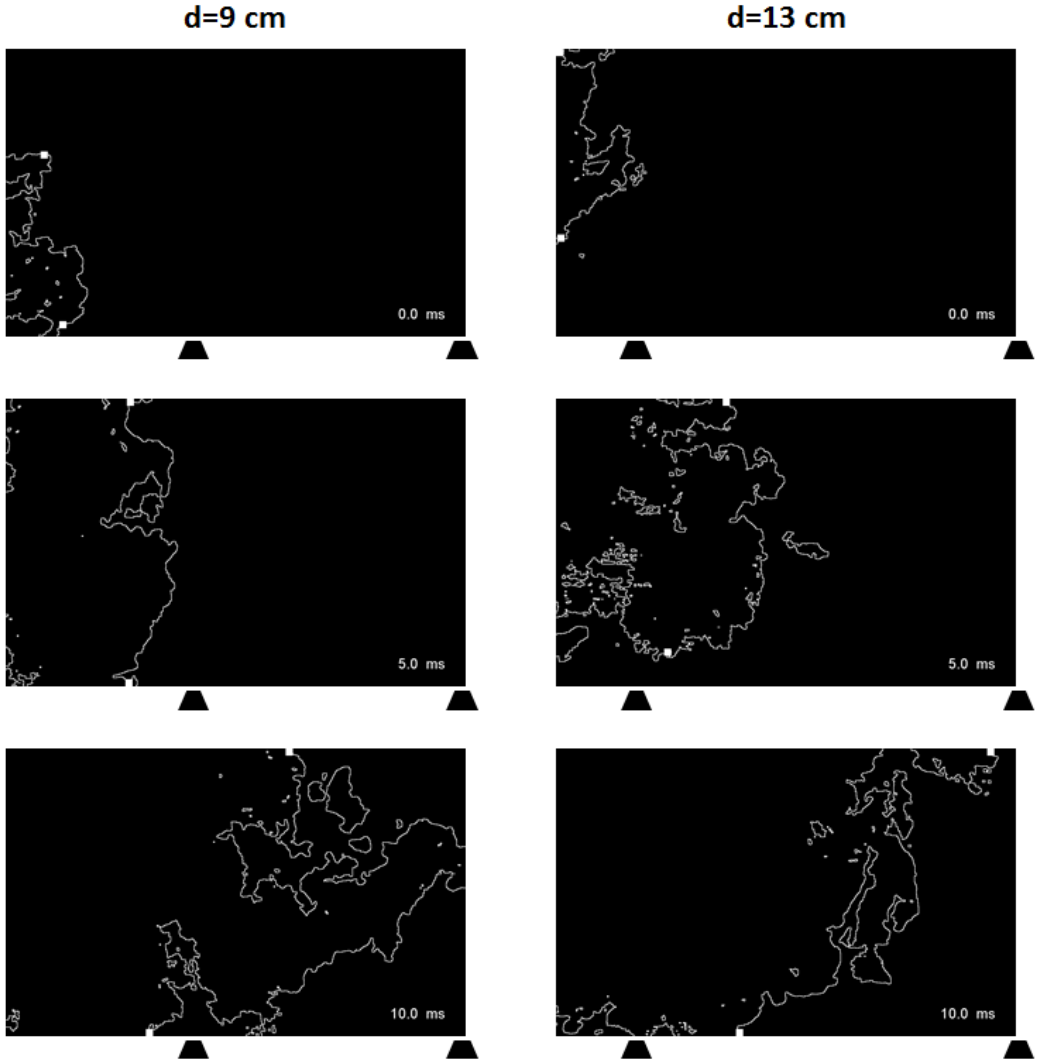

Figure 8.6: Propagation sequence over 2 injectors of the isothermal line marking the flame front. White squares indicate the detected top and bottom flame positions (TPF and BFP). Left $d = 9\ cm$. Right $d = 13\ cm$.

in the wrinkling factor due to 3-D effects that make a second flame branch appear through an azimuthal trajectory burning preferentially the right branch (richer mixture) of the fuel spray. This effect can be clearly observed in Fig. 8.13 for $d = 9\ cm$ at $t = 15.8\ ms$ and for $d = 13\ cm$ at $t = 13.4\ ms$ and $t = 17\ ms$, where black zones appear to the right-hand-side of the injectors and are disconnected from the main black region that represents the burnt gases (Fig. 8.13 will be described below, in section 8.3). Initial elevated wrinkling factor values for $d = 15$ and $d = 18\ cm$ are related to the initial development of the flame

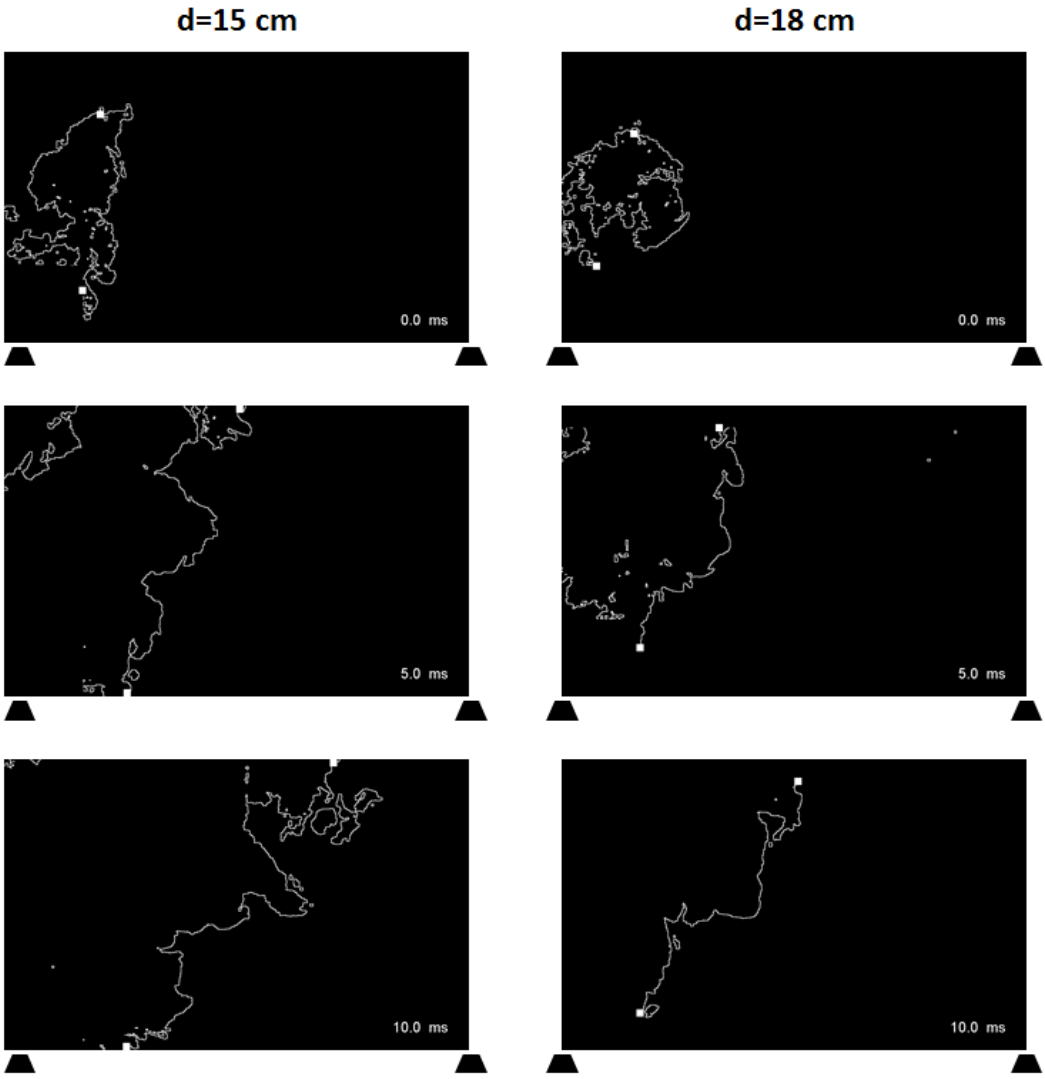

Figure 8.7: Propagation sequence over 2 injectors of the isothermal line marking the flame front. White squares indicate the detected top and bottom flame positions (TPF and BFP). Left $d = 15\ cm$. Right $d = 18\ cm$.

with a right and a left-hand-side propagation fronts, until the left front exits the images. The increased wrinkling for small injector-to-injector distances partly explains the faster propagation velocity in these cases. Signals in Fig. 8.8 cannot be compared to each other in timing terms because they are not synchronised with any common event. Another main contribution to flame wrinkling is the turbulence of the flow. Figure 7.2 from the previous chapter demonstrates that shorter inter-injector distances generate more turbulent kinetic energy (k) in the

IIR because neighbouring air jets come closer. For instance, at $z = 60\ mm$ in the centre of the IIR the $d = 9\ cm$ configuration presents ≈ 10 times more k than the $d = 18\ cm$ configuration at the same axial station at the centre of the IIR.

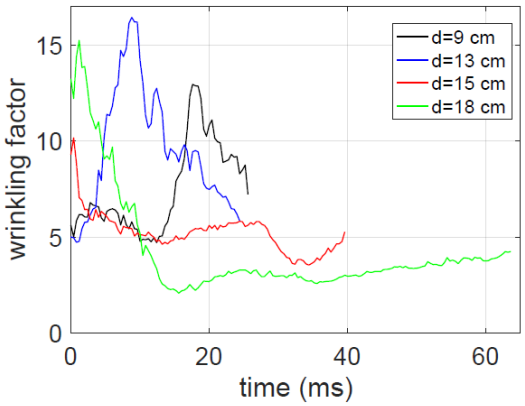

Figure 8.8: Wrinkling factor reported by the ratio between the flame length extracted from the isothermal line in the tomographic images and the shortest distance between the top and bottom leading edges.

Figure 8.9 (left) illustrates the temporal evolution of the horizontal position of the previously described leading edges of the flame front. In the figure, TFP stands for Top Flame Position (continuous lines) and BFP refers to Bottom Flame Position (dashed lines). Black and blue lines reveal steeper curves for short injector-to-injector distances while red and green show a slower flame propagation. In general, the TFP propagates at a higher velocity than the BFP, being this more remarkable for long inter-injector configurations because the BFP reveals very little movement due to the arch mechanism. The movement of the BFP can be, hence, used as a marker of the flame propagation mechanism. Differences between the TFP and the BFP can give information about the mean inclination of the flame during the ignition process. Figure 8.9 (right) indicates the temporal evolution of the mean flame front angle. This information can only be used qualitatively to stress that, for small values of d, the flat flame angle remains closer to 90^o (vertical flame front) a longer time showing strong fluctuations of the signal whereas, for large values of d, the flat flame angle descends quickly below 80^o and sustains this decreasing trend. Indeed, red and green lines reach 45^o representing a diagonal flame front towards the end of the propagation along the inter-injector region (IIR). The flat flame angle is more

representative of reality for $d = 15$ and $d = 18$ cm because the flame fronts are less wrinkled and, thus, closer to a flat flame. This also highlights the importance of the 3-D propagation of the flame for the short d configurations presenting the radial mechanism. For instance, in the bottom left image of Fig. 8.6 ($d = 9$ cm at $t = 10$ ms) the portion of flame situated to the right-hand-side of the first injector is generated by a flame propagation in the direction perpendicular to the page. This part cannot be taken into account by Fig. 8.9 (right) and it is, however, the most active part of the flame, proving that the presence of fuel droplets represents globally a benefit in this burner.

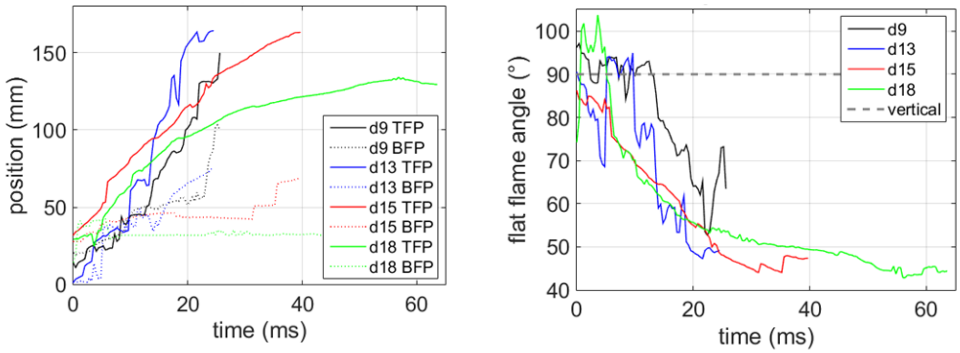

Figure 8.9: Left: temporal evolution of the TFP and BFP for each d. Right: temporal evolution of the angle formed with the horizontal line by the straight line joining the TFP and the BFP, named flat flame angle.

Analysing only the TFP does not account for the 3-D effect just mentioned above. However, the propagation of the top leading edge was further investigated. The instantaneous velocity of the TFP was calculated between images for short time steps throughout the entire recorded flame propagation in the visualisation window. The mean and standard deviation of these values were calculated. This is illustrated for each injector-to-injector distance in Fig. 8.10. Despite having wide standard deviations, the mean velocities show exactly the same trend as the one described before in Fig. 8.5. Due to an excessive wrinkling of the flame front, the automatic detection of the TFP was more difficult in small d configurations, yielding larger standard deviations than long d configurations. The mean velocities calculated for $d = 9$ and $d = 13$ cm are slightly underestimated with respect to the ones obtained in Fig. 8.5 because the wrinkling and the 3-D effects are not well represented by the movement of the TFP. Nevertheless, it is

very reassuring to find very close velocity values for all cases and, moreover, the break of slope when switching mechanisms.

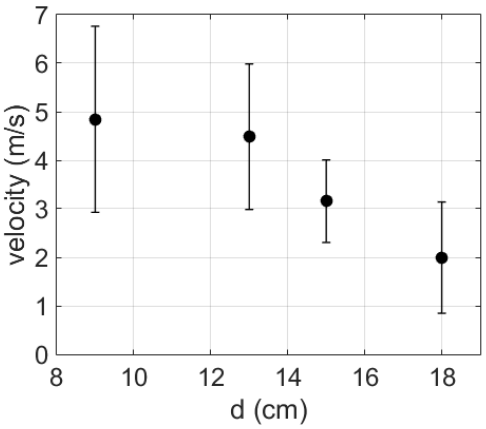

Figure 8.10: Mean flame propagation velocity extracted from the top leading edge of the isothermal line in the tomographic images for PIV. Bars indicate the standard deviation of the instantaneous velocity.

8.2 Pressure Signal During Ignition

The temporal evolution of the pressure signal describes the ignition process from a different point of view. Pressure signals resemble to those obtained in the single-injector burner for ignition Phases 2 and 3. Figure 8.11 (left) illustrates (in black, on the right axis) the dynamic pressure signal for an individual ignition test in the multi-injector chamber ($d = 9\ cm$, n-decane), with the characteristic initial vigorous fluctuations generated by the spark ($t < 10\ ms$). Coloured signals on the figure represent the integrated light intensity of the spontaneous flame emission in a square region placed over each of the injectors. The reader is reminded that the spark was triggered at injector 2. The latter shows a red initially decreasing signal due to the saturation of pixels by the intense emission of the spark. At $t = 7\ ms$ the integrated light intensity begins to grow indicating a steady ignition of injector 2. This is accompanied by a slight increase in the pressure signal generating a local maximum. Neighbouring injectors (1 and 3), in cyan and dark blue also register the intense spark light at short timings. The evolution of the dynamic pressure in the multi-injector differs from the one in the single-injector because the latter only presents one pressure peak and the former

contains as many local pressure peaks as injectors in the system. However, there exists always a larger pressure rise that is characteristic of the injector-to-injector configuration and that remains very repeatable. In Fig. 8.11 (left) this strong pressure peak is reported at $t = 22\ ms$ and it is perfectly coincident with the ignition of the second ignited injector (inj. 3). Injectors 1 (cyan) and 4 (green) are ignited simultaneously and in third place and are also coincident with a pressure peak close to $t = 28\ ms$. Injector 5 (magenta) is ignited in last place generating a very small pressure rise. The dynamic pressure then stabilises at $t \approx 45\ ms$, matching the timing described for $d = 9\ cm$ and n-heptane in table 8.1 in section 8.1.1.

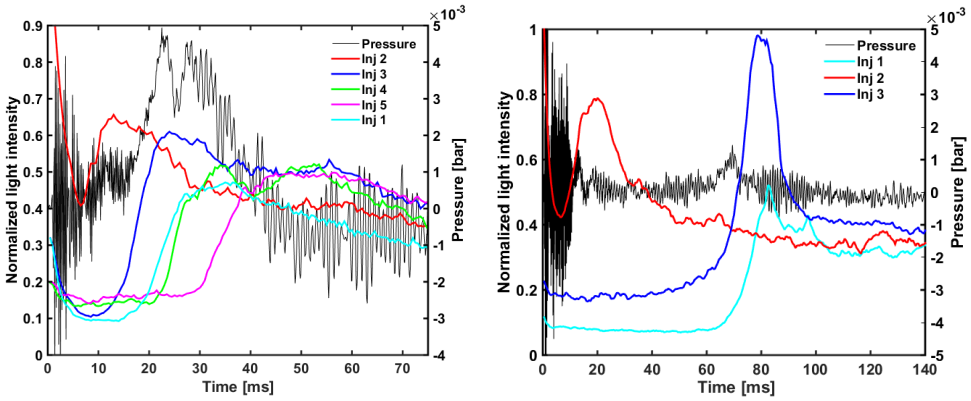

Figure 8.11: Temporal evolution of the dynamic pressure in the chamber and of the light intensity in each injector region for one ignition event at $d = 9\ cm$ (left) and another ignition event at $d = 18\ cm$ (right). The fuel used was n-decane.

Figure 8.11 (right) describes the temporal evolution of the pressure in the chamber and of the light intensity in each injector region for n-decane and $d = 18$ cm. While the spark pressure signal remains similar to that of Fig. 8.11 (left), the rest of the pressure signal is remarkably reduced: the maximum pressure peak is ≈ 5 times weaker. This is directly related to the power of the burner since the total fuel flow in the chamber is reduced by a factor of 3/5, but also, the longer ignition delay time suggests a less powerful heat release due to a reduced flame propagation velocity. The dynamic pressure reveals a local peak with the ignition of injector 2 (red), which is completed at $t = 20\ ms$. The ignition of injectors 1 (cyan) and 3 (dark blue) begins simultaneously at $t = 65\ ms$, as well as a rise in pressure. This time the pressure peak ($t = 70\ ms$) is reached before the luminosity maximums ($t \approx 80\ ms$) but remains coupled to these events. The

pressure then stabilises at about $t = 100\ ms$ for this case.

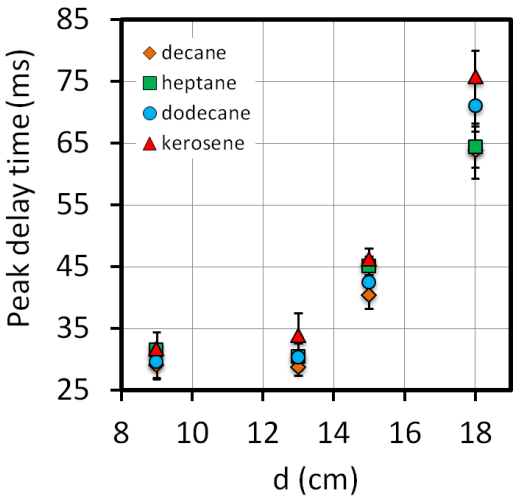

Figure 8.12: Mean delay times of the ignition pressure maximums for each fuel and each d. Error bars indicate the standard deviation.

For each of the 20 ignition tests carried per d and fuel, the position of the maximum pressure peak was extracted and the mean and standard deviations were calculated for each case. Figure 8.12 illustrates a plot of these mean (markers) and standard deviation values (error bars) for each case, similarly to Figs. 8.5 and 8.10. The trend described along this chapter is found once again. Short inter-injector distances appear to be quasi-independent of d and long spacings show a quasi-linear dependence of the peak delay time on d, highlighting the already mentioned break in slope. This pressure peak delay time is somehow characteristic of the second ignited injector and, therefore, is affected by the flame propagation in one inter-injector region. This explains the correct identification of the switching between the radial and the arch mechanisms. Regarding the different fuels, the kerosene yields the slowest timings while the n-decane yields the fastest and differences between fuels are more remarkable at long injector-to-injector distances. This is coherent with Fig. 8.5 and with the observations in [97].

8.3 Flame-Driven Droplet and Mixture Migration Effect

During the flame propagation, the thermal expansion of the burnt gases induces a velocity on the fresh mixture and droplets in front of the flame brush. This has been observed in gaseous configuration by [99] and in two-phase flows by [98]. In this work, tomographic HS-PIV image pairs of the air seeded with silicon oil droplets and fuel droplets during the passage of the flame supply interesting and exploitable information. The flame front evaporates quasi-instantly the seeding droplets, as detailed before (section 8.1.3). PIV cross-correlation calculations performed on the fresh mixture side of the flame provide instantaneous velocity fields weighted by the luminosity of the droplets meaning that, depending on the fuel droplet concentration and size, the resultant vectors describe a behaviour between the motion of the liquid and the gas phase.

Figure 8.13 illustrates a sequence of three instantaneous velocity fields for $d = 9\ cm$ (left) and for $d = 13\ cm$ (right), coloured by the radial velocity. The first velocity field shows a non-reacting flow, just as the one described in Figs. 7.1 and 7.2 of Chapter 7. When the flame approaches the flow ($t = 11.8\ ms$), entering from the left, the fresh mixture accelerates towards the right-hand-side with peak velocities over 5 $m.s^{-1}$ for the case of $d = 9\ cm$. The last field at $d = 9\ cm$ ($t = 18.8\ ms$) reveals that all the fresh mixture is strongly affected and a transport effect takes place, enhancing mixing and possibly making any unfavourable regions in terms of ϕ disappear. The configuration at $d = 13\ cm$ yields a very similar behaviour to $d = 9$, with an acceleration of the flow in the entire investigated domain.

Figure 8.14 describes the same for $d = 15$ and $d = 18\ cm$. For $d = 15\ cm$, a flow acceleration can be observed, but only on the top part of the visualization window, and it is less vigorous than for shorter injector-to-injector distances. The case at $d = 18\ cm$ reveals a suppression of the blue colours meaning that there is a relative acceleration of the flow in front of the flame, but the effect here is not strong enough to induce a significant migration of rich mixture towards lean regions.

Philip [99] (in gaseous) and Lancien [98] (in two-phase flow) also observed this characteristic acceleration ahead of the flame. Both use the mass conservation to explain this effect: the sudden change in volumetric expansion across the flame

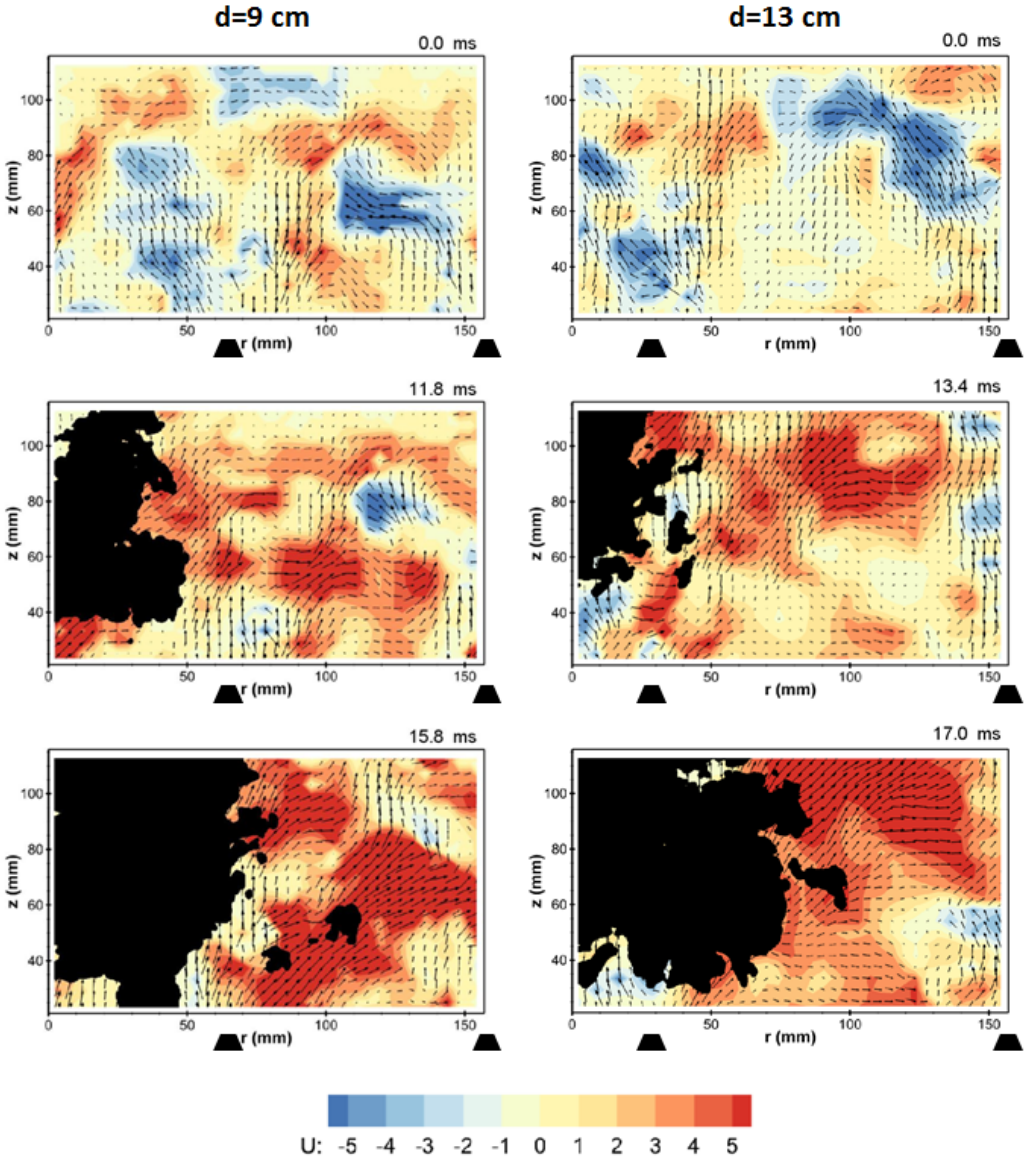

Figure 8.13: Time-resolved velocity fields of the igniting flow for $d = 9$ and $d = 13$ cm. Black zones represent the burnt gases. Colour maps represent the radial velocity (red to the right and blue to the left).

induces an augmentation of the velocity of the burnt gases which, in turn, propel the fresh gases immediately ahead of the flame. This can modify the issuing air jet geometry and the droplet trajectories, hence impacting the equivalence ratio locally. This effect could bring flammable mixture to regions initially non-flammable. Modification of the liquid field ahead of the flame has also been

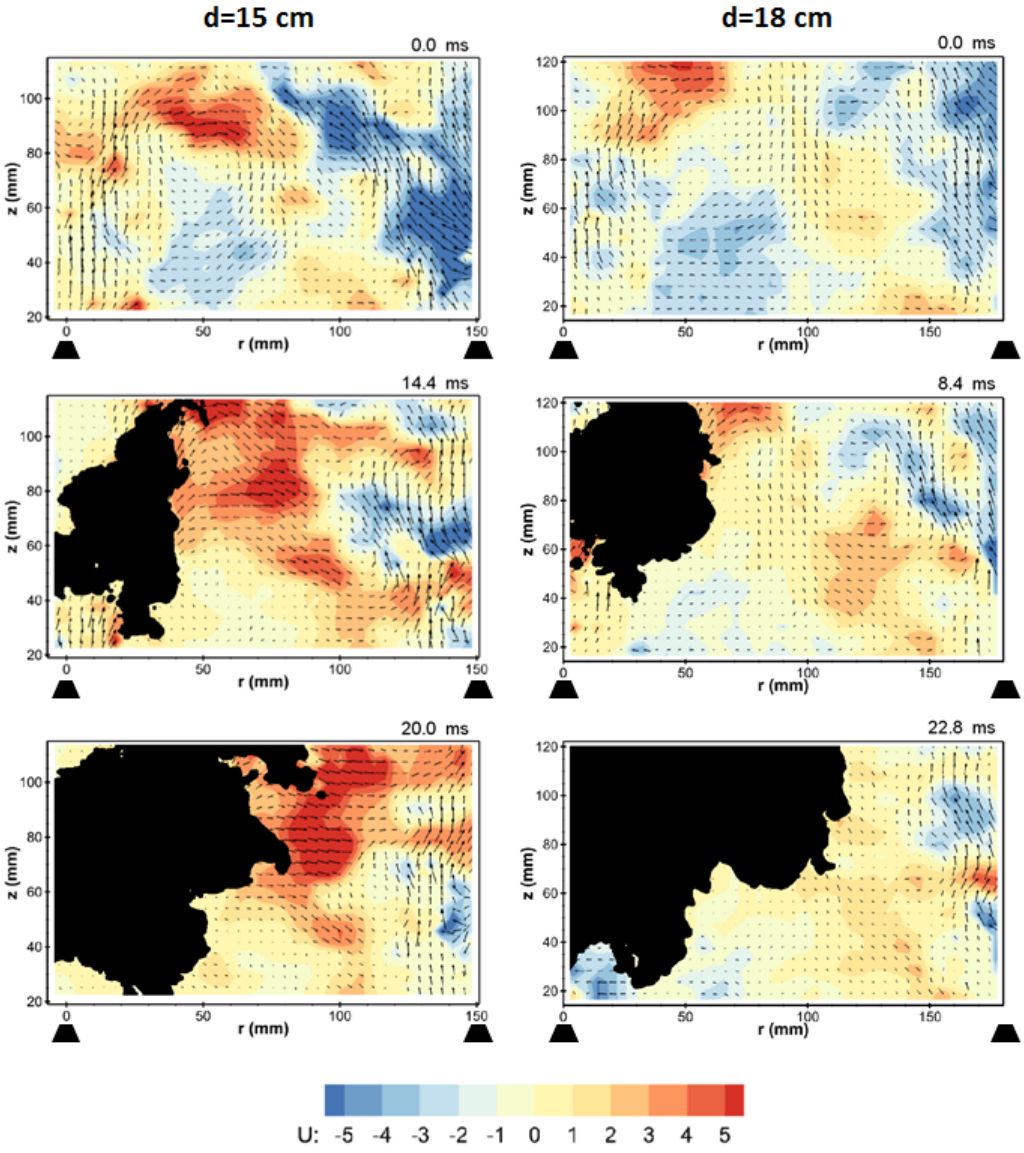

Figure 8.14: Time-resolved velocity fields of the igniting flow for $d = 15$ and $d = 18$ cm. Black zones represent the burnt gases. Colour maps represent the radial velocity (red to the right and blue to the left).

observed. Lancien et al. [98], in an LES of the MICCA-Spray facility, discovered that enhanced evaporation close to the propagating flame front yielded very small droplet diameters ≈ 3 μm and $\phi \approx 1$ in the flame front. These droplets disappeared by the $c = 0.1$ iso-line and the Takeno index revealed the combustion to be dominated by the premixed regime.

Conclusion to Part IV

Chapters 7 and 8 describe the effect of varying the injector-to-injector distance on the aerodynamics of the flow, on the mixture formation and on Phase 4 of aeronautical ignition.

Chapter 7 details the HS-PIV and Toluene-PLIF results in the CLSSB multi-injector facility providing an analysis on the modification with d of the velocity fields and of the equivalence ratio fields of the non-reacting flow around the injectors and in the inter-injector region (IIR). The flow motion in the IIR is proven to change outstandingly when increasing d, as well as the inner recirculation zone (IRZ). The former passes from a positive velocity to a negative velocity when increasing d and the latter shows strong negative velocities for small d values that become positive for increasing d (the IRZ disappears or is pushed far away when increasing d.) This has a very important effect on the transport of fuel vapour in the chamber yielding a homogeneous flammable IIR for small d and a heterogeneous non-flammable IIR for long injector spacings. The equivalence ration in the IRZ is also altered and becomes higher and higher for increasing values of d. The ensemble of these behaviours tend to connect neighbouring injectors for short spacings an to disconnect them for large spacings.

Chapter 8 gathers an analysis from different viewpoints of Phase 4. Firstly, the HS-visualisation images of the spontaneous flame emission during its propagation in the chamber enable to identify the radial mechanism for short inter-injector distances and the arch mechanism for long distances. A mean propagation velocity characteristic of each d was obtained from the images and reveals different trends for each propagation mechanism. Secondly, high-speed tomographic images for PIV during ignition enabled to extract an isothermal line representative of the flame front dynamics and wrinkling. Indeed, short inter-injector distances yielded higher wrinkling factors and higher mean propagation velocities than long spacings. In third place, the dynamic pressure was analysed

and compared to the luminosity of each injector zone and the mean pressure peak delay was compared between different $d's$, revealing again a two-slope function of d, thus, a switching between flame propagation mechanisms. To finish with, HS-PIV calculations during the flame propagation uncover the effect of the flame on the fresh mixture, which is pushed and forced to migrate in the direction of the propagation. This is very evident for short injector-to-injector distances and disappears for increasing d values.

To finish this part, four sketches are proposed to summarise the main conclusions extracted in chapters 7 and 8. Figure 8.15 describes the behaviour of the non-reacting flow for short injector-to-injector distances and it is followed by Fig. 8.16, representing the flame propagation in such conditions and indicating the specificities of the **radial propagation mechanism**.

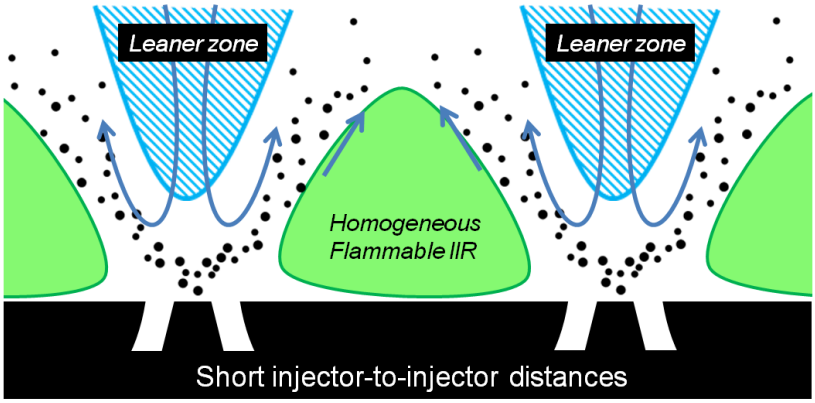

Figure 8.15: Sketch of the behaviour of the non-reacting flow for small injector-to-injector distances.

Figure 8.17 summarises the non-reactive flow properties under long injector-to-injector configurations. The flame propagation following the **arch mechanism** is then detailed in Fig. 8.18, as well as the properties of the igniting flow.

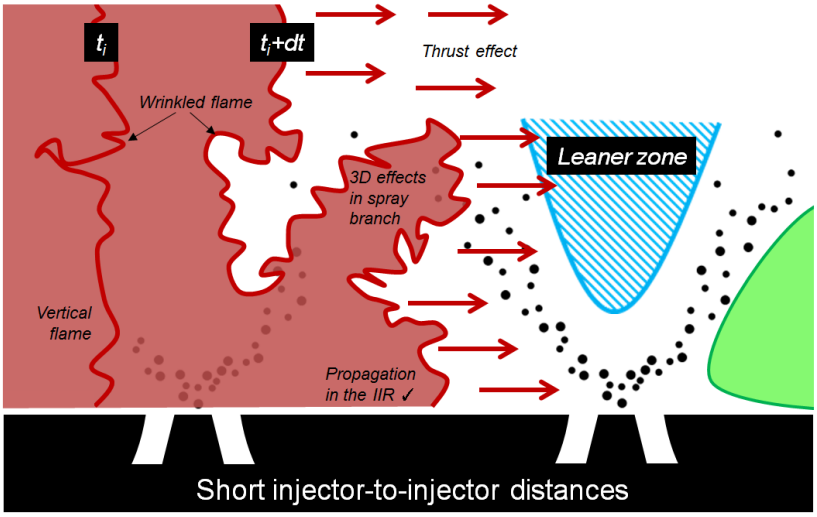

Figure 8.16: Sketch of the behaviour of the flame propagation and of the igniting flow for small injector-to-injector distances: the **radial propagation mechanism**.

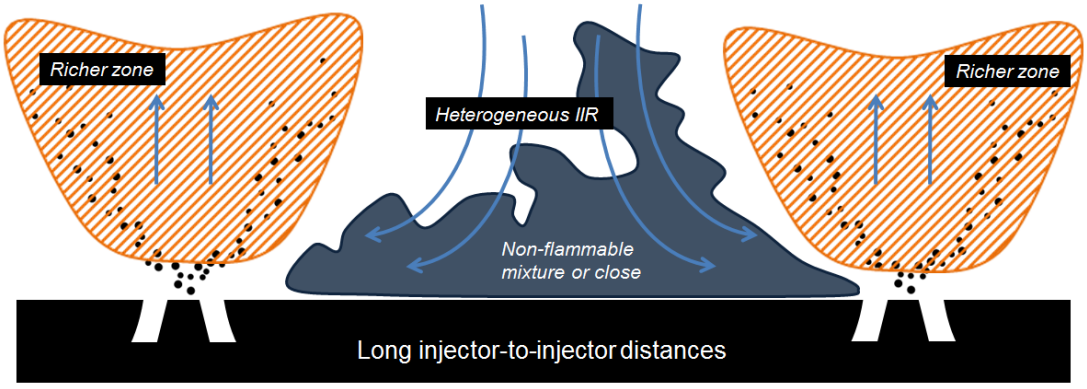

Figure 8.17: Sketch of the behaviour of the non-reacting flow for long injector-to-injector distances.

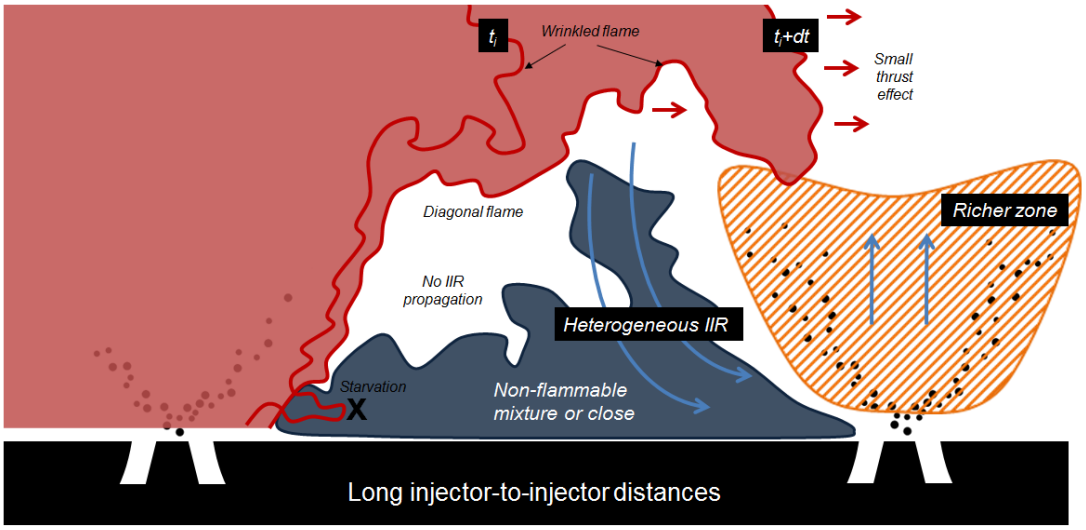

Figure 8.18: Sketch of the behaviour of the flame propagation and of the igniting flow for long injector-to-injector distances: the **arch propagation mechanism**.

Part V

CONCLUSION

Chapter 9

Conclusion and Perspectives

Contents

7.2 billion passengers are expected to travel in 2035, nearly doubling the aviation demand of 2016. Under such a growing market, environmental policies become more and more stringent and impose strong reductions of the pollutant emissions, especially of the nitrogen oxides (NO_x). In response to this necessity, combustion experts propose low-NO_x combustion chamber designs that work in lean combustion configurations. These new conditions can reduce the flame stability and in-flight flame-out events could become more frequent. For safety reasons, the certification of these new engines demands proven in-flight relight capabilities under controlled and safe conditions. Provided the difficulties of the engine reignition in high altitude, more realistic and simplified studies are needed to give new insight and improve the understanding of the critical multi-physical mechanisms that govern each of the aeronautical ignition phases, including the

sparking (Phase 1), the flame kernel development (Phase 2), the stabilisation of the first flame (Phase 3) and the lightaround (Phase 4). This thesis is an experimental investigation of ignition Phases 2, 3 and 4 in swirling, confined and atmospheric pressure conditions, involving lean, two-phase flows.

9.1 Conclusion

This work has been carried in the framework of the ANR TIMBER project and aims to extend the existing knowledge on aeronautical ignition in spray flows, moving towards more realistic conditions than what has been already covered by the state of the art. Despite the high complexity of aeronautical ignition and the large number of parameters involved in it, this process can be divided into the different characteristic phases mentioned above and described in detail in the introduction. The scope has been placed on the analysis of the mechanisms controlling each phase. Experiments concerning Phases 2 and 3 were carried in the KIAI-Spray single-injector facility and Phase 4 was tackled in the CLSSB multi-injector facility. A variety of optical, laser and conventional diagnostics was thoroughly applied to both burners to extract as much information as possible, resulting in a database useful for the industry and for numerical model validation. The main conclusions of these works are given in the following sections.

9.1.1 Analysis of Ignition Phases 2 and 3

The first part of this work consisted in describing the non-reacting flow properties in the KIAI-Spray single-injector burner in terms of the carrier and dispersed phases and the mixture formation. This was a previous necessary step to assessing Phase 2. Concerning the latter, the ignition probability map of the chamber was evaluated, as well as the flame kernel shape and evolution for different sparking locations. Different kernel extinction mechanisms and ignition mechanisms with characteristic timings and locations were proposed and demonstrated to be universal. To finish this part, Phase 3 was addressed by the description of the flame stabilisation, the stabilised flame and the reacting flow. The observations to highlight are:

- The local non-reacting flow varies very strongly in time and space and it can be aerodynamically divided into the well-known IRZ, ORZ and JZ.

The JZ presents the highest airflow and droplet velocities and turbulent kinetic energies, resulting in high strain rate fluctuations sometimes too high to enable flame kernels to survive. The equivalence ratio fluctuations in the JZ range beyond high and low flammability limits providing alternating beneficial and detrimental mixtures for flame development. The IRZ reveals low ϕ and $F = 0$ in most of its domain. k shows low values at high axial stations but high values at low axial stations. The ORZ shows a $F \approx 1$ and low turbulence and velocities everywhere. The combination of these parameters is disastrous for ignition in the IRZ and slightly better in the JZ but optimum in the ORZ. This is completely backed by the ignition probability map. The correlations between ignition probability and F and ϕ are extrapolated to other studies.

- The properties of the flow in the exact spark location are important, but so it is the kernel trajectory. In the IRZ, flame kernels suffer from fuel starvation and often from turbulent strain. Conditions in the JZ sometimes enable ignition through the spray branch but others cause misfire either by downstream convection or by continuous or multiple shredding. In the top-limit of the ORZ, kernels are often broken into two diverging pieces: the one trapped in the ORZ usually survives. Kernels starting in the ORZ have more probabilities of yielding successful ignitions the more time they reside in it. The proposed extinction mechanisms move a step further in the description of the *second mode of ignition failure* that was proposed in [37], and together with the ignition mechanisms provide a new classification that can be extended to other experiments and simulations. A coupled investigation with several LES carried at CERFACS enables to deepen the analysis and demonstrates once again the benefits of two-way numerical-experimental collaborations.

- Flame stabilisation is marked by the kernel growth due to interaction with the spray branch. After this, the ORZ traps the flame and it swirls in a single-injector lightaround process until it anchors to the spray cone and then lifts. Maximum heat release is coincident with maximum pressure. LES results demonstrate the ability to reproduce the dynamics of the stabilised flame. As a curiosity and a potential future work, droplet-flame interactions are observed: droplets cross the flame fronts and enter regions

of hot gases in the ORZ.

9.1.2 Analysis of Ignition Phase 4

The second part of this work is devoted to the analysis of Phase 4 in the CLSSB multi-injector facility. The impacts of the injector-to-injector distance (d) and of the fuel volatility were evaluated. Four distances and four fuels were tested. The non-reacting flow was first investigated aerodynamically and in terms of local equivalence ratio. This enabled to explain the flame propagation mechanisms between injectors. The flame propagation was studied in terms of flame trajectory, flame topology, propagation velocities and dynamic pressures. The main conclusions here are:

- The non-reacting flow switches its aerodynamics and local mixture properties for short ($d < 14\ cm$) and long ($d > 14\ cm$) distances. Short distances present strong IRZ and open air jets merging with neighbouring jets. Spray droplet bridges also interconnect adjacent injectors. The flow velocity is positive in the IIR and brings rich mixture from the spray branches while mixture is leaner in the IRZ because it does not enter in contact with the spray branches. Long distances isolate the injectors aerodynamically and in terms of ϕ. The aerodynamics here are opposite: the IRZ is pushed downstream or disappears and the IIR experiences negative velocities. The fuel vapour is carried from the spray branches to the top of each injector (to the virtual IRZ) and the mixture descending from the top towards the IIR has poor interaction with droplets. In addition, the IIR reveals a heterogeneous ϕ with no straight or direct flammable paths between neighbouring injectors. The observed behaviour of ϕ differs from previous investigations on gaseous flows.

- Short distances reveal a radial propagation mechanism with highly wrinkled flames that develop in the entire IIR. Long inter-injector distances yield an arch propagation mechanism where the flame is unable to progress in the IIR; it must grow downstream and expand pushed by the thermal expansion of hot gases to then find a flammable pathway from the top to the next injector. Ignition delay times are much shorter for the radial mechanism. The mean flame propagation velocity is independent of d for small values

of d whereas it is inversely proportional to d for long distances. This was found via two different optical analyses and via the dynamic pressure signal. It is the first time that these switching mechanisms are observed in spray flows in near-aeronautical configurations.

- To finish, a thrust effect was observed to push the fresh mixture ahead of the flame front. This was much stronger for low d values covering all the injector vicinity, weaker for long injector-to-injector distances and merely nonexistent for very large distances.

9.2 Perspectives

The present study answers some of the key questions of reignition. However, it opens new ones and suggests the initiation of new works.

9.2.1 Database Extension

The applied experimental diagnostics have generated a multi-physical database of great utility for numerical studies. This database could be improved in several ways. For instance, the lowest axial station presenting reliable fuel droplet data is $z = 10\ mm$ because PDA cannot perform high quality measurements in too dense spray regions. Furthermore, PDA is a bad estimator of the volume or mass fluxes and this is a very interesting parameter both for simulations and for physical understanding. Other techniques are being evaluated, such as the Digital Holography, which shows promising results of precise flux and droplet concentration characterisation. Indeed, a high-speed version of the Holography technique could even characterise the spray fluctuating fields and be used simultaneously with the sparking to assess the effect of the spark on the droplets. Obtaining droplet temperatures would be another step in characterising the dispersed flow from which numerical studies would benefit, given the difficulty of evaporation models to thoroughly describe the reality. This would be feasible through the application of the Global Rainbow Technique (GRT), which has been already done in a very similar spray at CORIA [150, 151]. Despite the large literature background on minimum ignition energy studies, it would be advantageous to characterise ignition Phase 1 through spectroscopic measurements to characterise the evolution of radicals, atoms and molecules in the transition from

plasma to chemical reactions at different chamber regions, with different characteristic droplet sizes and concentrations. In this direction, the LIBS technique (Laser Induced Breakdown Spectroscopy) is being considered.

Another interesting investigation is to vary other parameters such as the swirl number and the flow velocity. This would yield different ignition probability maps and, hopefully, the same ignition and kernel extinction mechanisms in other chamber regions and with other characteristic times. Since the effect of the wall temperature was noted to be so important, a study of ignition at varying wall temperatures would uncover important information. It is reminded that realistic relight conditions present low wall temperatures. In a general way, processes involving such multi-physical situations would benefit from more high-speed and simultaneous diagnostics, as demonstrated by [150].

9.2.2 Improvement of Quantitative Equivalence Ratio Measurements in Two-Phase Flows

The limits of the Toluene-PLIF under heterogeneous spray flows have been described in chapters 3 and 4. The main problem is to discriminate sub-pixel droplets from the vapour phase in moderately dense spray zones. To do this, we can imagine the coupling of other techniques to the Toluene-PLIF simultaneously detecting the sub-pixel droplets. This would then enable to identify the biased pixels. Another possible solution is to reduce the field of view and focus on small regions in each of the zones of interest in the chamber, thus increasing the spatial resolution and reducing the sub-pixel droplet population. Performing inverse Tracer-PLIF could be an interesting approach: this implies mixing the tracer vapour with the air and injecting it through the co-flow. Fuel vapour would lower the fluorescence signal proportionally to its concentration and the problem of fluorescing sub-pixel droplets would be avoided.

An alternative to the PLIF technique on a tracer to quantify the mixture fraction or the equivalence ratio is the LIBS, which provides information on the concentration of the different species present in the laser-induced plasma.

9.2.3 Further Coupled Experimental-LES Analyses

Given that the joint experimental-numerical analyses have been so beneficial, it is planned to continue working in this direction to explore all the chamber

zones and the mechanisms identified by the experiments. As said above, LES would benefit from studies on Phase 1 since energy deposition models still do not master the energy, temperature distributions and typical plasma sizes and shapes at early instants. Simulations on ignition Phase 4 in the CLSSB are being now addressed at CERFACS.

9.2.4 Moving Towards More Realistic Relight Conditions

More complex facilities are necessary to evaluate the performance of real injector systems and more realistic chambers. These facilities become very complex in design, fabrication and operation because they need to provide access to optical and conventional diagnostics. Moving towards low pressures; low co-flow temperatures, which inhibit droplet evaporation; and low flow rates, which minimise atomisation, supposes a technological challenge. Indeed, impact of liquid on the walls and surface run-off is not desirable for the application of optical diagnostics and this must be solved without modifying the local flow properties in the chamber. The fifth phase of aeronautical ignition also needs investigation, this is the transition from the ignited chamber to nominal engine operating conditions. The APLAREP project has among its objectives to deal with such situations. Further configurations should include chamber walls with effusion holes and dilution holes to evaluate the impact of these on the flow, kernel and flame propagation both in single-injector and multi-injector facilities.

References

[1] B. A. Çeper. Use of hydrogen-methane blends in internal combustion engines. In *Hydrogen Energy-Challenges and Perspectives*. InTech, 2012.

[2] Rolls-Royce plc. *The Jet Engine*. 5 edition, 1986.

[3] R. von der Bank, S. Donnerhack, A. Rae, M. Cazalens, A. Lundbladh, and M. Dietz. Lemcotec: Improving the core-engine thermal efficiency. In *ASME Turbo Expo 2014: Turbine Technical Conference and Exposition*. American Society of Mechanical Engineers, 2014.

[4] A. H. Lefebvre. *Gas Turbine Combustion*. Taylor and Francis, 2nd edition, 1998.

[5] J. Ebner, P. Schober, O. Schafer, R. Koch, and S. Wittig. Modelling of shear-driven liquid wall films: effect of accelerated air flow on the film flow propagation. *Progress in Computational Fluid Dynamics, an International Journal*, 4(3-5):183–190, 2004.

[6] B. Rossow. *Processus photophysiques de molécules organiques fluorescentes et du kérosène applications aux foyers de combustion : applications aux foyers de combustion*. PhD thesis, Paris 11, 2011.

[7] R. W. Read. *Experimental Investigations into High-Altitude Relight of a Gas Turbine*. PhD thesis, University of Cambridge.

[8] C. Hughes and J. Gazzaniga. Low-speed wind tunel performance of high-speed counterrotation propellers at angle-of-attack. In *25th Joint Propulsion Conference*, 1989.

[9] J. M. Beer and N. A. Chigier. *Combustion aerodynamics*. Krieger Pub Co, Malabar, Fl, 1983.

[10] N. Syred, N. A. Chigier, and J. M. Beer. Flame stabilization in the recirculation zones of jets with swirl. *Proceedings of the Combustion Institute*, 13(1):617–624, 1971.

[11] G. Hannebique. *Etude de la structure des flammes diphasiques dans les bruleurs aéronautiques*. PhD thesis, Universite de Toulouse, 2013.

[12] P. S. Sanchez. *Modeling the dispersion and evaporation of sprays in aeronautical combustion chambers*. PhD thesis, Universite de Toulouse, 2012.

[13] D. Paulhiac. *Modelisation de la combustion d'un spray dans un bruleur aeronautique*. PhD thesis, Universite de Toulouse, 2015.

[14] C. F. Edwards and R. C. Rudoff. Structure of a swirl-stabilized spray flame by imaging, laser doppler velocimetry, and phase doppler anemometry. *Proceedings of the Combustion Institute*, 23(1):1353–1359, 1991.

[15] J. Apeloig. *Etude experimentale du role de la phase liquide dans les phenomenes d'instabilites thermo-acoustiques agissant au sein de turbomachines diphasiques*. PhD thesis, Universite de Toulouse, 2013.

[16] D. Bradley, P. H. Gaskell, X. J. Gu, M. Lawes, and M. J. Scott. Premixed turbulent flame instability and no formation in a lean-burn swirl burner. *Combustion and Flame*, 115(4):515–538, 1998.

[17] S. R. N. De-Zilwa, J. H. Uhm, and J. H. Whitelaw. Combustion oscillations close to the lean flammability limit. *Combustion Science and Technology*, 161:231–58, 2000.

[18] A. H. Lefebvre. *Atomization and Sprays*. Taylor and Francis, 1989.

[19] H. Albrecht, W. H. Bloss, W. Herden, R. Maly, B. Saggau, and E. Wagner. New aspects on spark ignition. Report 0148-7191, SAE Technical Paper, 1977.

[20] P. Seers. *Spark ignition: An experimental and numerical investigation*. PhD thesis, The University of Texas at Austin, 2003.

[21] B. Peterson, D. L. Reuss, and V. Sick. On the ignition and flame development in a spray-guided direct-injection spark-ignition engine. *Combustion and Flame*, 161(1):240–255, 2014.

[22] S. F. Ahmed and E. Mastorakos. Spark ignition of lifted turbulent jet flames. *Combustion and Flame*, 146(1–2):215–231, 2006.

[23] R. Maly and M. Vogel. Initiation and propagation of flame fronts in lean ch4-air mixtures by the three modes of the ignition spark. *Proceedings of the Combustion Institute*, 17(1):821–831, 1978.

[24] R. Teets and J. Sell. Calorimetry of ignition sparks. *SAE transactions*, 97:371–383, 1988.

[25] Guenther Von Elbe Bernard Lewis. *Combustion, Flames and Explosions of Gases*. Harcourt Brace Jovanovich Publishers, London, 1987.

[26] I. Glassman. *Combustion, 2nd Edition*. Academic Press, 1987.

[27] J. Rager. *Funkenerosion an Zündkerzenelektroden*. PhD thesis, Universität des Saarlandes, 2006.

[28] K. G. Moesl, K. G. Vollmer, T. Sattelmayer, J. Eckstein, and H. Kopecek. Experimental study on laser-induced ignition of swirl-stabilized kerosene flames. *Journal of Engineering for Gas Turbines and Power*, 131(2):021501–8, 2009.

[29] D. Mittinti and E. Dabora. Plasma jet ignition studies. *Proceedings of the Combustion Institute*, 20(1):169–177, 1984.

[30] P. D. Rooney. Laser versus conventional ignition of flames. *Optical Engineering*, 33(2), 1994.

[31] G. C. Gebel, T. Mosbach, W. Meier, and M. Aigner. Optical and spectroscopic diagnostics of laser-induced air breakdown and kerosene spray ignition. *Combustion and Flame*, 162(4):1599–1613, 2015.

[32] S. H. Lee, H. Do, and J. Yoh. Simultaneous optical ignition and spectroscopy of a two-phase spray flame. *Combustion and Flame*, 165:334–345, 2016.

[33] T.X. Phuoc and F.P. White. Laser induced spark ignition of ch4/air mixtures. *Combustion and Flame*, 119:203–216, 1999.

[34] T.X. Phuoc and F.P. White. An optical and spectroscopic study of laser-induced sparks to determine available ignition energy. *Proceedings of the Combustion Institute*, 29:1621–1628, 2002.

[35] D. Bradley, C. G. W. Sheppard, I. M. Suardjaja, and R. Woolley. Fundamentals of high-energy spark ignition with lasers. *Combustion and Flame*, 138:55–77, 2004.

[36] S. F. Ahmed. The probabilistic nature of ignition of turbulent highly-strained lean premixed methane-air flames for low-emission engines. *Fuel*, 134:97–106, 2014.

[37] E. Mastorakos. Forced ignition of turbulent spray flames. *Proceedings of the Combustion Institute*, 36(2):2367–2383, 2017.

[38] M. Boileau, G. Staffelbach, B. Cuenot, T. Poinsot, and C. Bérat. Les of an ignition sequence in a gas turbine engine. *Combustion and Flame*, 154(1):2–22, 2008.

[39] E. Mastorakos. Ignition of turbulent non-premixed flames. *Progress in Energy and Combustion Science*, 35(1):57–97, 2009. 0360-1285 doi: DOI: 10.1016/j.pecs.2008.07.002.

[40] A. D. Birch, D. R. Brown, and M. G. Dodson. Ignition probabilities in turbulent mixing flows. *Proceedings of the Combustion Institute*.

[41] M. Smith, A. D. Birch, D. R. Brown, and M. Fairweather. Studies of ignition and flame propagation in turbulent jets of natural gas, propane and a gas with high hydrogen content. *Proceedings of the Combustion Institute*, 21:1403–1408, 1986.

[42] S. F. Ahmed, R. Balachandran, T. Marchione, and E. Mastorakos. Spark ignition of turbulent nonpremixed bluff-body flames. *Combustion and Flame*, 151(1-2):366–385, 2007.

[43] C. Letty, E. Mastorakos, A. R. Masri, M. Juddoo, and W. O'Loughlin. Structure of igniting ethanol and n-heptane spray flames with and without swirl. *Experimental Thermal and Fluid Science*, 43:47–54, 2012.

[44] H. El-Rabii, K. ZÄHringer, J. C. Rolon, and F. Lacas. Laser ignition in a lean premixed prevaporized injector. *Combustion Science and Technology*, 176(9):1391–1417, 2004.

[45] A. Eyssartier, B. Cuenot, L. Gicquel, and T. Poinsot. Using les to predict ignition sequences and ignition probability of turbulent two-phase flames. *Combustion and Flame*, 160(7):1191–1207, 2013.

[46] S. R. Turns. *An Introduction to Combustion: Concepts and Applications*. McGraw-Hill, New York, 2000.

[47] D. R. Ballal and A.H. Lefebvre. A general model of spark ignition for gaseous and liquid fuel-air mixtures. *Proceedings of the Combustion Institute*, 18:1737–1746, 1981.

[48] Shy S. Liu C. Huang, C. and Y. Yan. A transition on minimum ignition energy for lean turbulent methane combustion in flamelet and distributed regimes. *Proceedings of the Combustion Institute*, 31:1401–1409, 2007.

[49] K. Rao and A. H. Lefebvre. Minimum ignition energies in flowing kerosine-air mixtures. *Combustion and Flame*, 27:1–20, 1976.

[50] J. L. Beduneau, B. Kim, L. Zimmer, and Y. Ikeda. Measurements of minimum ignition energy in premixed laminar methane/air flow by using laser induced spark. *Combustion and Flame*, 132(4):653–665. 0010-2180.

[51] S. S. Shy, C. C. Liu, and W. T. Shih. Ignition transition in turbulent premixed combustion. *Combustion and Flame*, 157(2):341–350. 0010-2180.

[52] C. Cardin, B. Renou, G. Cabot, and A. M. Boukhalfa. Experimental analysis of laser-induced spark ignition of lean turbulent premixed flames: New insight into ignition transition. *Combustion and Flame*, 160(8):1414–1427, 2013.

[53] D. R. Ballal and A. H. Lefebvre. Ignition of liquid fuel sprays at subatmospheric pressures. *Combustion and Flame*, 31:115–126, 1978.

[54] D. Ballal and A. Lefebvre. The influence of spark discharge characteristics on minimum ignition energy in flowing gases. *Combustion and Flame*, 24:99–108, 1975.

[55] D. Ballal and A. Lefebvre. The influence of flow parametrs on minimum ignition energy and quenching distance. *Proceedings of the Combustion Institute*, 15:1473–81, 1976.

[56] D. Ballal and A. Lefebvre. Ignition and flame quenching of flowing heterogeneous fuel-air mixtures. *Combustion and Flame*, 35:155–168, 1979.

[57] S. F. Ahmed, R. Balachandran, and E. Mastorakos. Measurements of ignition probability in turbulent non-premixed counterflow flames. *Proceedings of the Combustion Institute*, 31(1):1507–1513, 2007.

[58] E. S. Richardson and E. Mastorakos. Numerical investigation of forced ignition in laminar counterflow non-premixed methane-air flames. *Combustion Science and Technology*, 179:21–37, 2007.

[59] T. Marchione, S. F. Ahmed, and E. Mastorakos. Ignition of turbulent swirling n-heptane spray flames using single and multiple sparks. *Combustion and Flame*, 156(1):166–180, 2009.

[60] Vandel A. Cabot G. Renou B. Cordier, M. and A. M. Boukhalfa. Laser-induced spark ignition of premixed confined swirled flames. *Combustion Science and Technology*, 185(3):379–407, 2013.

[61] H. Nomura, M. Hayasaki, and Y. Ujiie. Effects of fine fuel droplets on a laminar flame stabilized in a partially prevaporized spray stream. *Proceedings of the Combustion Institute*, 31(2):2265–2272, 2007.

[62] S. F. Ahmed and Epaminondas Mastorakos. Spark ignition of a turbulent shear-less fuel–air mixing layer. *Fuel*, 164:297–304, 2016.

[63] M. Klein, N. Chakraborty, and R. S. Cant. Effects of turbulence on self-sustained combustion in premixed flame kernels: A direct numerical simulation (dns) study. *Flow, Turbulence and Combustion*, 81(4):583–607, 2008.

[64] C. Nicoli, B. Denet, and P. Haldenwang. Rich spray-flame propagating through a 2dlattice of alkane droplets in air. *Combustion and Flame*, 162(12):4598–4611, 2015.

[65] C. Letty, B. Renou, J. Reveillon, S. Saengkaew, and G. Gréhan. Experimental study of droplet temperature in a two-phase heptane/air v-flame. *Combustion and Flame*, 160(9):1803–1811, 2013.

[66] A. P. Wandel. Influence of scalar dissipation on flame success in turbulent sprays with spark ignition. *Combustion and Flame*, 161(10):2579–2600, 2014.

[67] N. Chakraborty, E. Mastorakos, and R. S Cant. Effects of turbulence on spark ignition in inhomogeneous mixtures: a direct numerical simulation study. *Combustion Science and Technology*, 179:293–317, 2007.

[68] V Subramanian, P Domingo, and L Vervisch. Large eddy simulation of forced ignition of an annular bluff-body burner. *Combustion and Flame*, 157:579–601, 2010.

[69] R. Abdel-Gayed, K. Al-Khishali, and D. Bradley. Turbulent burning velocities and flame straining in explosions. *PProceedings of the Royal Society of London A*, 391:393–414, 1984.

[70] B. Renou. An experimental study of freely propagating premixed flames at various lewis numbers. *Combustion Science and Technology*, 162(1):347–370, 2001.

[71] M. Mansour, N. Peters, and L.-U. Schrader. Experimental study of turbulent flame kernel propagation. *Experimental Thermal and Fluid Science*, 32:1396–1404, 2008.

[72] B. Galmiche, F. Halter, and F. Foucher. Effects of high pressure, high temperature and dilution on laminar burning velocities and markstein lengths of iso-octane/air mixtures. *Combustion and Flame*, 159(11):3286–3299, 2012.

[73] M. Cordier. *Allumage et propagation de flamme dans les écoulements fortement swirlés : études expérimentales et numériques*. PhD thesis, INSA de Rouen, 2013.

[74] A. Neophytou, E. Mastorakos, and R. S. Cant. The internal structure of igniting turbulent sprays as revealed by complex chemistry dns. *Combustion and Flame*, 159(2):641–664, 2012.

[75] J. Reveillon and L. Vervisch. Analysis of weakly turbulent dilute-spray flames and spray combustion regimes. *Journal of Fluid Mechanics*, 537:317 – 347, 2005.

[76] K. Canneviere. *Simulation numerique directe de la combustion turbulente diphasique: Application a l'etude de la propagation et de la structure des flammes*. PhD thesis, INSA de Rouen, 2003.

[77] N. G. Rosa. *Phenomenes d'allumage d'un foyer de turbomachine en conditions de haute altitude*. PhD thesis, Universite de Toulouse, 2008.

[78] G. Linassier. *Etude experimentale et numerique de l'allumage des turboreacteurs en conditions de haute altitude*. PhD thesis, Universite de Toulouse, 2012.

[79] S. K. Aggarwal. A review of spray ignition phenomena: Present status and future research. *Progress in Energy and Combustion Science*, 24(6):565–600, 1998.

[80] S. K. Aggarwal. Single droplet ignition: Theoretical analyses and experimental findings. *Progress in Energy and Combustion Science*, 45:79–107, 2014.

[81] A. Neophytou, E. S. Richardson, and E. Mastorakos. Spark ignition of turbulent recirculating non-premixed gas and spray flames: A model for predicting ignition probability. *Combustion and Flame*, 159(4):1503–1522, 2012.

[82] A. Neophytou. *Spark Ignition and Flame Propagation in Sprays*. PhD thesis, University of Cambridge, England, 2010.

[83] Kariuki J. Dawson J. R. Mastorakos E. Bach, E. and H. J. Bauer. Spark ignition of single bluff-body premixed flames and annular combustors. *AIAA Paper No. 2013-1182*, 2013.

[84] R W Read, J W Rogerson, and S Hochgreb. Flame imaging of gas-turbine relight. *AIAA Journal*, 48(9):1919–1927, 2010.

[85] R W Read, J W Rogerson, and S Hochgreb. Planar Laser-Induced Fluorescence Fuel Imaging During Gas-Turbine Relight. *Journal of Propulsion and Power*, 29(4):961–974, April 2013.

[86] J. F. Bourgouin, D. Durox, T. Schuller, J. Beaunier, and S. Candel. Ignition dynamics of an annular combustor equipped with multiple swirling injectors. *Combustion and Flame*, 160(8):1398–1413, 2013.

[87] M. Philip, M. Boileau, R. Vicquelin, T. Schmitt, D. Durox, J. F. Bourgouin, and S. Candel. Simulation of the ignition process in an annular multiple-injector combustor and comparison with experiments. *Journal of Engineering for Gas Turbines and Power*, 137(3):031501, 2014.

[88] M. Philip, M. Boileau, R. Vicquelin, E. Riber, T. Schmitt, B. Cuenot, D. Durox, and S. Candel. Large eddy simulations of the ignition sequence of an annular multiple-injector combustor. *Proceedings of the Combustion Institute*, 35(3):3159–3166, 2015.

[89] M. Cordier, A. Vandel, B. Renou, G. Cabot, A. M. Boukhalfa, L. Esclapez, D. Barré, B. Cuenot, and L. Gicquel. Experimental and numerical analysis of an ignition sequence in a multiple-injectors burner. In *Proceeding of ASME Turbo Expo GT 2013 - 94681*.

[90] D. Barré, L. Esclapez, M. Cordier, E. Riber, B. Cuenot, G. Staffelbach, B. Renou, A. Vandel, L. Y. M. Gicquel, and G. Cabot. Flame propagation in aeronautical swirled multi-burners: Experimental and numerical investigation. *Combustion and Flame*, 161(9):2387–2405, 2014.

[91] E. Machover and E. Mastorakos. Spark ignition of annular non-premixed combustors. *Experimental Thermal and Fluid Science*, 73:64–70, 2016.

[92] E. Machover and E. Mastorakos. Experimental and numerical investigation on spark ignition of linearly arranged non-premixed swirling burners. *Combustion Science and Technology*, 189(8):1326–1353, 2017.

[93] E. Machover and E. Mastorakos. Experimental investigation on spark ignition of annular premixed combustors. *Combustion and Flame*, 178:148–157, 2017.

[94] E. Machover and E. Mastorakos. Numerical investigation of the stochastic behavior of light-round in annular non-premixed combustors. *Combustion Science and Technology*, 189(9):1467–1485, 2017.

[95] Y. H. Kao, B. T. Samir, , and S. M. Jeng. Aerodynamics study of a linearly-arranged 5-swirler array. *Proceedings of ASME Turbo Expo*, 2014.

[96] N. A Worth and J. R. Dawson. Cinematographic oh-plif measurements of two interacting turbulent premixed flames with and without acoustic forcing. *Combustion and Flame*, 159(3):1109–1126, 2012.

[97] K. Prieur, D. Durox, J. Beaunier, T. Schuller, and S. Candel. Ignition dynamics in an annular combustor for liquid spray and premixed gaseous injection. *Proceedings of the Combustion Institute*, 36(3):3717–3724, 2017.

[98] T Lancien, K. Prieur, D Durox, S. Candel, and R. Vicquelin. Large-eddy simulation of light-round in an annular combustor with liquid spray injection and comparison with experiments. *Proceedings of ASME Turbo Expo*, 2017.

[99] M. Philip. *Dynamique de l'allumage circulaire dans les foyers annulaires multi-injecteurs*. PhD thesis, CentraleSupelec Universite Paris-Saclay, 2016.

[100] Y. H. Kao, M. Denton, X. Wang, S. M. Jeng, and M. C. Lai. Experimental spray structure and combustion of a linearly-arranged 5-swirler array. *Proceedings of ASME Turbo Expo*, (56680), 2015.

[101] K. Kumar. *Global Combustion Responses of Practical Hydrocarbon Fuels: n-heptane, iso-octane, n-decane, n-dodecane and ethylene*. PhD thesis, Case Western Reserve University, 2007.

[102] T. H. Xu and C. Tropea. Improving the performance of two-component phase doppler anemometers. *Measurement Science and Technology*, 5(8):969, 1994.

[103] C. Tropea. *The Development of the Phase Doppler Technique*, pages 279–292. Springer Berlin Heidelberg, Berlin, Heidelberg, 1999.

[104] G. Gréhan, G. Gouesbet, A. Naqwi, and F. Durst. Evaluation of a phase doppler system using generalized lorenz-mie theory. *Proc. Int. Conf. on Multiphase Flows '91 Tsukuba*, pages 291–296, 1991.

[105] K. Dullenkopf, M. Willmann, S. Wittig, F. Schöne, M. Stieglmeier, C. Tropea, and C. Mundo. Comparative mass flux measurements in sprays using a patternator and the phase-doppler technique. *Particle and Particle Systems Characterization*, 15(2):81–89, 1998.

[106] F. Durst, C. Tropea, and T.-H. Xu. The slit effect in phase doppler anemometry. *Fluid dynamic measurement and its applications: Modern techniques and measurements in fluid flows*, pages 38–43, 1994.

[107] H. E. Albrecht, N. Damaschke, M. Borys, and C. Tropea. *Laser Doppler and Phase Doppler Measurement Techniques*. Experimental Fluid Mechanics. Springer Berlin Heidelberg, 2002.

[108] T. Providakis. *Etude de la dynamique de flamme swirlé dans un injecteur diphasique multipoints étagé*. PhD thesis, Ecole Centrale Paris, 2013.

[109] C. E. Willert and M. Gharib. Digital particle image velocimetry. *Experiments in Fluids*, 10(4):181–193, 1991.

[110] M. Riethmuller, L. David, and B. Lecordier. *Particle Image Velocimetry*, pages 159–281. John Wiley and Sons, Inc., 2012.

[111] M. Raffel, C. E. Willert, and J. Kompenhans. *Particle Image Velocimetry: A Practical Guide.* Springer, 1998.

[112] A. K. Prasad, R. J. Adrian, C. C. Landreth, and P. W. Offutt. Effect of resolution on the speed and accuracy of particle image velocimetry interrogation. *Experiments in Fluids*, 13(2):105–116, 1992.

[113] J. Lemetayer. *Etude par PIV par fluorescence de l'interaction d'un spray avec un écoulement gazeux en aérodynamique contrôlée - Application à l'injection directe essence*. PhD thesis, INSA Rouen, 2016.

[114] C. Schulz and V. Sick. Tracer-lif diagnostics: quantitative measurement of fuel concentration, temperature and fuel/air ratio in practical combustion systems. *Progress in Energy and Combustion Science*, 31(1):75–121, 2005.

[115] N. Pasquier-Guilbert. *Mesures couplées de richesse et de vitesse pour la combustion instationnaire en écoulement stratifié.* PhD thesis, Universite de Rouen, 2004.

[116] B. H. Y. Cheung. *Tracer-based planar laser-induced fluorescence diagnostics: quantitative photophysics and time-resolved imaging.* PhD thesis, Stanford University, 2011.

[117] W. Koban, J. D. Koch, R. K. Hanson, and C. Schulz. Oxygen quenching of toluene fluorescence at elevated temperatures. *Applied Physics B*, 80(6):777–784, 2005.

[118] H. L. U. Rehman, A. Mohammed-Taifour, J. Weiss, and P. Seers. *PLIF Experiments on Evaporating Isolated Droplet and Droplets Array.* AIAA AVIATION Forum. American Institute of Aeronautics and Astronautics, 2016.

[119] X. Mercier, M. Orain, and F. Grisch. Investigation of droplet combustion in strained counterflow diffusion flames using planar laser-induced fluorescence. *Applied Physics B*, 88(1):151–160, 2007.

[120] B. Frackowiak, A. Strzelecki, and G. Lavergne. A liquid–vapor interface positioning method applied to plif measurements around evaporating monodisperse droplet streams. *Experiments in Fluids*, 46(4):671–682, 2009.

[121] D. Wolff, H. Schlüter, V. Beushausen, and P. Andresen. Quantitative determination of fuel air mixture distributions in an internal combustion engine using plif of acetone. *Berichte der Bunsengesellschaft für physikalische Chemie*, 97(12):1738–1740, 1993.

[122] S. Sahu, Y. Hardalupas, and A. M. K. P. Taylor. Simultaneous droplet and vapour-phase measurements in an evaporative spray by combined ilids and plif techniques. *Experiments in Fluids*, 55(2):1673, 2014.

[123] P. Xavier, A. Vandel, G. Godard, B. Renou, F. Grisch, G. Cabot, A. M. Boukhalfa, and M. Cazalens. Investigation of combustion dynamics in a cavity-based combustor with high-speed laser diagnostics. *Experiments in Fluids*, 57(4):50, 2016.

[124] A. C. Eckbreth. *Laser Diagnostics for Combustion Temperature and Species*. Combustion science and technology book series. Taylor and Francis, 1996.

[125] F. Grisch and M. Orain. Role of planar laser-induced fluorescence in combustion research. *AerospaceLab*, (1):1–14, 2009.

[126] K. Kohse-Hoinghaus. Laser techniques for the quantitative detection of reactive intermediates in combustion systems. *Progress in Energy and Combustion Science*, 20(3):203–279, 1994.

[127] K. A. Watson, K. M. Lyons, J. M. Donbar, and C. D. Carter. Scalar and velocity field measurements in a lifted ch4–air diffusion flame. *Combustion and Flame*, 117(1):257–271, 1999.

[128] A. Bresson. *Quantitative imaging techniques: laser-induced fluorescence applied to the turbulent flows and combustion*. PhD thesis, Université de Rouen, 2000.

[129] H. El-Rabii. *Etude de l'allumage par laser de melanges en phases liquides dispersees et gazeuses*. PhD thesis, Ecole Centrale Paris, 2004.

[130] M. G. Zabetakis. *Flammability characteristics of combustible Gases and Vapors*. ISA, Research Triangle Park, North Carolina 27709, 1999.

[131] O. Colin and M. Rudgyard. Development of high-order taylor–galerkin schemes for les. *Journal of Computational Physics*, 162(2):338–371, 2000.

[132] P. Lax and B. Wendroff. Systems of conservation laws. *Comm. Pure Appl. Math*, 13:217, 1960.

[133] T. J&amp Poinsot and SK Lelef. Boundary conditions for direct simulations of compressible viscous flows. *J. Comput. Phys.*, 101(1):104–129, 1992.

[134] F. Nicoud, H. B. Toda, O. Cabrit, S. Bose, and J. Lee. Using singular values to build a subgrid-scale model for large eddy simulations. *Phy. Fluids*, 23(8):085106, 2011.

[135] F. Shum-Kivan, J. Marrero-Santiago, A. Verdier, E. Riber, B. Renou, G. Cabot, and B. Cuenot. Experimental and numerical analysis of a turbulent spray flame structure. *Proceedings of the Combustion Institute*, 36(2):2567–2575, 2017.

[136] S Jerzembeck, N Peters, P. Pepiot-Desjardins, and H Pitsch. Laminar burning velocities at high pressure for primary reference fuels and gasoline: Experimental and numerical investigation. *Combustion and Flame*, 156(2):292–301, 2009.

[137] P. Pepiot. *Automatic strategies to model transportation fuel surrogates*. PhD thesis, Stanford University, USA, 2008.

[138] G. Lacaze, E. Richardson, and T. Poinsot. Large eddy simulation of spark ignition in a turbulent methane jet. *Combustion and Flame*, 156(10):1993–2009, 2009.

[139] A. N. Lipatnikov and J. Chomiak. Molecular transport effects on turbulent flame propagation and structure. *Progress in Energy and Combustion Science*, 31(1):1–73, 2005.

[140] J. Reveillon and F. X. Demoulin. Effects of the preferential segregation of droplets on evaporation and turbulent mixing. *Journal of Fluid Mechanics*, 583:273–302, 2007.

[141] A. Verdier, J. Marrero-Santiago, A. Vandel, G. Godard, G. Cabot, and B. Renou. Local extinction mechanisms analysis of spray jet flame using high speed diagnostics. *Submitted to Combustion and Flame*, 2018.

[142] R. W. Bilger. The structure of turbulent nonpremixed flames. *Proceedings of the Combustion Institute*, 22(1):475–488, 1989.

[143] L. Esclapez, E. Riber, and B. Cuenot. Ignition probability of a partially premixed burner using les. *Proceedings of the Combustion Institute*, 35(3):3133–3141, 2015.

[144] G. C Gebel, T. Mosbach, W. Meier, and M. Aigner. Laser-induced blast waves in air and their effect on monodisperse droplet chains of ethanol and kerosene. *Shock Waves*, 25(4):415–429, 2015.

[145] R. George. *Developpement de nouvelles strategies d'allumage laser : application a la propulsion aeronautique et/ou spatiale.* PhD thesis, Universite Paris-Saclay, 2017.

[146] R. Hadef and B. Lenze. Measurements of droplets characteristics in a swirl-stabilized spray flame. *Experimental Thermal and Fluid Science*, 30(2):117–130, 2005.

[147] R. Mercier, T. F. Guiberti, A. Chatelier, D. Durox, O. Gicquel, N. Darabiha, T. Schuller, and B. Fiorina. Experimental and numerical investigation of the influence of thermal boundary conditions on premixed swirling flame stabilization. *Combustion and Flame*, 171:42–58, 2016.

[148] R. Yuan, J. Kariuki, A. Dowlut, R. Balachandran, and E. Mastorakos. Reaction zone visualisation in swirling spray n-heptane flames. *Proceedings of the Combustion Institute*, 35(2):1649–1656, 2015.

[149] R. S. Miller, K. Harstad, and J. Bellan. Evaluation of equilibrium and non-equilibrium evaporation models for many-droplet gas-liquid flow simulations. *International Journal of Multiphase Flow*, 24(6):1025–1055, 1998.

[150] A. Verdier. *Experimental study of dilute spray combustion.* PhD thesis, INSA de Rouen, 2017.

[151] A. Verdier, J. Marrero-Santiago, A. Vandel, S. Saengkaew, G. Cabot, G. Grehan, and B. Renou. Experimental study of local flame structures and fuel droplet properties of a spray jet flame. *Proceedings of the Combustion Institute*, 36(2):2595–2602, 2017.